The system quartz-albite-orthoclase-anorthite-H_2O as a geobarometer: experimental calibration and application to rhyolites of the Snake River Plain, Yellowstone, USA

Der Naturwissenschaftlichen Fakultät der Gottfried Wilhelm Leibniz Universität Hannover

zur Erlangung des Grades
Doktor der Naturwissenschaften (Dr. rer. nat.)

vorgelegte Dissertation
von
M. Sc. Sören Wilke

geboren am 22.08.1987 in Hannover

ACKNOWLEDGEMENTS

I would first like to acknowledge the Deutsche Forschungsgemeinschaft (DFG) for funding the project HO1337/31

Further thanks to my supervisors for their support: Prof. Dr. François Holtz and Dr. Renat Almeev. I would also like to thank the reviewers of this dissertation: Prof. Dr. François Holtz, Prof. Dr. Eric H. Christiansen and Prof. Dr. Michel Pichavant.

This research would not have been possible without massive support from the technical staff of the workshop and I owe thanks especially to Julian Feige, Ulrich Kroll, Björn Ecks and Manuel Christ. Many thanks to the staff of the electron microprobe Prof. Dr. Jürgen Koepke, Dr. Renat Almeev, Dr. Tim Müller, Dr. Eric Wolff and Dr. Chao Zhang and to Prof. Dr. Harald Behrens for help with IHPV and KFT.

Thanks to Dr. Roman Botcharnikov and Dr. David Naeve for their ideas on experimental and statistical procedures.

Operating an IHPV is challenging and I would like to thank Dr. Adrian Fiege and Dr. André Stechern for teaching me how to do it and helping me with troubleshooting.

I would like to thank Carolin Klahn who started the work that I herewith complete (hopefully) and Torsten Bolte who provided samples and know how on the Snake River Plain. Further thanks go to Dominik Mock who with his B.Sc. Thesis contributed to my work and in general provided what you could call a good time instead of making it harder.

My work massively profited from being written in a working atmosphere of friendship, expertise and cake to which the following persons, in different propotions of the listed attributes, greatly contributed: Torsten Bolte, Jakub Ciazela, Martin Erdmann, Dr. Svenja Erdmann, Lennart Fischer, Stefan Linsler, Dr. Tim Müller, Dawid Murawski, Dr. David Naeve, Dr. Olivier Namur, Dr. Martin Oeser-Rabe, Dongmei Qi, Mahender Singh Rajpurohit, Dr. Lars Schomborg, Marize Muniz da Silva, Dr. André Stechern, Dr. Anna-Maria Welsch, Dr. Chao Zhang and all the phd students of the institute, the unsung heroes of science. It has been a privilege. Thank you.

Finally I would like to thank my Family; my parents Karin and Joachim – no one could wish for better parents. Thanks to my brother Ron, to Herbert, who inspired me, Irmtraut, who teached me, Harmannus and Erika. A special thanks to Anne.

ABSTRACT

In the rhyolite system Qz-Ab-Or-(An-H_2O) the position of the cotectic curve separating the quartz and feldspar(s) stability fields depends on pressure, making it a potential geobarometer applicable to high SiO_2 volcanic products if the melt H_2O contents are known. Until the recent years, the applicability of this geobarometer has been very limited, as the pressure effect can be largely obscured by the near ubiquitous presence of normative anorthite (An, $CaSi_2Al_2O_8$) in the melt. In this study new phase diagrams are presented that make it possible to constrain the position of eutectic points and cotectic curves at various pressures and melt normative An contents. Data were derived experimentally by conducting crystallization experiments to determine phase diagrams at following conditions: 200 MPa, 1.4 wt.% H_2O, 3.5 wt.% An; 200 MPa, 1.3 wt.% H_2O, 7 wt.% An; 500 MPa, 3 wt.% H_2O, 3.5 wt.% An; 500 MPa, 1.4 wt.% H_2O, 3.5 wt.% An and 500 MPa, 1.3 wt.% H_2O, 7 wt.% An. Using this database and previous results on phase equilibria, a geobarometer is constructed based on the effect of the main parameters influencing the cotectic compositions in the rhyolitic system: pressure, melt water content and melt An content. This new geobarometer DERP (**D**etermining **E**utectic **R**hyolite **P**ressures) is calibrated to calculate pressures of magma storage from the compositions of cotectic glasses with up to 7 wt.% normative melt An. DERP is calibrated for any melt H_2O content in the pressure range 50 – 500 MPa and its application is restricted to high silica rhyolitic systems saturated with respect to quartz and feldspar(s). DERP was tested successfully against various independent methods of pressure estimation in rhyolites available in the literature (with $r^2 > 80\%$ and an overall error of less than 100 MPa). The comparison of pressures estimated with DERP and rhyolite-MELTS, which are two barometers based on the same approach, indicates that rhyolite-MELTS, calibrated using an old dataset, underestimates the effect of An. With DERP now available, pressure estimates can be made for the relatively dry rhyolites of the Snake River Plain, Yellowstone (SRPY), USA, where this was hardly possible before. The SRPY was formed by the movement of the northamerican Plate over a fix mantle plume. This process created over the course of the last ~ 17 Ma several eruptive complexes and caused numerous volcanic eruptions with huge volumes of rhyolitic material deposited in the area. The eruptive centers are McDermit (McD, 16.5 Ma), Owyhee-Humboldt (OH, 15.3 Ma), Bruneau-Jarbidge (BJ, 12.7 Ma), Twin Falls (TF, 10.5 Ma), Picabo (P, 10.2 Ma), Heise (H, 6.6 Ma) and Yellowstone Plateau (YP, 2 Ma). DERP was used in combination with the independent TitaniQ geobarometer to estimate magma storage pressures for four of these eruptive centers (BJ, TF, H and YP). A focus was set to samples from the Twin Falls eruptive center, where a drill core obtained by ICDP project HOTSPOT close to the city of Kimberly, Idaho (USA), allows for a detailed insight into the stratigraphy. Results show that the magma storage pressure is constant within an eruptive complex but decreases with time between different eruptive complexes among the SRPY. Estimated pressures are 351 ± 35 MPa for Bruneau-Jarbidge, 264 ± 31 MPa for Twin Falls, ~230 MPa for Heise and ~140 MPa for Yellowstone Plateau. Reasons for these abrupt deacreases over time might lay in changes of the elastic thickness of the crust in the SRPY and its geometry on its lower side during the interaction with the hot mantle plume.

ZUSAMMENFASSUNG

Im rhyolithischen System Qz-Ab-Or-(An-H_2O) ist die Position der kotektischen Kurve, welche das Stabilitätsfeld des Quarzes von dem der Feldspäte trennt, direkt abhängig vom Druck, womit dieses System das Potential besitzt, als Geobarometer für SiO_2-reiche Vulkanite zu dienen. Bis in die jüngste Vergangenheit war der Nutzen dieses Effektes für die Geobarometrie sehr beschränkt, da der Einfluss des Druckes durch andere Effekte überlagert werden kann, etwa durch die Anwesenheit normativen Schmelz-Anorthits (An, $CaAl_2Si_2O_8$). In der vorliegenden Arbeit werden neue Phasendiagramme vorgestellt, welche eine präzise Bestimmung der Position von eutektischem Punkt und kotektischen Kurven für verschiedene Drücke und Schmelz-An Gehalte ermöglichen. Diese Daten wurden experimentell bestimmt, wobei folgende Systeme untersucht wurden: 200 MPa, 1.4 wt.% H_2O, 3.5 wt.% An; 200 MPa, 1.3 wt.% H_2O, 7 wt.% An; 500 MPa, 3 wt.% H_2O, 3.5 wt.% An; 500 MPa, 1.4 wt.% H_2O, 3.5 wt.% An and 500 MPa, 1.3 wt.% H_2O, 7 wt.% An. Diese neuen Daten ermöglichen die Konstruktion eines Geobarometers, das auf dem nun vertieften Verständnis des Einflusses der drei Parameter Druck, normativer An-Gehalt der Schmelze und H_2O-Gehalt der Schmelze beruht. Dieses neue Geobarometer, im weiteren bezeichnet als DERP (**D**etermining **E**utectic **R**hyolite **P**ressures), ist dazu kalibriert, den Equilibrierungsdruck von Schmelzen aus der Zusammensetzung kotektischer Gläser zu berechnen, die bis zu 7 gew.% normativen Schmelz-An enthalten. Die Kalibration von DERP gilt für jeden beliebigen Schmelz-H_2O Gehalt und über einen Druckbereich von 50 bis 500 MPa. Die Anwendung von DERP beschränkt sich dabei auf SiO_2-reiche Systeme, die saturiert sind mit Quarz und mindestens einem Feldspat. DERP wurde erfolgreich getestet bei einem Vergleich mit verschiedenen unabhängigen, in der Fachliteratur beschriebenen geobarometrischen Methoden, deren berechnete Drücke für Rhyolithe mit einer Genauigkeit $r^2 > 80\%$ und einer durchschnittlichen Abweichung von unter 100 MPa reproduziert werden konnten. Der Vergleich von Drücken, die mit DERP und der rhyolite-MELTS Software berechnet wurden, zeigt, dass rhyolite-MELTS den Einfluss des normativen Schmelz-Anorthits klar unterschätzt. Mit Hilfe von DERP lassen sich nun Drücke selbst für relativ trockene Rhyolithe wie die der Snake River Plain, Yellowstone, (SRPY), USA berechnen, wo dies bisher nur schwer möglich war. Die SRPY ist durch den Kontinentaldrift der nordamerikanischen Platte in südöstlicher Richtung über einen ortsfesten Mantel-Hotspot entstanden. Im Zuge dieses Prozesses bildeten sich im Verlauf der letzten etwa 17 Millionen Jahre (Ma) eine Reihe vulkanischer Eruptionskomplexe. Für vier dieser Eruptionskomplexe (Brunea-Jarbidge, BJ; Twin Falls, TF; Heise, H; Yellowstone Plateau, YP) wurden mit DERP und dem TitaniQ barometer Drücke berechnet. Ein Schwerpunkt der Untersuchung lag dabei auf Proben des Twin Falls Komplexes, aus dessen Gebiet ein Bohrkern aus einer Bohrung des ICDP Projektes HOTSPOT vorlag. Für die untersuchten Eruptionskomplexe wurden die folgenden Drücke berechnet: 351 ± 35 MPa für BJ, 264 ± 31 MPa für TF, ~230 MPa für H und ~140 MPa für YP. Innerhalb eines Komplexes variieren die Drücke jedoch kaum. Der Grund für diese abrupten Wechsel in der Kristallisationtiefe könnte mit Änderungen der mechanischen Eigenschaften der kontinentalen Kruste zusammen hängen, zum Beispiel der Elastizität oder der Dicke aber auch mit der Topographie ihrer Unterseite.

TABLE OF CONTENTS

The system quartz-albite-orthoclase-anorthite-H_2O as a geobarometer: experimental calibration and application to rhyolites of the Snake River Plain, Yellowstone, USA

CHAPTER I - Experimental investigation of the system Qz-Ab-Or-An-H_2O

I-1 Introduction

I-1.1 Geobarometry in rhyolites

Rhyolites represent a very common volcanic material and are often related to explosive volcanism with strong environmental impacts (e.g. Newhall & Self, 1982; Wilson & Walker, 1985; Fierstein & Hildreth, 1992; Bonadonna *et al*., 2005; Blundy & Cashman, 2008; Branney *et al*., 2008; Castro & Dingwell, 2009; Ellis *et al*., 2013). Eruptive styles depend on ascent mechanisms, on magma storage conditions such as temperature (T) and pressure (P) and on compositional parameters such as melt volatile content. However, despite an excellent knowledge of the petrology of rhyolitic systems, it is not trivial to obtain information on the depth of magma chambers for a natural system. Methods commonly applied are the amphibole geothermobarometry (Anderson & Smith, 1995; Bachmann & Dungan, 2002; Ridolfi & Renzulli, 2012) and the calculation of fluid saturation pressures (e.g. Liu *et al*., 2006). However, Ca- and water-poor rhyolites are devoid of amphibole. Furthermore, the application of the fluid saturation approach implies that the H_2O and CO_2 content of glass is representative of pre-eruptive storage conditions, which is not necessarily the case. Another

approach in quartz-bearing volcanic rocks is to exploit the sensitivity of the titanium content of quartz to pressure and temperature, the TitaniQ geothermobarometer (Thomas *et al*., 2010; Huang & Audétat, 2012). Titanium-in-quartz geobarometry is widely applied for rhyolitic systems, but its accuracy is still under debate (Thomas & Watson, 2012; Wilson *et al*., 2012; Thomas *et al*., 2015): the two different models which are available in literature yield very different results for the same input parameters (Thomas *et al*., 2010; Huang & Audétat, 2012). Regardless of which calculation model is applied, the TitaniQ approach also requires an accurate knowledge of T from independent geothermometers (see Putirka, 2008 for a review), and $a\mathrm{TiO_2}$ (Ghiorso & Gualda, 2013, Kularatne & Audétat, 2014).

I-1.2 The haplogranite system Qz-Ab-Or

One alternative for constraining pressure in rhyolitic systems is to apply the knowledge of phase relationships in these systems. Phase diagrams in the haplogranite system quartz (Qz, SiO_2) – albite (Ab, $NaAlSi_3O_8$) – orthoclase (Or, $KAlSi_3O_8$), considered as the best simplified system to interpret granites and rhyolites, have been investigated experimentally in detail for more than 60 years. In particular, early experiments at water-saturated conditions (e.g. Tuttle & Bowen, 1958; Luth *et al*., 1964; Luth, 1969; Steiner *et al*., 1975) showed that increasing pressure leads to a shift of the cotectic curves separating the quartz and the feldspar(s) primary fields away from the Qz apex. Thus, in a first approximation, if the calculated CIPW normative Qz-Ab-Or content of a rhyolitic melt saturated with quartz and feldspar is plotted on a ternary diagram, its position can be used to constrain the pressure at which those phases equilibrated. This procedure, usually referred to as the "ternary projection", is widely used in the recent literature to constrain the depth of rhyolitic magma chambers (e.g. Blundy & Cashman, 2001; El-Sayed, 2003; Almeev *et al*., 2012; Gualda & Ghiorso 2013a, 2013b, 2014; Putirka *et al*., 2014; Bolte *et al*., 2015).

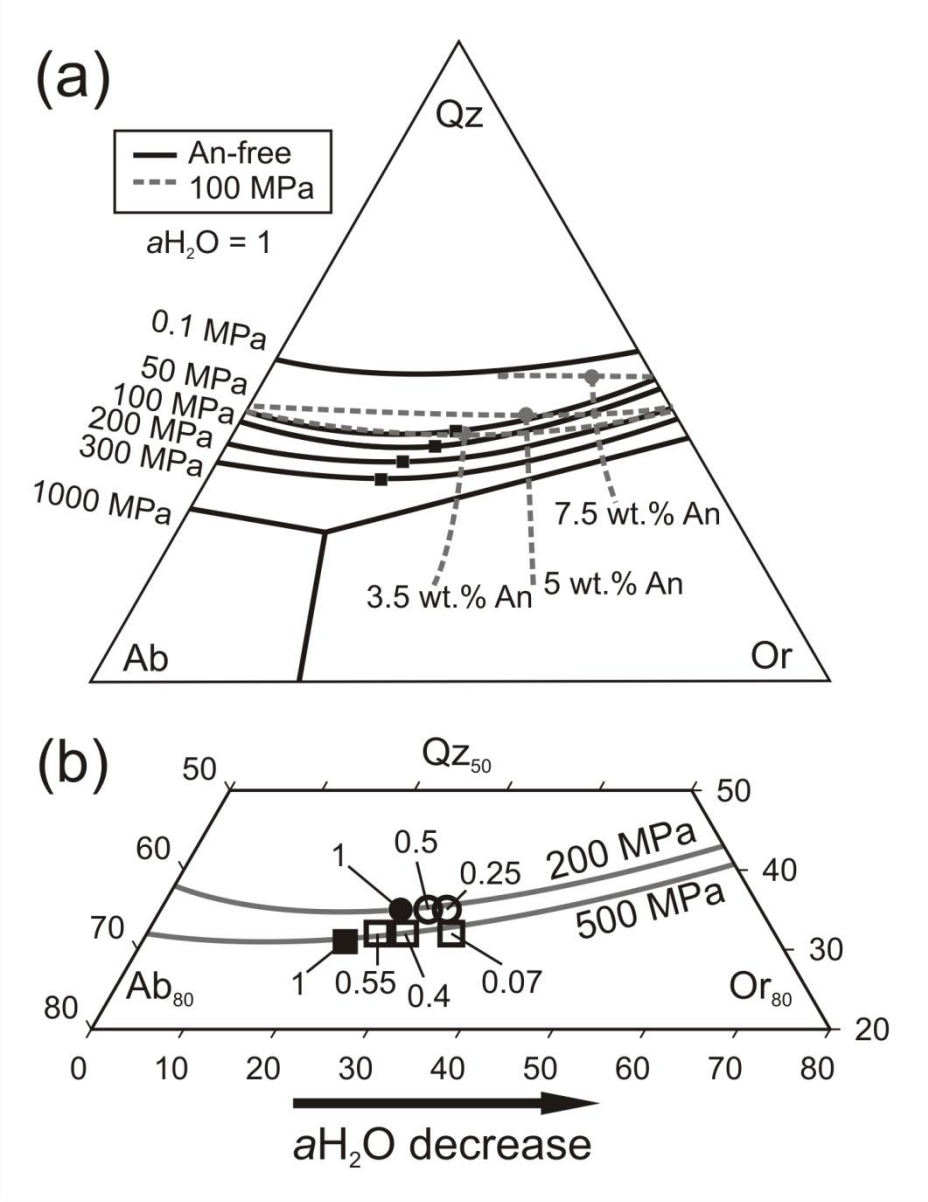

Figure 1: (a) Ternary projection of cotectic curves and minimum points at various levels of P and normative melt An. Black squares and lines are free of An and only differ by pressure as noted in the diagram and contain data from Tuttle & Bowen (1958) and Luth *et al*., (1964). Grey circles and lines represent the effect of different levels of normative melt An as noted in the diagram at 100 MPa constant P. Data from James & Hamilton (1969). (b) Ternary projection of An-free eutectic points with varying aH_2O as noted in the diagram at 200 and 500 MPa. Data from Tuttle & Bowen (1958), Holtz *et al*. (1992b) and Becker *et al*. (1998).

I-1.3 The effects of water and normative melt anorthite

Although the pressure effect on the position of the quartz-feldspar cotectic has been known for more than 60 years, applying the early studies to constrain pressures in natural systems remained difficult because the position of the cotectic curves also varies as a function of melt

H_2O and normative anorthite contents (An, $CaAl_2Si_2O_8$). The effect of water activity on phase equilibria was not systematically quantified until the 1990s (Holtz *et al*.,1992b; Pichavant *et al*., 1992; Becker *et al*., 1998; Holtz *et al*., 2001a; Kirschen & Pichavant, 2001). These studies confirmed that a decrease in pressure shifts the eutectic point in the Qz-Ab-Or projection towards the Qz apex, reducing the size of the Qz stability field, and discovered that a decrease in water activity reduces the size of the sanidine stability field in favor of albite with little changes to the Qz stability field. However, all these experimental studies were carried out in the simplified haplogranite system, including only SiO_2, Al_2O_3, Na_2O and K_2O and their application to natural rhyolites, containing mainly FeO and CaO as additional oxides, is restricted. This limitation was initially overcome by the experiments of James & Hamilton (1969), conducted in the quaternary system Qz-Ab-Or-An, which demonstrated that the presence of CaO leads to a shift of the eutectic point away from the Ab-apex, which is comparable, yet not similar, to the effect of decreasing pressure, as illustrated in Figure 1(a). These observations thus indicate that the well-known pressure dependence of the cotectic curves in the haplogranite system cannot directly be implemented for the description of natural rhyolites. Blundy & Cashman (2001) proposed a correction procedure that accounts for normative melt An in order to overcome this issue. The approach proposed by Blundy & Cashman (2001) relies mainly on the three phase diagrams determined by James & Hamilton (1969) and was implemented in rhyolite-MELTS (Gualda & Ghiorso, 2014) and this model has since then been applied intensively to estimate magma storage pressures in various locations (Bégué *et al.,* 2014a, 2014b; Gardner *et al.,* 2014; Pamukcu *et al*., 2015).

Although the correction proposed by Blundy & Cashman (2001) improved significantly the accuracy of pressure determination from cotectic compositions, recent experimental results from Wilke *et al.* (2015) indicate that this approach based on the experimental database of James & Hamilton (1969), only obtained at 100 MPa and more importantly under water-

saturated conditions, are insufficient to establish an accurate geobarometer from the composition of Ca-bearing cotectic melts. In particular, it is known that the effect of water activity plays a significant role on the composition of plagioclase (e.g. Lange *et al*., 2009), which may affect the primary field of plagioclase and the position of cotectics in the system Qz-Ab-Or-An (c.f. Figure 2).

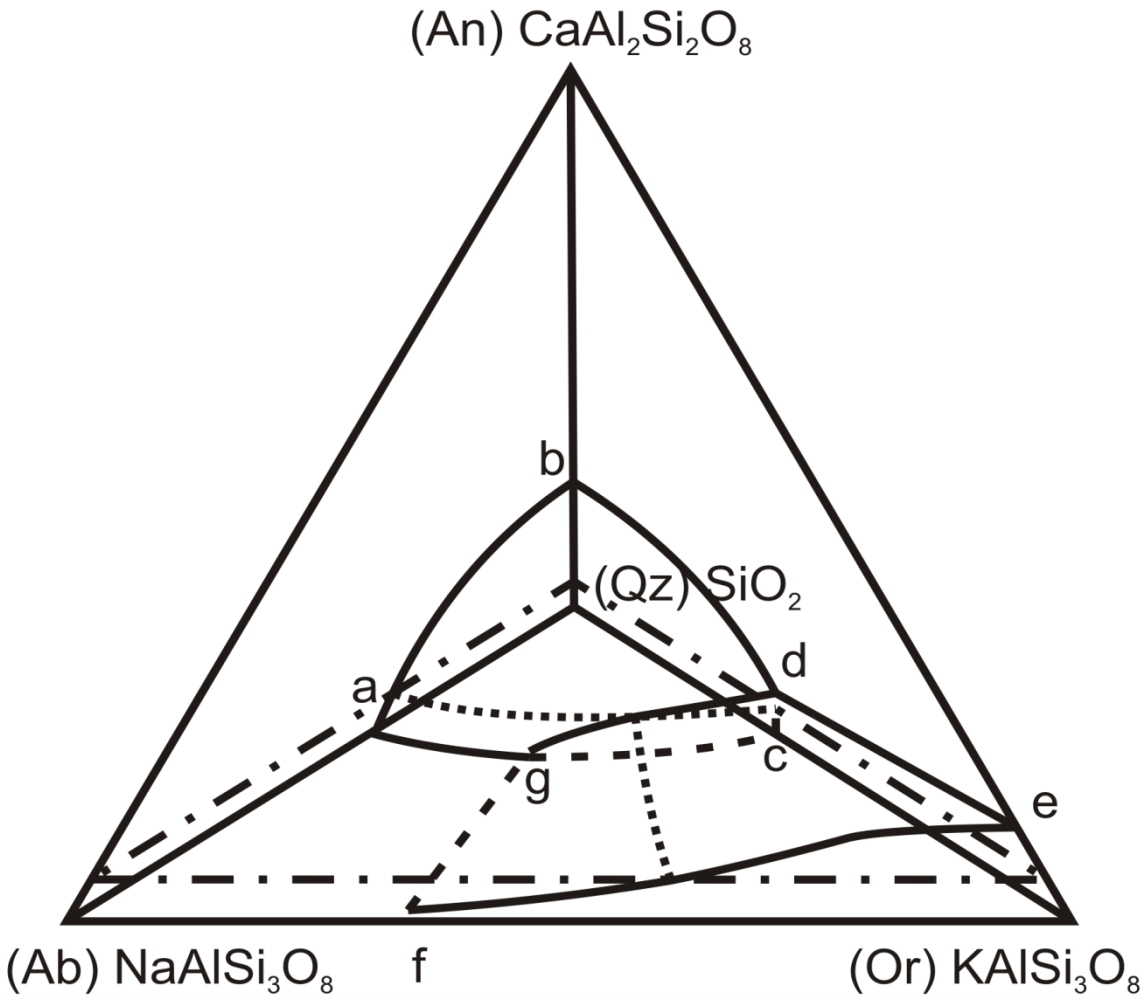

Figure 2: The quarternary system Qz-Ab-Or-An after James & Hamilton (1969). The drawn lines connecting a, b and c illustrate the position of the quartz stability field, while the lines connecting d, e, f and g mark the position of the sanidine field. The dash-dotted line represents a hypothetical projection section for a system with ~5 wt.% normative An plotted into the ternary Qz-Ab-Or diagram. Dotted lines indicate the position of the cotectic curves, where the section is cutting the phase stability fields.

In this study, the composition of cotectic melts (melts coexisting with quartz and one feldspar) and eutectic melts have been determined for water-undersaturated, Ca-bearing rhyolitic

systems at 200 and 500 MPa. The low water activities (equivalent to H_2O contents of ~1.3 and 3 wt.%) have been chosen so that the results can be directly applied to water-poor, high temperature rhyolitic systems such as those observed in the Snake River Plain, Yellowstone, USA (e.g. Bonnichsen *et al*., 2008, Almeev *et al*., 2012, Bolte *et al*., 2015). The results, combined with those of previous studies, are used to propose an empirical approach to determine the pressure of magma storage from the composition of melts in equilibrium with quartz and feldspar(s).

I-2 Experimental and analytical procedure

I-2.1 Preparation of the starting material and experimental procedure

I-2.1.a) Experimental outline

For the investigation of phase relationships in multicomponent systems, such as the system Qz-Ab-Or-An(-H_2O), the determination of the primary fields of mineral phases, of the eutectic composition and of the position of the cotectic curves can best be determined by performing crystallization experiments focusing on the determination of the liquidus phase and the liquidus temperatures in various compositions. In rhyolitic systems the experimental compositions have typically different proportions of the main components Qz, Ab, Or and An. Wilke *et al*. (2015) demonstrated that this method is applicable to systems that are closer in composition to natural rhyolites and contain a fixed concentration of FeO and TiO_2. In this study five phase diagrams obtained at 200 MPa and 500 MPa are described for three different compositions: 3.5 wt.% An and 1.4 wt.% H_2O (Table 1, A & D), 3.5 wt.% An and 3 wt.% H_2O (Table 1, C), 7 wt.% An, 1.3 wt. H_2O (Table 1, B & E). A sixth phase diagram with 3.5 wt.% An and 3 wt.% H_2O was investigated at 200 MPa by Wilke *et al*. (2015) and is listed in Table 1 as system F as it closely complements the experiments of this study. Small amounts of FeO (1 to 2.5 wt.%) and TiO_2 (0.2 to 0.4 wt.%) were added to better simulate conditions

close to natural rhyolites. For each phase diagram obtained at a fixed pressure and at fixed H_2O, An, FeO and TiO_2 contents in the system (Table 1), experiments were carried out at various temperatures in order to determine the respective liquidus phase and liquidus temperature of several compositions with different Qz-Ab-Or ratios. The starting materials were pre-hydrated glass powders with known H_2O concentrations and no additional volatile components were added in the experimental capsules. This approach was applied to obtain phase diagrams at well constrained water activities and differs from previous studies on phase relations in the system Qz-Ab-Or(-An-)H_2O (Tuttle & Bowen, 1958; Luth *et al*., 1964; James & Hamilton, 1969; Manning, 1981; Pichavant, 1987; Holtz *et al*., 1992b). In these previous studies, either gels or dry glasses were used and volatiles were added in the capsules to ensure the presence of a fluid phase. For experiments at water-saturated conditions this procedure was not problematic since water activity was unity in the presence of an excess of water. For water-undersaturated conditions, CO_2 was added to reduce the water activity of the fluid phase. However, to avoid high proportions of a fluid phase in the capsule, which would lead to incongruent dissolution of silicates into the fluid phase and would modify the melt composition, the amounts of CO_2 and H_2O which should be added are very low (see Figure 1 in Holtz *et al*., 1992b) and the uncertainty on the resulting water activity is rather high. Thus in this study it was preferred to apply a fluid absent approach, in which the water activity can be hold perfectly constant for a series of experiments by preparing hydrous glasses with well characterized H_2O concentrations.

I-2.1.b) Synthesis of the starting material

The glasses were synthesized by mixing oxide (SiO_2, TiO_2, Al_2O_3, Fe_2O_3) and carbonate ($CaCO_3$, Na_2CO_3, K_2CO_3) powders in the desired proportions and melting them twice at 1600°C in a 1 atmosphere furnace using a platinum crucible. Each melting step was followed by crushing the derived glass in a steel mortar and then grinding it in an agate mortar. Dry

glass powders were then sealed with the desired amount of H_2O by arc welding in $Au_{80}Pd_{20}$ capsules (30 mm in length and 6 mm in diameter). In order to generate hydrous starting materials the capsules were held at 1200°C and 200 MPa for 24 hours in an internally heated pressure vessel (IHPV, see Berndt *et al*., 2002 for description) pressurized with Ar (200 or 500 MPa). A slow speed saw was used to cut top- and bottom parts of each hydrous glass cylinder in order to check for homogeneity in major element and H_2O-contents. The remainder of each pre-hydrated glass cylinder was once more crushed and ground as described above and then used as a starting material for the crystallization experiments.

Table 1: List of experimentally investigated systems.

No	P [Mpa]	H_2O [wt.%]	An [wt.%][a]	SM[b]
A	200	1.4	3.5	HYW
B	200	1.3	7	HYS
C	500	3	3.5	REF[c]
D	500	1.4	3.5	HYW
E	500	1.3	7	HYS
F	200	3	3.5	REF[c]

[a] Normative melt anorthite content

[b] Starting Material

[c] described by Wilke et al (2015)

A total of 26 different starting compositions containing approximately 1.3 wt.% H_2O were synthesized for this study (Table 2a). The 18 starting compositions named HYS1 to HYS8 as well as HYS15 to HYS21 and HYS23 to HYS25 contain 7 wt.% An, 2.5 wt.% FeO and 0.4 wt.% TiO_2. These compositions were used to constrain phase diagrams at 200 and 500 MPa for the systems B and E (Table 1). The eight compositions named HYW1 to HYW8 contain 3.5 wt.% An, 1 wt.% FeO and 0.2 wt.% TiO_2. The FeO and TiO_2 contents were lower than for the compositions with 7 wt.% An considering that the expected liquidus temperatures were lower and that less Fe and Ti is incorporated in melts at lower T. HYW compositions were

used for phase diagrams at 200 and 500 MPa in systems A and D (Table 1). The experiments for system C at 500 MPa (see Table 1) were conducted with the glasses AC50, BA5, BC5, BD25, C, DC5 and D, containing ~3 wt.% H_2O and 3.5 wt.% normative An, 1 wt.% FeO and 0.2 wt.% TiO_2. They were synthesized for and described in the study of Wilke *et al*., (2015). The composition of starting materials used for the investigation in system F as described in Wilke *et al*., (2015, their Table 1) are listed here as Table 2b for completeness. During the progress of experimental work for system D (see Table 1), it was observed that starting materials HYW1-8 were insufficient for determining eutectic points with satisfactory precision. In order to investigate compositions closer to the eutectic point, 50:50 mixtures of the starting materials HYW3+5, HYW3+6, HYW3+8 and HYW5+8 were created by mixing appropriate amounts of each material in an agate mortar. The composition of these mixed starting materials is known only from stoichiometric calculations. For crystallization experiments, approximately 30 mg of pre-hydrated glass powder was loaded into a $Au_{80}Pd_{20}$ capsule (12 mm in length and 2.8 mm in diameter) that was closed subsequently by arc-welding. For every experiment, eight capsules were placed next to each other in the IHPV.

I-2.1.c) Experimental procedure

The experiments for systems A to E were conducted in in an IHPV in a temperature range of 870 to 1050°C which was reached with a heating rate of 50°C min^{-1}. The duration of the experiments varied between ~160 h (~6 days) and 340 h (~14 days) depending on T. Experiments were quenched at isobaric conditions (200 or 500 MPa) by switching of the furnace, resulting in a cooling of ~300°C within the first minute. The intrinsic oxygen fugacity (fO_2) of the IHPV as calculated using the model of Pitzer and Sterner (1994) was between QFM +1.75 and +1.85 for experiments conducted at 200 MPa and between QFM +2 and +2.3 for experiments conducted at 500 MPa. It is known however, that in an IHPV the fO_2 in the sample container decreases with the water activity (e.g. Botcharnikov *et al*., 2005).

From comparisons with previous studies (Berndt *et al*., 2002, Botcharnikov *et al*., 2005, Almeev *et al*., 2012), the effective fO_2 in the experiments was approximately QFM -1.2 for the systems A and B, QFM -0.3 for the system C and QFM -1 for the systems D and E.

The experimental investigation of system F was not conducted in the frame of this phd thesis but served as master thesis of Carolin Klahn (Klahn, 2013) and the results were published later by Wilke *et al.* (2015). As a result of this circumstance the experimental procedure used for the investigation of system F deviates slightly from the procedure applied for the other systems. Although not considered likely, it cannot be precluded that these processing differences have an impact on the results obtained for system F. The experimental procedure applied for the investigation of system F is therefore repeated here for completeness. For experiments in the system F (200 MPa, 3 wt.% H_2O, 3.5 wt.% An, see Table 1) 40 mg of hydrated starting glass (Table 2b) was loaded in each capsule that in this case consisted of Au_{100} and was also 12 mm in length and 2.8 mm in inner diameter. After sealing the capsules by arc welding they were loaded into cold seal pressure vessels (CSPV) pressurized with water. The experiments took place in a temperature range between 790 an 875°C at 200 MPa. All CSPV were calibrated under pressure prior to the experiments using three thermocouples arrayed in a distance of 20 mm. Only vessels with a temperature variation <10°C in the monitored hot zone were used for experiments. Following the method of Holtz *et al*., (1992b), the samples were heated directly from room T to the desired T which was reached within 30 to 60 min. Time-dependent experiments in a comparable system conducted by Becker *et al*., (1998) suggest that this heating ramp is sufficient as crystallization does not occur until 8 h of experimental run time. The intrinsic fO_2 at water saturated conditions in the vessels is corresponding to the Ni/NiO buffer, translating into QFM+0.66. However as it was mentiond above, fO_2 decreases in water-undersaturated environments. The effective fO_2 for experiments in System F is estimated to be QFM+0.4. During the experiments T was monitored by a K-

type thermocouple (Ni-CrNi) with an accuracy of ±5 °C. Up to 6 capsules were loaded into one vessel for each experimental run and each run lasted four weeks, a concession to the relatively low run T. After this time the experiments were quenched by removing the autoclave from the furnace and by cooling it in a stream of compressed air under isobaric conditions. Under these quenching conditions, T <200°C was reached within the first 5 min.

Table 2a: List of starting material prepared for this study

Name	HYS1		HYS2		HYS3		HYS4		HYS5		HYS6		HYS7		HYS8		HYS15		HYS16	
	[wt.%]	1σ	[wt.%]	1σ	[wt.%]	1σ	[wt.%]	1σ	[wt.%]	1σ	[wt.%]	1σ	[wt.%]	1σ	[wt.%]	1σ	[wt.%]	1σ	[wt.%]	1σ
SiO_2	75.35	0.63	75.04	0.54	71.45	0.43	75.84	0.22	72.67	0.62	69.12	0.66	70.17	0.24	72.89	0.35	78.28	0.49	78.71	0.74
TiO_2	0.42	0.04	0.42	0.04	0.44	0.02	0.41	0.02	0.42	0.03	0.40	0.03	0.43	0.02	0.42	0.02	0.41	0.03	0.41	0.03
Al_2O_3	12.19	0.23	12.01	0.23	14.76	0.12	12.09	0.11	13.36	0.21	16.40	0.26	15.48	0.13	14.44	0.10	10.79	0.14	9.72	0.21
FeO	2.17	0.23	2.01	0.26	1.59	0.39	2.60	0.10	2.23	0.34	1.98	0.23	2.27	0.20	1.91	0.10	1.59	0.32	1.91	0.63
CaO	1.41	0.14	1.34	0.07	1.34	0.05	1.36	0.03	1.40	0.08	1.39	0.09	1.38	0.03	1.40	0.03	1.35	0.07	1.38	0.07
Na_2O	3.79	0.17	1.42	0.10	2.36	0.11	2.55	0.09	1.94	0.14	5.52	0.20	3.82	0.12	4.45	0.12	2.03	0.11	0.00	0.00
K_2O	3.17	0.08	6.63	0.11	7.48	0.10	4.99	0.07	6.94	0.08	4.48	0.09	5.93	0.08	3.90	0.04	4.47	0.08	6.60	0.13
Total	98.49	1.51	98.87	1.35	99.42	1.22	99.85	0.64	98.96	1.50	99.28	1.55	99.49	0.81	99.41	0.77	98.93	1.24	98.73	1.80
n	30		30		40		36		30		30		40		40		60		60	
H_2O	1.23		1.27		1.44		1.00		1.34		1.12		1.32		1.34		1.32		1.38	
Qz	36.74		37.23		25.27		37.19		30.34		15.65		20.79		27.84		45.50		49.27	
Ab	32.04		12.04		19.93		21.60		16.42		46.68		32.30		37.67		17.14		0.00	
Or	18.75		39.16		44.24		29.48		41.01		26.45		35.06		23.04		26.44		38.99	
An	6.88		6.65		6.63		6.75		6.94		6.78		6.85		6.95		6.71		6.85	
Cor[a]	-0.04		0.06		0.36		0.02		0.11		-0.04		0.27		0.35		0.16		0.07	

n = number of analyses, Qz = normative quartz content calculated by CIPW-norm, Ab = albite , Or = orthoclase , An = anorthite, Cor = corundum

[a] negative corundum values reflect the amount of corundum that is missing to convert all available CaO to anorthite

[b] calculated composition of glass powder mixture

[c] for detailed description see Wilke *et al.* 2015

Table 2a: Continued

Name	HYS17		HYS18		HYS19		HYS20		HYS21		HYS23		HYS24		HYS25		HYW1		HYW2	
	[wt.%]	1σ	[wt.%]	1σ	[wt.%]	1σ	[wt.%]	1σ	[wt.%]	1σ	[wt.%]	1σ	[wt.%]	1σ	[wt.%]	1σ	[wt.%]	1σ	[wt.%]	1σ
SiO_2	77.01	0.47	74.61	0.29	74.22	0.22	72.08	0.30	73.01	0.24	79.37	0.39	77.12	0.39	78.65	0.17	79.51	0.35	78.48	0.32
TiO_2	0.41	0.02	0.41	0.02	0.42	0.02	0.44	0.01	0.44	0.02	0.42	0.02	0.43	0.02	0.42	0.02	0.21	0.01	0.21	0.02
Al_2O_3	10.84	0.12	12.05	0.10	11.84	0.09	13.19	0.11	13.33	0.14	10.31	0.13	12.81	0.11	11.40	0.08	10.58	0.15	10.37	0.13
FeO	1.74	0.53	1.76	0.17	2.38	0.14	2.37	0.09	2.34	0.14	2.03	0.32	1.75	0.39	2.35	0.09	0.93	0.11	1.25	0.11
CaO	1.36	0.05	1.37	0.04	1.37	0.04	1.37	0.03	1.35	0.03	1.38	0.05	1.37	0.05	1.39	0.04	0.70	0.02	0.69	0.03
Na_2O	0.75	0.06	0.00	0.00	0.76	0.05	1.24	0.08	3.09	0.10	3.21	0.10	5.88	0.20	5.01	0.18	3.13	0.12	1.16	0.08
K_2O	6.69	0.08	8.84	0.09	7.68	0.07	8.02	0.07	5.21	0.06	2.20	0.05	0.00	0.00	0.00	0.00	3.63	0.08	6.52	0.10
Total	98.81	1.33	99.05	0.71	98.67	0.62	98.72	0.69	98.78	0.73	98.93	1.07	99.36	1.16	99.22	0.58	98.70	0.85	98.68	0.80
n	25		31		20		20		20		20		19		20		40		40	
H_2O	1.49		1.36		1.44		1.43		1.36		1.45		1.30		1.33		1.32		1.55	
Qz	43.11		36.73		35.97		29.64		30.65		47.99		38.86		44.95		45.31		44.42	
Ab	6.31		0.00		6.46		10.52		26.14		27.12		49.79		42.39		26.46		9.82	
Or	39.53		52.24		45.39		47.42		30.79		13.02		0.00		0.00		21.47		38.54	
An	6.48		6.77		6.20		6.73		6.70		6.87		6.80		6.89		3.47		3.45	
Cor[a]	-0.11		-0.01		-0.22		-0.02		0.15		0.14		0.64		0.63		0.24		0.14	

n = number of analyses, Qz = normative quartz content calculated by CIPW-norm, Ab = albite , Or = orthoclase , An = anorthite, Cor = corundum

[a] negative corundum values reflect the amount of corundum that is missing to convert all available CaO to anorthite

[b] calculated composition of glass powder mixture

[c] for detailed description see Wilke *et al.* 2015

Table 2a: Continued

Name	HYW3		HYW4		HYW5		HYW6		HYW7		HYW8		HYW3+5[b]		HYW3+6[b]		HYW3+8[b]		HYW5+8[b]	
	[wt.%]	1σ	[wt.%]	1σ	[wt.%]	1σ	[wt.%]	1σ	[wt.%]	1σ	[wt.%]	1σ	[wt.%]	1σ	[wt.%]	1σ	[wt.%]	1σ	[wt.%]	1σ
SiO_2	72.65	0.32	76.48	0.31	76.60	0.39	75.80	0.30	77.73	0.31	73.86	0.28	74.62		74.22		73.25		75.23	
TiO_2	0.22	0.01	0.21	0.01	0.22	0.02	0.22	0.02	0.22	0.02	0.22	0.01	0.22		0.22		0.22		0.22	
Al_2O_3	13.83	0.15	11.59	0.12	12.24	0.19	12.06	0.15	11.04	0.17	14.10	0.12	13.03		12.94		13.97		13.17	
FeO	1.14	0.08	0.96	0.12	0.95	0.24	1.14	0.09	1.00	0.12	0.74	0.07	1.05		1.14		0.94		0.84	
CaO	0.70	0.03	0.68	0.03	0.67	0.04	0.70	0.04	0.68	0.03	0.65	0.02	0.68		0.70		0.67		0.66	
Na_2O	2.29	0.12	0.00	0.00	2.79	0.13	1.70	0.10	0.59	0.08	4.63	0.14	2.54		1.99		3.46		3.71	
K_2O	7.99	0.10	8.80	0.08	5.81	0.09	7.22	0.08	7.60	0.11	4.41	0.07	6.90		7.60		6.20		5.11	
Total	98.81	0.81	98.79	0.71	99.28	1.09	98.85	0.76	98.87	0.84	98.61	0.71	99.05		98.83		98.71		98.95	
n	40		25		40		20		40		20		calc.		calc.		calc.		calc.	
H_2O	1.18		1.45		1.32		1.39		1.52		1.16		1.25		1.29		1.17		1.24	
Qz	26.50		40.71		36.07		36.00		43.10		28.22		31.29		31.25		27.36		32.14	
Ab	19.35		0.00		23.65		14.40		4.97		39.20		21.50		16.88		29.28		31.43	
Or	47.22		52.01		34.32		42.66		44.94		26.04		40.77		44.94		36.63		30.18	
An	3.45		3.37		3.33		3.49		3.38		3.22		3.39		3.47		3.33		3.27	
Cor[a]	0.15		0.83		0.14		0.17		0.60		0.54		0.15		0.16		0.34		0.34	

n = number of analyses, Qz = normative quartz content calculated by CIPW-norm, Ab = albite , Or = orthoclase , An = anorthite, Cor = corundum

[a] negative corundum values reflect the amount of corundum that is missing to convert all available CaO to anorthite

[b] calculated composition of glass powder mixture

[c] for detailed description see Wilke *et al.* 2015

Table 2a: Continued

Name	AC5[c]		AC7[c]		BA5[c]		BC2[c]		BC5[c]		C[c]		D[c]		DC5[c]	
	[wt.%]	1σ	[wt.%]	1σ	[wt.%]	1σ	[wt.%]	1σ	[wt.%]	1σ	[wt.%]	1σ	[wt.%]	1σ	[wt.%]	1σ
SiO_2	74.45	0.25	75.80		76.97	0.22	73.54	0.23	75.63	0.19	72.58	0.22	74.16	0.23	72.95	0.20
TiO_2	0.20	0.01	0.19		0.19	0.01	0.19	0.01	0.20	0.02	0.21	0.02	0.18	0.01	0.20	0.01
Al_2O_3	11.89	0.12	11.65		11.31	0.11	12.51	0.10	12.33	0.13	13.15	0.09	13.78	0.10	13.26	0.10
FeO	0.58	0.11	0.91		0.93	0.06	0.70	0.06	0.81	0.07	0.79	0.03	0.99	0.07	0.69	0.05
CaO	0.66	0.02	0.69		0.67	0.05	0.66	0.03	0.65	0.04	0.67	0.03	0.69	0.04	0.68	0.02
Na_2O	1.68	0.09	1.65		2.80	0.15	2.30	0.09	2.76	0.11	1.79	0.05	4.83	0.14	3.27	0.09
K_2O	7.14	0.11	6.42		4.40	0.05	6.67	0.07	5.48	0.05	8.08	0.04	3.06	0.03	5.56	0.06
Total	96.59	0.71	97.41		97.37	0.65	96.57	0.59	97.86	0.60	97.27	0.48	97.80	0.63	96.61	0.54
n	20		calc.		10		20		10		10		27		20	
H_2O	2.76		2.85		3.10		3.43				2.88		2.66			
Qz	35.59		39.56		44.13		32.78		36.71		29.29		34.06		30.75	
Ab	14.22		13.94		24.65		19.46		23.32		15.17		42.32		27.71	
Or	42.18		37.94		27.02		39.41		32.41		47.77		18.73		32.84	
An	3.30		3.43		3.44		3.28		3.23		3.31		3.57		3.39	
Cor[a]	0.19		0.74		0.76		0.31		0.68		0.24		1.32		0.61	

n = number of analyses, Qz = normative quartz content calculated by CIPW-norm, Ab = albite , Or = orthoclase , An = anorthite, Cor = corundum

[a] negative corundum values reflect the amount of corundum that is missing to convert all available CaO to anorthite

[b] calculated composition of glass powder mixture

[c] for detailed description see Wilke *et al.* 2015

Table 2b: List of starting materials used for system F (Klahn, 2013) and published in Wilke *et al*. (2015, their Table 1)

Glass name	A start hydr	1σ	B start hydr	1σ	C start hydr	1σ	D start hydr	1σ	AC5 start hydr	1σ	BA5 start hydr	1σ	BC2 start hydr	1σ	BC5 start hydr	1σ	AC2 start calc	BD5 start calc	DA2 start calc	DA7 start calc	DC5 start calc	DC7 start calc
SiO_2	76.86	0.36	77.58	0.62	72.58	0.22	74.16	0.23	74.45	0.25	76.97	0.22	73.54	0.23	75.63	0.19	73.47	75.87	76.32	74.97	73.39	73.08
TiO_2	0.19	0.01	0.18	0.01	0.21	0.02	0.18	0.01	0.20	0.01	0.19	0.01	0.19	0.01	0.20	0.02	0.18	0.18	0.19	0.18	0.18	0.18
Al_2O_3	11.14	0.18	11.45	0.30	13.15	0.09	13.78	0.10	11.89	0.12	11.31	0.11	12.51	0.10	12.33	0.13	12.79	12.62	11.67	12.99	13.49	13.37
FeO	0.90	0.10	0.93	0.10	0.79	0.03	0.99	0.07	0.58	0.11	0.93	0.06	0.70	0.06	0.81	0.07	0.94	0.96	0.92	0.96	0.97	0.96
MgO	0.11	0.02	0.09	0.02	0.10	0.01	0.10	0.02	0.11	0.02	0.10	0.02	0.11	0.02	0.10	0.02	0.10	0.10	0.11	0.10	0.10	0.10
CaO	0.69	0.05	0.69	0.06	0.67	0.03	0.69	0.04	0.66	0.02	0.67	0.05	0.66	0.03	0.65	0.04	0.69	0.69	0.69	0.69	0.69	0.69
Na_2O	1.61	0.10	3.66	0.18	1.79	0.05	4.83	0.14	1.68	0.09	2.80	0.15	2.30	0.09	2.76	0.11	1.73	4.24	2.25	3.86	3.30	2.68
K_2O	6.04	0.05	2.72	0.04	8.08	0.04	3.06	0.03	7.14	0.11	4.40	0.05	6.67	0.07	5.48	0.05	7.24	2.89	5.45	3.95	5.30	6.20
H_2O (nIR)	2.84		3.05		2.88		2.66		2.76		3.10		3.43									
H_2O (KFT)	2.48		2.83		3.02																	
Total	100.38		100.35		100.25		100.46		99.46		100.47		100.12		97.96		97.14	97.55	97.59	97.72	97.42	97.26
n	24		17		10		27		20		10		20		9							
Qz	42.16		43.66		29.29		34.06		35.59		44.13		32.78		36.71		33.45	37.88	40.13	35.14	31.64	31.50
Ab	13.62		30.97		15.17		42.32		14.22		24.65		19.46		23.32		14.64	35.88	19.04	32.66	27.92	22.68
Or	35.70		16.08		47.77		18.73		42.18		27.02		39.41		32.41		42.79	17.08	32.21	23.34	31.32	36.64
An	3.42		3.42		3.31		3.57		3.30		3.44		3.28		3.23		3.42	3.42	3.42	3.42	3.42	3.42
Co	0.70		1.23		0.24		1.32		0.19		0.76		0.31		0.68		0.85	1.26	0.81	1.11	1.07	1.00

Starting material measured by EPMA (hydr.) or calculated (calc) stoichiometrically. 1σ = standard deviation, *n* = number of analyses, NIW = near infrared, KFT = Karl-Fischer Titration, Qz = normative quartz content, Ab = norm. Albite content, Or = norm. orthoclase content, An = norm. anorthite content, Co = norm. corundum content

I-2.2 Analytical techniques

I-2.2.a) NIR-spectroscopy

The water content of all HYS and HYW starting glasses was determined by Near-Infrared (NIR) spectroscopy (Bruker IFS88 FTIR spectrometer coupled with an A590 IR microscope). The procedure was identical to that applied by Wilke *et al*. (2015) and is briefly summarized here. The samples were prepared as doubly polished glass plates of ~300 µm thickness and the analyzed spot size was 100 x 100 µm. The water concentration was calculated using the absorption bands at 5200 cm^{-1} and 4520 cm^{-1} that are assigned to stretching and bending combination modes of H_2O molecules and vibration modes of hydroxyl groups respectively. A tangential background correction and the absorption coefficients ε4520 = 1.41 $mol^{-1} * cm^{-1}$ and ε5200 = 1.66 $mol^{-1} * cm^{-1}$ as determined by Withers & Behrens (1999) for rhyolitic glass were used. The density of the material was estimated to be 2.35 ± 0.02 g/cm^3 and the effect of compositional variation on the glass density in the investigated rhyolitic system (Withers & Behrens, 1999) leads to a variation of the calculated glass H_2O content of less than ± 0.02 wt.%. Parts from the top and the bottom of the synthesized starting materials HYS 1, 2, 5 and 6 were also analyzed by Karl Fischer Titration (KFT) measurements to confirm the NIR results. The titration procedure is described by Behrens *et al*. (1996). The results of the KFT measurements agree within error with the findings from NIR spectroscopy.

I-2.2.b) Electron Probe Micro Analyzer

The Cameca SX 100 Electron Probe Microanalyzer (EPMA) of the Institute for Mineralogy of the Leibniz University of Hannover was used to determine the chemical composition of starting materials and experimental samples. Minerals that formed during crystallization experiments were analyzed using a focused beam with 15 kV excitation voltage, 15 nA beam current and 10 s counting time for all elements. At each session standard minerals were measured as a reference material and these measurements were used to correct the data from

the experiments for the daily shift of the machine. Whenever possible, five measurements were taken on different grains for every feldspar phase per sample. Quartz was only determined qualitatively. For the analysis of glasses two different measurement settings where used. In an early stage a 15 kV excitation voltage, 4 nA beam current, a beam diameter defocused to 10 µm and 10 s counting times for each element was employed. In a later stage another analytical setting with a 15 kV excitation voltage, 15 nA beam current, a beam diameter defocused to 10 µm and counting times of 4 s for Na and K and 10 s for other elements was applied. This second setting with higher beam current did not lead to observable loss of alkalis, but significantly increased counting statistics. All glass measurements were standardized using measurements of a rhyolitic glass standard, a natural high-silica obsidian named "MM-3" that was well characterized by Nash (1992). In general, 20 glass measurements were taken per sample. In some cases, however, the high sample crystallinity restricted the number of glass analyses to lower values. Samples that were found to be above the liquidus were analyzed ten times in order to check for homogeneity and to confirm that they were identical with the starting glasses, which was used as an indication that no crystals were present elsewhere in the capsule.

I-3 Results

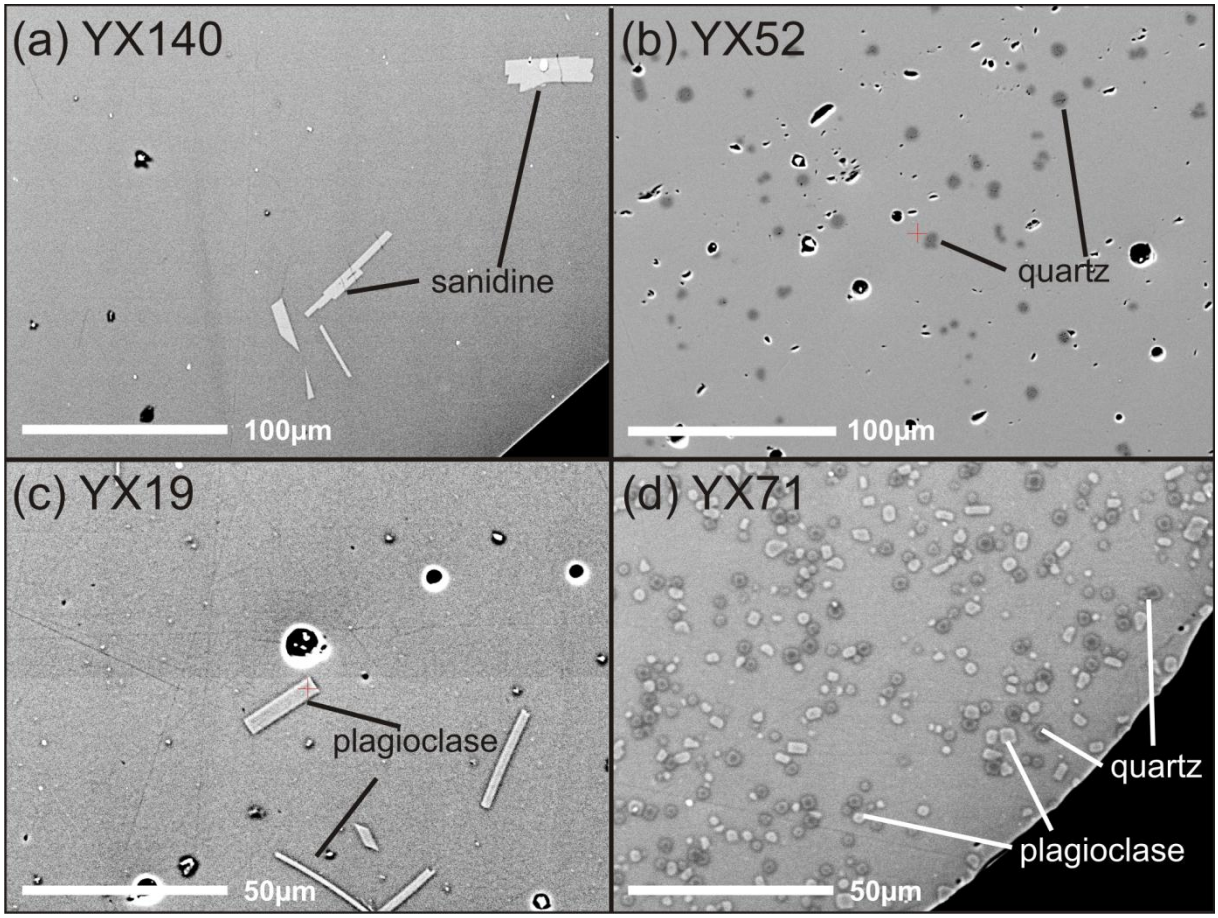

Figure 3: BSE images of experimental samples. (a) is an image of sample YX140 from an experimental run at 990°C and 500 MPa for 280 hours using starting material HYW3, leading to sanidine crystallization. (b) is an image of sample YX52 from an experimental run at 1050°C and 500 MPa for 191 hours using starting material HYS4, leading to quartz crystallization. (c) is an image of sample YX19 from an experimental run at 990°C and 200 MPa for 168 hours using starting material HYS3, leading to quartz crystallization. (d) is an image of sample YX71 from an experimental run at 1020°C and 500 MPa for 216 hours using starting material HYS24, leading to crystallization of both quartz and plagioclase. The images were edited digitally to increase the contrast for better visibility of the crystals.

I-3.1 Crystallization experiments

More than 200 successful experiments are used to constrain phase relationships for the six different systems listed in Table 1. Glass was observed in all run products. Most experimental samples were containing one or two solid phases, which were identified as quartz (qtz, if addressed as a crystallized mineral phase), sanidine (san) or plagioclase (plg). BSE images in Figure 3 show typical phase assemblages resulting from the experiments. Note that the size of the feldspar crystals seldom exceeds 10 µm. In some cases, especially where intergrowth of

feldspar and quartz occurs, feldspar crystals or fragments of them are smaller than 1 µm, making a reliable analysis by microprobe challenging and in some rare cases impossible. For samples that were derived from experiments directly below the liquidus (max. 30°C) the degree of crystallization is usually <10 vol% (calculated by mass balance). The evolution of crystal volume in the sample and of crystal size is shown in Figure 4 for different temperatures. The experimental results and the Ab-Or-An contents of feldspars are given together with run duration and temperatures in Tables 3 – 8. The compositions of the experimental glasses of systems A – E are given in Appendix Tables 1 – 5. The composition of experimental glasses of system F is published in Wilke *et al*. (2015). The compositions of the feldspars from systems A – E are listed in Appendix Table 6. As the composition of feldspars from system F was not published by Wilke *et al*. (2015) it is listed here in Appendix Table 7. The composition of the feldspars is plotted in Figure 5. The Qz-Ab-Or content of glasses, normed to 100%, is plotted in ternary diagrams in Figures 6 – 11 where different symbols indicate the composition of the coexisting mineral assemblage. Feldspars that contain ~ Or>35 wt.% are referred to as sanidine. Other feldspars are referred to as plagioclase, to avoid confusion from more complex nomenclature. This rule of discrimination for feldspars leads to two easily distinguishable populations for all experimental systems with the exception of system D (c.f. Figure 5). Reasons for this behavior are discussed below in the system D section. In rare cases small amounts of magnetite crystallized in some samples but the results of glass measurements indicate that Fe may also alloy with the Pd of the container material. Therefore, the amount of magnetite present in the run products is difficult to discuss in this study. The problem of Fe loss in the samples is further addressed in the discussion section of this paper. In the following descriptions and discussions samples will be referred to as above the liquidus, if no tectosilicate phases are present as run product. The experimental products obtained in the different starting materials with identical An and water contents are

used to draw ternary phase diagrams for the investigated conditions and to bracket the cotectic curves separating the primary fields (Figures 6 – 11).

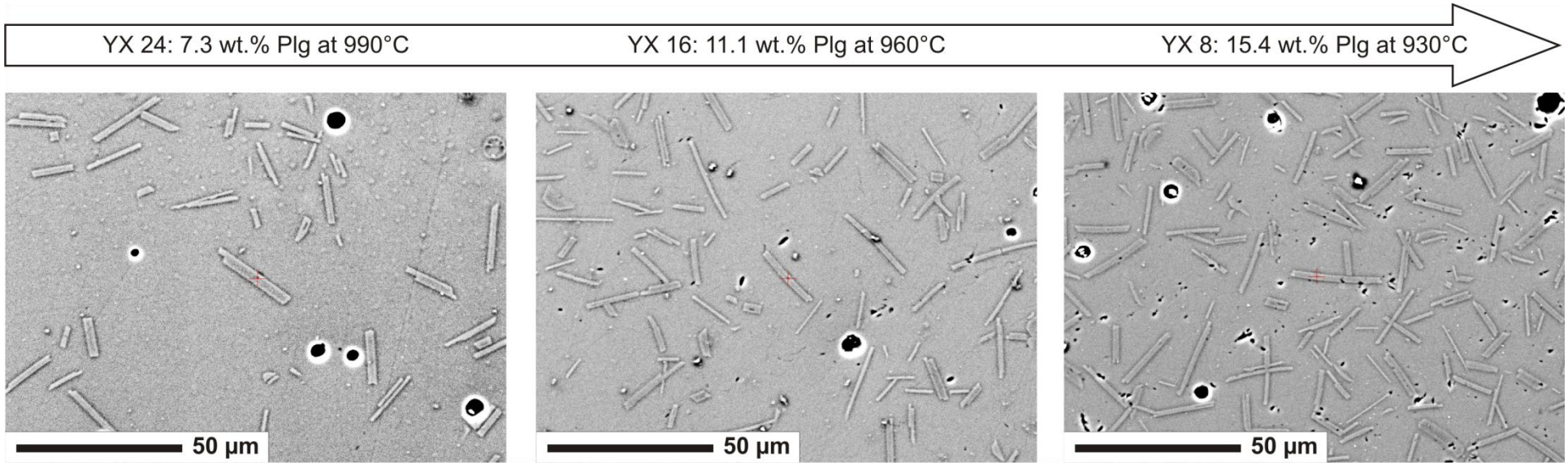

Figure 4: BSE images of crystallization experiment samples from starting glass HYS 8 (6.95 wt.% normative An). The experiments were conducted at 200 MPa (system B). The amount of crystallized plagioclase, the only crystal phase in this row of experiments, was calculated by mass balance. Normative An contents of the produced glasses are YX24: 5.6 wt.%, YX16: 5.1 wt.% An, YX8: 4.4 wt.% An. The images were edited digitally to increase the contrast for better visibility of the crystals.

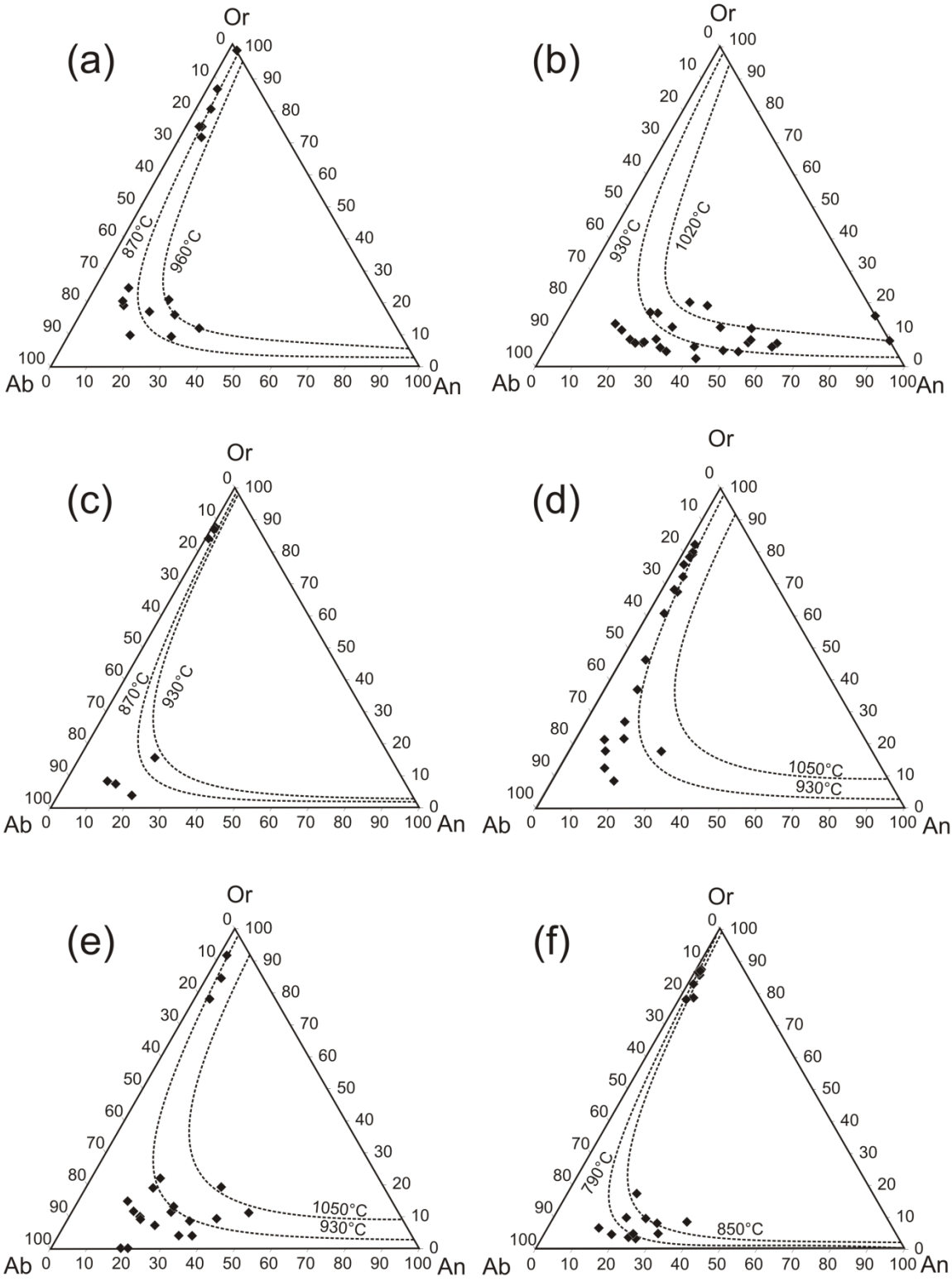

Figure 5: Ternary plot of the composition of feldspars produced. The letters (a) to (f) correspond to the experimental systems as listed in Table 1. Dashed lines indicate the solvus position at the highest and lowest experimental T (Elkins & Groove, 1990). Systems A, C, E and F show two distinct populations of feldspars. System B shows no signs of sanidine crystallization. In system D the subdivision in two distinctly different feldspars is less sharp, a problem extensively discussed in the results section devoted to this system.

I-3.2 Detailed descriptions of the investigated experimental systems

I-3.2.a) System A: 200 MPa, 1.4 wt.% H_2O, 3.5 wt.% normative An content

Experiments in this system were undertaken over a temperature range between 960 and 870°C. Products and run conditions are listed in Table 3. Two feldspar populations can be clearly distinguished (Figure 5). Qtz was observed as the only stable tectosilicate phase in eight samples, only plg in four samples and only san in three samples (all with starting composition HYW3). A considerable amount of samples were found to be cotectic and either host both qtz and plg (six samples) or qtz and san (three samples). No sample was found to contain both plg and san. The fitted liquidus lines in Figure 6 agree with the experimental results from all samples except for products from starting material HYW8, an indication that equilibrium might not have been reached for these samples. One possible reason might be that the liquidus temperature of the composition of HYW8 is much higher than the investigated ones and that equilibrium conditions would only be reached if high proportions of plg would crystallize (note that this would also strongly change the An composition of the coexisting melt; see discussion below). It can be concluded that the position of the eutectic point in a rhyolitic system with 3.5 wt.% An at an aH_2O of ~0.15 and 200 MPa should be approximately $Qz_{41}Ab_{19}Or_{40}$. This is in good agreement with the eutectic composition of $Qz_{42}Ab_{21}Or_{37}$ obtained in a previous study for a comparable system with~3 wt.% H_2O (Wilke *et al*., 2015). According to previous results on the effect of aH_2O on the eutectic composition (Holtz *et al*., 1992b, 2001a), changing water activity is mainly affecting the Ab/Or ratio. The minimum temperature is estimated to be at 885 ± 15°C.

Table 3: Run conditions an products of system A

	t	T		H_2O	melt					feldspar		
Run	[h]	[°C]	Products	[wt.%]	Qz	Ab	Or	An	Cor[a]	Ab	Or	An
HYW1	24	1200	starting glass	1.32	45.3	26.5	21.5	3.5	0.2			
YX98	286	960	qtz		38.0	31.4	25.0	3.1	-0.1			
YX90	310	930	qtz, plg		40.6	29.6	23.1	3.9	0.1	62.5	9.4	28.1
YX122	275	900	qtz, plg		37.2	28.4	26.5	2.9	0.3	64.5	17.2	18.3
YX130	340	870	qtz, fsp[b]		36.0	28.1	28.7	2.4	0.1	not possible		
HYW2	24	1200	starting glass	1.55	44.4	9.8	38.5	3.4	0.1			
YX99	286	960	qtz		42.7	10.1	39.9	3.8	0.1			
YX91	310	930	qtz		40.8	10.8	41.6	3.8	0.2			
YX123	275	900	qtz		41.0	10.0	41.1	3.5	0.3			
YX131	340	870	qtz, san		39.1	10.4	42.5	3.6	0.5	11.3	86.8	1.9
HYW3	24	1200	starting glass	1.18	26.5	19.4	47.2	3.4	0.2			
YX100	286	960	-		27.9	19.6	46.8	3.6	0.3			
YX92	310	930	san		29.9	19.8	44.0	3.6	0.2	23.2	71.7	5.1
YX124	275	900	san		33.2	18.1	40.8	3.4	0.6	21.4	75.1	3.6
YX132	340	870	san		37.3	17.3	38.6	2.8	0.6	22.1	75.1	2.8
HYW4	24	1200	starting glass	1.45	40.7	0.0	52.0	3.4	0.8			
YX101	286	960	-		41.1	0.0	51.2	3.4	1.0			
YX93	310	930	-		40.9	0.0	50.9	3.5	1.0			
YX125	275	900	qtz		41.7	0.0	50.3	3.4	1.1			
YX133	340	870	qtz, san		41.0	0.0	50.7	3.6	1.2	0.0	98.9	1.1
HYW5	24	1200	starting glass	1.32	36.1	23.7	34.3	3.3	0.1			
YX102	286	960	-		35.3	24.0	34.6	3.5	0.0			
YX94	310	930	plg		35.7	23.9	34.4	3.5	0.0	53.6	12.1	34.3
YX126	275	900	qtz, plg		36.6	21.6	35.0	2.7	0.4	58.1	16.3	25.6
YX134	340	870	qtz, plg		36.3	21.4	35.6	2.4	0.4	57.4	21.0	21.7
HYW6	24	1200	starting glass	1.39	36.0	14.4	42.7	3.5	0.2			
YX103	286	960	-		36.5	14.6	42.4	3.4	0.2			
YX95	310	930	-		36.2	14.8	43.0	3.4	-0.1			
YX127	275	900	-		37.0	14.0	41.9	3.4	0.4			
YX135	340	870	qtz, san		37.4	13.7	42.3	3.4	0.4	16.2	80.6	3.3
HYW7	24	1200	starting glass	1.52	43.1	5.0	44.9	3.4	0.6			
YX104	286	960	-		43.6	5.2	44.3	3.4	0.6			
YX96	310	930	qtz		41.6	5.7	45.9	3.6	0.4			
YX128	275	900	qtz		41.4	5.1	45.5	3.6	0.7			
YX136	340	870	qtz		40.0	5.1	47.1	3.5	0.7			
HYW8	24	1200	starting glass	1.16	28.2	39.2	26.0	3.2	0.5			
YX105	286	960	plg		27.5	40.3	27.2	2.3	-0.1	73.4	9.9	16.7
YX97	310	930	plg		30.1	37.4	28.1	1.8	0.0	70.5	19.2	10.4
YX129	275	900	plg		34.7	31.3	28.3	1.8	0.5	70.1	20.6	9.4
YX137	340	870	qtz, plg		34.7	32.1	28.1	1.8	0.3	66.4	24.7	8.9

Qz = normative quartz content, Ab = n. albite, Or = n. orthoclase, An = n. anorthite, Cor = n. corundum

qtz = quartz minerals present in the sample, plg = plagioclase minerals present, san = sanidine

[a] negative corundum values reflect the amount of Cor that is missing to convert all available CaO to An

[b] microprobe analyses of feldspar composition failed due to small crystal size

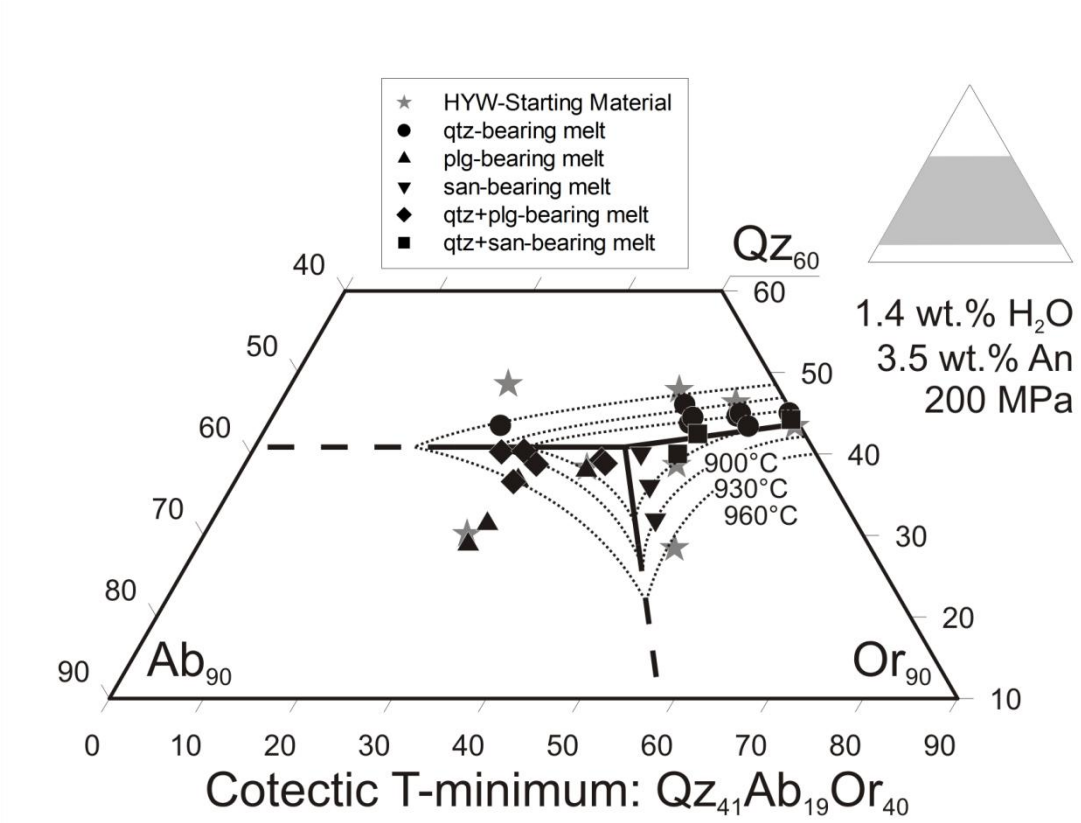

Figure 6: Ternary projection (Qz+Ab+Or = 100) of melt compositions derived from experiments in the system A with 1.4 wt.% H_2O, 3.5 wt.% An, 200 MPa. Different symbols represent melts coexisting with different mineral phase assemblages. Drawn lines represent cotectic curves in areas where sufficient data is available to constrain their position. Dashed lines indicate a projection of the cotectic curves, not verified by existing data. Dotted lines represent liquidus lines.

I-3.2.b) System B: 200 MPa, 1.3 wt.% H_2O, 7 wt.% normative An content

Experiments in this system were undertaken over a temperature range between 1020 and 930°C. Products and run conditions are listed in Table 4. Plg was found to be the only feldspar phase crystallizing in this system (Figure 7). This indicates that the system has no eutectic composition at which qtz, san and plg may coexist but rather a cotectic T-minimum. Qtz was observed as the only stable tectosilicate phase in five samples and only plg in 21 samples. Six samples were found to be cotectic hosting both qtz and plg. The fitted liquidus lines agree with most samples except for products with low Qz and high Ab values that differ the most in composition from the eutectic points position (Figure 7). This can be an indication that equilibrium might not have been reached for these samples. It is concluded that the position of the thermal T-minimum point in this rhyolitic system with 7 wt.% An at an aH_2O of ~0.15 and 200 MPa should be approximately $Qz_{45}Ab_{12}Or_{43}$. The minimum temperature is estimated to be at 945 ± 15°C.

Table 4: Run conditions an products of system B

	t	T		H_2O	melt					feldspar		
Run	[h]	[°C]	Products	[wt.%]	Qz	Ab	Or	An	Cor[a]	Ab	Or	An
HYS 1	24	1200	starting glass	1.23	36.7	32.0	18.8	6.9	0.0			
YX25	168	1020	-		38.4	32.0	18.3	7.3	0.0			
YX17	168	990	plg		38.5	30.9	20.1	6.9	0.0	55.2	2.6	42.2
YX9	180	960	qtz, plg		38.7	29.9	22.0	5.0	0.2	62.1	4.8	33.1
YX1	157	930	qtz, plg		36.4	29.9	24.3	4.3	0.1	62.9	8.6	28.4
HYS2	24	1200	starting glass	1.27	37.2	12.0	39.2	6.6	0.1			
YX26	168	1020	-		37.0	12.7	40.1	6.4	-0.2			
YX18	168	990	-		37.5	12.4	39.4	6.6	-0.2			
YX10	180	960	-		37.7	11.7	39.2	6.8	-0.1			
YX2	157	930	plg		37.5	11.8	39.4	6.5	-0.1	30.9	7.3	61.8
HYS3	24	1200	starting glass	1.44	25.3	19.9	44.2	6.6	0.4			
YX27	168	1020	plg		25.0	21.0	43.9	6.7	0.2	35.4	12.0	52.6
YX19	168	990	plg		25.2	19.7	43.9	6.8	0.4	38.6	7.6	53.9
YX11	180	960	plg		26.0	19.0	45.2	5.3	0.2	43.7	12.3	44.0
YX3	157	930	plg		27.0	18.7	45.5	4.7	0.2	43.8	19.1	37.1
HYS4	24	1200	starting glass	1.00	37.2	21.6	29.5	6.7	0.0			
YX28	168	1020	-		38.7	21.8	29.2	7.2	0.0			
YX20	168	990	-		38.5	21.1	29.3	7.1	0.1			
YX12	180	960	qtz, plg		38.1	21.2	30.3	5.9	-0.1	46.6	5.1	48.3
YX4	157	930	qtz, plg		37.0	20.5	33.4	4.5	0.0	48.1	20.1	31.8
HYS5	24	1200	starting glass	1.34	30.3	16.4	41.0	6.9	0.1			
YX29	168	1020	-		31.4	16.2	41.6	6.9	0.1			
YX21	168	990	-		31.6	15.3	41.6	7.0	0.2			
YX13	180	960	plg		31.9	15.3	41.7	6.9	0.2	32.8	6.2	61.0
YX5	157	930	plg		32.4	15.4	42.7	5.8	0.2	37.4	8.4	54.2
HYS6	24	1200	starting glass	1.12	15.7	46.7	26.5	6.8	0.0			
YX30	168	1020	plg		16.8	47.2	28.2	4.9	-0.4	67.3	7.5	25.3
YX22	168	990	plg		18.7	42.6	29.9	4.8	-0.1	70.0	8.6	21.4
YX14	180	960	plg		20.4	40.6	31.0	4.2	-0.1	70.8	11.5	17.7
YX6	157	930	plg		21.8	38.1	31.5	3.3	-0.3	71.6	13.5	15.0
HYS7	24	1200	starting glass	1.32	20.8	32.3	35.1	6.9	0.3			
YX31	168	1020	plg		20.8	34.3	35.8	6.4	0.0	53.8	6.3	40.0
YX23	168	990	plg		22.2	31.1	36.9	5.6	0.3	56.7	12.4	30.9
YX15	180	960	plg		22.4	30.4	37.6	5.0	0.0	58.4	16.8	24.8
YX7	157	930	plg		23.4	29.2	38.0	4.2	-0.1	60.3	17.0	22.6
HYS8	24	1200	starting glass	1.34	27.8	37.7	23.0	7.0	0.3			
YX32	168	1020	-		27.5	40.4	23.4	6.5	-0.2			
YX24	168	990	plg		30.2	36.3	24.3	5.6	0.5	63.2	6.0	30.8
YX16	180	960	plg		30.1	35.2	25.0	5.1	0.2	66.6	7.7	25.7
YX8	157	930	plg		31.3	34.0	25.8	4.4	0.0	69.2	7.4	23.4

Qz = normative quartz content, Ab = n. albite, Or = n. orthoclase, An = n. anorthite, Cor = n. corundum

qtz = quartz minerals present in the sample, plg = plagioclase minerals present

[a] negative corundum values reflect the amount of Cor that is missing to convert all available CaO to An

Table 4: Continued

Run	t [h]	T [°C]	Products	H2O [wt.%]	melt Qz	Ab	Or	An	Cor[a]	feldspar Ab	Or	An
HYS15	24	1200	starting glass	1.32	45.5	17.1	26.4	6.7	0.2			
DYX9	161	1020	qtz		44.1	17.8	26.7	7.4	0.1			
DYX5	164	990	qtz		43.0	17.6	27.3	7.5	0.2			
DYX1	187	960	qtz, plg		39.8	18.6	30.7	5.9	0.0	42.6	4.7	52.6
HYS16	24	1200	starting glass	1.38	49.3	0.0	39.0	6.8	0.1			
DYX10	161	1020	qtz		46.4	0.0	40.4	7.6	0.2			
DYX6	164	990	qtz		45.9	0.0	42.2	7.6	0.2			
DYX2	187	960	qtz, plg		42.4	0.0	45.3	7.0	0.1	0.0	8.1	91.9
HYS17	24	1200	starting glass	1.49	43.1	6.3	39.5	6.5	-0.1			
DYX11	161	1020	-		43.3	6.1	38.8	7.1	0.1			
DYX7	164	990	-		43.1	6.2	38.4	7.1	-0.1			
DYX3	187	960	qtz		41.3	6.5	40.0	7.1	-0.1			
HYS18	24	1200	starting glass	1.36	36.7	0.0	52.2	6.8	0.0			
DYX12	161	1020	-		37.2	0.0	51.6	7.1	0.1			
DYX8	164	990	-		37.3	0.0	51.2	7.2	0.1			
DYX4	187	960	plg		36.9	0.0	51.7	6.9	0.0	0.0	15.9	84.1

Qz = normative quartz content, Ab = n. albite, Or = n. orthoclase, An = n. anorthite, Cor = n. corundum
qtz = quartz minerals present in the sample, plg = plagioclase minerals present
[a] negative corundum values reflect the amount of Cor that is missing to convert all available CaO to An

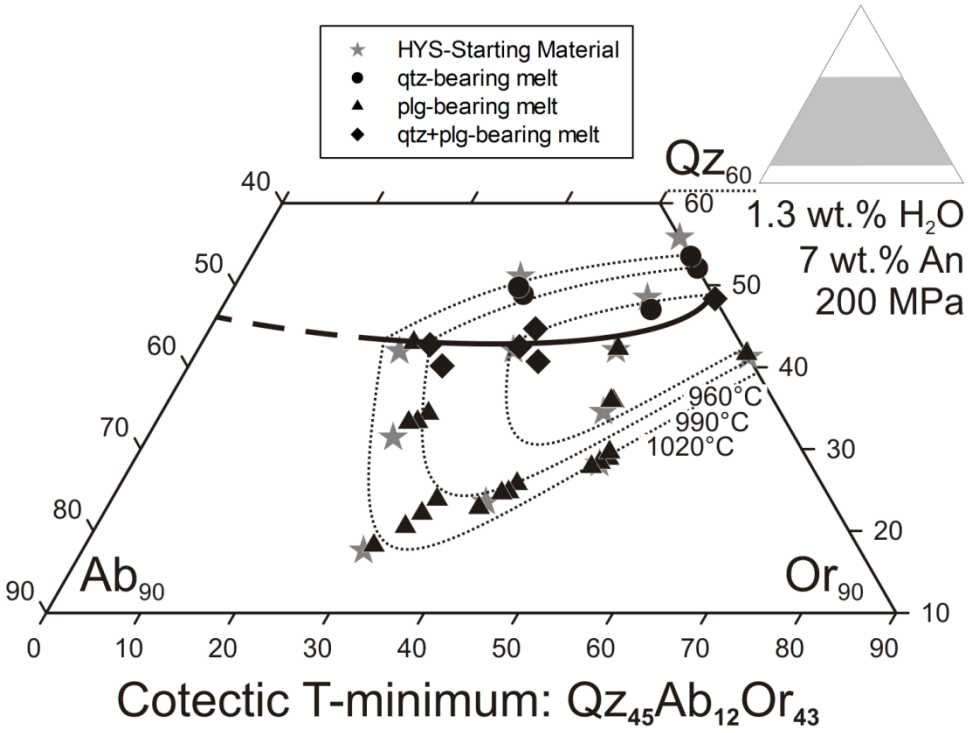

Figure 7: Ternary projection (Qz+Ab+Or = 100) of melt compositions derived from experiments in the system B with 1.3 wt.% H_2O, 7 wt.% An, 200 MPa. Different symbols represent melts coexisting with different mineral phase assemblages. Drawn lines represent cotectic curves in areas where sufficient data is available to constrain their position. Dashed lines indicate a projection of the cotectic curves, not verified by existing data. Dotted lines represent liquidus lines.

I-3.2.c) System C: 500 MPa, 3 wt.% H_2O, 3.5 wt.% normative An content

Experiments in this system were undertaken over a temperature range between 930 and 870°C. Products and run conditions are listed in Table 5. Two feldspar populations can be clearly distinguished in this system (Figure 8). Qtz was observed as the only stable tectosilicate phase in seven samples, only plg in three samples and only san in two samples. Three samples were found to be cotectic and either host both qtz and plg (one sample) or qtz and san (two samples). No sample was found to host both plg and san. The fitted liquidus lines agree well with all samples. It is concluded that the eutectic point position of a rhyolitic system with 3.5 wt.% An at an aH_2O of ~0.3 and 500 MPa should be approximately $Qz_{35}Ab_{28}Or_{37}$. The minimum temperature is estimated to be at 840 ± 15°C.

Table 5: Run conditions an products of system C

	t	T		H_2O	melt					feldspar		
Run	[h]	[°C]	Products	[wt%]	Qz	Ab	Or	An	Cor	Ab	Or	An
AC 7	24	1040	starting glass	2.73	39.6	13.9	37.9	3.4	0.7			
YX81	286	930	qtz		36.5	14.3	42.4	3.4	0.3			
YX57	261	900	qtz		36.7	14.1	40.7	3.4	0.3			
YX73	196	870	qtz, san		34.7	15.9	38.6	4.6	0.5	15.0	84.1	0.8
AC 5	24	1040	starting glass	2.76	35.6	14.2	42.2	3.3	0.2			
YX58	261	900	-		35.6	14.2	42.2	3.3	0.2			
YX74	196	870	qtz, san		34.4	14.0	43.7	3.4	0.2	11.4	87.7	0.9
BA 5	24	1040	starting glass	3.10	44.1	24.6	27.0	3.4	0.8			
YX83	286	930	qtz		39.8	22.9	28.7	3.4	0.7			
YX59	261	900	qtz		36.4	25.0	29.3	3.6	0.4			
YX75	196	870	qtz		34.9	24.5	31.0	3.8	0.5			
BC 5	24	1040	starting glass	2.95	36.7	23.3	32.4	3.2	0.7			
YX84	286	930	-		36.7	23.3	32.4	3.2	0.7			
YX60	261	900	qtz		35.3	24.1	32.2	3.4	0.4			
YX76	196	870	qtz		33.9	23.9	33.8	3.4	0.5			
BC 25	24	1040	starting glass	3.42	32.8	19.5	39.4	3.3	0.3			
YX61	261	900	-		32.8	19.5	39.4	3.3	0.3			
YX77	196	870	-		32.4	19.6	40.5	3.3	0.2			
C	24	1040	starting glass	2.95	29.3	15.2	47.8	3.3	0.2			
YX85	286	930	-		29.3	15.2	47.8	3.3	0.2			
YX62	261	900	san		30.1	15.3	46.3	3.3	0.2	11.4	87.7	0.9
YX78	196	870	san		32.3	15.1	44.1	3.6	0.2	12.1	87.0	0.9
DC5	24	1040	starting glass	2.81	30.7	27.7	32.8	3.4	0.6			
YX63	261	900	-		30.7	27.7	32.8	3.4	0.6			
YX79	196	870	plg		30.2	27.3	34.0	3.3	0.4	63.8	15.6	20.6
D	24	1040	starting glass	2.66	34.1	42.3	18.7	3.6	1.3			
YX86	286	930	plg		32.8	39.7	19.3	3.1	1.2	75.9	3.9	20.2
YX64	261	900	plg		34.0	37.7	20.3	2.5	1.0	78.5	7.4	14.0
YX80	196	870	qtz, plg		33.5	36.3	22.0	2.2	0.8	80.3	8.3	11.4

Qz = normative quartz content, Ab = n. albite, Or = n. orthoclase, An = n. anorthite, Cor = n. corundum
qtz = quartz minerals present in the sample, plg = plagioclase minerals present, san = sanidine

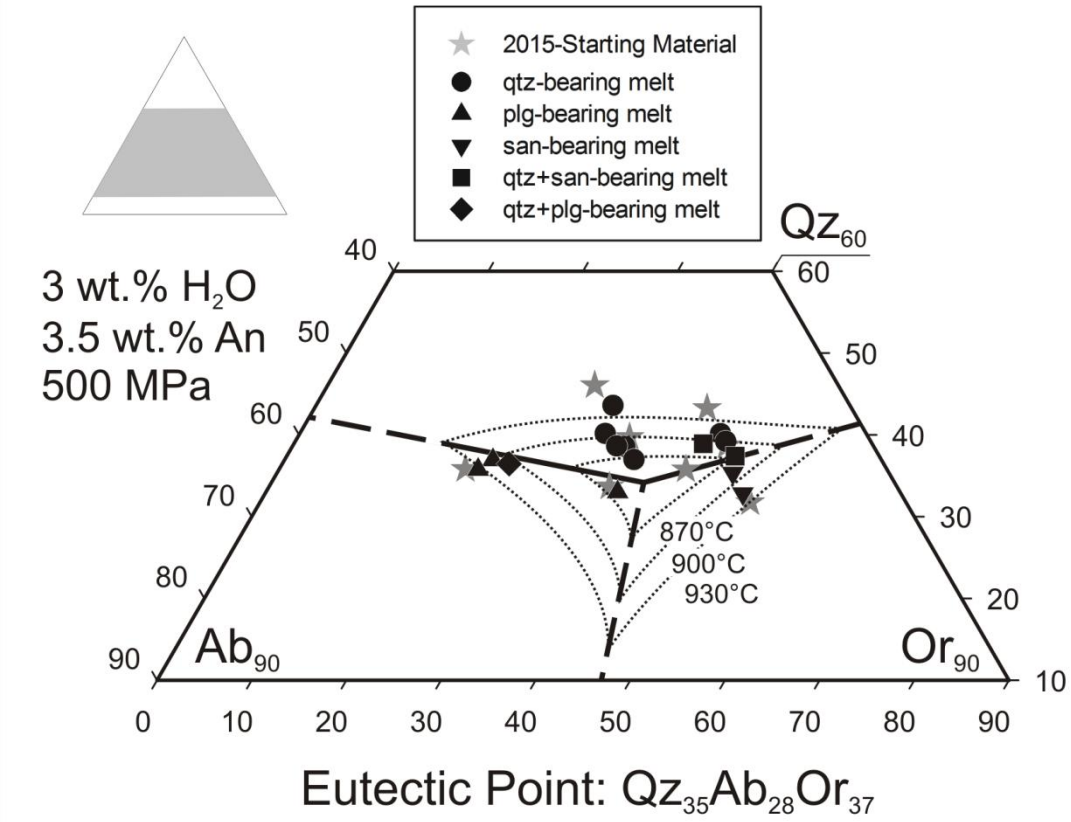

Figure 8: Ternary projection (Qz+Ab+Or = 100) of melt compositions derived from experiments in the system C with 3 wt.% H_2O, 3.5 wt.% An, 500 MPa. Different symbols represent melts coexisting with different mineral phase assemblages. Drawn lines represent cotectic curves in areas where sufficient data is available to constrain their position. Dashed lines indicate a projection of the cotectic curves, not verified by existing data. Dotted lines represent liquidus lines.

I-3.2.d) System D: 500 MPa, 1.4 wt.% H_2O, 3.5 wt.% normative An content

Experiments in this system were undertaken over a temperature range between 1050 and 930°C. Products and run conditions are listed in Table 6. Distinguishing between two different feldspar populations works for all but two samples (Figure 5). The feldspars found in samples YX156 and YX164, both produced from HYW3+8, lay within the san field (barely in case of YX156) but have the lowest Or contents of san recorded for this study. This makes the classification these feldspars somewhat arbitrary. The melt composition of YX156 obtained at 960°C is considerably depleted in normative An. The initial value of ~3.5 wt.% An in the starting material has decreased down to 2.75 wt.%, which is usually an indicator for plg crystallization. This phenomenon could be explained as a result of cotectic co-precipitation of

san and plg on a scale below the resolution of the microprobe. The sample is excluded from Figure 9 because of its unclear phase assemblage but the Qz-Ab-Or coordinates given in Table 6 fit a position where the san-plg cotectic curve for this system could occur, considering the An depleted nature of the sample. Sample YX164, obtained at a lower temperature of 930°C, shows the uncommon feldspar composition and also contains qtz. The glass composition can be interpreted as a near eutectic composition, albeit for a melt An content of 2.59 wt.%. A similar explanation can clarify a problem concerning sample YX167 produced from starting material HYW5. Five experiments in a temperature range from 1050°C to 930°C were conducted with HYW5. This composition has a liquidus temperature below 1050°C (YX118), qtz is the liquidus phase (YX110; 1020°C) and later cotectic precipitation of qtz and plg occurs at 960°C (YX159). The identification of plagioclase in YX159 is unproblematic with a composition of $Ab_{57}Or_{18}An_{25}$. However, in an experiment at 930°C with composition HYW5 (YX167), a feldspar composition that could be attributed to san is observed, although it is suspiciously low in Or (Table 6). It is not possible however, that plg would vanish and be completely replaced by san as a result of further cooling. Considering the vastly undercooled nature of YX167, the unusual and heterogeneous composition of its constituent feldspar and the known crystallization history of HYW5, it is thus concluded that YX167 is a eutectic sample comparable to YX164 with qtz coexisting with two potentially intergrown feldspar phases that are indistinguishable by microprobe. As YX167 is only moderately depleted in An, containing 3.12 wt.% (c.f. Appendix Table 6), its potential to indicate the position of the eutectic point if system D is, however, substantially higher. Sample YX167 is excluded from figure 9 as well, as a clear phase identification by microprobe was not possible. Although the problematic experiments YX156, YX164 and YX167 do provide some information about the phase relations in system D, the focus is layed on the samples with clear phase identification to determine the cotectic curves and the eutectic

point. Qtz was observed as the only stable tectosilicate phase in 13 samples, only plg in two samples and only san in two samples as well. Some samples were found to be cotectic and either host both qtz and plg (five sample) or qtz and san (six samples). The fitted liquidus lines agree well with all samples. It is concluded that the eutectic point position of a rhyolitic system with 3.5 wt.% An at an aH_2O of ~0.1 and 500 MPa should be approximately $Qz_{36}Ab_{25}Or_{39}$. The minimum temperature is estimated to be at 1005 ± 15°C.

Table 6: Run conditions an products of system D

	t	T		H_2O	melt					feldspar		
Run	[h]	[°C]	Products	[wt.%]	Qz	Ab	Or	An	Cor[a]	Ab	Or	An
HYW 1	24	1200	starting glass	1.32	45.3	26.5	21.5	3.5	0.2			
YX114	213	1050	qtz		40.5	29.1	23.4	3.9	0.4			
YX106	214	1020	qtz		36.5	32.3	24.6	4.0	0.0			
YX138	280	990	qtz		35.6	31.2	25.3	4.1	0.3			
HYW 2	24	1200	starting glass	1.55	44.4	9.8	38.5	3.4	0.1			
YX115	213	1050	qtz		42.0	9.9	40.0	3.8	0.4			
YX107	214	1020	qtz		39.7	10.8	42.0	4.0	0.3			
YX139	280	990	qtz		38.1	10.6	43.6	3.9	0.4			
HYW 3	24	1200	starting glass	1.18	26.5	19.4	47.2	3.4	0.2			
YX116	213	1050	-		41.7	0.5	50.5	3.3	1.0			
YX108	214	1020	-		27.7	19.3	46.9	3.4	0.2			
YX140	280	990	san		28.6	18.4	46.0	3.5	0.6	17.9	79.1	3.0
YX158	230	960	san		32.7	18.7	42.4	3.5	0.5	21.7	76.0	2.2
YX166	257	930	qtz, san		33.1	18.8	40.6	3.7	0.6	23.9	72.2	3.9
HYW 4	24	1200	starting glass	1.45	40.7	0.0	52.0	3.4	0.8			
YX117	213	1050	-		41.7	0.5	51.1	3.3	0.9			
YX109	214	1020	-		41.4	0.4	51.2	3.3	0.9			
YX141	280	990	qtz		40.0	0.5	52.5	3.4	1.0			
HYW 5	24	1200	starting glass	1.32	36.1	23.7	34.3	3.3	0.1			
YX118	213	1050	-		37.3	22.4	33.9	3.5	0.3			
YX110	214	1020	qtz		36.1	23.6	33.9	3.5	0.1			
YX142	280	990	qtz		35.2	23.4	35.0	3.5	0.3			
YX159	230	960	qtz, plg		33.5	23.4	36.9	3.3	0.3	57.0	17.6	25.3
YX167	257	930	qtz, san[b]		33.1	23.3	37.3	3.1	0.3	34.7	60.7	4.6
HYW 6	24	1200	starting glass	1.39	36.0	14.4	42.7	3.5	0.2			
YX119	213	1050	-		37.3	14.1	42.2	3.5	0.3			
YX111	214	1020	-		36.5	14.9	42.5	3.4	0.2			
YX143	280	990	qtz		37.4	13.9	42.1	3.4	0.4			
YX160	230	960	qtz		35.3	14.2	44.1	3.5	0.4			
YX168	257	930	qtz, san		34.9	14.8	43.1	4.0	0.4	15.6	82.3	2.1
HYW 7	24	1200	starting glass	1.52	43.1	5.0	44.9	3.4	0.6			
YX120	213	1050	-		43.9	5.0	44.2	3.4	0.6			
YX112	214	1020	qtz		41.6	5.3	45.6	3.4	0.6			
YX144	280	990	qtz		39.9	5.2	47.3	3.6	0.6			

Qz = normative quartz content, Ab = n. albite, Or = n. orthoclase, An = n. anorthite, Cor = n. corundum
qtz = quartz minerals present in the sample, plg = plagioclase minerals present, san = sanidine
[a] negative corundum values reflect the amount of Cor that is missing to convert all available CaO to An
[b] this crystallization of sanidine is intensively discussed in the text

Table 6: Continued

	t	T		H_2O	melt					feldspar		
Run	[h]	[°C]	Products	[wt.%]	Qz	Ab	Or	An	Cor[a]	Ab	Or	An
HYW 8	24	1200	starting glass	1.16	28.2	39.2	26.0	3.2	0.5			
YX121	213	1050	-		28.0	40.3	25.6	3.6	0.3			
YX113	214	1020	plg		27.1	41.7	26.2	2.9	-0.1	74.5	8.4	17.1
YX145	280	990	plg		30.6	36.3	27.0	2.5	0.4	75.0	12.4	12.6
YX161	230	960	qtz, plg		31.5	34.9	28.1	2.3	0.4	72.1	17.7	10.1
YX169	257	930	qtz, plg		30.0	35.9	28.5	2.5	0.2	70.6	21.3	8.1
HYW3+5	24	1200	starting glass	1.25	31.3	21.5	40.8	3.4	0.1			
YX154	230	960	qtz, san		32.9	20.1	40.5	3.5	0.4	27.7	67.5	4.8
YX162	257	930	qtz, san		33.4	20.8	38.9	3.4	0.4	28.2	68.2	3.6
HYW3+6	24	1200	starting glass	1.29	31.3	16.9	44.9	3.5	0.2			
YX155	230	960	qtz, san		33.5	15.9	44.3	3.4	0.5	17.4	79.9	2.7
YX163	257	930	qtz, san		34.1	17.0	41.6	3.8	0.5	19.0	78.4	2.6
HYW3+8	24	1200	starting glass	1.17	27.4	29.3	36.6	3.3	0.3			
YX156	230	960	san[b]		31.5	26.6	36.1	2.8	0.5	53.9	36.9	9.2
YX164	257	930	qtz, san[b]		31.2	27.4	35.9	2.6	0.4	47.0	46.2	6.8
HYW5+8	24	1200	starting glass	1.24	32.1	31.4	30.2	3.3	0.3			
YX157	230	960	qtz, plg		33.0	29.5	32.0	2.5	0.4	65.2	21.6	13.2
YX165	257	930	qtz, plg		32.6	28.6	33.2	2.4	0.3	62.3	26.9	10.8

Qz = normative quartz content, Ab = n. albite, Or = n. orthoclase, An = n. anorthite, Cor = n. corundum
qtz = quartz minerals present in the sample, plg = plagioclase minerals present, san = sanidine
[a] negative corundum values reflect the amount of Cor that is missing to convert all available CaO to An
[b] this crystallization of sanidine is intensively discussed in the text

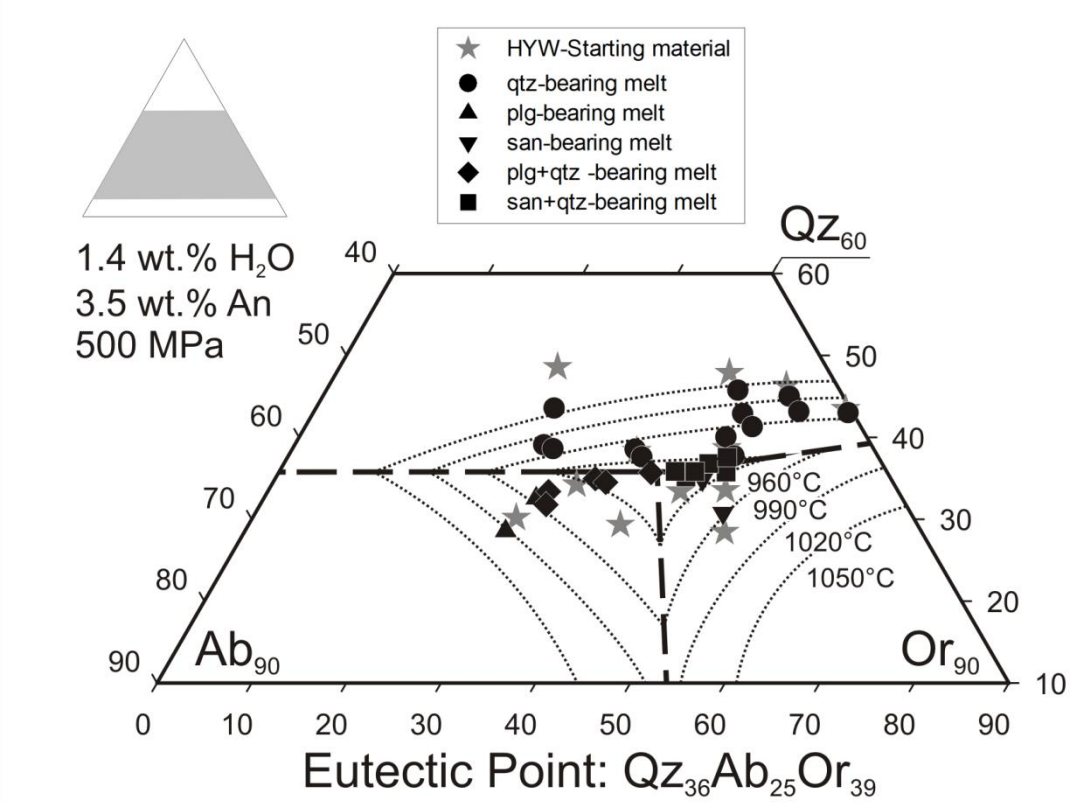

Figure 9: Ternary projection (Qz+Ab+Or = 100) of melt compositions derived from experiments in the system D with 1.4 wt.% H_2O, 3.5 wt.% An, 500 MPa. Different symbols represent melts coexisting with different mineral phase assemblages. Drawn lines represent cotectic curves in areas where sufficient data is available to constrain their position. Dashed lines indicate a projection of the cotectic curves, not verified by existing data. Dotted lines represent liquidus lines.

I-3.2.e) System E: 500 MPa, 1.3 wt.% H_2O, 7 wt.% normative An content

Experiments in this system were undertaken over a temperature range between 1050 and 930°C, with no experiments conducted at the 960°C T step. Products and run conditions are listed in Table 7. Two feldspar populations can be clearly distinguished in this system (Figure 5). Qtz was observed as the only stable tectosilicate phase in five samples, only plg in 11 samples and only san in one sample. Some samples were found to be cotectic and either host both qtz and plg (seven samples) or qtz and san (two samples). No sample was found to host both plg and san. The fitted liquidus lines agree well with samples that are close in compositions to the cotectic point but disagree with more Ab bearing samples. This effect appears to be the same as the one observed for system B. Apparently it is related to the higher

normative An content of the system, either by increasing the compositional distance between starting material and eutectic point or by a change in the distance between two liquidus curves of the same T. It is concluded that the eutectic point position of a rhyolitic system with 7 wt.% An at an aH_2O of ~0.1 and 500 MPa should be approximately $Qz_{38}Ab_{18}Or_{44}$. The minimum temperature is estimated to be at 960 ± 15°C.

Table 7: Run conditions an products of system E

	t	T		H_2O	melt					feldspar		
Run	[h]	[°C]	Products	[wt.%]	Qz	Ab	Or	An	Cor[a]	Ab	Or	An
HYS 1	24	1200	starting glass	1.23	36.7	32.0	18.8	6.9	0.0			
YX49	191	1050	qtz, plg		36.3	32.8	20.7	6.7	0.1	59.5	4.1	36.4
YX33	162	1020	qtz, plg		34.8	33.0	22.7	5.9	0.1	62.8	9.2	28.0
YX41	186	990	qtz, plg		32.3	32.1	25.5	4.6	-0.1	62.6	19.0	18.4
HYS 2	24	1200	starting glass	1.27	37.2	12.0	39.2	6.6	0.1			
YX50	191	1050	-		38.1	12.3	39.0	6.9	-0.1			
YX34	162	1020	qtz		36.7	12.2	39.9	7.0	0.0			
YX42	186	990	qtz		34.6	13.0	40.7	6.7	-0.3			
HYS 3	24	1200	starting glass	1.44	25.3	19.9	44.2	6.6	0.4			
YX51	191	1050	-		26.5	20.1	42.9	6.9	0.5			
YX35	162	1020	plg		25.6	20.7	43.8	6.7	0.4	41.9	10.3	47.9
YX43	186	990	plg		26.2	19.4	44.2	5.5	0.2	44.2	18.2	37.7
HYS 4	24	1200	starting glass	1.00	37.2	21.6	29.5	6.7	0.0			
YX52	191	1050	qtz		36.8	23.0	29.8	6.6	-0.2			
YX36	162	1020	qtz, plg		35.0	23.3	31.7	6.4	-0.1	50.1	10.1	39.9
YX44	186	990	qtz, fsp		32.5	22.5	34.3	5.1	-0.3	not possible		
HYS 5	24	1200	starting glass	1.34	30.3	16.4	41.0	6.9	0.1			
YX53	191	1050	-		31.1	16.6	41.0	6.8	-0.1			
YX37	162	1020	-		31.3	16.5	41.3	6.9	0.1			
YX45	186	990	-		31.9	16.1	41.8	6.5	0.1			
YX87	286	930	san		33.2	15.3	41.4	5.4	0.0	17.8	78.1	4.2
HYS 6	24	1200	starting glass	1.12	15.7	46.7	26.5	6.8	0.0			
YX54	191	1050	plg		17.4	45.1	28.4	5.3	-0.2	70.7	10.0	19.3
YX38	162	1020	plg		18.3	45.0	29.8	3.6	-0.6	71.6	11.7	16.7
YX46	186	990	plg		18.9	41.9	30.0	3.2	-0.7	71.6	14.9	13.5
HYS 7	24	1200	starting glass	1.32	20.8	32.3	35.1	6.9	0.3			
YX55	191	1050	plg		21.2	33.8	35.8	6.1	-0.1	57.2	8.4	34.4
YX39	162	1020	plg		21.4	33.1	37.2	5.0	-0.2	59.3	14.4	26.3
YX47	186	990	plg		23.1	31.1	37.1	4.1	-0.3	59.2	22.0	18.8
HYS 8	24	1200	starting glass	1.34	27.8	37.7	23.0	7.0	0.3			
YX56	191	1050	plg		27.2	39.5	23.0	6.7	-0.1	63.1	4.1	32.8
YX40	162	1020	plg		28.8	38.2	24.3	5.7	-0.1	68.0	7.3	24.7
YX48	186	990	plg		29.4	36.4	25.0	4.2	-0.4	71.0	9.2	19.8

Qz = normative quartz content, Ab = n. albite, Or = n. orthoclase, An = n. anorthite, Cor = n. corundum
qtz = quartz minerals present in the sample, plg = plagioclase minerals present
[a] negative corundum values reflect the amount of Cor that is missing to convert all available CaO to An

Table 7: Continued

	t	T		H_2O	melt					feldspar		
Run	[h]	[°C]	Products	[wt.%]	Qz	Ab	Or	An	Cor[a]	Ab	Or	An
HYS 17	24	1200	starting glass	1.49	43.1	6.3	39.5	6.5	-0.1			
YX65	216	1020	qtz		39.4	6.5	41.5	7.5	-0.1			
HYS 18	24	1200	starting glass	1.36	36.7	0.0	52.2	6.8	0.0			
YX66	216	1020	-		37.4	0.4	51.9	6.6	-0.1			
HYS 19	24	1200	starting glass	1.44	39.3	7.9	52.8	6.5	0.0			
YX67	216	1020	-		37.3	6.3	44.9	6.6	-0.1			
YX88	286	930	qtz, san		34.6	6.9	46.4	6.5	-0.2	6.3	91.7	2.0
HYS 20	24	1200	starting glass	1.43	36.0	6.5	45.4	6.2	-0.2			
YX68	216	1020	-		30.9	10.0	46.7	7.0	0.1			
YX89	286	930	qtz, san		34.3	10.4	45.1	6.1	0.0	11.4	84.6	4.0
HYS 21	24	1200	starting glass	1.36	30.6	26.1	30.8	6.7	0.2			
YX69	216	1020	-		32.0	24.9	30.8	7.0	0.3			
HYS 23	24	1200	starting glass	1.45	48.0	27.1	13.0	6.9	0.1			
YX70	216	1020	qtz		38.8	31.7	16.0	8.0	0.3			
HYS 24	24	1200	starting glass	1.30	38.9	49.8	0.0	6.8	0.6			
YX71	216	1020	qtz, plg		38.3	49.8	0.0	5.7	1.1	81.0	0.2	18.8
HYS 25	24	1200	starting glass	1.33	44.9	42.4	0.0	6.9	0.6			
YX72	216	1020	qtz, plg		39.0	48.6	0.0	6.2	1.0	78.9	0.2	21.0

Qz = normative quartz content, Ab = n. albite, Or = n. orthoclase, An = n. anorthite, Cor = n. corundum
qtz = quartz minerals present in the sample, plg = plagioclase minerals present
[a] negative corundum values reflect the amount of Cor that is missing to convert all available CaO to An

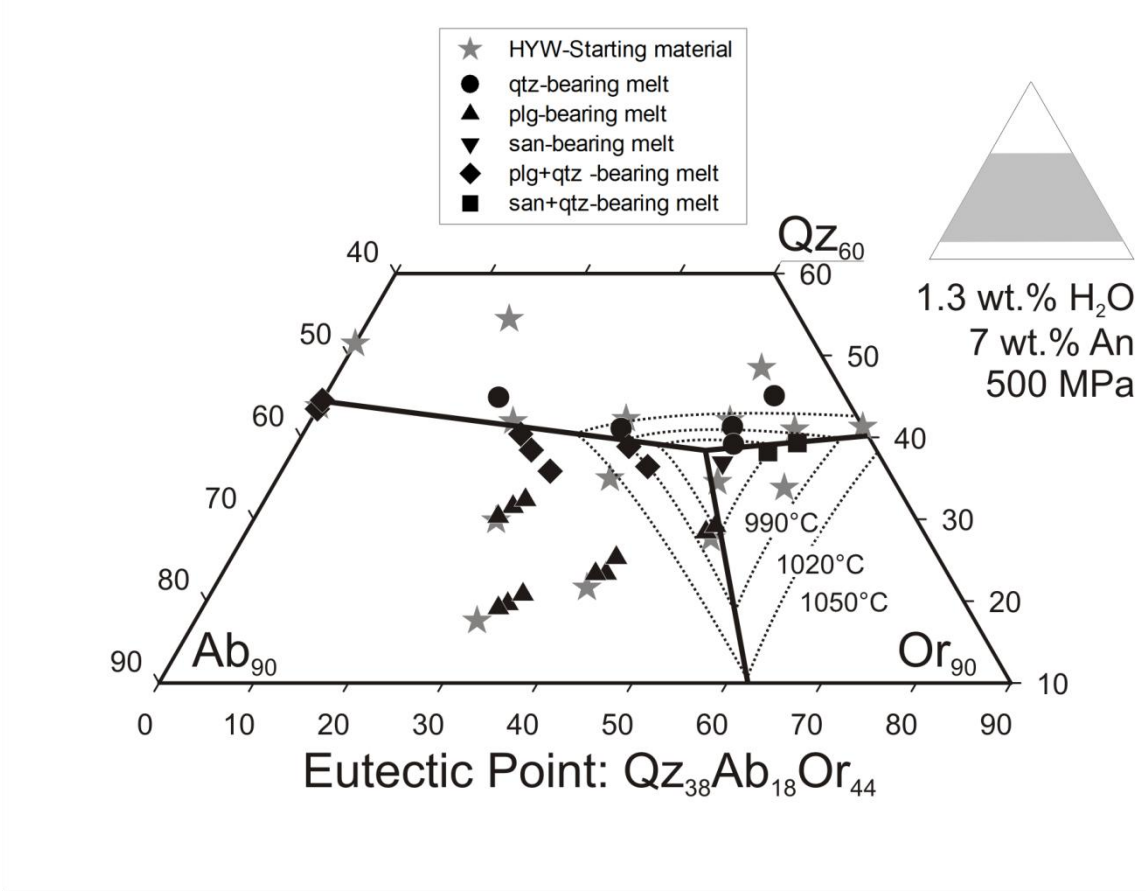

Figure 10: Ternary projection (Qz+Ab+Or = 100) of melt compositions derived from experiments in the system E with 1.3 wt.% H_2O, 7 wt.% An, 500 MPa. Different symbols represent melts coexisting with different mineral phase assemblages. Drawn lines represent cotectic curves in areas where sufficient data is available to constrain their position. Dashed lines indicate a projection of the cotectic curves, not verified by existing data. Dotted lines represent liquidus lines.

I-3.2.f) System F: 200 MPa, 3 wt.% H_2O, 3.5 wt.% normative An content

System F was investigated experimentally by Klahn (2013) and the results are published in Wilke et al. (2015) and only a brief summary shall be given here. Experiments in this system were undertaken over a temperature range between 850 and 790°C. Products and run conditions are listed in Table 8. The glass composition data from Wilke *et al*. (2015) is plotted in a ternary diagram in Figure 11 that is not from Wilke *et al*. (2015) but was redrawn to match the style of the other ternary diagrams presented here, making a comparison between the different systems easier. Wilke *et al*. (2015) state that the eutectic point position of a

rhyolitic system with 7 wt.% An at an aH_2O of ~0.1 and 500 MPa should be approximately $Qz_{42}Ab_{21}Or_{37}$. The minimum temperature is estimated to be at 795 ± 10°C.

Table 8: Run conditions an products of system F (Wilke et al 2015, their Table 2)

Exp. Run	T [°C]	Products
A start ($Qz_{46.51}$ $Ab_{14.75}$)	1040	starting glass
A3	850	gl + mt
A7	830	gl + mt + qtz
A4	810	gl + mt + qtz
AC2 start ($Qz_{37.29}$ $Ab_{16.01}$)	1040	starting glass
AC27	830	gl + mt + san
AC25	810	gl + mt + san
AC5 start ($Qz_{43.96}$ $Ab_{15.05}$)	1040	starting glass
AC53	850	gl + mt
AC55	810	gl + mt + san
AC56	790	gl + mt + san
B start ($Qz_{48.57}$ $Ab_{33.84}$)	1040	starting glass
B3	850	gl + mt + qtz
B4	810	gl + mt + qtz + plg
BA5 start ($Qz_{46.06}$ $Ab_{25.73}$)	1040	starting glass
BA58	850	gl + mt + qtz
BA55	810	gl + mt + qtz
BC2 start ($Qz_{36.89}$ $Ab_{22.05}$)	1040	starting glass
BC25	810	gl + mt + san
BC26	790	gl + mt + san
BC5 start ($Qz_{37.95}$ $Ab_{28.44}$)	1040	starting glass
BC54	810	gl + mt
BC56	790	gl + mt + plg
BD5 start ($Qz_{42.18}$ $Ab_{39.18}$)	1040	starting glass
BD58	850	gl + mt + plg
BD57	830	gl + mt + plg
C start ($Qz_{34.06}$ $Ab_{16.32}$)	1040	starting glass
C3	850	gl + mt
C7	830	gl + mt + san
C4	810	gl + mt + san
D start ($Qz_{35.81}$ $Ab_{44.50}$)	1040	starting glass
D3	850	gl + mt + plg
D4	810	gl + mt + plg
DA2 start ($Qz_{44.38}$ $Ab_{20.68}$)	1040	starting glass
DA25	810	gl + mt + qtz
DA26	790	gl + mt + qtz + plg
DA7 start ($Qz_{39.03}$ $Ab_{35.54}$)	1040	starting glass
DA78	850	gl + mt + plg
DA77	830	gl + mt + plg
DC5 start ($Qz_{35.39}$ $Ab_{30.43}$)	1040	starting glass
DC58	850	gl + mt
DC54	810	gl + mt + plg
DC56	790	gl + mt + plg
DC7 start ($Qz_{35.22}$ $Ab_{24.80}$)	1040	starting glass
DC72	790	gl + mt + san

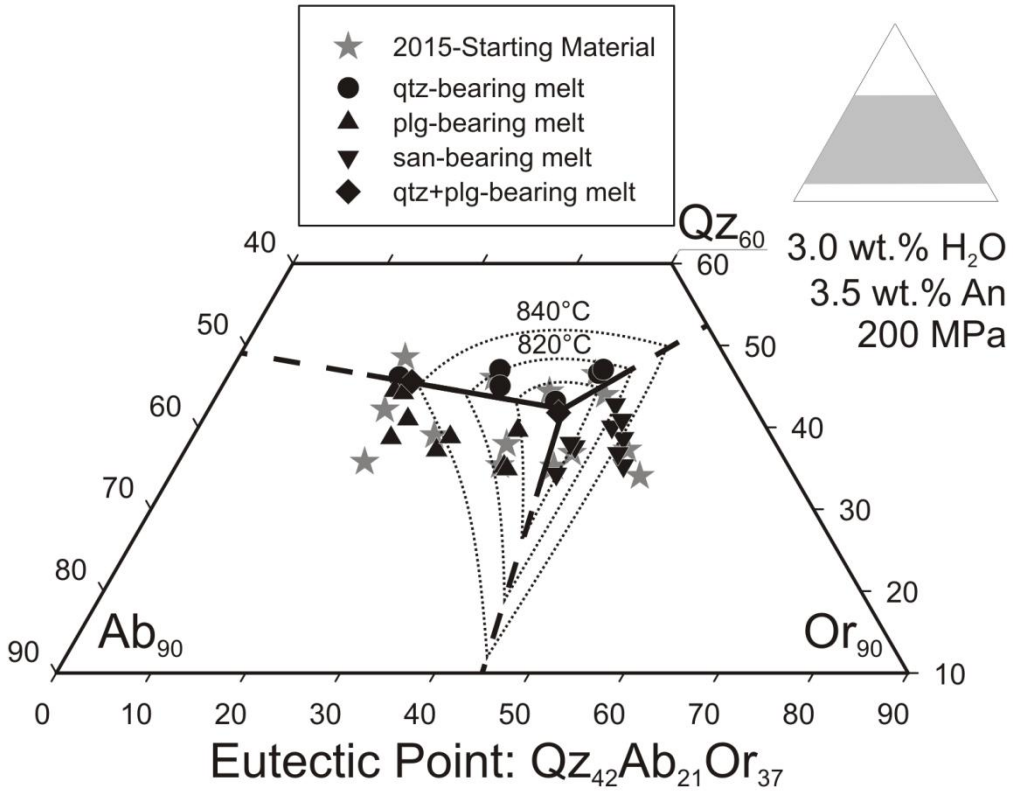

Figure 11: Ternary projection (Qz+Ab+Or = 100) of melt compositions derived from experiments in the system F with 3.0 wt.% H_2O, 3.5 wt.% An, 200 MPa. Different symbols represent melts coexisting with different mineral phase assemblages. Drawn lines represent cotectic curves in areas where sufficient data is available to constrain their position. Dashed lines indicate a projection of the cotectic curves, not verified by existing data. Dotted lines represent liquidus lines. The experiments for system F displayed here were conducted by Klahn (2013) and published by Wilke *et al*. (2015). This figure is a redrawn ternary diagram of the data presented in Wilke *et al*. (2015).

I-4 Discussion

I-4.1 Attainment of equilibrium and limitations for the interpretation of data

I-4.1.a) Attainment of equilibrium

Experimental petrology on highly viscous rhyolitic systems is always confronted with the question of the attainment of equilibrium. Possible problems are nucleation delay due to undercooling and sluggish crystal growth. As nucleation occurs preferably at grain boundaries of the initial starting glass (Pichavant, 1987; Becker *et al*., 1998), the use of finely grained glass powders as starting material in experiments helps to avoid nucleation delay related to undercooling. Another significant factor for the attainment of equilibrium is the experimental

run duration. Becker *et al*. (1998) conducted experiments comparable to the ones presented in this study on rhyolitic melts with 1 wt.% H_2O at 960 – 1180°C and concluded that near-equilibrium conditions slightly below the liquidus are attained within 72 hours. The viscosity of the melt, calculated using the model of Hess & Dingwell (1996), ranges from $10^{5.71}$ to $10^{4.09}$ poise which is only slightly lower or in the same range than the melt viscosity in this study ($10^{6.35}$ to $10^{4.58}$ poise). Thus, the diffusivity of cations in the silicate melt is similar in both experimental studies. The run duration of the experiments of this study (157 to 261 hours) is higher than the 72 hours duration set by Becker *et al*., (1998) and the longer duration was intentionally chosen to compensate the slightly higher melt viscosity.

Different tests can be conducted to check for the attainment of equilibrium in the experiments. One is to examine the relationship between plg and melt composition in the samples. Figure 12 shows a plot of the molar Ca/Na ratio of melt and coexisting plg in samples in which both phases coexisted. As pointed out by Sisson & Grove (1993) the partition coefficient $K_DCa/Na_{plagioclase\text{-}melt}$ depends only on melt water content. The samples in this study (systems A to E) fall on a K_D line of ~1.7 (see Figure 12), which is consistent with existing data in systems bearing ~2 wt.% H_2O (Baker & Eggler, 1983; Sisson & Grove, 1993). The samples from the comparatively water-rich system D show no distinct deviation from this trend, yet have little variety and very small Ca/Na ratios for both phases. This might be related to the constantly low CaO content of all starting materials in this system, as the trend is clearest for the CaO rich systems B and E. The overall agreement of the dataset to a constant K_D value of 1.7, especially as this value is in excellent agreement with literature results mentioned above, can be regarded as evidence that equilibrium was approached during most experiments. Feldspars that are in varying states of disequilibrium with their host melt would be expected to scatter strongly in their K_D values.

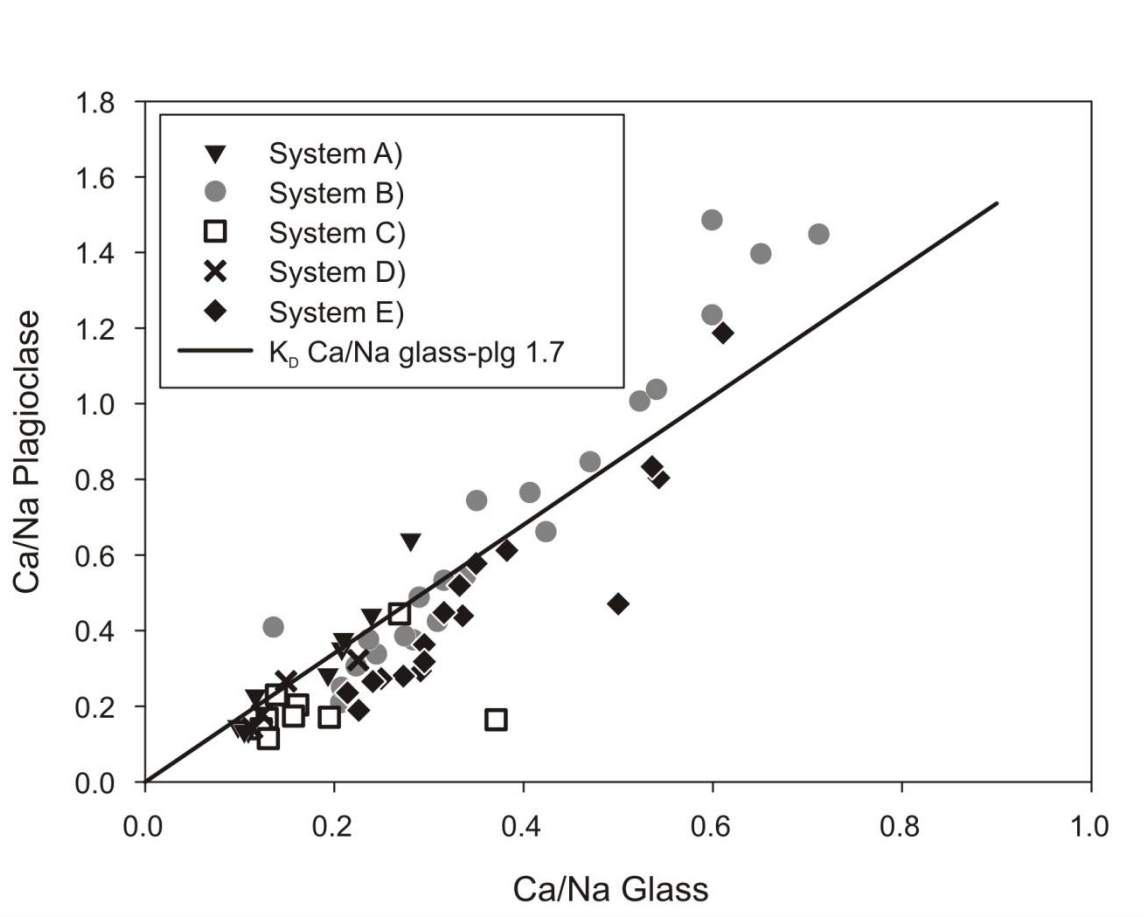

Figure 12: Plot of Ca/Na (molar) of plagioclase and coexisting glass phase from the experimental systems A - E of this study. The black line shows the approximate K_D value of 1.7.

To further investigate the attainment of equilibrium, reversal experiments were also performed following the approach described by Pichavant (1987). Four compositions were selected for which the liquidus conditions were bracketed between 1020 and 1050°C (YX34, YX35, YX112 and YX113). Thus, the run products of these experiments (all performed at 500 MPa) contained qtz (YX34, YX112) or plg (YX35, YX113) at 1020°C and were crystal free at 1050°C. The run products obtained at 1020°C were sealed in $Au_{80}Pd_{20}$ capsules and heated again to 1050°C at 500 MPa for 336 h in an IHPV. If near-equilibrium conditions are attained, the products of these reversal experiments should be crystal-free. Liquidus conditions were obtained for the reversal runs (1050°C) with YX34, YX35 and YX112. In the product of the reversal run with YX 113 however, plagioclase was still present. One possible

reason for this discrepancy could be technical, for example due to slight differences in temperature during the crystallization and reversal runs at 1050°C that might occur due to potential inhomogeneous temperature distribution within the IHPV hot zone. More likely, however, is that the failed attempt of resorbing the minerals in YX113 means that the crystallization experiment with YX113 starting material HYW8 at 1050°C (YX121) that showed no sign of crystallization, was indeed undercooled and not in a true state of equilibrium. It can be assume that the reason why the reversal of YX113 failed while the other reversal experiments succeeded is related to the bigger compositional distance between YX113 (and HYW8), and the system's eutectic point. This effect potentially affects other samples that deviate substantially in composition from their eutectic point. Fortunately, this is not a significant problem when determining cotectic curves, as the melt compositions are still directly linked to the coexisting phase(s) and hence indicative of the stability field position. However, disequilibrium does make the determination of liquidus line positions more difficult: if the sample was quenched before the attainment of equilibrium, then the melt composition of an experimental product derived at a certain T is not indicative of the liquidus. The liquidus lines on Figures 6 – 10 were drawn bearing this in mind, but it must be emphasized that, especially at lower system T, some samples with a great compositional distance to the eutectic point were discarded when doing so.

I-4.1.b) An content of melts in experiments containing plagioclase

A problem for the correct determination of the position of cotectic curves and eutectic points, as already mentioned in the results section of this study, can be the change in the melts normative An content with crystallization. The crystallization of plg leads to a depletion of the host melt in Ca causing a drop in the melt An content. As a main goal of this study is to describe rhyolite systems at a certain level of normative melt An it is imperative to be aware that a sample with changed melt An, when compared to the standardized An content of the

starting material, will reflect the situation of the system at the samples An level, inevitably deviating from the system intended to investigate in the first place. As James & Hamilton (1969) have pointed out, a decrease in normative melt An will cause the eutectic point of a system to shift towards the Ab apex. The opposite effect can be observed in a few samples that underwent significant crystallization of qtz and are now enriched in An. As the experiments are designed to observe the situation in a system close to the liquidus, extensive qtz crystallization is rather uncommon but has to be addressed where it happened. The problem of changing An contents can be tackled by closely examining especially those samples of high interest for the fixing of the cotectic curves and, if serious deviations are found, consider them less reliable for an exact determination of the positions. It is worth noting that due to the available knowledge on the impact of An (James & Hamilton, 1969; Wilke *et al*., 2015) even samples with altered melt An deliver the information that the position of a cotectic curve (separating qtz and a feldspar) at this position is shifted to higher or lower Qz values, depending on the original An content of the starting material.

I-4.1.c) Water concentration of melts

As water-undersaturation affects the position of the eutectic point (Holtz *et al*., 1992b), differences in the water content between samples could in principal lead to problems when determining such a point. The use of pre-hydrated glass powders with known water contents as starting materials instead of adding water to a dry glass for every sample is one approach to minimize such differences. Although carefully prepared, the different starting material groups show differences in their water content determined by NIR spectroscopy. For the starting materials of the HYS group the average water content is 1.33 ± 0.12 wt.% with the lowest value measured for HYS4 (1 wt.%) and the highest value for HYS17 (1.49 wt.%). For the starting materials of the HYW group that were intended to be identical with the HYS group in respect to water, the mean water content is 1.36 ± 0.13 wt.% with the lowest value measured

for HYW8 (1.16 wt.%) and the highest value for HYW2 (1.55 wt.%). The mixed powders were created by a combination of glasses described by Wilke *et al*. (2015) and span a range of water contents from 2.48 wt.% to 3.43 wt.% with the original intention of having a water content of 3 wt.%. Reasons for such variations could be the relatively high mass of material processed for the creation of the starting material (typically 0.7 g) that required the use of a comparably large and therefore less precise syringe for the transfer of water. Differences in air moisture, preparation time and welding losses are other potential sources of errors at the time of preparation. Variations in the material density are only likely to affect water content calculated using the Lambert-Beer law by 0.02 wt.% H_2O and are not a major source of uncertainty in water contents (Withers & Behrens, 1999; Wilke *et al*., 2015).

I-4.1.d) Loss of Fe

The systems investigated in this study contained FeO and TiO_2 in order to reflect the behavior of natural rhyolitic melts. EPMA measurements of the starting glasses from crystallization experiments, however, show considerable variations in FeO contents for starting materials with an identical initial FeO concentration. It was also noted that FeO contents may vary significantly within an investigated sample. For example, HYS24, which was designed to contain ~2.5 wt.% FeO, yields a value of 1.75 wt.% with an unusually high standard deviation of 0.39 wt.% (see Table 2a). Alloying between Fe in the rhyolitic charge and Pd of the capsules is most probably responsible for this drop in FeO content (Barr & Grove, 2010). It is to be assumed that the FeO depletion is a function of the distance to the capsule material. As the fragments of the run products used for preparation (polished section) were randomly picked, the initial position in the capsule and especially the distance from the sample container is not known and no systematical correction is possible. Variations in FeO content in the analysis therefore cannot be used to investigate the crystallization of Fe-bearing phases as any systematic effect potentially suffers from a random overlying alloying influence.

I-4.2 Comparison with previous studies in An-bearing systems

The expanded database of phase equilibria in An-bearing rhyolitic systems is useful to predict quantitatively the effect of normative An on eutectic and cotectic compositions at various pressures and aH_2O. Table 9 lists all eutectic compositions that are known to the author and relevant for the following discussion. The error on the Az-Ab-Or proportions listed in Table 9 is difficult to estimate accurately, considering that several factors which are difficult to quantify need to be taken into account. For example the position of the eutectic point is depending on the shape of the isotherms in the Figures 6 – 11. The exact composition of cotectic melts in this study is constrained from microprobe analyses but glass analyses were not performed in early studies (Tuttle & Bowen, 1958; Luth *et al*., 1964, James & Hamilton, 1969; Steiner *et al*., 1975). Using the same approach, except for the aH_2O which is probably more accurate in this study (see above), Holtz *et al*. (1992b) estimated uncertainties of ± 2 to 2.5 wt.% on the normative Qz, Ab and Or contents. A similar error is also realistic for this study even if the aH_2O is better constrained, since an additional source of error (compared to Holtz *et al*., 1992b) is the possible variation of An content in the melt in run products containing plg.

Table 9: List of known minimum points

Eut. P. No	Reference	Ref. No.	P [MPa]	aH_2O	T [°C]	An [wt.%]	Qz [wt.%]	Ab [wt.%]	Or [wt.%]	Ab-join [wt.% Qz]	Or-join [wt.% Qz]
#1	Tuttle & Bowen 1958	a)	50	1	760	0	39	29	32	43	47
#2	Tuttle & Bowen 1958	a)	100	1	720	0	37	37	26	41	46
#3	Tuttle & Bowen 1958	a)	200	1	685	0	35	39	26	38	43
#4	Tuttle & Bowen 1958	a)	300	1	680	0	32	42	26	35	41
#5	Steiner *et al*. 1975	b)	400	1	660	0	30	47	23	32	43
#6	Luth *et al*. 1964	c)	500	1	650	0	27	50	23	31	37
#7	Luth *et al*. 1964	c)	1000	1	630	0	22	56	22	26	n.a.
#8	Holtz *et al*. 1992b	d)	200	1	685	0	36	39	25	40	43
#9	Holtz *et al*. 1992b	d)	200	0.5	775	0	35	36	29	40	41
#10	Holtz *et al*. 1992b	d)	200	0.25	830	0	35	34	31	n.a.	n.a.
#11	Holtz *et al*. 1992b	d)	500	1	645	0	31	47	22	32	43
#12	Holtz *et al*. 1992b	d)	500	0.55	735	0	32	43	25	n.a.	n.a.
#13	Holtz *et al*. 1992b	d)	500	0.4	790	0	32	40	28	n.a.	n.a.
#14	Becker *et al.* 1998	e)	500	0.07	990	0	32	35	33	32	38
#15	James & Hamilton 1969	g)	100	1	730	3	39	30	31	n.a.	n.a.
#16	James & Hamilton 1969	g)	100	1	745	5	42	22	36	n.a.	n.a.
#17	James & Hamilton 1969	g)	100	1	780	7.5	48	10	42	n.a.	n.a.
#18	This study*	h)	200	0.15	885	3.5	41	19	40	n.a.	44
#19	Wilke *et al*. 2015*	i)	200	0.47	790	3.5	42	21	37	n.a.	n.a.
#20	This study**	h)	200	0.13	945	7	45	12	43	n.a.	48
#21	This study*	h)	500	0.09	1005	3.5	36	25	39	n.a.	n.a.
#22	This study*	h)	500	0.28	840	3.5	35	28	37	n.a.	n.a.
#23	This study**	h)	500	0.08	975	7	38	18	44	46	n.a.

* + 1 wt.% FeO + 0.2 wt.% TiO_2

** + 2 wt.% FeO + 0.4 wt.% TiO_2

In Figure 13 (a) to (c) the An-bearing eutectic compositions (#15 to #23, Table 9) are plotted together with An-free eutectics (#2, #10 and #14) for given P and aH_2O. The experimental results from this study confirm the trend already known from the data of James & Hamilton (1969): The increase of the An component in the melt causes the eutectic point to shift away from the Ab apex as the plg stability field expands. However, a detailed investigation of the results of James & Hamilton (1969) and of the datasets obtained in this study and that of Wilke *et al*. (2015) reveals significant differences. Figure 13 (a) to (c) indicates that the effect of An on the shift of the eutectic point that is deduced from the experimental dataset at 200 MPa (c.f. Figure 13(b)) with aH_2O range 0.13 - 0.25) and 500 MPa (c.f. Figure 13(c)) with aH_2O range 0.07 - 0.09) is more pronounced than that observed by James & Hamilton (1969) (c.f. Figure 13 (a)) with $aH_2O = 1$). The main reason for this difference is likely to be related

to a higher uncertainty in the determination of the eutectic points in the study of James & Hamilton (1969). In particular, the seminal results of James & Hamilton (1969) were obtained almost half a century ago using significantly less accurate analytical instruments. This may explain the apparently very small effect on of An on the eutectic composition when comparing the systems with 0 and 3.5 wt.%, the relatively strong effect when comaring systems with 3.5 and 5 wt.% An and an intermediate effect when comparing systems with 5 and 7.5 wt.% An (Figure 13(a)). This strongly non-linear effect of An on the eutectic composition predicted by the results of James & Hamilton (1969) is difficult to reconcile in the light of more recent knowledge on plagioclase crystallization and may simply be due to a larger uncertainty of the eutectic points.

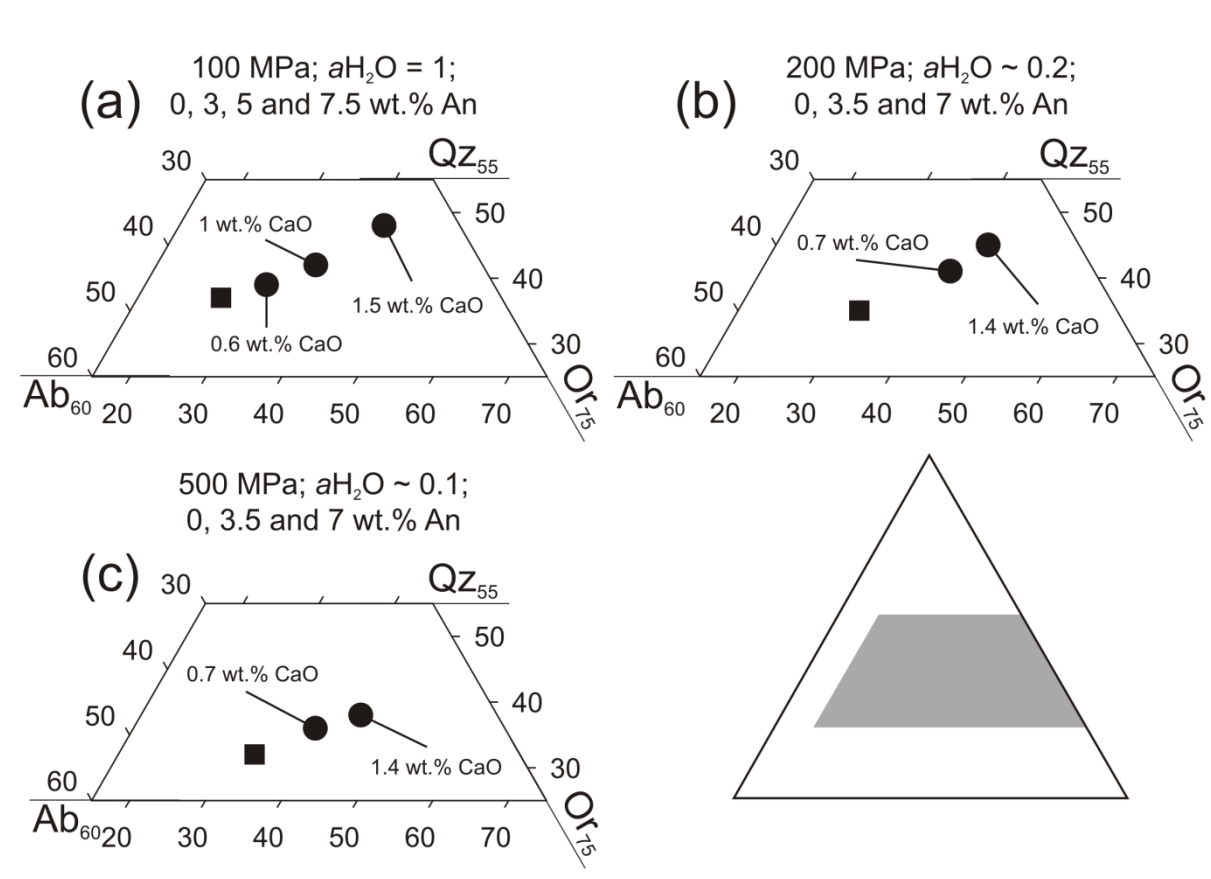

Figure 13: Ternary projection of known An-bearing minimum points plotted together with a comparable An-free minimum point obtained at similar P and aH_2O. Data from (a) Tuttle & Bowen (1958) and James & Hamilton (1969) (b) Holtz *et al*. (1992b) and this study (c) Becker *et al*. (1998) and this study.

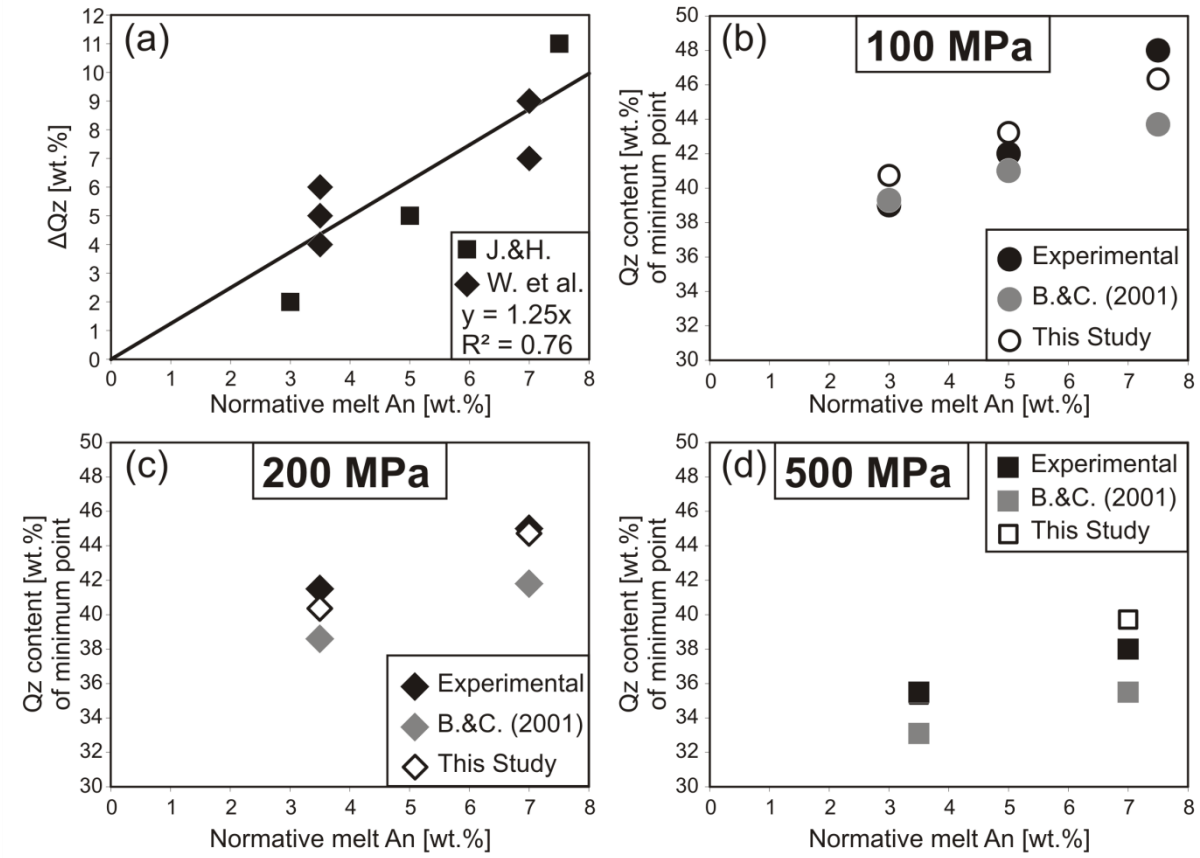

Figure 14: (a) Difference in Qz content between An-bearing minimum points and correlated An-free reference minimum points obtained at the same pressure (ΔQz). J.&H. refers to James & Hamilton (1969) and W. et al. includes point from both Wilke *et al*. (2015) and this study. (b) to (d) comparison between minimum points estimated either by the method described by Blundy & Cashman (2001) (grey symbols) or the correlation equation noted in figure (a) (ΔQz [wt.%] = 1.25 An [wt.%]; hollow symbols). Black symbols represent the actual experimentally determined Qz content of a minimum point at the given An-content.

In addition to a shift of the Ab/(Ab+Or) ratio of the eutectic point as a function of the An content of the system, the results confirm the slight increase of Qz content with increasing An content already described by James & Hamilton (1969). Figure 14(a) shows a plot of the increase in Qz of the eutectic points with increasing An content relative to An-free reference point obtained at the same pressure. The effect of $a\mathrm{H_2O}$ on the Qz content of the eutectic point was considered to be negligible, as already demonstrated by Pichavant (1987) and Holtz *et al*. (1992b). To create Figure 14(a) the Qz content of all investigated eutectic compositions in the An-bearing systems was compared to the Qz content of the water-saturated minimum at the given pressure. For the 100 MPa dataset from James & Hamilton (1969) the 37 wt.% Qz

of #2 (Tuttle & Bowen, 1958; c.f. Table 9) was used as An-free reference. For eutectic points from An-bearing systems at 200 MPa (Wilke *et al*., 2015; this study) the 35 wt.% Qz of #3 (Tuttle & Bowen, 1958; c.f. Table 9) was chosen. For eutectic points from An-bearing systems at 500 MPa (this study) the 31 wt.% Qz of #11 (Holtz *et al*., 1992b, c.f. Table 9) was chosen. There is another determination of the position of the eutectic point in the water-saturated haplogranite system by Luth *et al*. (1964, #6 in Table 9), claiming its Qz content to be 27 wt.%. As this determination was made more than 50 years ago without the assistance of a microprobe (see discussion above) and disagrees with results from Holtz *et al*. (1992b), Becker *et al*. (1998) and the results from this study, the eutectic point positions of Luth *et al*. (1964) are neglected in all following considerations. The general trend observed in Figure 14(a) indicates that the presence of 1 wt.% normative An in a melt causes a shift in Qz content of the eutectic composition by ~1.25 wt.% and can be described by the formulation:

$$[1] \qquad Qz_{\text{An-free}}\,[wt.\%] = Qz[wt.\%] - 1.25 * An\,[wt.\%]$$

In equation [1] Qz refers to the normative Qz content of the eutectic point of an An-bearing system projected on the Qz-Ab-Or-plane (Qz + Ab + Or = 100) while $Qz_{\text{An-free}}$ represents the Qz value of a hypothetical, An-free eutectic point at the same pressure. An is the normative An content of system. The coefficient of determination calculated for this formula $r^2 \sim 0.75$ is modest. However, calculating equation [1] using the James & Hamilton (1969) only results in a factor of 1.26 * An ($r^2 = 0.93$) while using only the results from this study and from Wilke et al (2015) results in 1.24 * An ($r^2 = 0.58$). It is concluded from this that equation [1] is correct within expectable error and additional data is unlikely to cause dramatic changes.

Equation [1] can be compared with the An-correction equation given by Blundy & Cashman (2001) which can also be used to estimate the effect of An on the shift of the eutectic point. In order to do so, An free eutectic point #2 determined by Tuttle & Bowen (1958) at 100 MPa

was used to calculate the Qz content of an eutectic point at 3, 5 and 7.5 wt.% An, corresponding to the existing experimental dataset from James & Hamilton (1969) (see Figure 14(b)). The An-free water-saturated eutectic points #8, 200 MPa, and #11, 500 MPa, both from Holtz *et al*. (1992b), were used to predict the Qz content of an eutectic point at 3.5 and 7 wt.% An, corresponding to the experimental results of Wilke *et al*. (2015) and this study (see Figures 14(c) and (d), respectively). For the plot of the experimental data at 200 MPa and 3.5 wt.% An in Figure 14(c) (black symbol), an average Qz value of 41.5 wt.% was estimated from two experimentally determined eutectic points, one with $a H_2O = 0.47$ (42 wt.% Qz, #19, Table 9) and the other one with $a H_2O = 0.15$ (41 wt.% Qz, #18, Table 9), as the two points differ only in water activity, which should not lead to a shift in the Qz component of the eutectic point (Holtz *et al*., 1992b). Similarly, the Qz content of a system with 3.5 wt.% An at 500 MPa was assumed to be 35.5 wt.% for the plot of experimental data in Figure 14(d). The Blundy & Cashman (2001) equation predicts accurately the Qz content of the eutectic points determined by James & Hamilton (1969) for 3 and 5 wt.% An at 100 MPa (#15 and #16, respectively, Table 9) but underestimate the Qz content at 7.5 wt.% An (#17) (c.f. Figure 14(b)). This partial agreement with data of James & Hamilton (1969) could be expected, since the model of Blundy & Cashman (2001) is based on that dataset. However, the Qz content of the eutectic points determined in this study (#18 + #20 to #23, Table 9) are systematically slightly underestimated by an average value of ~ 3 wt.% Qz, which is not the case for equation [1] with an average variation of ~ 1 wt.% Qz (c.f. Figure 14(c) and (d)). Using the Blundy & Cashman (2001) equation to predict Ab and Or values of the experimentally determined eutectic points yields differences considerably higher compared to the Qz content calculations, but this discrepancy does not affect strongly the pressure estimated from the cotectic composition of rhyolitic melts (Gualda & Ghiorso, 2013a).

CHAPTER II - Construction of a new geobarometer

II-1 DERP – Determining Eutectic Rhyolite Pressures

As equation [1] accounts for the influence of An on the Qz content of eutectic and cotectic compositions, it is now possible to link the normative Qz content of natural, eutectic melts to the P at which they formed. A series of equations based on a combination of linear fits to the data listed in Table 9 is presented here that improve geobarometry based on the position of cotectic curves in the system Qz-Ab-Or-An-H_2O and on the projection of natural sample compositions on a reference Qz-Ab-Or system.

Important for this procedure is to note that the position of any composition in the ternary projection Qz-Ab-Or can be described exactly using only the two parameters: Qz and the feldspar ratio Ab/(Ab+Or) (Qz+Ab+Or = 100). If the effects of P, H_2O content and normative melt An content variability on both parameters are known and if a rhyolitic melt is coexisting with quartz and one or two feldspars (cotectic or eutectic), then the composition can be linked to a unique P, as described below.

II-1.1 General formulation of the barometer for An-free eutectic compositions

The twelve eutectic points #1 to #5 and #8 to #14 (Table 9) were used to fit P as a linear function of the Qz content of eutectic points. The 500 MPa and 1000 MPa experiments from Luth *et al*. (1964, #6 and #7, Table 9) were discarded because of the large error on Qz contents and likelihood that the relationship between Qz and P becomes non-linear at pressures higher than 500 MPa. Note that the eutectic points from the water-undersaturated systems #8 to #14 can be used here as melt water content does not affect the Qz content of the eutectic point (Holtz *et al*., 1992b). The relationship between Qz content of An-free eutectic melts ($Qz_{An\text{-}free}$) and P is:

$$[2] \quad P\,[\mathrm{MPa}]_{eutec} = \left(\frac{(Qz_{An\text{-}free}\,[wt.\%] - 38.26)}{(-1.45)}\right) * 100$$

Where $Qz_{An\text{-}free}$ [wt.%] is the normative Qz content (Qz + Ab + Or = 100) of a melt that is either free of CaO or has been corrected for the presence of An using equation [1]. The coefficient of determination for equation [2] is $r^2 = 0.81$. It is emphasized that equation [2] is only valid for eutectic compositions.

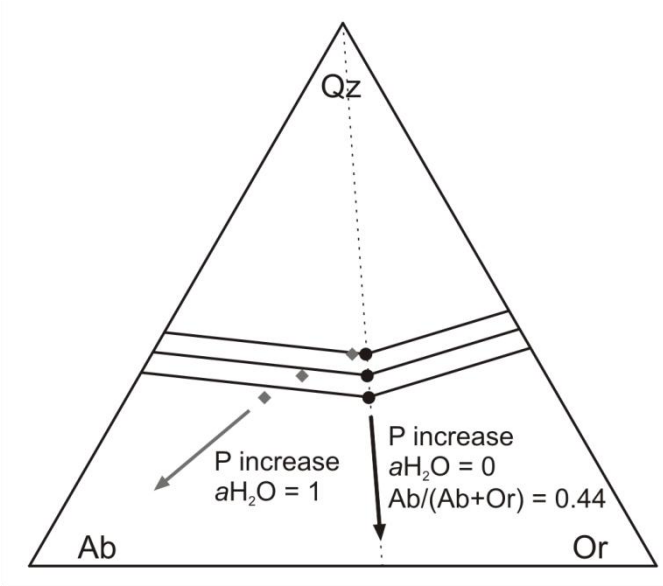

Figure 15: Minimum points calculated for dry systems with aH_2O = 0 (black dots) using equation [3]. Grey diamonds indicate the position of the corresponding minimum points determined experimentally in water saturated systems.

II-1.2 Eutectic compositions in the H_2O-free Qz-Ab-Or reference system

As emphasized, equation [2] can only be applied for eutectic melts. Such eutectic quenched melts (glasses) are not often encountered in eruptive products and most rhyolitic rocks represent magmas that are saturated with only one or two tectosilicate phases. Thus, the position of the cotectic curves in the system Qz-Ab-Or needs to be modeled. Since the position of eutectic points is shifting with water activity, its evolution has to be modeled first.

It is assumed that the Qz contents of eutectic points are not affected by H_2O activity, which was already observed by Pichavant (1987) and Holtz *et al*. (1992b) and which is also confirmed in this study (Table 9). The effect of H_2O activity on the feldspar ratio is described in the following equation:

$$[3] \quad Ab/(Ab+Or)_{\text{dry}} = Ab/(Ab+Or)_{\text{real}} - 0.028 * H_2O \ [wt.\%]$$

where $Ab/(Ab+Or)_{real}$ refers to the actual feldspar ratio of a water-bearing eutectic composition at given pressure. Equation [3] was fitted using the points #9 and #10 obtained at 200 MPa with point #8 serving as H_2O-saturated reference and points #12, #13 and #14 obtained at 500 MPa with point #11 serving as H_2O-saturated reference. In order to calibrate equation [3], the maximum amount of water that can be incorporated into eutectic water saturated compositions (aH_2O = 1) at a given pressure was estimated using the P only dependent model of Liu *et al*. (2005) (c.f. Holtz *et al*., 2001b). Equation [3] can be used to extrapolate the feldspar ratio of all water bearing eutectic points from haplogranitic systems in Table 9 (#1 to #14) for H_2O-free conditions. The result is a constant average feldspar ratio of 0.44 (± 0.03) for all dry, haplogranitic eutectics regardless of pressure (see Figure 15). This extrapolation is extremely difficult to verify experimentally because absolutely dry systems can hardly be realized. However, the constant Ab/(Ab+Or) feldspar ratio of 0.44 for dry eutectic melts, independently on pressure, was a prerequisite for a simple formulation of this empirical barometer (see below).

II-1.3 Extension of the model to cotectic compositions

To make the geobarometry applicable to not only eutectic but also cotectic melts it is important to model the position of the cotectic curves for the dry reference system shown in Figure 15. Since the feldspar ratio of dry eutectics is at constant 0.44 independently from

pressure (see above), the position of the cotectic curves can be easily modeled from the phase relations in the H_2O-free and An-free Qz-Ab-Or system.

To fix the position of the cotectic curves separating the quartz and the feldspar primary fields in the dry Qz-Ab-Or system, the effect of pressure on the shift of the eutectic points of the dry ternary Qz-Ab-Or and the binary systems Qz-Ab and Qz-Or was assumed to be identical (same increase of Qz content as a function of increasing pressure, see equation [2]). The cotectic curves separating the quartz and the feldspar primary fields were assumed to be straight lines conntecting the eutectic point of the ternary system with eutectic points in the binary systems Qz-Ab and Qz-Or (Figure 15). Based on the observations in the phase diagrams established previously (systems #1 to #5, #8, #9, #11 and #14, see references in Table 9), equations [4] and [5] were formulated to predict the difference in quartz content between a given cotectic composition and the corresponding eutectic point as a function of the Ab/(Ab+Or) ratio in a dry system.

If $Ab/(Ab+Or)_{corr} > 0.44$:

$$[4] \qquad \Delta Qz\ (Ab - Qz)\ [wt.\%] = 2.88 \left(\frac{\left(\frac{Ab}{(Ab+Or)corr} \right) - 0.44}{0.56} \right)$$

Whereas, if $Ab/(Ab+Or)_{corr} < 0.44$:

$$[5] \qquad \Delta Qz\ (Or - Qz)\ [wt.\%] = 8.66 \left(\frac{0.44 - \left(\frac{Ab}{(Ab+Or)corr} \right)}{0.44} \right)$$

In these equations, ΔQz is the difference in Qz between a cotectic composition and the eutectic point corresponding to that particular cotectic curve. $Ab/(Ab+Or)_{corr}$ is the feldspar ratio of any H_2O- and An-free cotectic composition, thus a composition that has been corrected for the effect of these influence parameters. The effect of water on a natural cotectic composition can be corrected using equation [3]. A procedure to correct the feldspar ratio for

the effect of An is described below. If $Ab/(Ab+Or)_{corr}$ is > 0.44, then the sample is located along the Ab-Qz cotectic line and equation [4] has to be applied. If $Ab/(Ab+Or)_{corr}$ is < 0.44, the sample is located along the Or-Qz cotectic line and equation [5] has to be applied. The reference value of 0.44 is fixed for any pressure, since it is assumed that the feldspar ratio of dry eutectic points does not vary with pressure (c.f. Figure 15).

II-1.4 Applying the reference system to natural compositions – the geobarometer

The dry reference system established above and shown in Figure 15 has the important advantage that any composition constrained by normative Qz content and Ab/(Ab+Or) ratio can, after the subtraction of the effects of H_2O and normative melt An, only correspond to a single definite P value. In other words, the cotectic lines separating the quartz and feldspar primary fields never overlap in the dry Qz-Ab-Or system. This condition, which was a prerequisite for this empirical barometer, could only be fulfilled by assuming the same effect of pressure on the Qz content of the ternary and binary eutectic points and by calculating the constant average Ab/(Ab+Or) value of dry haplogranites of 0.44 using equation [3]. Having defined this reference system, cotectic compositions free off or corrected for H_2O and normative melt An content can now be used for geobarometry. Correcting feldspar ratios for the presence of H_2O is achieved using equation [3] and a H_2O correction for Qz content is not necessary. Correcting Qz contents for normative melt An is achieved using equation [1]. The effect of normative melt An ond the feldspar ratio Ab/(Ab+Or) can be corrected using the equation:

$$[6] \qquad Ab/(Ab+Or)_{\text{An -free}} = Ab/(Ab+Or)_{\text{dry}} + 0.041 * An \ [wt.\%]$$

Equation [6] was created in a procedure similar to that of equation [1]. A linear fit was applied to the experimentally determined eutectic points #15 to #23, using the An-free points

#2, #9, #10, #13 and #14 that have similar P and H_2O contents as reference points. For practical purposes, equations [3] and [6] can be combined:

[7] $$Ab/(Ab+Or)_{\text{corr}} = Ab/(Ab+Or)_{\text{real}} + 0.041 * An\ [wt.\%] - 0.028 * H_2O\ [wt.\%]$$

Taking ΔQz into account, equation [2] can be extended to make it applicable for cotectic compositions:

[8] $$P\ [MPa] = 100\left(\frac{(Qz\ [wt.\%] - 1.25 * An\ [wt.\%] - \Delta Qz\ [wt.\%] - 38.26)}{(-1.45)}\right)$$

This geobarometer, henceforth referred to as DERP (**D**etermination of **E**utectic **R**hyolite **P**ressures), is applicable to rhyolitic glass compositions in equilibrium with quartz and at least one feldspar for pressures up to 500 MPa, with normative melt An contents of up to 7 wt.% and any amount of dissolved H_2O. The only inputs required are the normative melt Qz, Ab, Or, An and H_2O contents. However, note that these values may change also with variations in TiO_2, FeO and MgO contents, owing to the CIPW calculation scheme. An MS-Excel sheet will be provided in the electronic Appendix of this study that will allow P calculations either directly from glass major element compositions, using an implemented CIPW calculation mechanism, or from Qz, Ab, Or, An and H_2O contents.

II-2 Constraints with respect to accuracy

II-2.1 Compositional restrictions

Although the experiments presented in this study simulate natural compositions more closely than any other systematic investigation known to the author, natural rhyolites contain a number of components which may have potential impacts on the Qz-Ab-Or-projection. As an example, both F and B are known to shift the eutectic point in the ternary projection in a comparable way to the pressure effect (Manning, 1981; Pichavant, 1987). While the effect of

B is probably negligible for common rhyolites containing less than 1 wt.% B, small amounts of F in the melt may cause a significant error predicting crystallization pressures with DERP (Manning, 1981). Manning (1981) experimentally investigated three rhyolitic systems with different F contents and the results indicate that even 0.25 wt.% F in a melt will lead to an overestimation of ~100 MPa. It was chosen not to implement the effect of F directly into DERP because three experimentally investigated systems (100 MPa) are deemed an insufficient database to extent the DERP barometer. The formulation of DERP implies that excess aluminum (normative corundum) does not affect the pressure estimation. This assumption is justified by experiments testing the effect of excess aluminum on the phase relation in haplogranitic system and showing that the liquidus temperatures may be slightly lower in peraluminous melts but that the position of the cotectic curves of systems saturated with an Al-rich phase (mullite) is not significantly different from that of the haplogranitic system (Holtz *et al*., 1992a).

Table 10: P estimates of natural samples from independent geobarometers and from DERP

Sample	Type[1] (glass)	Barometer	$P_{proposed}$ [MPa]	1σ [MPa]	P_{DERP} [MPa]	1σ [MPa]	$P_{MC\text{-}DERP}$[4] [MPa]	1σ [MPa]	Source
Young Toba Tuff	matrix	Amphibole	300	40	370	58	318	122	Chesner & Luhr 2010
Bishop Tuff	inclusion	QUILF	270	60	302	140	303	144	Frost & Lindsley 1992
Oruanui	matrix	Amphibole	132	63	130	66	146	199	Allan *et al.* 2012
Oruanui	inclusion	Fl. sat.[2]	120	31	52	54	n. p.		Liu *et al.* 2006
Mamaku	inclusion	Fl. sat.[2]	95	35	75	12	69	58	Bégué *et al.* 2014b
Blacktail Creek Tuff	matrix	TitaniQ[3]	175	75	235	90	198	102	Bolte *et al.* 2015
Hideaway Park Topaz Rhyolite	inclusion	Fl. sat./TitaniQ[3]	290	n.a.	239	174	n.p.		Mercer *et al.* 2015
Bandelier Tuff	inclusion	TitaniQ[3]	193	40	251	100	251	90	Audétat 2013
Central Plateau Member Rhyolite	matrix	TitaniQ[3]	241	46	298	21	291	76	Vazquez *et al.* 2009
Chalk Mt. Rhyolite	inclusion	TitaniQ[3]	190	70	173	47	181	101	Audétat 2015
Whakamaru eruption	matrix	Amphibole	119	51	129	51	113	121	Matthews *et al.* 2012

[1] Type of glass used for P determination in this study. Inclusions in both quartz and feldspar were used depending on available data

[2] Fluid saturation pressure

[3] TitaniQ pressures included in this Table exclusively calculated by the method proposed by Huang & Audétat (2012)

[4] P calculated with DERP by Monte-Carlo simulation with mean composition and 1σ of published rhyolite data; 1000 r-norm distributed compositions.

n.a. = not available; n.p. = not possible

II-2.2 Comparison with independent geobarometers

In order to evaluate the accuracy of DERP geobarometry, it is useful to compare the calculated results with independent pressure estimates from other geobarometers, as far as possible. A problem is the general lack of existing data from other barometers, especially for amphibole free rhyolitic melts. Gualda & Ghiorso (2013a) provide a number of studies where independent data are listed that are suitable to check for the accuracy of geobarometry using the compositions of cotectic rhyolitic melts. Starting from this list rhyolitic melt data is compiled in Table 10 from various locations suitable for DERP geobarometry for which P estimates are available. These independent P estimates are derived from different methods, including amphibole-, TitaniQ-, QUILF-geobarometry and fluid saturation pressures (see references in Table 10). DERP was used in two ways to calculate pressures for these samples. One approach consisted in calculating the pressure from the glass compositions for the corresponding petrological units (Table 10, Coloumn P_{DERP}). However, when several compositions were available, this approach can lead to high uncertainties, especially for strongly heterogeneous datasets. To avoid such a problem, a second P value was calculated (listed as $P_{MC\text{-}DERP}$ in Table 10) using a Monte-Carlo approach. In this approach, 1000 normally-distributed compositions were calculated based on the mean compositions and standard deviations given in the publications. Each of these compositions was then used to calculate P with DERP. The mean value and standard deviation of the 1000 calculated pressures is then given in Table 10. This method leads to a higher standard deviation on the pressure but minimizes possible strong inaccuracies due to a few erratic data or too strongly heterogeneous datasets. To illustrate the accuracy of DERP, the $P_{proposed}$ of Table 10 is plotted against both pressures calculated with DERP in Figure 16. Both calculation approaches manage to reproduce the independently calculated P within reasonable error. The mean difference between the independent P and the P calculated by DERP is 41 MPa for P_{DERP} and

29 MPa for $P_{MC\text{-}DERP}$. For P_{DERP} the highest difference with an independent geobarometer is 70 MPa for the Young Toba Tuff (Chesner & Luhr, 2010). In this case P_{DERP} predicts a value (370) MPa which is higher than estimated by amphibole geobarometry (300 MPa), whereas ~ 320 MPa are calculated with $P_{MC\text{-}DERP}$.

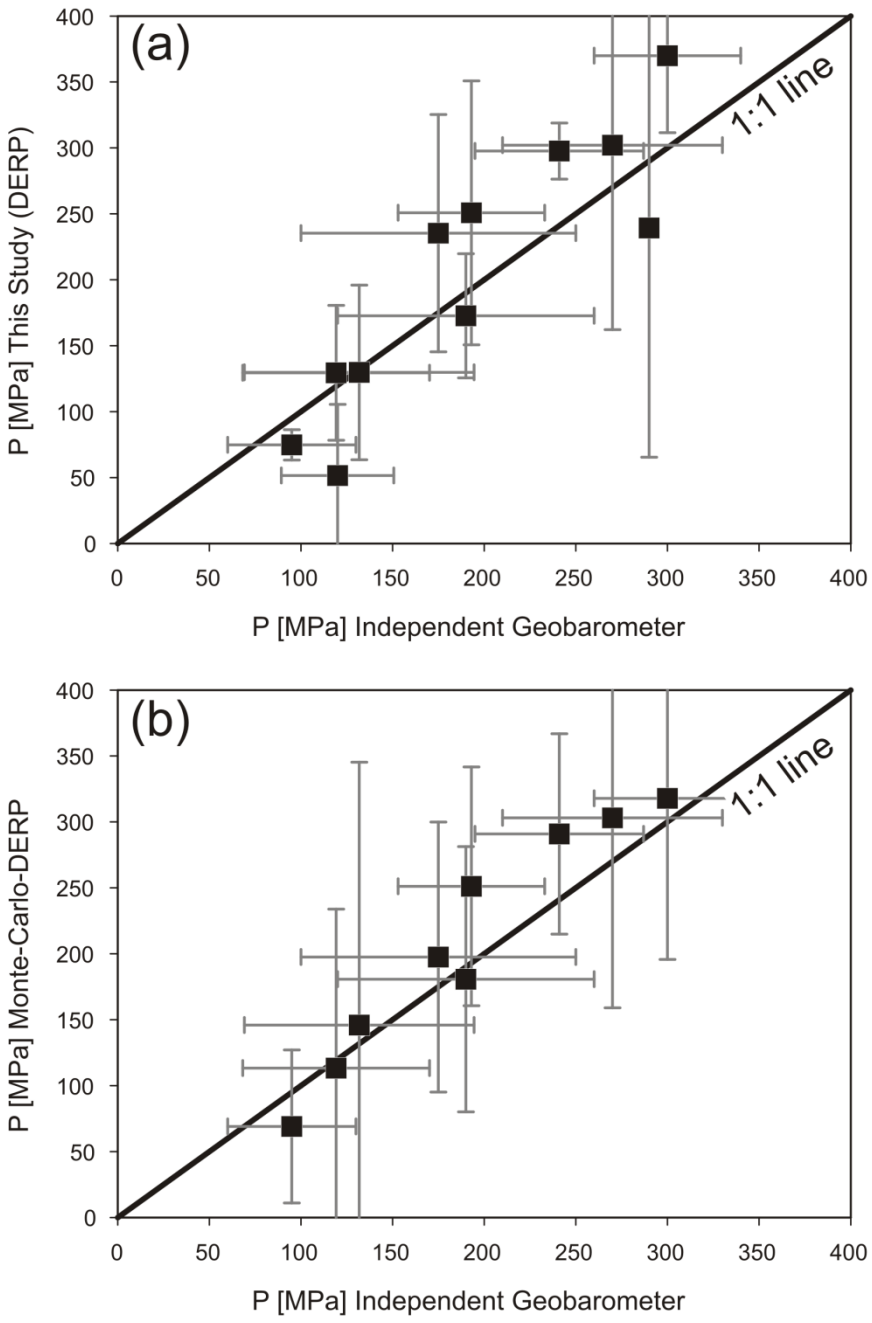

Figure 16: Plot of pressures from literature with pressures calculated with DERP as listed in Table 10. In (a) the P for DERP was calculated as the mean value of P calculated for all available compositions in the dataset. In (b) mean composition and standard deviation of a sample were used for a Monte-Carlo-simulation and the P was calculated with DERP for 1000 random normal distributed compositions resulting from that simulation.

II-3 Constraints with respect to precision

The uncertainty of pressure estimation using DERP is mainly related to two factors: the accuracy of the phase diagrams that are used to construct the barometer as well as the analytical uncertainties related to the determination of natural glass analyses. As explained in detail before, the approach to constrain the position of the eutectic points in the ternary phase diagrams Figures 6 – 11 is resulting from a number of observations (analysis of residual melts in the experiments, constraints from liquidus temperature isopleths, constraints from liquidus phase) which are taken into account in the final representation of the phase diagram. The resulting uncertainty on the compositions of the eutectic points is estimated to be at least ±2 to 2.5 wt.% (see above) but may be higher for cotectic curves which are sometimes poorly constrained in some parts of the Qz-Ab-Or diagram, especially for Ab-Qz and Ab-Or rich compositions. Additional errors may arise from the assumption of linear shape of cotectic curves in the Qz-Ab-Or diagram and the assumption that the effect of water on the shift of the eutectic point is linearly correlated with melt water content (see equation [3]). The second major source of error related to the analytical uncertainty of the investigated natural glass compositions may differ depending on the quality of the data. DERP is based on calculation of a CIPW-norm and a systematic error on the measurement of SiO_2, Al_2O_3, CaO, Na_2O and K_2O concentrations may substantially change the calculated pressure. The calculated pressure may be significantly affected if analytical errors lead to a shift of a cotectic glass composition recalculated for the projection in the dry reference system Qz-Ab-Or, from a position on the Qz-Ab cotectic curve to a position on the Qz-Or cotectic curve (eutectic transit) or vice versa.

Table 11: Major element composition of natural rhyolitic glass of the Blacktail Creek Tuff (BCT) from Bolte *et al*. (2015)

BCT nat. gl.	wt.% ox.	std.dev	relative (%)
SiO_2	77.02	0.82	1.1
TiO_2	0.18	0.01	5.6
Al_2O_3	11.95	0.18	1.5
FeO	1.21	0.11	9.1
MgO	0.13	0.06	46.2
CaO	0.50	0.03	6.0
Na_2O	2.93	0.17	5.8
K_2O	5.70	0.25	4.4
H_2O	2.00	0.50	25.0

A natural glass composition analyzed in one sample of the Blacktail Creek Tuff (BCT, Table 11, see also Table 1 in Bolte *et al*., 2015) was chosen to illustrate the precision that can be obtained with the cotectic approach and to simulated the effect of random errors in composition that occur inevitably either due to analytical uncertainties or as a result of natural inhomogeneities (Gualda & Ghiorso, 2014) on the results of DERP-geobarometry. The BCT sample analyzed by Bolte *et al*. (2015) was chosen as a reference because the melt was coexisting with quartz and two feldspars and the quenched glass matrix was extensively measured (n = 58), but also because the P of this system was estimated with a wide variety of methods including TitaniQ and an independent experimental approach (phase relationships of natural sample). It is assumed here that the determined P range of 130 – 240 MPa given by Bolte *et al*. (2015) represents the state of the art in current petrological methods. If the mean value of the BCT composition (Table 11) is used to calculate P with DERP, the resulting pressure is 235 MPa. For the Monte-Carlo-simulation a set of 1000 normally distributed compositions was generated based on the mean value and standard deviation given for the BCT by Bolte *et al*. (2015) for the relevant oxides SiO_2, Al_2O_3, FeO, MgO, CaO, Na_2O, K_2O and H_2O using the statistic software R. Figure 17 shows a histogram of calculated pressures with all these oxides allowed to vary independently. The overall scatter is large with

calculated pressures from ~ -200 to 500 MPa. The peak of calculated pressures with frequencies >100 is, however, clearly centered in the range 100 to 300 MPa. For this Monte-Carlo-simulation of pressures, the mean value is 198 MPa with 1σ of 102 MPa (see Table 11), a result that falls within the pressure range proposed by Bolte *et al*. (2015). While the mean P calculated with the Monte-Carlo simulation matches the P proposed in Bolte *et al*. (2015) more accurately than the P calculated from the mean melt composition only, the high 1σ of 102 MPa seems not to reflect the performance of the DERP geobarometer in respect to reproducibility and overall error considering the results shown in Figure 16.

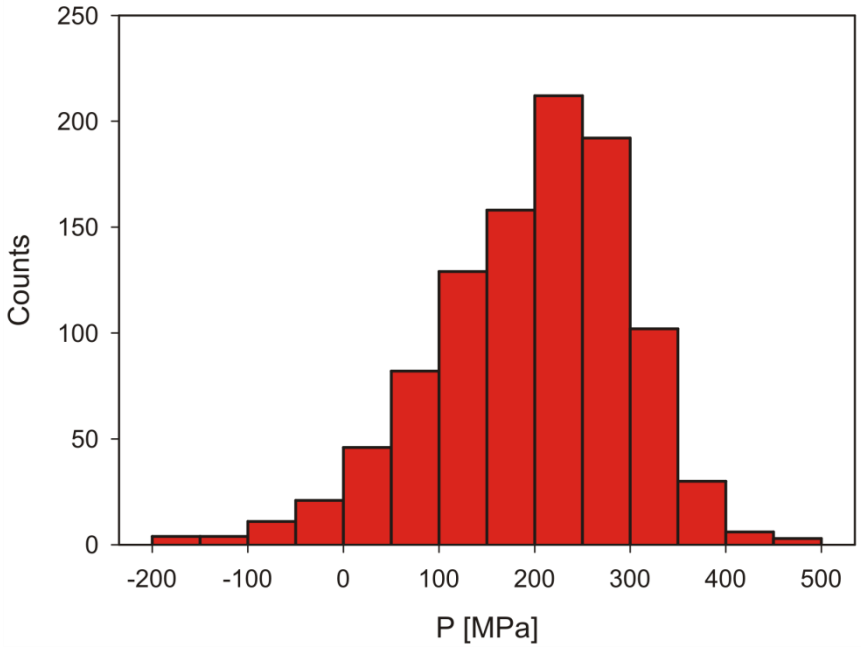

Figure 17: Histogram of calculated pressures for 1000 compositions derived for the Blacktail Creek Tuff (BCT) (see Table 11) by normally-distributed Monte-Carlo-simulation.

To demonstrate the implications of compositional shifts and of the precision of analytical datasets on pressures calculated with DERP, Monte-Carlo simulations were performed to check for the individual role of the main oxide components (SiO_2, Al_2O_3,FeO, MgO, CaO, Na_2O, K_2O and H_2O), applied to the BCT composition described above. In these simulations

only one of the oxides was allowed to vary normal distributed while all others were held constant at the mean value. The results are shown in Figure 18. Figure 18(a) shows that a variation of SiO_2 content of 1 wt.%, which would correspond to approximately 0.7 wt.% normative Qz in case of the BCT rhyolite, results in a change in P of ~ 45 MPa. The change in pressure with changing SiO_2 is linear since the ratio of all other parameters influencing the normative contents (Ab, Or, An) and the H_2O content remain constant. The histogram in Figure 18(b) shows that SiO_2 alone cannot be responsible for the full range of pressures determined in the multivariant Monte-Carlo simulation shown in Figure 17. The role of Al_2O_3 is shown in Figure 18(c) and (d). At high Al_2O_3 contents, there is a range of compositions where Al_2O_3 does not influence P because the CIPW norm predicts normative corundum and the proportions of Qz/Ab/Or/An remain constant. In the compositional range without normative corundum, the calculated P decreases with decreasing Al_2O_3 because the amount of normative An is decreasing with a concomitant very slight increase in normative Qz (the CiPW norm calculates small amounts of wollastonite). The small variation of the slope of the curve in Figure 18(c) observed at ~ 11.7 wt.% Al_2O_3 is a result of a change of the reference cotectic curve with changing An content (eutectic transit). The compositions with more than 11.7 wt.% Al_2O_3 plot along the Qz-Or cotectic, whereas compositions with less Al_2O_3 plot along the Qz-Ab cotectic. The interplay of subtle changes in the CIPW norm and of projections either on the Qz-Ab or the Qz-Or cotectics also explain the various trends observed in the diagrams with changing CaO, Na_2O and K_2O (Figures 18(e) to (k)). A detailed analysis of figures 18(g) to (k) shows that the correct analysis of the alkalis is crucial for an accurate determination of pressure. Figures 18(g) and (i) show that the most extreme P calculations are likely related to changes in Na_2O and K_2O content. In the BCT composition, variations of 0.1 wt.% Na_2O can affect the P estimated with DERP by ~ 50 MPa. This strong effect is observed in the Na_2O range ~2.6 to 3 wt.%. In this compositional range, the

compositions are peraluminous and plot on the Qz-Ab cotectic. The effect of water on DERP is illustrated in Figure 18(m) and (n). The two different slopes of the curves in this figure are related to projections of the BCT composition on the Qz-Ab cotectic on one hand (for low water contents) and on the projections on the Qz-Or cotectic on the other hand (for high water contents). For samples plotting on the Qz-Or cotectic, a change of 1 wt.% H_2O results in a variation of the predicted P of ~ 35 MPa, whereas the effect is lower for samples plotting on the Qz-Ab cotectic. As illustrated above, problems with the determination of Na_2O and K_2O contents can have strong consequences on P estimated by DERP. However, depending on the compositional field of the glasses (projection onto the Qz-Ab or Qz-Or cotectic; peralouminous composition or not) small compositional changes may be negligible or may have important implications for the pressure estimation. As a consequence, a unique uncertainty value on the pressure estimation cannot be proposed and it is recommended to test the effect of possible compositional variations with DERP (available as MS-Excel sheet in the electronic appendix of this study) for each case study.

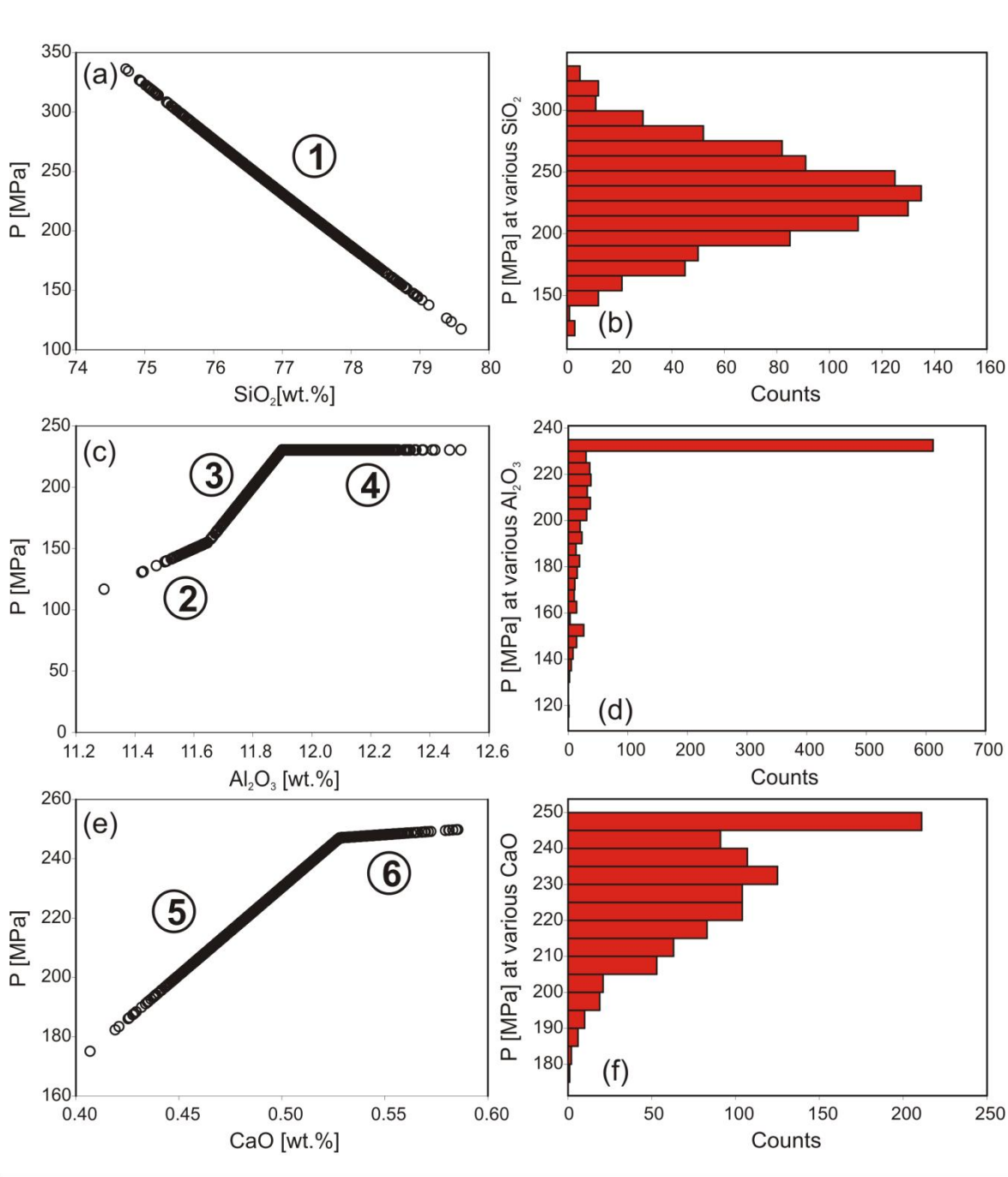

Figure 18: Illustration of the impact of varying different oxides on the calculated pressure. For each relevant oxide pressure was calculated for 1000 Gaussian normal-distributed values, while the others were held constant at their mean value (BCT, Table 11). Circled numbers correspond to changes in Pressure-Oxide-dependency predicted by DERP that can be explained as follows: (1) Linear Qz-P dependence (2) Corundum deficit limiting An formation (3) Corundum deficit after eutectic transit (change from Qz-Ab cotectic to Qz-Or cotectic) (4) Excess corundum (5) An-P dependence (6) Eutectic transit.

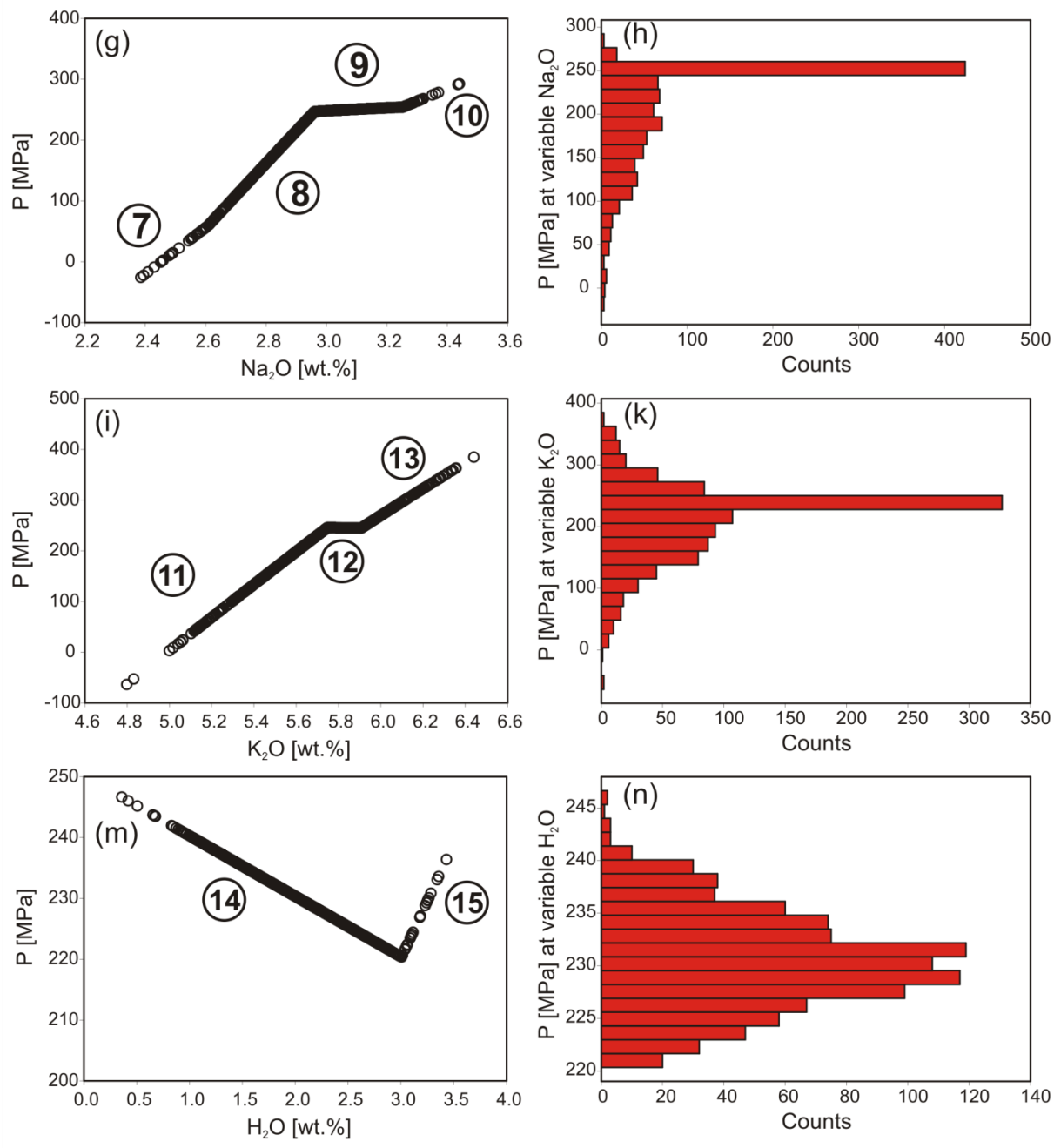

Figure 18: Continued. (7) Ab-P dependence (8) Eutectic transit (9) Corundum deficit limiting An formation (10) Corundum deficit limiting Ab formation (no An) (11) Or-P dependence (12) Corundum deficit limiting An formation (13) eutectic transit (14) Qz-Or-cotectic H_2O-P dependence (15) Qz-Ab-cotectic H_2O-P dependence.

II-4 Comparison with the rhyolite-MELTS model

As mentioned above the rhyolite-MELTS pressure estimation procedure is based on the same properties of the granitic system (positions of cotectic lines as function of pressure) as DERP. It is therefore interesting to test if the calibration (and calculation mechanism) presented in this study, based on new experimental constraints, leads to a significant improvement when compared to rhyolite-MELTS. Figure 19(a) and (b) compare P calculated with rhyolite-MELTS (x-axis) and DERP (y-axis). The rhyolite-MELTS P are derived from Bégué *et al*. (2014a) in case of Figure 19(a) and from Pamukcu *et al*. (2015) in case of Figure 19(b). In both cases the pressures calculated with DERP are significantly higher than the ones calculated by rhyolite-MELTS. For the glasses analyzed by Bégué *et al*. (2014b) 3 wt.% H_2O was used to calculate pressures with DERP, the smallest geologically relevant amount for the Taupo Volcanic Zone. It is also emphasized that Pamukcu *et al*. (2015) determined pressures from glasses considered to be eutectic compositions that coexisted with quartz and two feldspars. To evaluate the reason for the P gap observed between rhyolite-MELTS and DERP, the difference in P estimates between the two geobarometers for the data given by Pamukcu *et al*. (2015) is plotted against normative An content in Figure 20. The results show that there is a general positive correlation between the pressure difference from the two models and the An content of the glasses. It can be concluded that the differences in pressure estimation between DERP and rhyolites-MELTS can largely be accounted to the different handling of the effect of normative melt An content on eutectic compositions. To the knowledge of the author, rhyolite-MELTS applies a correction for the influence of An based on the model of Blundy & Cashman (2001). However, as demonstrated above 14(b) to (d), the Blundy & Cashman (2001) correction underestimates the effect of An on the position of thermal minima in the ternary projection. It has to be assumed that this problem is reflected in the rhyolite-MELTS

barometer, implying that pressures calculated with this model from An-rich glasses may be underestimated.

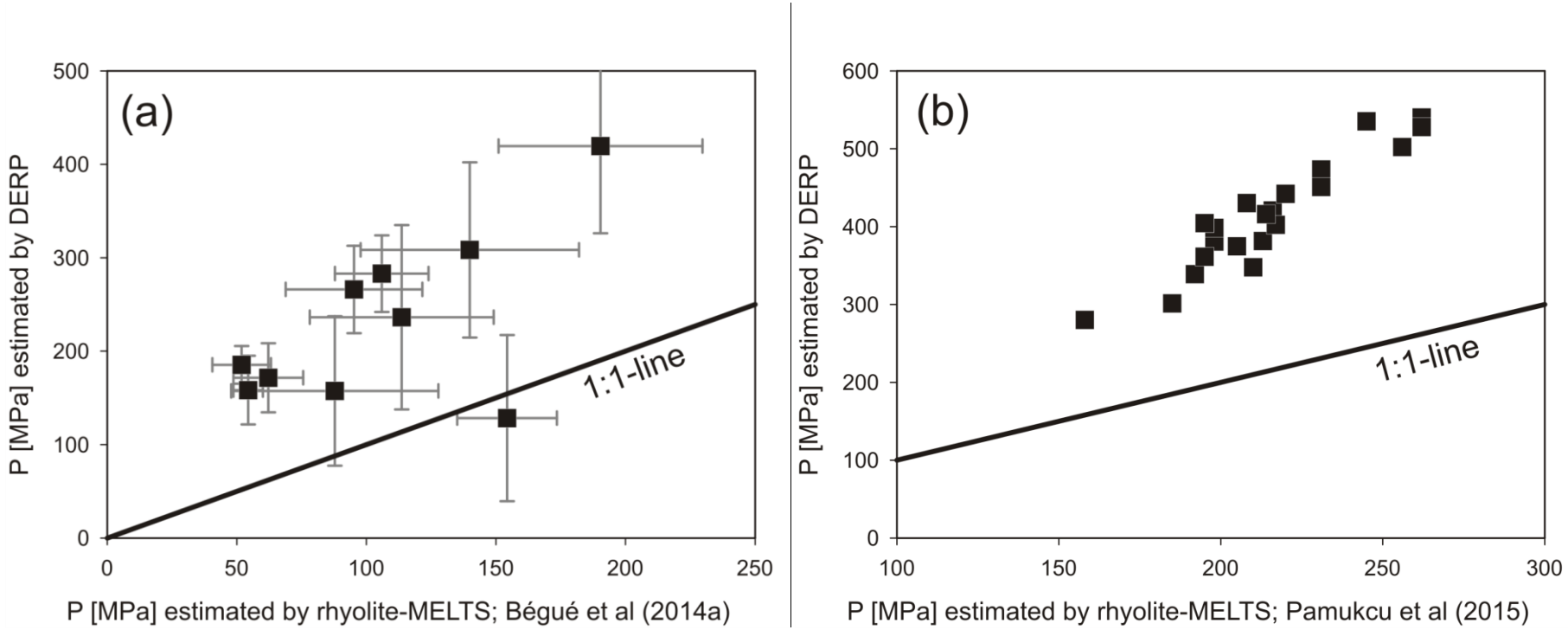

Figure 19(a): Plot of pressures estimated either with rhyolite-MELTS by Bégué *et al*. (2014) (x-axis) or DERP (y-axis). Every data point refers to a rhyolitic eruption in the Taupo Volcanic Zone (see Bégué *et al*. (2014b) for geological details. The error bars represent 1σ of the average of numerous samples analyzed for every eruption. For the calculation with DERP, the water content was assumed to be 3 wt.%. (b) Plot of pressures estimated for Peach Spring Tuff either with rhyolite-MELTS by Pamukcu *et al*. (2015) (x-axis), Q2F-condition, or DERP (y-axis). As Pamukcu *et al*. (2015) implied water saturation for their calculations, the results of the calculations with DERP were obtained inferring a melt water content of 4 wt.%. See text for a discussion of the melt water content issue. As no error was given for the data of Pamukcu *et al*. (2015), no error can be calculated for the DERP estimated pressures.

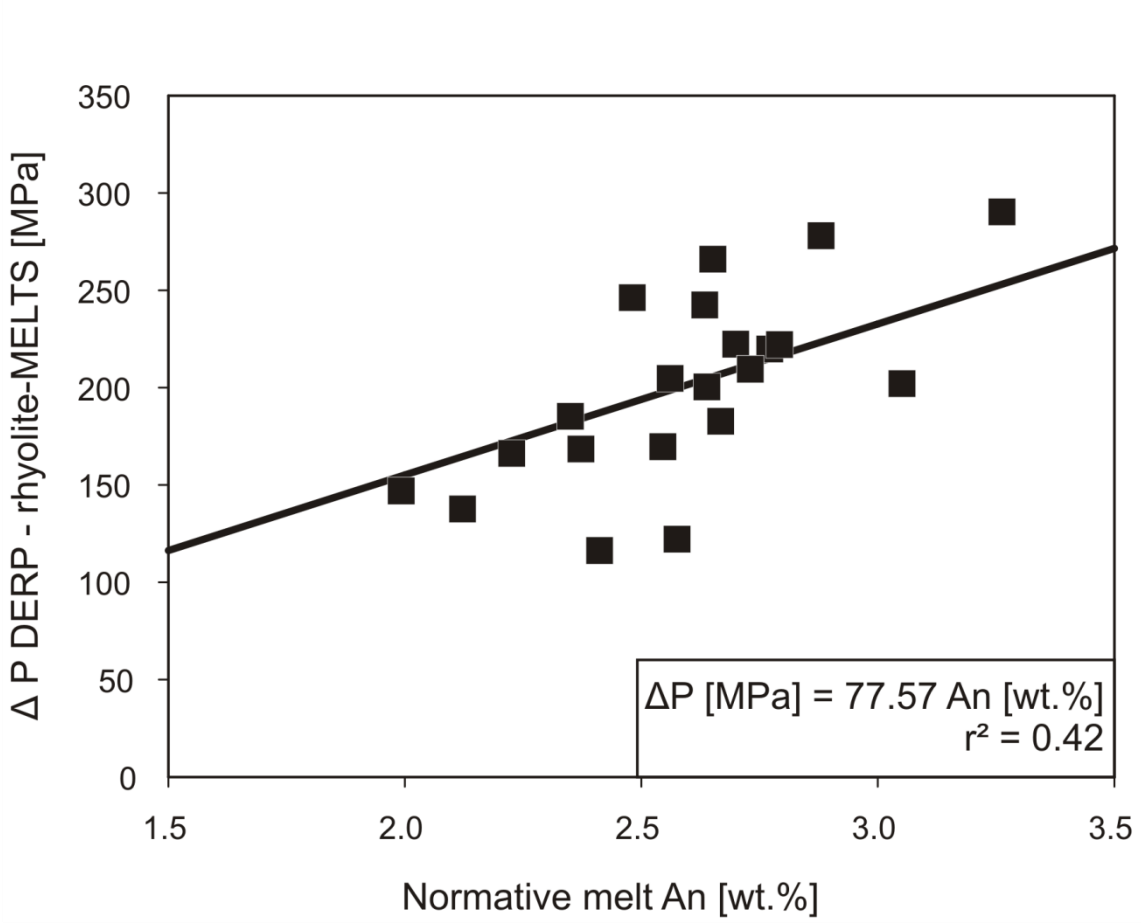

Figure 20: Plot of the difference in P [MPa] (ΔP) from estimations calculated with rhyolite-MELTS with P calculated from DERP for the dataset of Pamukcu *et al*. (2015), as a function of the normative An content of glass analyses. The pressure difference between the two models is increasing with the normative An content. The black line represents a linear trend calculated by least squares that matches the data with a coefficient of determination of 42%. The equation of the linear fit given in the figure may be applied for a rough correction of calculated pressures with rhyolite-MELTS.

CHAPTER III - Geobarometry in the Snake River Plain, Yellowstone, USA

III-1 General aim of the chapter

The DERP geobarometer described in chapter II of this study provides petrologists with a powerful new tool to determine magma storage pressures of rhyolites. In this chapter it shall be demonstrated how DERP can contribute valuable information to an extensive petrological field study and help developing a better understanding of the geology and the processes that lead to its formation. The prerequisites for DERP geobarometry are fulfilled by a comparably large number of rhyolites that only need to host a glass matrix in equilibrium with quartz and at least one feldspar. The required input data: the rhyolite-glass content of normative Qz, Ab, Or, An and of H_2O is comparably easy to obtain with petrological standard analyses. This makes DERP an ideal candidate to estimate pressures for large numbers of samples of different origin, allowing to closely investigate complex volcanic processes even over long distances and long periods of time. An example for such a province of complex volcanic history is the Snake River Plain, Yellowstone USA (SRPY), where a hot mantle plum has produced several eruptive complexes in the overlaying north american plate during its drift towards SW. Twin Falls is one of these eruptive complexes of the SRPY. It was active during a time interval of ~12.7 – 8.5 Ma (Cathy & Nash, 2009) and has been described extensively in a considerable number of studies, most notable probably Bonnichsen *et al*. (2008) and Ellis *et al*. (2010). In the frame of the ICDP project HOTSPOT several deep drilling operations have been carried out in the SRPY. One of these, the Kimberly drillhole that was realized close to the city of the same name, Idaho, USA, produced a core that allows access to rhyolites that are thought to be not exposed on the surface. They therefore were, prior to the drilling operation, not accessible for investigations. The combination of core samples, samples

collected from outcrops in the field and published literature data provides a high resolution record of Twin Falls eruptive history over time. To understand this history, two central problems shall be investigated in depth here. 1st: what exactly is the stratigraphic order of the Twin Falls eruptive complex? And 2nd: what were the magma storage conditions of the Twin Falls rhyolites, did they change over time and do they differ from the ones of neighboring eruptive complexes? To solve these questions 9 samples from the Twin Falls area and one sample of each of the younger eruptive complexes Picabo (10.2 – 9.2 Ma), Heise (6.6 – 4.4 Ma) and Yellowstone Plateau (2.0 – 0.6 Ma; Cathey& Nash, 2009) were investigated by electron microprobe. The compositions of the phases are compared with literature data for possible correlations between eruption units and then used to estimate magma storage temperatures and pressures. Besides DERP, the TitaniQ geobarometer (Thomas *et al*., 2010; Huang & Audètat, 2012) is used to both compare the performance of the geobarometers in a practical application and increase the reliability of pressures estimated for the eruption units.

III-2 Geological background

III-2.1 Structure and origin of the Snake River Plain, Yellowstone (SRPY)

The Snake River Plain, Yellowstone (SRPY), located mostly in southern Idaho, USA, is an excellent example of a study area, where DERP geobarometry can provide important contributions to the investigation of structure and development of rhyolitic magma chambers. Formed by the southwest movement of the northamerican plate over a fix mantle plume, usually referred to as "hotspot", for at least the last 16 Ma, the SRPY has been and still is in the focus of an enormous amount of publications from various contributors (e.g. Hildreth *et al*., 1991; Honjo *et al*., 1992; Perkins *et al*., 1995; Perkins & Nash, 2002; Cathey & Nash, 2004; Nash *et al*., 2006; Bindeman *et al*., 2007; Andrews *et al*., 2008; Bonnichsen *et al*., 2008; Branney *et al*., 2008; Vazquez *et al*., 2009; Almeev *et al*., 2012; Ellis *et al*., 2013; Bolte

et al., 2015 and many more). The volcanism of the SRP is bimodal, producing large volumes of both basalts and rhyolites (Ellis *et al*., 2013). The rhyolitic volcanism that shall be the primary focus of this study was broadly time-transgressive (Pierce & Morgan, 1992) and formed several volcanic eruptive centers of ~100 km in diameter: McDermitt (16.5 Ma), Owyhee-Humboldt (15.3 Ma), Bruneau-Jarbidge (12.7 Ma), Twin Falls (10.5 Ma), Picabo (10.2 Ma), Heise (6.6 Ma), Yellowstone Plateau (2.05 Ma) (Cathey & Nash, 2009; see Figure 21). The abbreviations introduced in Figure 21 for the eruptive centers are used in the following text. It must be noted, however that exceptions to the time-transgressive eruption trend exist on several scales (Bonnichsen *et al*., 2008) and the attribution of some eruptive units to a specific eruptive center is still under debate. Rhyolites from SRPY in general show a number of distinctive features, such as low water contents, hot storage T and an evolved mineral assemblage consisting mainly of pyroxene, feldspar, quartz and sometimes magnetite and/or ilmenite. This mineral assemblage can be used for constraining magma storage temperatures but is not suitable for traditional geobarometry as neither amphibole-geobarometry nor a fluid saturation pressure approach is practicable (Cathey & Nash, 2009; Ridolfi *et al*., 2010; Almeev *et al*., 2012; Bolte *et al*., 2015). Branney *et al*. (2008) list a number of additional characteristics for this “SR-type” volcanism of which the elevated content of HFSE and halogens, the large and devastating character of the rhyolitic eruptions and the unusual lack of pumice lapilli shall be mentioned here.

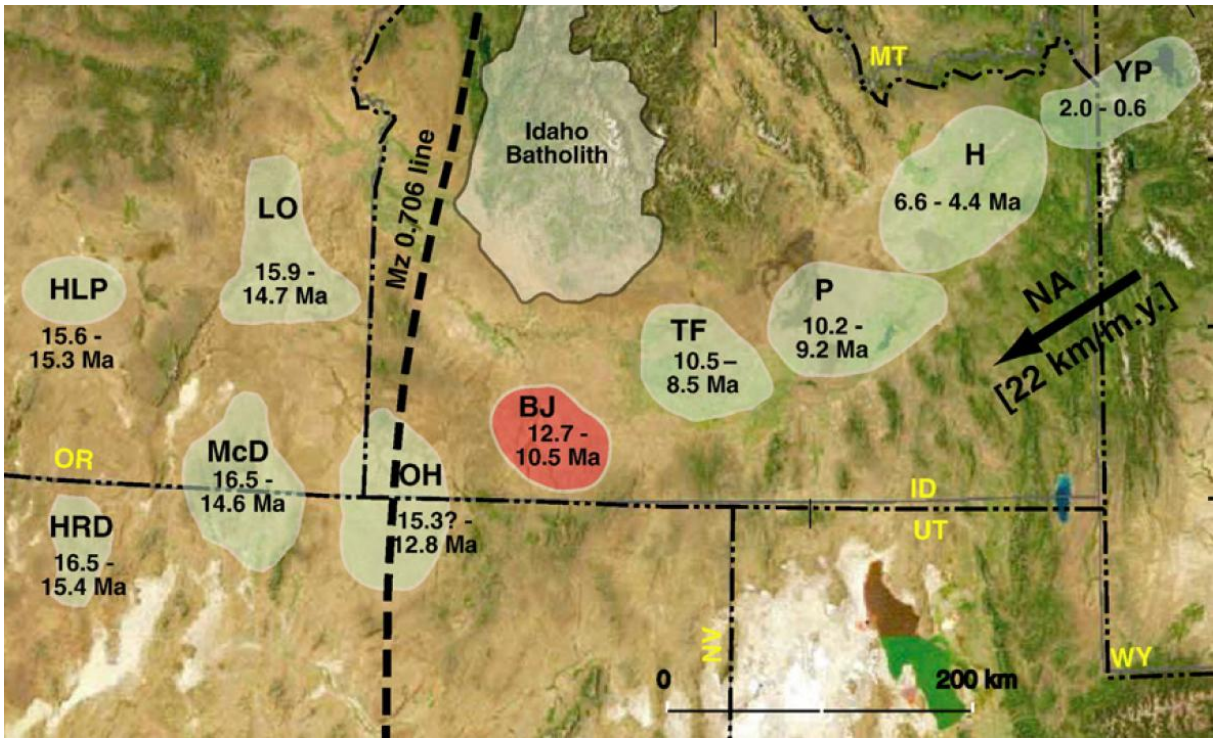

Figure 21: Image showing the position of major rhyolitic volcanic eruptive centers in the SRPY with their time of activity (Cathy & Nash, 2009). HLP = High Lava Plains, LO = Lake Owyhee, HRD = High Rock Desert, McD = McDermitt, OH = Owyhee-Humboldt, BJ = Bruneau-Jarbidge, TF = Twin Falls, P = Picabo, H = Heise, YP = Yellowstone Plateau.

The structure of the magma plumbing system beneath the SRPY is the object of ongoing research. Ellis *et al*. (2010) proposed that volcanic eruptive centers such as Twin Falls are fed by a network of multiple, interconnected magma chambers of comparable, yet not similar composition. During an eruption, several, if not all, magma chambers contribute melts that mix prior to or during eruption. Bonnichsen *et al*. (2008) state that the energy for those magma chambers does indeed come from the intrusion of huge volumes of basaltic magma into the crust, which is also reflected in the younger rhyolites produced in the SRPY. Bonnichsen *et al*. (2008) further emphasize that the SRPY magmatic system is active for several eruptive centers simultaneously, despite the time-transgressive trend observed in the large scale perspective. The SRPY magmatic system would therefore be best described as a swath of active rhyolite chambers over a wide regional range with merely a local focus determined by the plates position over the mantle plume.

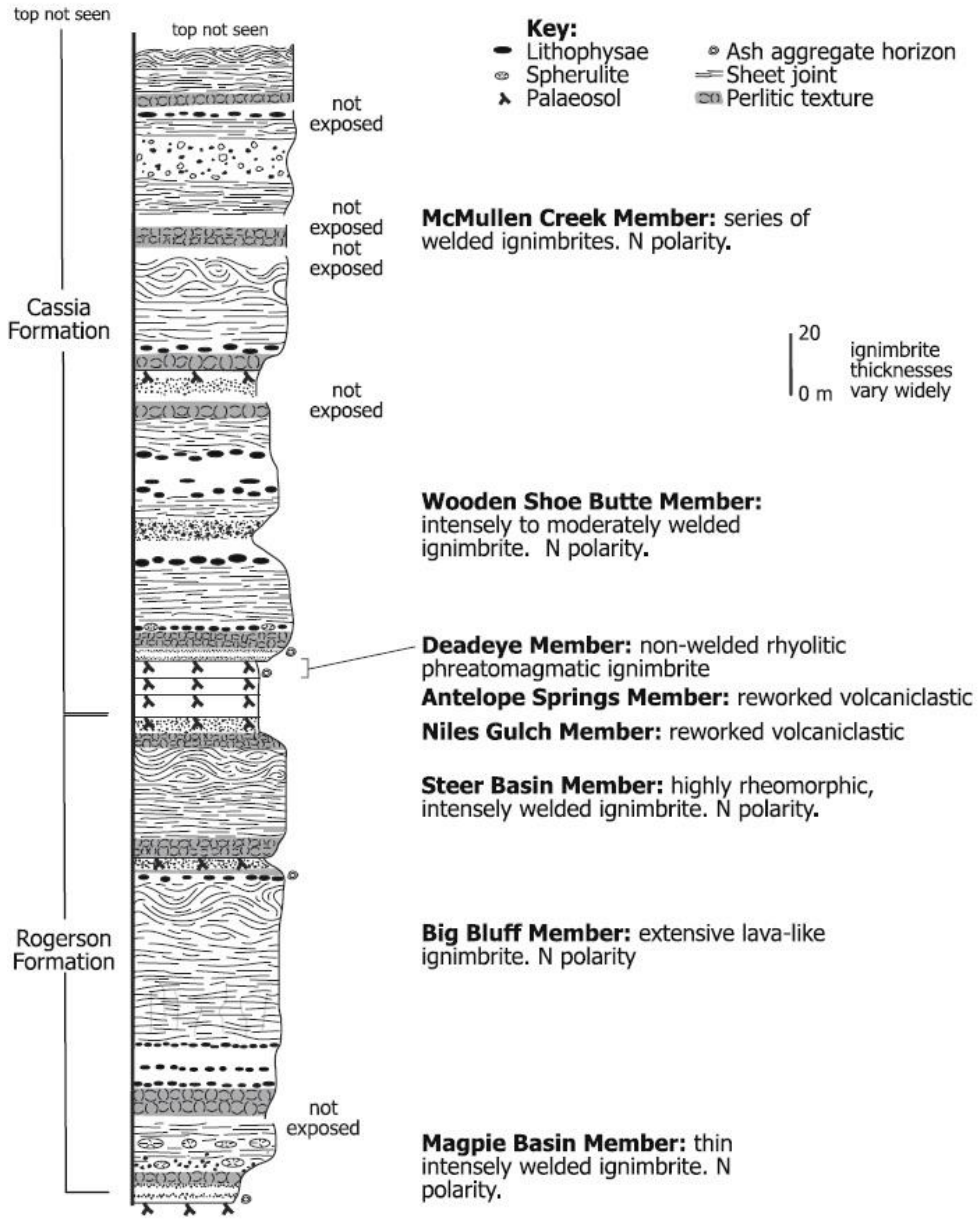

Figure 22: Generalized stratigraphy of the Rogerson and Cassia Formations, Twin Falls eruptive center, SRPY, as observed in the Cassia Mountains, close to the triple border point Idaho-Utah-Nevada. From Ellis *et al.* (2010, their Figure 2)

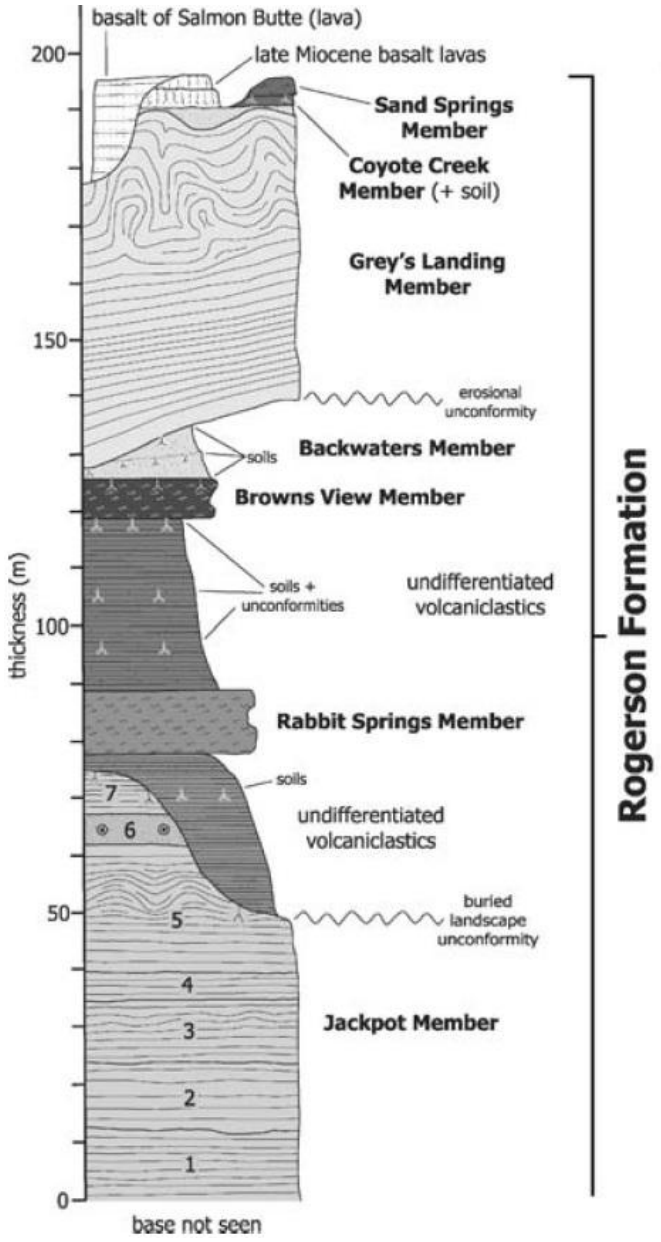

Figure 23: General vertical section through the Rogerson Formation, Twin Falls eruptive center, SRPY, as observed in the Rogerson Graben, west of the Cassia Mountains. From Andrews *et al*. (2008, their Figure 2)

III-2.2 The Twin Falls eruptive center

The volcanic stratigraphy of rhyolitic volcanites from the Twin Falls eruptive center is complex and the object of ongoing research. Major investigations have been carried out in the Cassia Mountains (Wright *et al*., 2002; Ellis *et al*., 2010) (see Figure 22) and in the Rogerson Graben (Andrews *et al*., 2008) (see Figure 23) to identify and describe numerous rhyolitic units. The Rogerson Formation, beeing older than the Cassia Formation, is usually described to begin with the ~11.3 Ma old Magpie Basin Member (Bonnichsen *et al*., 2008; Ellis *et al*.,

2010), although Hughes & McCurry (2002) see this unit not as an early member of the Twin Falls but as a late member of the older Bruneau Jarbidge eruptive complex. The same disagreement between Ellis *et al*. (2010) and Hughes & McCurry (2002) is found for the next unit, the Big Bluff Member (10.98 ± 0.07 Ma, Ellis, 2009). Bonnichsen *et al*. (2008) agree with Ellis *et al*. (2010) that the Big Bluff Member is part of the Twin Falls eruption history but also mention that it might be identical with what has been described as Jackpot Rhyolite Member 1 to 6 by Andrews *et al*. (2008). The Steer Basin Member, 10.63 ± 0.07 Ma in age (Ellis, 2009), is acknowledged by Hughes & McCurry (2002) and Bonnichsen *et al*. (2008) as a product of Twin Falls and linked by Bonnichsen *et al*. (2008) to the Jackpot Rhyolite Member 7 from Andrews *et al*. (2008). According to Ellis *et al*. (2010), based on their observation in the Cassia Mountains, the Rogerson Formation ends with the Steer Basin Member and the next rhyolite unit, the 10.63 to 10.13 Ma old Deadeye Member, marks the beginning of the Cassia Formation. Andrews *et al*. (2008) as well as Andrews & Branney (2011) and Ellis *et al*. (2015), however, count the Greys Landing ignimbrite as part of the Rogerson Formation, backed up by unambiguous observation in the Rogerson Graben locality. Unfortunately, no accurate age determinations are available for the Greys Landing Ignimbrite but from stratigraphic considerations it must be much younger with an age between ~9 to 7.5 Ma (Bonnichsen *et al*., 2008). Andrews & Branney (2011) mention that the Rogerson Formation and the Cassia Formation are at least partially correlated, as some units of both localities are thought to have been produced by the same eruption event. However, as the Greys Landing Ignimbrite is not present in the Cassia Mountains outcrop (Ellis *et al*, 2010), probably because it has been eroded in this locality, the situation remains not entirely clear. As mentioned, in the Cassia Mountains the Steer Basin Member is not followed by the Greys Landing Ignimbrite but by the Deadeye Member (Ellis *et al*, 2010). The next rhyolitic unit in this locality is the Wooden Shoe Butte Member, dated as 10.13 ± 0.03 Ma old by

Perkins & Nash (2002). The youngest preserved unit in the Cassia mountains is with 8.94 ± 0.07 (Nash *et al*., 2006) the McMullen Creek Member. As its end has not been observed, it is yet unclear whether it marks the end of the Cassia Formation and if it is overlain by the missing Greys Landing Ignimbrite.

Table 12: Schematic summary of the stratigraphy of the Twin Falls eruptive center as described by Hughes & McCurry (2002), Andrews *et al*. (2008), Bonnichsen *et al*. (2008), Ellis *et al*. (2010), Andrews & Branney (2011) and Ellis *et al*. (2015).

Age [Ma]	Member	Formation	Eruptive Center
~ 11.3	Magpie Basin	Rogerson	Twin Falls or B-J
10.98 ± 0.07	Big Bluff or Jackpot 1 - 6	Rogerson	Twin Falls or B-J
10.63 ± 0.07	Steer Basin or Jackpot 7	Rogerson	Twin Falls
10.63 - 10.13	Deadeye	Cassia	Twin Falls
10.13 ± 0.03	Wooden Shoe Butte	Cassia	Twin Falls
8.97 ± 0.07	McMullen Creek	Cassia	Twin Falls
8.97 - 7.5	Greys Landing	Rogerson	Twin Falls
7.5 - 5.5	Sand Springs	Rogerson	Twin Falls
7.5 - 5.5	Shoshone Falls	unknown	Twin Falls

III-3 Detailed description of the samples

Table 13: List of phases observed in the investigated samples. Sorted by age.

Sample	Unit	glass	Qtz	San	Plg	Aug	Pig	Mgt	Ilm	Other
SRP12-A05A	Steer Basin	x	x	x	x	x	x	x	x	
SRP12-19B	Arbon Valley	x	x	x	x			x	x	Bt
SRP12-A02a	Wooden Shoe B.	x	x	x	x	x	x	x	x	
SRP12-A02b	Wooden Shoe B.	x	x	x	x		x	x	x	
KRH1-2052	Kimberly Rh. 1	x			x	x	x	x		
SRP09-24c	Greys Landing	x	x	x	x	x	x	x	x	
KRH2-1946	Kimberly Rh. 2	x	x	x	x	x	x	x		
KRH2-1796	Kimberly Rh. 2		x	x	x	x		x	x	
KRH2-1401	Kimberly Rh. 2	x	x	x	x	x	x	x		
KRH3-716	Kimberly Rh 3			x	x	x	x	x	x	
SRP09-13	Wolverine Ck.	x	x		x	x		x		
SRP09-10E	Huckleberry R.	x	x	x	x	x	x	x		Fa

Qtz = quartz, San = sanidine, Plg = plagioclase, Aug = augite, Pig = pigeonite, Mgt = magnetite, Ilm = ilmenite, Bt = biotite, Fa = fayalite

In total, 12 different samples have been investigated. Table 13 gives an overview of the abundant phases. Quartz, sanidine, plagioclase, augite, pigeonite, magnetite and ilmenite were found to be very common in most samples with however a few notable exceptions. Most samples also hosted accecory zircon and apatite and rare pyrite but a systematic investigation of these phases is beyond the scope of this study. Biotite was found in the Arbon Valley tuff of sample SRP12-19B that is lacking pyroxene in return. This result is in good agreement with observations from Kellogg *et al*. (1994) that describe Arbon Valley as one of the rare locations in the SRP where biotite is a common mineral in a rhyolite. A single fayalite crystal was found in the sample SRP09-10E from Huckleberry Ridge tuff. As at the same time quartz is a common phase in that sample it is safe to assume that the fayalite did not crystallize from the rhyolitic magma but entered from another source directly prior to or even during the eruption. Whether this is a consequence of the increasing mafic influence in younger rhyolites of the SRP described by Bonnichsen *et al*. (2008) or whether the fayalite crystal was simply

gripped from wallrock during ascend or older, underlaying basalts after expulsion yet remains unclear.

III-3.1 The Kimberly drill core

The Kimberly drill core was retrieved in the frame of project HOTSPOT, supported by ICDP, between January 2011 and June 2011 in the Twin Falls eruptive center (Shervais *et al*., 2013). It provides a continous record of almost 2 km rhyolitic ignimbrites seperated in three different units, labeled rhyolite units 1, 2 and 3 (KRH1-3) in the following description (Figure 24). Note that the numbers that distinguish KRH samples of the same unit refer to the depth of the samples position in feet within the drillcore. Five samples from the Kimberly drillcore were selected for analysis by EPMA. One sample sample from 625 m (2052 ft) belonging to KRH3 and located at its top, close to the border to KRH2, one sample from 218 m (716 ft) belonging to KRH1 and located at its bottom, close to the border of KRH2 and three samples belonging to KRH2 located at 427 m (1401 ft), 547 m (1796 ft) and 593 m (1946 ft). The focus on KRH2 was chosen because of its potential to shed light on the stratigraphy of the Cassia Formation above the McCullen Creek Member and its suitability for DERP geobarometry.

Rhyolite unit 3 (KRH3) was recovered between 122 and 244 m depth. This rhyolitic lava flow contains plagioclase, k-feldspar, pigeonite, augite, magnetite, sparse ilmenite and accessory apatite but no preserved glass matrix (Christiansen *et al*., 2013). It is tentatively correlated based on stratigraphic considerations with the rhyolite of Shoshone Falls by Christiansen *et al*. (2013).

Rhyolite unit 2 (KRH2) was recovered between 427 and 600 m depth. The high-silica rhyolite lava flow contains quartz, plagioclase, k-feldspar, augite, pigeonite, magnetite, sparse ilmenite and accessory apatite and zircon in a glassy matrix. However, a detailed look at several thin sections from this unit does reveal some internal differences. While KRH2-1946 and KRH2-1401 show the same phase assemblage with only ilmenite missing, ilmenite was observed for

sample KRH2-1796 that in return lacks pigeonite and a glass phase. That no glass could be found in KRH2-1796 does however not mean the sample is of a distinctly different material than the other two KRH2 samples. BSE images of KRH2-1796 (e.g. Figure 25) show a matrix of glassy morphology that is visualized with two different shades of grey. These two different phases form swathes that change in size, often in a radial pattern. The composition of the swathes is feldspathic. The reason of the formation of this kind of matrix, in contrast to the preserved glass in the other two KRH2, could be a difference in the cooling temperature after eruption. The samples KRH2-1946 and KRH2-1401 come from the bottom and the top of the unit (c.f. Figure 24). It is likely that after the eruption they were deposited in close contact to the underlaying ground or the atmosphere, respectively. That would lead to a faster cooling rate, while in the middle of the ignimbrite flow the heat is preserved over a longer period, causing the glassmatrix of sample KRH2-1796 to crystallize. Anyway it is clear that at least in parts of the Kimberly Rhyolite unit 2 glass was preserved. Christiansen *et al*. (2013) mention that no matching eruptive unit is known for KRH2 from the outcrops. A possible candidate could be the Greys Langing Member, considering the position of the Kimberly stratigraphy relative to the Cassia formation and the missing of the Greys Landing Member on Top of it as a link to the Rogerson formation. Beeing the only rhyolite unit in the drillcore to contain quartz, feldspar and a glass phase, Rhyolite unit 2 is the only unit suitable for DERP geobarometry.

Rhyolite unit 1 (KRH1) was recovered between 610 m and the end of the borehole at 1958 m depth with no indication of the actual thickness of that unit. Rhyolite 1 is a low-silica ignimbrite with plagioclase, pigeonite, augite, magnetite and accessory apatite, zircon, and pyrite. It is tentatively correlated with the tuff of McMullen Creek by Christiansen *et al*. (2013). This claim is backed up with additional evidence here, as the rather unusual phase assemblage of KRH1-2052, with quartz and sanidine both missing, is reported from fieldwork

in the Cassia and Rogerson Formation only for the McMullen Creek Member (Ellis *et al*., 2010). If that correlation is correct, the Kimberly drillcore could help to complete the stratigraphy of the Cassia formation by providing the units of the missing top (c.f. Figure 22).

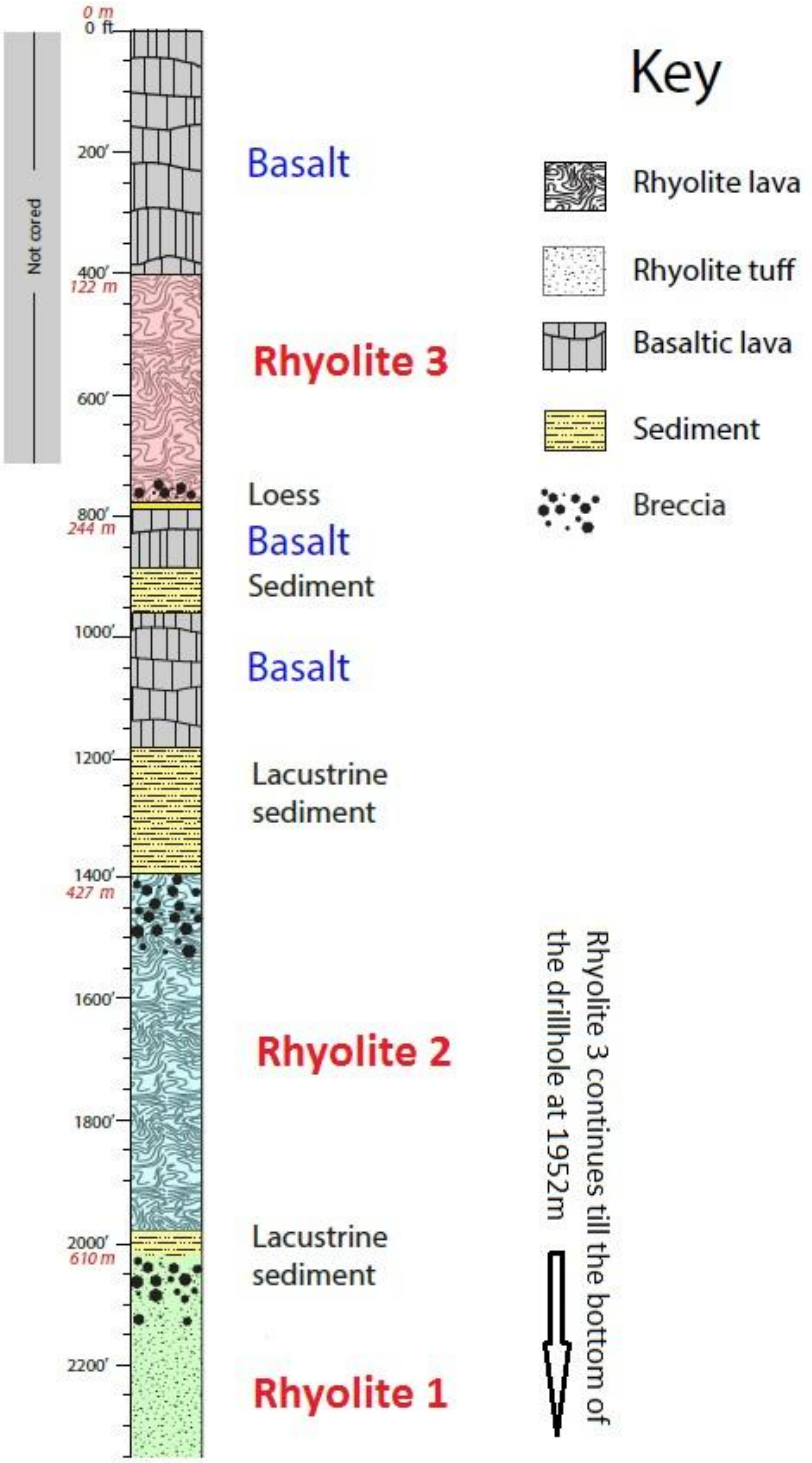

Figure 24: Generalized illustration of the Kimberly drillcore. Modified after Christiansen *et al*. (2013)

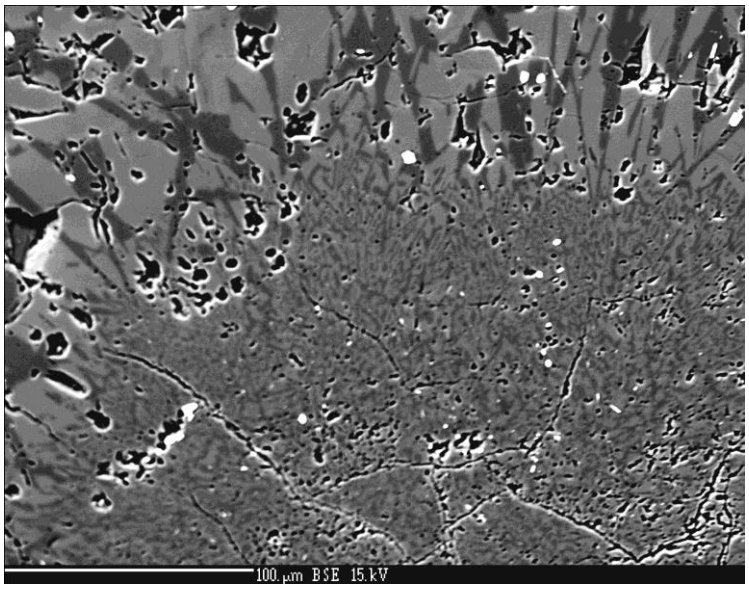

Figure 25: BSE image of the glassmatrix of sample KRH2-1796.

III-3.2 Surface samples from the Rogerson and Cassia formations

During two mapping campaigns in the SRPY carried out by the Institute for Mineralogy of the Leibniz University of Hannover in 2009 and 2012, an extensive collection of rocks was collected, including rhyolites from Bruneau-Jarbidge, Twin Falls, Heise and Yellowstone Plateau eruptive complex. From this collection samples suitable for DERP geobarometry (quartz, feldspar(s), glass phase) were chosen for EPMA analyses. Two samples from the Twin Falls eruptive complex were chosen in order to investigate, together with the samples from the Kimberly drillcore, potential variations in magma storage depth within one eruptive complex over time.

One of these samples comes from tuff of the Steer Basin Member (SRP12-A05A), the last unit of the Rogerson Formation observed in the Cassia Mountains (Figure 22). The Steer Basin Member is described by Ellis *et al*. (2010) as a highly rheomorphic ignimbrite and was dated to be 10.63 Ma old (Ellis, 2009). Microscopy examination reveals a phase assemblage containing quartz, sanidine, plagioclase, augite, pigeonite, magnetite and ilmenite and a preserved glass phase, which agrees with the description from Ellis *et al*. (2010) and makes this sample a fruitful target for geothermobarometry.

The second investigated sample of Twin Falls is an ash flow from the Greys Landing Member (SRP09-24c) that might be correlated to the Rhyolites of the Kimberly drillcore (KRH-2). The Greys Landing Member is described intensively by Ellis *et al*. (2015) and sample SRP09-24c was found to host the same phase assemblage as the Steer Basin Member (c.f. Table 13). No data from an accurate age dating of the Greys Landing Member is available but its age can be bracketed between 8.97 and 7.5 Ma from stratigraphic considerations.

In addition to these two samples formerly unpublished data are presented here collected in two samples from the Wooden Shoe Butte Member (c.f. Table 12 and 13) that were measured by Peter Nowaczyk in the frame of a student project. The two samples SRP12-A02a and SRP12-A02b of the Wooden Shoe Butte Member, described as an intensely welded ignimbrite by Ellis *et al*. (2010), both contain glass, quartz, sanidine, plagioclase pigeonite, magnetite and ilmenite, while augite was observed only in SRP12-A02a. Ellis *et al*. (2010) list the same phase assemblage including augite. The age of the Wooden Shoe Butte Member has been dated as 10.13 Ma by Perkins & Nash (2002) using the $^{40}Ar/^{39}Ar$ method.

III-3.3 Surface samples from other eruptive complexes

Three samples were investigated that each were derived from other eruptive centers than Twin Falls in the SRPY. The reasoning behind this decision is that the comparison of these samples with the ones from Twin Falls might help distinguish variations in processes within a single eruptive complex and between different ones.

The Tuff of Arbon Valley (SRP12-19B) is by most authors regarded as a product of the Picabo eruptive complex (Pierce & Morgan, 1992; Kellogg *er al.*, 1994). Among a glass phase it contains quartz, plagioclase, sanidine, no pyroxenes but magnetite, ilmenite and, most notably, abundant biotite (see Table 13). The presence of biotite is highly unusual for rhyolites of the SRPY and indicates a significantly higher amount of water present in the melt. Because of this remarkable difference Morgan & McIntosh (2005) suggested that the Arbon

Valley Tuff might be a producte of basin and range volcanism and not directly be connected to the eruptive complexes of the hotspot volcanism that the other rhyolites are attributed to. The age of the Arbon Valley Tuff was found to be 10.20 Ma by Kellogg *et al.* (1994) using the $^{40}Ar/^{39}Ar$ method.

The Wolverine Creek Tuff (SRP09-13) from the Heise eruptive complex (Morgan and McIntosh, 2005) contains quartz, plagioclase, augite, magnetite and a preserved glass matrix (see Table 13). It was dated 5.95 Ma old (Morgan & McIntosh, 2005).

With an age of 2.13 Ma the Huckleberry Ridge Tuff (SRP09-10E) from the Yellowstone Plateau volcanic eruptive center is the youngest unit investigated in this study (Ellis *et al*., 2012). Its phase assemblage consists of quartz, sanidine, plagioclase, augite, pigeonite and magnetite as well as a glass phase (see Table 13). A single fayalite crystal was found in this sample. As at the same time quartz is a common phase in that sample, it is safe to assume that the fayalite did not crystallize from the rhyolitic magma but entered from another source directly prior to or even during the eruption. Whether this is a consequence of the increasing mafic influence in younger rhyolites of the SRP described by Bonnichsen *et al*. (2008) or whether the fayalite crystal was simply gripped from wallrock during ascend or older, underlaying basalts after expulsion yet remains unclear.

III-4 Analytical procedure

For the EPMA analyses described in this chapter the same Cameca SX-100 is used as for the analyses described in Chapter I. As the natural samples investigated in this chapter are more complex than the synthetic experimental products analyzed in Chapter I, the analytical routines for the microprobe had to be enhanced. The changes on the setting for glasses were minor as still 15 kV excitation voltage, 15 nA beam current, a beam diameter defocused to 10 µm and counting times of 4 s for Na and K and 10 s for other elements was applied. The

natural obsidian MM-3 described by Nash (1992) once more served as reference standard. The only change on the glass setting was to include MnO and MgO to the measured oxides. Feldspars and pyroxenes were measured using 15 kV excitation voltage, 15 nA beam current, a focused beam and 10 s counting time on all elements. Unlike the mineral setting in Chapter I, this setting for natural minerals included the measurement of MnO, MgO and BaO. Magnetites and ilmenites were measured using 15 kV excitation voltage, 40 nA beam current, a focused beam and 10 s counting time on all measured elements.

Titanium contents in quartz were measured alongside with Si, Al and Fe using a high beam current of 100 nA, a defocused 10 µm beam diameter, a long peak time of 360 s and a background peak time of 180 s on both sides. This approach is comparable to the one used by Zhang *et al*. (2014) and accompanied by measurements of a reference quartz calibrated by Audétat *et al.* (2015) to contain 52 ± 3 ppm Ti to check for reproducibility of the results.

III-5 Geothermobarometrical methodology

Several models are employed in this study to derive information on magma storage T, P, oxygen fugacity, water content and $a\mathrm{TiO_2}$ from compositional features of the samples. Five different thermometers are used. The plagioclase-melt geothermometer (equation 24a) and the plagioclase-sanidine thermometer (equation 27b) from Putirka (2008) are applied to derive T information from feldspars. The T calculations from pyroxenes are based on the QUILF software from Andersen *et al*. (1993). The ILMAT model from Lepage (2003) and the method described by Ghiorso & Evans (2008) are used to estimate T and $f\mathrm{O_2}$ and the model from Ghiorso & Evans (2008) provides in addition values to calculate the $a\mathrm{TiO_2}$. $a\mathrm{TiO_2}$ is an important input parameter for the TitaniQ geothermobarometer (Thomas *et al*., 2010; Huang & Audetat, 2012) that is used here as a geobarometer and therefore also requires the input of T. Note that there are currently two different calculation models for TitaniQ available

(Thomas *et al*., 2010, Huang & Audetat, 2012) and their validity is still under debate (Huang & Audetat, 2012; Thomas *et al*., 2012; Wilson *et al*., 2012; Thomas *et al*., 2015). In this study both models are applied and the estimated pressures are compared with the independent DERP geobarometer. As mentioned, TitaniQ requires knowledge of $a\mathrm{TiO_2}$. Not all investigated samples however contained suitable pairs of magnetite and ilmenite for a calculation of $a\mathrm{TiO_2}$ with the model of Ghiorso & Evans (2008). Therefore a second model from Kularatne & Audetat (2014) that calculates $a\mathrm{TiO_2}$ from melt composition of a sample and its magma storage T, is also used. The melt water content, which is important for DERP geobarometry, can e.g. be calculated from a plagioclase-melt hygrometer (Putirka, 2008; equation 25b). The function of the DERP geobarometer is discussed in great detail in Chapter II of this study. Just as a quick reminder: DERP calculates magma storage pressures of rhyolites in a pressure range up to 500 MPa and requires the composition (including $\mathrm{H_2O}$-content) of a cotectic melt (glass) in equilibrium with quartz and at least one feldspar as input parameters.

III-6 Results

III-6.1 Microprobe data

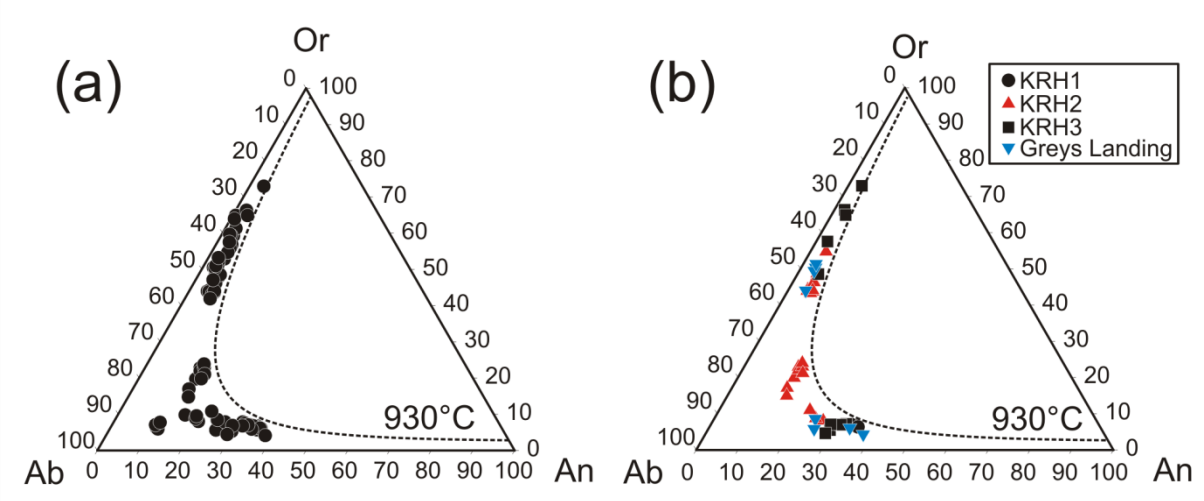

Figure 26: (a) Ternary composition of natural feldspars of all feldspar bearing samples listed in Table 13. (b) Ternary composition of feldspars from the Kimberly drill core samples and the potential correlative, the Greys Landing Member ignimbrite. Dashed lines drawn following the model of Elkins & Groove (1990).

The composition of minerals measured by microprobe in the natural samples is listed in the Appendix Tables 8 to 13. Figure 26(a) shows a ternary projection of the feldspar components for the natural samples. The feldspars in their composition mostly follow a path along the border of the miscibility gap for T < 930°C (which is used to draw the dotted curve). A notable exception are the feldspars from the Arbon Valley tuff (SRP12-19B) who tend to be remarkably rich in the albite component (Ab > 80 wt.%). Besides this group of feldspars from the Arbon Valley Member, three more groups can be distinguished. A group of feldspars with Or ranging ~40 to 80 wt.% that is referred to here as sanidine, following the denominationscheme used in the chapters I and II of this study. Another group of feldspars is identified with Or < 10 wt.% and Ab < 80 wt.%. The third group that consists solely of feldspars from KRH2 samples has Or > 10 wt.% but also Ab < 80 wt.% (c.f. Figure 26(b)). A comparison between the feldspars from Greys Landing and KRH2 shows a good agreement for the sanidines, while in case of plagioclase, where Or < 30 wt.% the situation is more

complex (see Figure 26(b)). The matching sanidine compositions are especially remarkable as the composition of sanidines from KRH3 significantly differs, while in KRH1 no sanidines were observed at all. Plagioclases from KRH2 seem to be divided into two compositionally different subgroups as mentioned above. The larger group is depleted in the An component with only ~15 wt.%, significantly differing from the other feldspars in Figure 26(b). The second, smaller group with An contents > 20 wt.% matches largely with the other plagioclases from KRH1, KRH3 and Greys landing. Note that the relative size of the two plagioclase subgroups could be an effect of the relatively small totally number of measured minerals and does not necessarily reflect the relative abundance of these populations correctly. Minerals from both subgroups were measured in all three investigated samples from KRH2 (c.f. Appendix Table 8).

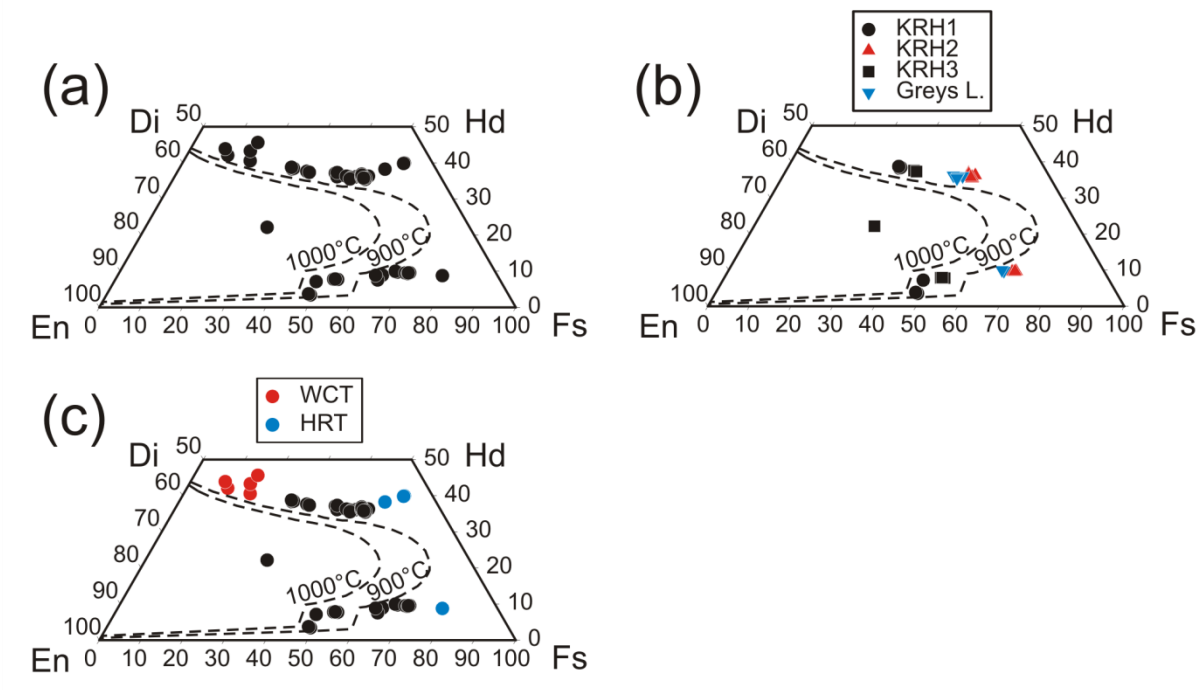

Figure 27: (a) Ternary composition of natural pyroxenes of all pyroxene bearing samples listed in Table 13. (b) Ternary composition of pyroxenes from the Kimberly drill core samples and the potential correlative, the Greys Landing Member ignimbrite. (c) Variation of figure 27(a) with the non-Twin Falls samples Wolverine Creek Tuff (WCT) and Huckleberry Ridge Tuff (HRT) highlighted in red and blue, respectively. Dashed T-lines redrawn from Lindsley (1983) calculated for 5 kbar. These lines are for relative orientation only. Precise temperature estimates from pyroxene composition can be found in the geothermometry section of this study.

The composition of pyroxenes, shown in Figure 27(b) gives additional evidence for the KRH2 – Greys Landing correlation hypothesis. The compositions of both pigeonites and augites from the two samples match well, while the pyroxenes from KRH1 and KRH3 appear to have formed at higher temperatures. Remarkable also that piegeonites from KRH1 and KRH2 show the highest enstatite contents of all investigated samples, an evidence for higher magma storage T that will be investigated further in the geothermometry section of this study. Note that both the most enstatite-poor and ferrosilite-poor pyroxenes come from samples of other eruptive complexes than Twin Falls. As it is highlighted in Figure 27(c), the three augites and the pigeonite measured in the sample SRP09-10E from Huckleberry Ridge Tuff contain the least amount of En of all investigated samples, indicating a lower magma storage T. Augites from Wolverine Creek Tuff (sample SRP09-13) that are highlighted in red in Figure 27(c) contain the lowest amounts of Fs.

Table 14: Glass composition of the natural samples

Name	SRP12-A05A		SRP12-19B		SRP12-A02a		SRP12-A02b		KRH1-2052	
Member	Steer Basin		Arbon Valley		Wooden S. B.		Wooden S. B.		Kimberly Rh. 1	
	[wt.%]	1σ	[wt.%]	1σ	[wt.%]	1σ	[wt.%]	1σ	[wt.%]	1σ
SiO_2	75.06	0.34	75.28	0.22	74.84	0.31	74.68	0.45	76.00	0.33
TiO_2	0.27	0.03	<0.04		0.26	0.01	0.25	0.03	0.36	0.02
Al_2O_3	11.62	0.11	12.91	0.14	11.65	0.13	11.57	0.11	11.59	0.12
FeO	1.66	0.12	0.78	0.10	1.59	0.17	1.40	0.18	1.21	0.16
CaO	0.63	0.06	0.43	0.04	0.61	0.05	0.65	0.14	0.40	0.03
Na_2O	2.49	0.13	3.74	0.15	2.64	0.11	2.51	0.31	2.82	0.13
K_2O	6.02	0.21	4.68	0.14	5.70	0.13	6.19	0.47	5.36	0.10
total	97.82		97.83		97.30		97.26		97.79	
n	22		40		20		19		20	
Qz	35.0		34.1		35.2		34.3		37.5	
Ab	21.1		31.7		22.4		21.2		23.8	
Or	35.6		27.6		33.7		36.6		31.7	
An	2.8		2.1		3.0		2.0		2.0	
Cor	-0.1		0.9		0.0		-0.4		0.4	

Table 14: Continued

Name	SRP09-24c		KRH2-1946		KRH2-1401		SRP09-13		SRP09-10E	
Member	Greys Landing		Kimberly Rh. 2		Kimberly Rh. 2		Wolverine Ck.		Huckleberry R.	
	[wt.%]	1σ	[wt.%]	1σ	[wt.%]	1σ	[wt.%]	1σ	[wt.%]	1σ
SiO_2	75.46	0.33	73.85	0.32	73.70	0.37	74.91	0.31	75.40	0.39
TiO_2	0.26	0.02	0.28	0.02	0.31	0.02	0.12	0.02	0.12	0.03
Al_2O_3	11.66	0.15	11.43	0.12	11.34	0.09	11.98	0.17	11.94	0.14
FeO	1.69	0.24	1.76	0.08	1.86	0.09	1.20	0.07	1.49	0.12
CaO	0.52	0.04	0.56	0.03	0.63	0.03	0.48	0.03	0.51	0.05
Na_2O	2.84	0.15	3.05	0.14	3.23	0.17	3.22	0.11	3.06	0.13
K_2O	5.73	0.09	5.10	0.06	4.66	0.12	4.98	0.09	4.97	0.11
total	98.16		96.04		95.74		96.89		97.49	
n	66		10		20		93		23	
Qz	34.8		34.3		34.6		35.2		36.4	
Ab	24.0		25.8		27.3		27.3		25.9	
Or	33.9		30.1		27.5		29.4		29.4	
An	2.1		2.4		2.7		2.4		2.6	
Cor	-0.2		-0.1		-0.1		0.4		0.6	

In Table 14 the glass composition of the natural samples are listed, including the normative Qz, Ab, Or and An content calculated from the CIPW norm. The SiO_2 content of the glasses ranges from 73.7 wt.% to 77.23 wt.% and the normative Qz content from 34.1 wt.% to 37.5 wt.% while the normative An content varies from 1.9 wt.% to 3 wt.%. The normative Qz-Ab-Or content of the glasses is plotted in Figure 28. As explained in detail in chapter I and II of this study, natural compositions plotted into the ternary Qz-Ab-Or system cannot directly be used to obtain pressure information, as they usually contain normative melt An and H_2O. The equations that were used to construct the DERP geobarometer in chapter II, however, allow for a correction of these effects. To demonstrate this, the compositions of the glasses that are represented in Figure 28 as black diamonds were corrected for the effect of H_2O and An using the equations [1] and [7] from chapter II. For this demonstration an overall water content of 2 wt.% of all samples was assumed. The corrected Qz-Ab-Or values are plotted in Figure 28 as grey diamonds. The grey diamonds are directly comparable to the (H_2O-corrected!) cotectic curves that were drawn into the diagram. Figure 28 shows that the investigated samples in

general plot close to the 200 MPa cotectic, with a few exceptions that will be discussed in detail in the geobarometry section of this study. While this Figure is due to its resolution not really suited to distinguish between different glasses, it is a good illustration of the fundamental working process behind DERP.

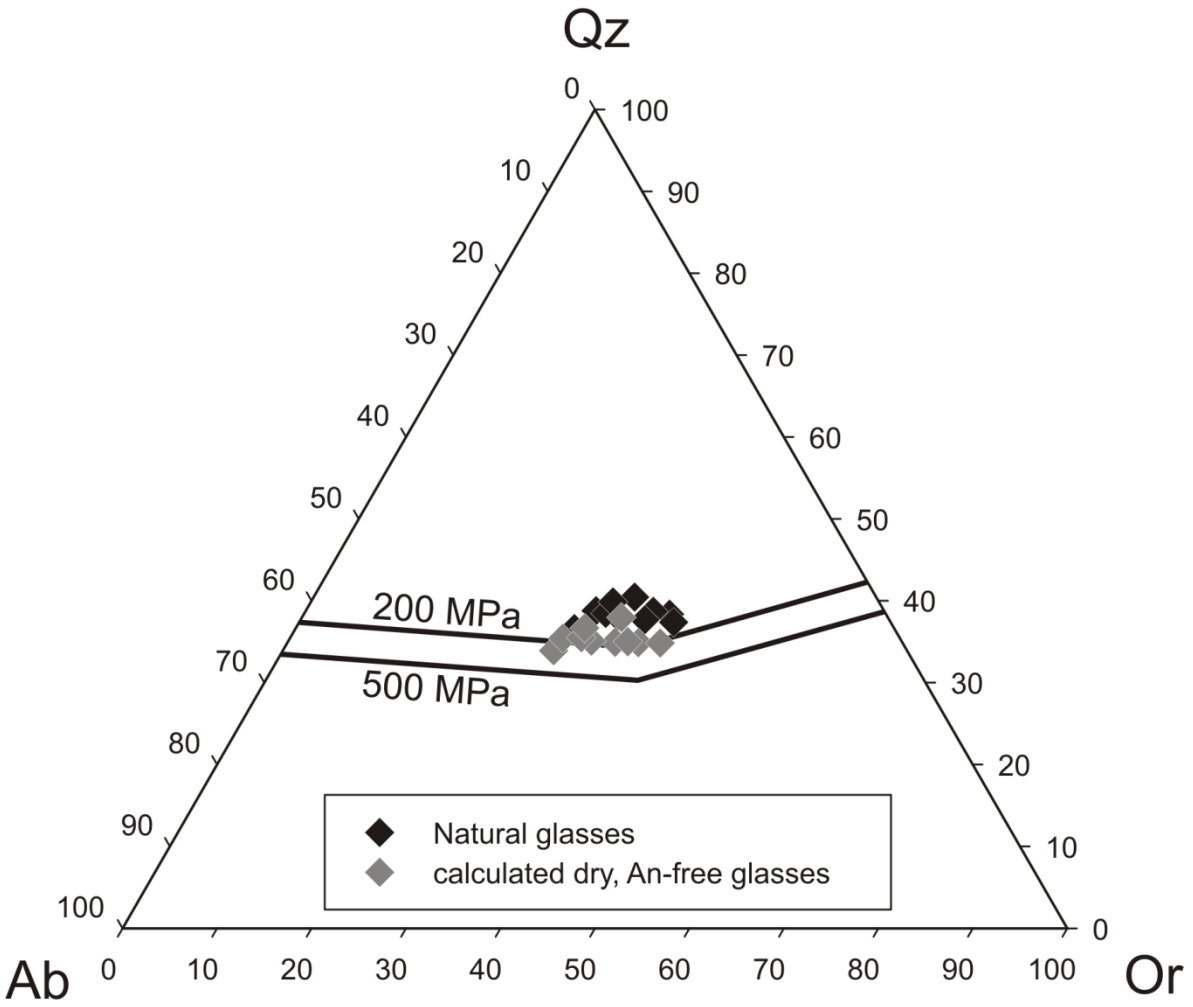

Figure 28: Ternary projection of the CIPW-calculated normative quartz – albite – orthoclase content (normed to Qz+Or+Ab=100%). Black diamonds represent the measured average glass composition of one sample (number of analyses given in Table 14). The glasses were recalculated to contain no normative melt An and no H_2O using DERP equations listed in Chapter II and described in the text. These corrected compositions are plotted as grey diamonds. They can be used to constrain pressure from the projection in the Qz-Ab-Or system assuming that the glasses represent cotectic melts coexisting with quartz and at least one feldspar. 2 wt.% H_2O was assumed for all compositions. The cotectic lines are drawn for H_2O-free conditions and are extrapolated from the datasets of Tuttle & Bowen (1958) and Holtz *et al*. (1992b). The grey diamonds can be directly compared to the cotectic lines to estimate the magma storage pressure of the melt.

Titanium contents in quartz were measured for samples SRP12-A05A, SRP12-19B, SRP09-24c, KRH2-1401, KRH2-1796, SRP09-13 and SRP09-10E and the results are listed in detail in Appendix Table 16. At least three measurements were taken on every quartz crystal and the number of analysed crystals ranges from 6 in sample KRH2-1796 to 17 in sample SRP12-A05A. For every sample at least one quartz crystal was checked for homogeneity by measuring a traverse of constant point distance over the whole grain. While some inhomogeneities were found in some quartz crystals, these variations are minor compared to the variations in Ti content of different quartz grains within one sample (c.f. Appendix Table 16).

For the Arbon Valley Tuff (SRP12-19B), the Wolverine Creek Tuff (SRP09-13) and the Huckleberry Ridge Tuff (SRP09-10E) the vast majority of quartz crystals was found to have Ti contents below the detection limit of 13 ppm. In both SRP09-13 and SRP09-10E, however, one single crystal was found to host exceptional high Ti contents, 191 ppm Ti and 187 ppm Ti, respectively (c.f. Appendix Table 16). In the other four samples the Ti contents were found to be significantly higher, with an average of 232 ppm Ti for the Tuff of Steer Basin (SRP12-A05A), 176 ppm Ti for Kimberly Rhyolite 2 in the -1401 and 196 ppm Ti in the -1796 sample and 238 ppm Ti for the quartz of Greys Landing Ignimbrite. Considering standard deviations for these measurements range between ~15 to 30 ppm these Ti measurements neither support nor deny directly the Greys Landing – Kimberly Rhyolite 2 correlation hypothesis. Quartz crystals that differ significantly in Ti content from the majority of crystals within a sample were discarded to calculate the averages but are nonetheless listed in Appendix Table 16.

III-6.2 Geothermobarometry

Magma storage temperatures have been calculated for all natural samples using the 5 different thermometers described above. The results are listed in Table 15. All estimates were calculated from compositions published in this study, either in Table 14 or Appendix Tables 8 – 13. For temperature estimations with the feldspar based thermometers from Putirka (2008) and the QUILF program (Andersen *et al*., 1993), where the input of P is required, 200 MPa was used, considering that this pressure is a rough average value for the natural samples as deduced from Figure 28. These three thermometers are relatively insensitive to a change in P within 200 MPa and no significant impact on the T estimates has to be expected. Calculated temperatures in general span a range from ~800 to 930°C with sometimes considerable disagreement between thermometers within a single sample. In some cases such disagreement can be clearly attributed to disequilibrium between two phases, e.g. in sample KRH2-1946 the plagioclase-sanidine thermometer yields a value of 575°C. Where calculated temperatures from many thermometers are available such outliers are spotted easily and can be discarded for future considerations. They are written in italics in Table 15. In some cases however, especially in samples with only few phases suitable for the applied geothermometers, it is hard to judge whether the actual magma storage T was calculated correctly. As the samples in Table 15 are sorted by relative eruption age one might be tempted to search for a possible evolution of the temperature over time, which can, however, from this table not be confirmed. The vast majority of calculated temperatures for samples from the Twin Falls eruptive complex lay between ~850 and 900°C, with the Fe-Ti-oxide thermometers showing a bit wider of a spread. Notable exceptions with two independent geothermometers (plagioclase-sanidine and magnetite-ilmenite) giving significantly lower values are KRH2-1796 and the relatively young Huckleberry Ridge tuff SRP09-10E. KRH2-1796 is assumed to have been stored at the same T as the other KRH2 samples. All samples from that rhyolite unit KRH2,

however, seem to produce questionable T estimates from feldspars, probably due to the two different plagioclase populations observed in Figure 26(b) of which one might be xenocrysts not in actual equilibrium with the rest of the system. QUILF based pyroxene thermometry and the magnetite-ilmenite thermometers for sample KRH2-1946 estimate T to be on the usual 850 - 900°C level.

The 850 – 900°C calculated as magma storage temperature at the Twin Falls eruptive complex is distinctively lower than the ~950°C estimated for the Bruneau Jarbidge eruptive complex by Honjo *et al*. (1992) and Cathey & Nash (2009). Only a single geothermometer (plagioclase-melt) is applicable on the SRP09-13 sample from Wolverine Creek Tuff yielding 867°C. This agrees with the 825 – 875°C temperature range that was determined by Bolte et al. (2015) for the Blacktail Creek Tuff that originated from the same eruptive complex (Heise). The huckleberry Ridge tuff, a product of the Yellowstone Plateau eruptive complex, might have formed at even lower temperatures of 800 – 825°C as indicated by QUILF and plagioclase-sanidine thermometry, although that is in disagreement with the 886°C estimated by the plagioclase-melt Thermometer. Vazquez *et al*. (2009) calculated some temperature estimates for very young (72 – 257 ka) rhyolites of Yellowstone Plateau and although their results span a wide range of 150 °C, this estimated range starts as low as 750°C and is interpreted by them as a time transgressice cooling process. From these findings one might speculate if the melt storage temperature within the SRPY is overall decreasing with time.

P estimates were calculated for most natural samples using DERP and TitaniQ. No estimates were made for samples of the KRH1 and KRH2 units, as their lack of quartz unfortunately makes them unsuitable for both geobarometers. DERP was used to calculate P from the glass compositions listed in Table 14 following the procedure explained in detail in Chapter II of this study. For the calculation it was assumed that the melts contain 2 wt.% H_2O, a reasonable water content for rhyolites of the SRP (Almeev *et al*., 2012; Bolte *et al*., 2015). As discussed

in chapter II, the water content has not a major influence on pressures estimated with DERP. The choice to work with constant 2 wt.% H_2O rather than using the water contents estimated by the plagioclase-geohygrometer of Putirka (2008) listed in Table 15 was made because at least some plagioclases may be xenocrysts not in equilibrium with the host glass matrix (see Figure 26). Any error in DERP P estimation produced by assigning individual but inaccurate water contents to the glasses would therefore likely be higher than working with a constant realistic value.

Table 15: Results of geothermometrical calculations for the natural samples

	plg-melt[1] eqn. 24a		plg-melt[1] eqn. 24b		plg-san[1] eqn. 27b		pig-aug[2] QUILF		magnetite-ilmenite Ghiorso & Evans (2008)						magnetite-ilmenite ILMAT; Lepage (2003)			
Name	T [°C]	1σ [°C]	H_2O [wt.%]	1σ [wt.%]	T [°C]	1σ [°C]	T [°C]	1σ [°C]	T [°C]	1σ [°C]	*f*O2 NNO	1σ NNO	aTiO2	1σ	T [°C]	1σ [°C]	*f*O2 NNO	1σ NNO
SRP12-A05A	880	1	0.9	0.1	926	46	870	31	999	17	-0.73	0.00	0.56	0.01	1022	38	0.34	0.76
SRP12-19B	872	2	3.6	0.1	*661*	*11*	-	-	914	11	-1.30	0.02	0.45	0.00	935	18	-1.44	0.44
SRP12-A02a	845	3	1.9	0.1	911	19	876	102	939	37	-1.37	0.01	0.48	0.02	948	43	-2.54	0.35
SRP12-A02b	843	2	1.9	0.1	912	26	-	-	943	39	-1.28	0.20	0.49	0.03	926	11	-1.50	0.27
KRH1-2052	861	0	0.3	0.0	-	-	887	52	-	-	-	-	-	-	-	-	-	-
SRP09-24c	867	5	1.0	0.4	916	36	887	79	746	53	-1.55	0.20	0.39	0.03	*742*	*25*	-2.09	0.83
KRH2-1946	994	4	3.0	0.1	*575*	*108*	887	71	893	11	-1.10	0.13	0.48	0.02	893	28	-1.41	0.68
KRH2-1796	-	-	-	-	825	28	-	-	796	25	-2.12	0.01	0.32	0.01	808	28	-2.19	0.64
KRH2-1401	909	13	2.1	0.2	810	17	881	94	-	-	-	-	-	-	-	-	-	-
KRH3-716	-	-	-	-	853	32	917	45	796	41	-2.05	0.14	0.34	0.03	788	58	-2.66	1.05
SRP09-13	867	1	2.2	0.2	-	-	-	-	-	-	-	-	-	-	-	-	-	-
SRP09-10E	886	14	2.2	0.1	827	12	800	43	-	-	-	-	-	-	-	-	-	-

[1]see Putirka (2008)

[2]see Andersen et al. (1993)

Table 16: Results of geobarometrical calculations for the natural samples

		TitaniQ - input								TitaniQ - results				DERP
		G&E[a]	K&A[b]	input[c]						H & A (2012)[g]		Thomas (2010)[h]		
	Age[f]	$aTiO_2$	$aTiO_2$	$aTiO_2$	± $aTiO_2$	T	± T	Ti	± Ti	P	1σ	P	1σ	P[d]
Name	[Ma]					[°C]	[°C]	[ppm]	[ppm]	[MPa]	[MPa]	[MPa]	[MPa]	[MPa]
SRP12-A05A	10.63 ± 0.07	0.56	0.38	0.45	0.05	900	25	232	16	98	34	715	95	251
SRP12-19B[e]	10.21 ± 0.03	0.45	0.05	0.1	0.05	900	25	12[e]	5	916	538	2579	598	351
SRP12-A02a	10.13 ± 0.03							-	-					246
SRP12-A02b	10.13 ± 0.03							-	-					307
SRP09-24c	7.5 - 9	0.39	0.46	0.45	0.05	875	25	238	23	66	28	612	99	233
KRH2-1946	7.5 - 9		0.48					-	-					250
KRH2-1796	7.5 - 9	0.32	-	0.45	0.05	875	25	196	34	107	47	722	120	-
KRH2-1401	7.5 - 9	-	0.53	0.45	0.05	875	25	176	16	128	43	777	100	243
SRP09-13[e]	5.59 ± 0.05	-	0.22	0.22	0.05	875	25	12[e]	5	1599	583	1883	245	227
SRP09-10E[e]	2.13 ± 0.01	-	0.33	0.33	0.05	825	25	12[e]	5	2189	683	2111	234	144

[a] $aTiO_2$ calculated using the model of Ghiorso & Evans (2008); [b] $aTiO_2$ calculated using the model of Kularatne & Audetat (2014)

[c] aTiO2 used for the TitaniQ P estimation; [d] calculated assuming 2 wt.% H_2O

[e] Ti concentration in quartz below the 13 ppm detection limit the calculated TitaniQ P is therefore a minimum value

[f] ages from Morgan & McIntosh (2005), Bonnichsen *et al*. (2008), Ellis *et al*. (2010), Ellis *et al*. (2012)

[g] Huang & Audétat (2012); [f] Thomas *et al*. (2010)

Using TitaniQ for P estimates requires a careful choice of the input parameters T and $a\mathrm{TiO_2}$. Temperatures for every natural sample are available from Table 15. The estimates of different thermometers were combined, sometimes neglecting the results from single problematic estimates due to disequilibrium. The magnetite-ilmenite geothermometer of Ghiorso & Evans (2008) already listed in Table 15, can also be used for the determination of $a\mathrm{TiO_2}$. Table 15 and BSE images, however, show that the Ti-Fe-oxides in the samples are not always in equilibrium. Therefore a second approach of Kularatne & Audétat (2014) is employed that is based on the experimental calibration of rutile saturation in melts of a given T. For the $a\mathrm{TiO_2}$ calculations after Kularatne & Audétat (2014) the T listed in Table 16 was used and also served as input parameter for the P determination via TitaniQ. For the samples of the Twin Falls eruptive complex both methods (Kularatne & Audétat (2014) and Ghiorso & Evans (2008)) mostly agree within error for an overall $a\mathrm{TiO_2}$ of 0.45. For all investigated samples from other eruptive complexes the Ti content in quartz was below the 13 ppm detection limit, except for few xenolite crystals. Logically this should be caused by a very low $a\mathrm{TiO_2}$. Consequently the samples SRP09-13 from Heise and SRP09-10E from Yellowstone Plateau contain no ilmenite, rendering the model of Ghiorso & Evans (2008) inapplicable, while the model from Kularatne & Audétat (2014) produces reduced values compared to Twin Falls samples, due to very low melt $\mathrm{TiO_2}$ contents (c.f. Table 14). In case of the Arbon Valley tuff (SRP12-19B), presumably originating from Picabo, the situation is comparable. Here Ti was below detection limit not only in quartz but also in the melt, although the detection limit for Ti in melt is with 0.04 wt.% $\mathrm{TiO_2}$ way higher for the glass measurement setting. Still this is matchless amongst the natural samples investigated in this study and translates into an $a\mathrm{TiO2}$ <0.06 when using the model of Kularatne & Audétat (2014). A single ilmenite crystal was found in sample SRP12-19B. When used to calculated $a\mathrm{TiO2}$ after Ghiorso & Evans (2008) the resulting 0.45, while matching nicely the Twin Falls values, is in sharp contrast to the very

low Ti contents of the samples phases. That ilmenite therefore is likely a xenolite not in equilibrium with the Arbon Valley melt and probably even derived from a Twin Falls rhyolite during eruption.

TitaniQ was used to calculate P with both the calibrations of Thomas *et al*. (2010) and Huang & Audétat (2012). The first thing that catches the eye when examining those pressures is that TitaniQ is obviously not helpful for calculating P in samples where there is virtually no Ti in quartz. The TitaniQ pressures calculated for non-Twin Falls samples are clearly not reflecting any real natural situation. Comparing the results for the Twin Falls samples reveals that even there the results calculated after Thomas *et al*. (2010) with ~600 to 800 MPa seem to be unreasonably high. Results calculated after Huang & Audétat (2012) however range with 60 to 130 MPa well within what is geologically plausible. The pressures calculated after Thomas *et al*. (2010) are therefore discarded and only the results of TitaniQ calculated after Huang & Audétat (2012) are considered for further discussions. Results from DERP are with ~200 to 300 MPa somewhat higher than the Huang & Audétat (2012) TitaniQ estimates but actually not too far away, considering the uncertainties that come with both barometers. Exceptions for DERP calculated pressures are the Arbon Valley tuff, with 351 MPa noticeably higher and the Huckleberry Ridge tuff, with 144 MPa noticeably lower in P, so the lack of suitable amounts of Ti for geobarometry in these samples comes in especially unfortunate. The disagreement between DERP and TitaniQ could be attributed to problems calculating precise T and $a\mathrm{TiO_2}$. If e.g. P is recalculated for KRH2-1401 with TitaniQ (Huang & Audétat, 2012) using only slightly elevated values of 925°C and $a\mathrm{TiO_2} = 0.5$, by no means an unrealistic stretch of the calculated estimates, the resulting 263 ± 69 MPa are matching the DERP result (243 MPa) quite precisely. If it weren't for the sake of the comparison of the two geobarometers, it would probably be a better use of TitaniQ to calculate T, using DERP calculated pressures as input parameters.

III-7 Discussion

Regardless of the slight disagreement of the absolute values of P from TitaniQ and DERP, both geobarometers estimate constant P within the expectable error margin for the samples of Twin Falls eruptive center. Considering the large volumes of pyroclastic material erupted in the SRPY, it appears remarkable that the vertical position of a magma storage area apparently has been fixed over the whole lifetime of an eruptive center. This raises the question if the magma storage P is uniform over the whole SRPY or whether the situation in Twin Falls, with a mostly constant magma storage pressure of 264 ± 31 MPa over a lifetime of more than 2 Ma, is a singular phenomenon. With DERP there is now an excellent tool available to investigate this question. Table 17 lists all rhyolites of the SRPY with coexisting quartz, feldspar(s) and glass matrix of known composition either from literature or from this study. The number of available samples unfortunately varies strongly between the different eruptive centers. For the Bruneau-Jarbidge and the Twin Falls eruptive center several suitable compositions are available (Cathey & Nash, 2004; Ellis *et al*., 2010; this study). The database for younger eruptive complexes is sparse, comprising besides the Wolverine Creek Tuff and the Huckleberry Ridge Tuff only the Blacktail Creek Tuff of Bolte *et al*. (2015). P estimates from DERP indicate that the average P of the eruptive centers is 351 ± 35 MPa for Bruneau-Jarbidge and 264 ± 31 MPa for Twin Falls. For the three younger samples from Heise and Yellowstone Plateau no meaningful average can be calculated, but the two samples from Heise lay close to or slightly below the level of Twin Falls while the youngest sample from Huckleberry Ridge Tuff indicates a considerably lower magma storage P with 144 MPa. The P in table 17 was calculated with DERP assuming 1 wt.% H_2O for Bruneau-Jarbidge samples (Almeev *et al*., 2012) and 2 wt.% H_2O for all other samples. Calculating P for the Bruneau-Jarbidge samples with 2 wt.% H_2O would result in ~25 MPa higher P, not closing but widening the gap towards the Twin Falls samples.

Table 17: Ages and pressures of rhyolites from the Snake River Plain

Name	center	age [Ma]	1σ [Ma]	P_{DERP} [MPa]	Source: Age	Source: Composition
CPT III	BJ	12.7	0.3	409	Bonnichsen *et al*. (2008)	Cathey & Nash (2004)
CPT V	BJ	12.15	0.3	326	Bonnichsen *et al*. (2008)	Cathey & Nash (2004)
CPT VII	BJ	11.8	0.1	311	Bonnichsen *et al*. (2008)	Cathey & Nash (2004)
CPT IX	BJ	11.6	0.1	404	Bonnichsen *et al*. (2008)	Cathey & Nash (2004)
CPT XI	BJ	11.35	0.15	339	Bonnichsen *et al*. (2008)	Cathey & Nash (2004)
MBM	TF	11.3	-	261	Ellis *et al*. (2010)	Ellis *et al*. (2010)
BBM	TF	10.98	0.07	324	Ellis (2009)	Ellis *et al*. (2010)
CPT XIII	BJ	10.85	0.15	347	Bonnichsen *et al*. (2008)	Cathey & Nash (2004)
SRP12-A05A	TF	10.63	0.07	251	Ellis (2009)	this study
CPT XVj	BJ	10.55	0.15	362	Bonnichsen *et al*. (2008)	Cathey & Nash (2004)
CPT XVb	BJ	10.55	0.15	314	Bonnichsen *et al*. (2008)	Cathey & Nash (2004)
SRP12-19B	P	10.21	0.03	351	Perkins & Nash (2002)	this study
SRP12-A02a	TF	10.13	0.03	246	Perkins & Nash (2002)	this study
SRP12-A02b	TF	10.13	0.03	307	Perkins & Nash (2002)	this study
SRP09-24c	TF	8.25	0.74	233	Bonnichsen *et al*. (2008)	this study
KRH2-1946	TF	8.25	0.74	250	relative stratigraphy	this study
KRH2-1401	TF	8.25	0.74	243	relative stratigraphy	this study
BCT	H	6.62	0.03	235	Morgan & McIntosh (2005)	Bolte *et al*. (2015)
SRP09-13	H	5.59	0.05	227	Morgan & McIntosh (2005)	this study
SRP09-10E	YP	2.13	0.01	144	Ellis *et al*. (2012)	this study

Eruptive centers: BJ = Bruneau-Jarbidge, TF = Twin Falls, P = Picabo, H = Heise, YP = Yellowstone Plateau
CPT = Cougar Point Tuff, MBM = Magpie Basin Member, BBM = Big Bluff Member, BCT = Blacktail Creek Tuff,

The estimated P listed in Table 17 is plotted against the age of the samples in Figure 29. It shows that most units of Bruneau Jarbidge and Twin Falls eruptive centers can be discriminated by P. Two units from Twin Falls, the Wooden Shoe Butte Member, although only in one of two samples from that unit (SRP12-A02b) and the Big Bluff Member, however, partially overlap with the Bruneau-Jarbidge Domain. The unusual high pressure calculated for Wooden Shoe Butte sample SRP12-A02b can be seen as an indicator that local chemical heterogeneities within a single unit are very well possible. In case of the Big Bluff Member: whether this unit is part of the Twin Falls or Bruneau-Jarbidge eruptive center is actually not clear (see Table 12) (Hughes & McCurry, 2002; Bonnichsen *et al*., 2008). The

results displayed in Figure 29 might therefore be a valuable indicator that the Big Bluff Member originated from last activity stages of the Bruneau-Jarbidge eruptive center.

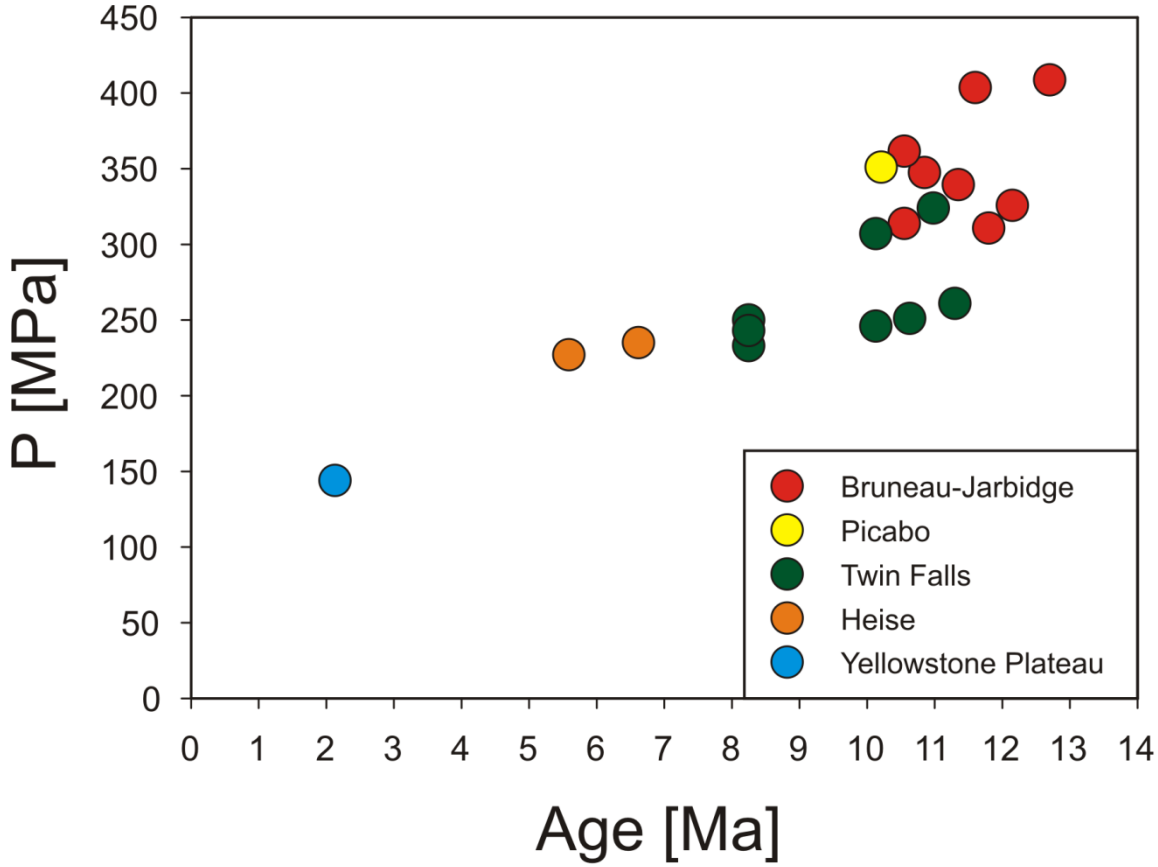

Figure 29: Plot of age and DERP calculated P as listed in Table 17.

The trend towards lower magma storage P for younger rhyolites observed in Figure 29 suffers somewhat from the lack of available data for material younger than 7 Ma. While the existence of a correlation between depth of magma storage and age will be used here as a working hypothesis to increase our understanding of the structure of the magma storage system underneath the SRP, it is clear that a better database on the younger units of the Heise and Yellowstone Plateau eruptive centers would enhance our general view of the evolution of the SRP volcanic systems. Following the assumption that rhyolitic melts of the SRP over time were stored at ever shallower depth inevitably leads to the question of the cause for this

change that must be reflected in the entire structural architecture of the SRP. The storage of rhyolites underneath volcanic eruptive centers is thought to take place in swathes of magma chambers of considerable lateral extend, likely >100 km that feed eruptions not only within but sometimes beyond the borders of their eruptive centers (Bonnichsen *et al*., 2008). This rhyolitic magma chamber network is proposed to be a product of ever-repeated crystallization and liquid separation to a point were interconnection and mixing of magmas is discontinued and compositionally different suites of minerals form as a result of differences in T and P (Ellis *et al*., 2014). The vertical extend of these magma chamber networks appears to be limited. The variation in DERP calculated pressures of more or less ±50 MPa for rhyolites of Twin Falls and Bruneau-Jarbidge suggests it is ~3 Km. Whether the source of the rhyolitic melts is recycling of older continental crust (Bonnichsen *et al*., 2008) or fractional crystallization of an underlaying basaltic magma body (Whitaker *et al*., 2008; Szymanowski *et al*., 2015) with subsequent ascend of the derived liquids is under debate. It appears however that seismic evidence strongly supports the existence of a huge basaltic magma body at 20 to 50 km depth at least underneath Yellowstone Plateau (Huang et *al*., 2015) that could easily provide heat and material to cause the formation of a wide rhyolitic magma chamber network at shallower depths. The basaltic magma body is thought to be a product of heat and extension accompanying the mantle plume but having formed by remelting of lower crust without physical contact to the mantle plum which stays below the moho at depth of ~70 km. Szymanowski *et al*. (2015) state that such a basaltic magma body involved in producing rhyolites by fractional crystallization would itself not directly extrude basaltic material to the surface but remain stuck underneath the rhyolites it is feeding. This is consistent with findings from Ellis *et al*. (2013) who propose that the source of mafic influence in the rhyolites of the SRPY is different from the actual basalt erupted in that area. It is possible that the volcanic eruptive centers of the SRP mark the areas where large basaltic magma bodies (LBBs) have

formed in the lower crust during its path over the hotspot. The question where and at which depth a LBB forms is likely controlled by the physical properties of the crust. Jean *et al*. (2014) have registrated stepwise changes in Pb-Sr ratios along the SRPY track not unlike the stepwise changes in DERP calculated P observed in this study and they link it to abrupt changes in elastic thickness of the crust observed by Lowry & Pérez-Gussinyé (2011). The abrupt change in P observed between Bruneau-Jarbidge, Twin Falls and potentially Yellowstone Plateau would therefore be a consequence of a LBB forming in an ever thinner continental crust. This somewhat speculative propose of a SRPY architecture of course needs backup from additional data. Besides organizing the missing P estimates for Heise and Yellowstone Plateau further detailed geophysical investigations like the one described by Huang *et al*. (2015) to search for LBBs underneath all volcanic eruptive centers would be useful to shed light on the complex history of rhyolitic melt generation in the SRP.

Concluding remarks

This study showed that the impact of normative melt An on the position of the eutectic point and the cotectic curves in the rhyolitic system has formerly been underestimated. This is problematic as the effect of P on the haplogranitic system Qz-Ab-Or is currently widely in use as a geobarometer for natural rhyolites, which will inevitably lead to P estimates systematically too low. A broadened experimental database on the effect is presented here that allows to model the effect of An way more precise. The data indicates that an increase in P of 100 MPa decreases the normative Qz content of the eutectic point in a rhyolitic system by 1.45 wt.%. An increase in normative melt An by 1 wt.% on the other hand which equals as little as 0.2 wt.% CaO, given a sufficient amount of Al_2O_3 is available for anorthite formation, will increase the Qz content of the eutectic point by 1.25 wt.%. The precise experimental calibration of this effect now allows for the development of a new generation of improved

ternary-projection based geobarometers. One such geobarometer is DERP (**D**etermining **E**utectic **R**hyolite **P**ressures) that is described here. It allows for the calculation of magma storage pressures of rhyolites with quartz and feldspar(s) coexisting with a preserved glass phase. The composition of the glass and the water content at magma storage conditions are the only necessary input informations. DERP is tested by reproducing 10 P estimates from independent geobarometers and able to do so within ±41 MPa and extensive Monte-Carlo simulations examining in detail the effect of every variable on the calculated result. It is concluded that DERP is a profound tool that enables the scientist to make quality P estimates quick and easily in situations where getting P estimates at all was formerly an extremely difficult task. DERP is used to investigate the formation of rhyolites in the Snake River Plain, Yellowstone (SRPY), USA where new insights are possible from project HOTSPOTS Kimberly drillcore samples of the Twin Falls eruptive center. The drillcore bears three rhyolite units and microprobe data presented here can play an important role in linking these rhyolites to correlatives observed in the field. P estimates based on DERP are presented for natural samples not only from Kimberly drill core but all major eruptive products of the Twin Falls center. They show that the magma storage P underneath Twin Falls was at constant 260 ± 40 MPa over a period of at least 2 Ma which is equivalent to a depth of ~6 to 9 km. For the older Brunea-Jarbidge eruptive center literature data was used to determine the magma storage P by DERP as 330 ± 50 MPa indicating the presence of a magma chamber network at ~8 to 12.5 km depth. For the younger eruptive centers Heise and Yellowstone Plateau the available data suitable for DERP geobarometry is currently sparse but what is available indicates that the trend towards shallower magma storage in younger eruptive centers might continue. These new insights in the architecture of the SRPY magma plumbing system provided by DERP are integrated in the models existing in the literature. They fit the idea of large basaltic magma bodies controlling the formation of overlaying, relatively flat but

extensive rhyolitic magma chamber networks that at the surface form the discrete eruptive centers observed in the field. Abrupt changes in the mechanical properties of the continental crust towards northeast of the Snake River Plain together with these discrete large basaltic magma bodies can explain the stepwise decrease of magma storage depth of rhyolites of the SRP.

References

Allan, A. S., Wilson, C. J., Millet, M. A., & Wysoczanski, R. J. (2012). The invisible hand: Tectonic triggering and modulation of a rhyolitic supereruption. Geology, 40(6), 563-566.

Almeev, R. R., Bolte, T., Nash, B. P., Holtz, F., Erdmann, M. and Cathey, H. E. (2012). High-temperature, low-H2O silicic magmas of the Yellowstone hotspot: an experimental study of rhyolite from the Bruneau–Jarbidge Eruptive Center, Central Snake River Plain, USA. Journal of Petrology, 53(9), 1837-1866.

Andersen, D. J., Lindsley, D. H., & Davidson, P. M. (1993). QUILF: A pascal program to assess equilibria among Fe□ Mg□ Mn□ Ti oxides, pyroxenes, olivine, and quartz. Computers & Geosciences, 19(9), 1333-1350.

Anderson, J. L. and Smith, D. R. (1995). The effects of temperature and f02 on the Al-in-hornblende barometer. American Mineralogist, 80, 549-559.

Andrews, G. D., & Branney, M. J. (2011). Emplacement and rheomorphic deformation of a large, lava-like rhyolitic ignimbrite: Grey's Landing, southern Idaho. Geological Society of America Bulletin, 123(3-4), 725-743.

Andrews, G. D., Branney, M. J., Bonnichsen, B., & McCurry, M. (2008). Rhyolitic ignimbrites in the Rogerson Graben, southern Snake River Plain volcanic province: volcanic stratigraphy, eruption history and basin evolution. Bulletin of Volcanology, 70(3), 269-291.

Audétat, A. (2013). Origin of Ti-rich rims in quartz phenocrysts from the Upper Bandelier Tuff and the Tunnel Spring Tuff, southwestern USA. Chemical Geology, 360, 99-104.

Audétat, A. (2015). Compositional Evolution and Formation Conditions of Magmas and Fluids Related to Porphyry Mo Mineralization at Climax, Colorado. Journal of Petrology, *doi: 10.1093/petrology/egv044*

Audétat, A., Garbe-Schönberg, D., Kronz, A., Pettke, T., Rusk, B., Donovan, J. J., & Lowers, H. A. (2015). Characterisation of a natural quartz crystal as a reference material for microanalytical determination of Ti, Al, Li, Fe, Mn, Ga and Ge. Geostandards and Geoanalytical Research, 39(2), 171-184.

Bachmann, O. and Dungan, M. A. (2002). Temperature-induced Al-zoning in hornblendes of the Fish Canyon magma, Colorado. American Mineralogist, 87(8-9), 1062-1076.

Baker, D. R., & Eggler, D. H. (1983). Fractionation paths of Atka (Aleutians) high-alumina basalts: constraints from phase relations. Journal of Volcanology and Geothermal Research, 18(1), 387-404.

Barr, J. A., & Grove, T. L. (2010). AuPdFe ternary solution model and applications to understanding the fO2 of hydrous, high-pressure experiments. Contributions to Mineralogy and Petrology, 160(5), 631-643.

Becker, A., Holtz, F. and Johannes, W. (1998). Liquidus temperatures and phase compositions in the system Qz-Ab-Or at 5 kbar and very low water activities. Contributions to Mineralogy and Petrology, 130(3-4), 213-224.

Bégué, F., Gualda, G. A., Ghiorso, M. S., Pamukcu, A. S., Kennedy, B. M., Gravley, D. M., Deering, C.D. & Chambefort, I. (2014a). Phase-equilibrium geobarometers for silicic rocks based on rhyolite-MELTS. Part 2: application to Taupo Volcanic Zone rhyolites. Contributions to Mineralogy and Petrology, 168(5), 1-16.

Bégué, F., Deering, C. D., Gravley, D. M., Kennedy, B. M., Chambefort, I., Gualda, G. A. R., & Bachmann, O. (2014b). Extraction, storage and eruption of multiple isolated magma batches in the paired Mamaku and Ohakuri eruption, Taupo Volcanic Zone, New Zealand. Journal of Petrology, 55(8), 1653-1684.

Behrens, H., Romano, C., Nowak, M., Holtz, F., & Dingwell, D. B. (1996). Near-infrared spectroscopic determination of water species in glasses of the system MAlSi 3 O 8 (M= Li, Na, K): an interlaboratory study. Chemical geology, 128(1), 41-63.

Berndt, J., Liebske, C., Holtz, F., Freise, M., Nowak, M., Ziegenbein, D. and Koepke, J. (2002). A combined rapid-quench and H2-membrane setup for internally heated pressure vessels: description and application for water solubility in basaltic melts. American Mineralogist, 87(11-12), 1717-1726.

Bindeman, I. N., Watts, K. E., Schmitt, A. K., Morgan, L. A., & Shanks, P. W. (2007). Voluminous low δ18O magmas in the late Miocene Heise volcanic field, Idaho: implications for the fate of Yellowstone hotspot calderas. Geology, 35(11), 1019-1022.

Blundy, J.and Cashman, K. (2001). Ascent-driven crystallisation of dacite magmas at Mount St Helens, 1980–1986. Contributions to Mineralogy and Petrology, 140(6), 631-650.

Blundy, J., & Cashman, K. (2008). Petrologic reconstruction of magmatic system variables and processes. Reviews in Mineralogy and Geochemistry, 69(1), 179-239.

Bolte, T., Holtz, F., Almeev, R. and Nash, B. (2015). The Blacktail Creek Tuff: an analytical and experimental study of rhyolites from the Heise volcanic field, Yellowstone hotspot system. Contributions to Mineralogy and Petrology, 169(2), 1-24.

Bonadonna, C., Connor, C. B., Houghton, B. F., Connor, L., Byrne, M., Laing, A., & Hincks, T. K. (2005). Probabilistic modeling of tephra dispersal: Hazard assessment of a multiphase rhyolitic eruption at Tarawera, New Zealand. Journal of Geophysical Research: Solid Earth (1978–2012), 110(B3).

Bonnichsen, B., Leeman, W. P., Honjo, N., McIntosh, W. C. and Godchaux, M. M. (2008). Miocene silicic volcanism in southwestern Idaho: geochronology, geochemistry, and evolution of the central Snake River Plain. Bulletin of Volcanology, 70(3), 315-342.

Botcharnikov, R. E., Koepke, J., Holtz, F., McCammon, C. and Wilke, M. (2005). The effect of water activity on the oxidation and structural state of Fe in a ferro-basaltic melt. Geochimica et Cosmochimica Acta, 69(21), 5071-5085.

Branney, M. J., Bonnichsen, B., Andrews, G. D. M., Ellis, B., Barry, T. L., & McCurry, M. (2008). 'Snake River (SR)-type'volcanism at the Yellowstone hotspot track: distinctive products from unusual, high-temperature silicic super-eruptions. Bulletin of Volcanology, 70(3), 293-314.

Cathey, H. E., & Nash, B. P. (2004). The Cougar Point Tuff: implications for thermochemical zonation and longevity of high-temperature, large-volume silicic magmas of the Miocene Yellowstone hotspot. Journal of Petrology, 45(1), 27-58.

Cathey, H. E., & Nash, B. P. (2009). Pyroxene thermometry of rhyolite lavas of the Bruneau–Jarbidge eruptive center, Central Snake River Plain. Journal of Volcanology and Geothermal Research, 188(1), 173-185.

Castro, J. M., & Dingwell, D. B. (2009). Rapid ascent of rhyolitic magma at Chaitén volcano, Chile. Nature, 461(7265), 780-783.

Chesner, C. A., & Luhr, J. F. (2010). A melt inclusion study of the Toba Tuffs, Sumatra, Indonesia. Journal of Volcanology and Geothermal Research, 197(1), 259-278.

Christiansen, E. H., McCurry, M., Bindemann, I., Champion, D., Knott, T., Branney, M.J., Bolte, T., Holtz, F., Shervais, J. (2013). Rhyolites in the Kimberly Drill Core, Project Hotspot: First Intracaldera Ignimbrite from the Central Snake River Plain, Idaho?, GSA conference Poster

El-Sayed, M. M. (2003). Neoproterozoic magmatism in NW Sinai, Egypt: magma source and evolution of collision-related intracrustal anatectic leucogranite. International Journal of Earth Sciences, 92(2), 145-164.

Elkins, L. T., Groove, L. G. (1990). Ternary feldspar experiments and thermodynamic models. American Mineralogist, 75, 554-559

Ellis, B. S. (2009). Rhyolitic explosive eruptions of the central Snake River Plain, Idaho: investigations of the lower Cassia Mountains succession and surrounding areas (Doctoral dissertation, University of Leicester)

Ellis, B. S., Bachmann, O., & Wolff, J. A. (2014). Cumulate fragments in silicic ignimbrites: The case of the Snake River Plain. Geology, 42(5), 431-434.

Ellis, B. S., Barry, T., Branney, M. J., Wolff, J. A., Bindeman, I., Wilson, R., & Bonnichsen, B. (2010). Petrologic constraints on the development of a large-volume, high temperature, silicic magma system: The Twin Falls eruptive centre, central Snake River Plain. Lithos, 120(3), 475-489.

Ellis, B. S., Cordonnier, B., Rowe, M. C., Szymanowski, D., Bachmann, O., & Andrews, G. D. M. (2015). Groundmass crystallisation and cooling rates of lava-like ignimbrites: the Grey's Landing ignimbrite, southern Idaho, USA. Bulletin of Volcanology, 77(10), 1-15.

Ellis, B. S., Mark, D. F., Pritchard, C. J., & Wolff, J. A. (2012). Temporal dissection of the Huckleberry Ridge Tuff using the 40 Ar/39 Ar dating technique. Quaternary Geochronology, 9, 34-41.

Ellis, B. S., Wolff, J. A., Boroughs, S., Mark, D. F., Starkel, W. A., & Bonnichsen, B. (2013). Rhyolitic volcanism of the central Snake River Plain: a review. Bulletin of volcanology, 75(8), 1-19.

Fierstein, J., & Hildreth, W. (1992). The plinian eruptions of 1912 at Novarupta, Katmai national park, Alaska. Bulletin of Volcanology, 54(8), 646-684.

Frost, B. R., & Lindsley, D. H. (1992). Equilibria among Fe-Ti oxides, pyroxenes, olivine, and quartz: Part II. Application. American Mineralogist, 77, 1004-1004.

Gardner, J. E., Befus, K. S., Gualda, G. A., & Ghiorso, M. S. (2014). Experimental constraints on rhyolite-MELTS and the Late Bishop Tuff magma body. Contributions to Mineralogy and Petrology, 168(2), 1-14.

Ghiorso, M. S., & Evans, B. W. (2008). Thermodynamics of rhombohedral oxide solid solutions and a revision of the Fe-Ti two-oxide geothermometer and oxygen-barometer. American Journal of Science, 308(9), 957-1039.

Ghiorso, M. S., & Gualda, G. A. (2013). A method for estimating the activity of titania in magmatic liquids from the compositions of coexisting rhombohedral and cubic iron–titanium oxides. Contributions to Mineralogy and Petrology, 165(1), 73-81.

Gualda, G. A. and Ghiorso, M. S. (2013a) Low-pressure origin of high-silica rhyolites and granites. The Journal of Geology, 121(5), 537-545.

Gualda, G. A. and Ghiorso, M. S. (2013b). The Bishop Tuff giant magma body: an alternative to the Standard Model. Contributions to Mineralogy and Petrology, 166(3), 755-775.

Gualda, G. A. and Ghiorso, M. S. (2014). Phase-equilibrium geobarometers for silicic rocks based on rhyolite-MELTS. Part 1: Principles, procedures, and evaluation of the method. Contributions to Mineralogy and Petrology, 168, 1-16

Hess, K.-U. & Dingwell, D.B. (1996). Viscosities of hydrous leucogranitic melts: a non-Arrhenian model. American Mineralogist., 81, 1297–1300.

Hildreth, W. E. S., Halliday, A. N., & Christiansen, R. L. (1991). Isotopic and chemical evidence concerning the genesis and contamination of basaltic and rhyolitic magma beneath the Yellowstone Plateau volcanic field. Journal of Petrology, 32(1), 63-138.

Holtz, F., Johannes, W. and Pichavant (1992a). Effect of excess aluminium on phase relations in the system Qz-Ab-Or : experimental investigation at 2 kbar and reduced H_2O-activity. European Journal of Mineralogy, 4, 137-152.

Holtz, F., Pichavant, M., Barbey, P. and Johannes, W. (1992b). Effects of H_2O on liquidus phase relations in the haplogranite system at 2 and 5 kbar. American Mineralogist, 77(11-12), 1223-1241.

Holtz, F., Becker, A., Freise, M. and Johannes, W. (2001a). The water-undersaturated and dry Qz-Ab-Or system revisited. Experimental results at very low water activities and geological implications. Contributions to Mineralogy and Petrology, 141(3), 347-357.

Holtz, F., Johannes, W., Tamic, N., & Behrens, H. (2001b). Maximum and minimum water contents of granitic melts generated in the crust: a reevaluation and implications. Lithos, 56(1), 1-14.

Honjo, N., Bonnichsen, B., Leeman, W. P., & Stormer Jr, J. C. (1992). Mineralogy and geothermometry of high-temperature rhyolites from the central and western Snake River Plain. Bulletin of Volcanology, 54(3), 220-237.

Huang, R. and Audétat, A. (2012). The titanium-in-quartz (TitaniQ) thermobarometer: a critical examination and re-calibration. Geochimica et Cosmochimica Acta, 84, 75-89.

Huang, H. H., Lin, F. C., Schmandt, B., Farrell, J., Smith, R. B., & Tsai, V. C. (2015). The Yellowstone magmatic system from the mantle plume to the upper crust. Science, 348(6236), 773-776.

Hughes, S. S., & McCurry, M. (2002). Bulk major and trace element evidence for a time-space evolution of Snake River Plain rhyolites, Idaho. Tectonic and Magmatic Evolution of the Snake River Plain Volcanic Province: Idaho Geological Survey Bulletin, 30, 161-176.

James, R. S. and Hamilton, D. L. (1969). Phase relations in the system NaAlSi3O8-KAlSi3O8-CaAl2Si2O8-SiO2 at 1 kilobar water vapour pressure. Contributions to Mineralogy and Petrology, 21(2), 111-141.

Jean, M. M., Hanan, B. B., & Shervais, J. W. (2014). Yellowstone hotspot–continental lithosphere interaction. Earth and Planetary Science Letters, 389, 119-131.

Kellogg, K.S., Harlan, S.S., Mehnert, H.H., Snee, L.W., Pierce, K.L., Hackett, W.R. and Rodgers, D.W. (1994). Major 10.2-Ma Rhyolitic Volcanism in the Eastern Snake River Plain, Idaho- Isotopic Age and Stratigraphic Setting of the Arbon Valley Tuff Member of the Starlight Formation. U.S. Geological Survey Bulletin 2091

Kirschen, M., & Pichavant, M. (2001). A thermodynamic model for hydrous silicate melts in the system $NaAlSi_3O_8$–$KAlSi_3O_8$–Si_4O_8–H_2O. Chemical Geology, 174(1), 103-114.

Klahn, C. (2013), Calibration of cotectic compositions co-existing with quartz and feldspar in rhyolitic systems – An experimental study at 200 MPa. Master Thesis at the Institute for Mineralogy, Leibniz University of Hannover

Kularatne, K., & Audétat, A. (2014). Rutile solubility in hydrous rhyolite melts at 750–900° C and 2kbar, with application to titanium-in-quartz (TitaniQ) thermobarometry. Geochimica et Cosmochimica Acta, 125, 196-209.

Lange, R. A., Frey, H. M., & Hector, J. (2009). A thermodynamic model for the plagioclase-liquid hygrometer/thermometer. American Mineralogist, 94(4), 494-506.

Lepage, L. D. (2003). ILMAT: an Excel worksheet for ilmenite–magnetite geothermometry and geobarometry. Computers & Geosciences, 29(5), 673-678.

Lindsley, D. H. (1983). Pyroxene thermometry. American Mineralogist, 68(5-6), 477-493.

Liu, Y., Zhang, Y. and Behrens, H. (2005). Solubility of H2O in rhyolitic melts at low pressures and a new empirical model for mixed H2O–CO2 solubility in rhyolitic melts. Journal of Volcanology and Geothermal Research, 143(1), 219-235.

Liu, Y., Anderson, A. T., Wilson, C. J., Davis, A. M. and Steele, I. M. (2006). Mixing and differentiation in the Oruanui rhyolitic magma, Taupo, New Zealand: evidence from volatiles and trace elements in melt inclusions. Contributions to Mineralogy and Petrology, 151(1), 71-87.

Lowry, A. R., & Pérez-Gussinyé, M. (2011). The role of crustal quartz in controlling Cordilleran deformation. Nature, 471(7338), 353-357.

Luth, W. C., Jahns, R. H. and Tuttle, O. F. (1964). The granite system at pressures of 4 to 10 kilobars. Journal of Geophysical Research, 69(4), 759-773.

Luth, W. C. (1969). The systems $NaAlSi_3O_8$-SiO_2 and $KAlSi_3O8$-SiO_2 to 20 kb and the relationship between H_2O content, PH_2O and P_{total} granitic magmas. American Journal of Science, 267, 325-341.

Manning, D. A. C. (1981). The effect of fluorine on liquidus phase relationships in the system Qz-Ab-Or with excess water at 1 kb. Contributions to Mineralogy and Petrology, 76(2), 206-215.

Matthews, N. E., Pyle, D. M., Smith, V. C., Wilson, C. J. N., Huber, C., & Van Hinsberg, V. (2012). Quartz zoning and the pre-eruptive evolution of the~ 340-ka Whakamaru magma systems, New Zealand. Contributions to Mineralogy and Petrology, 163(1), 87-107.

Mercer, C. N., Hofstra, A. H., Todorov, T. I., Roberge, J., Burgisser, A., Adams, D. T., & Cosca, M. (2015). Pre-Eruptive Conditions of the Hideaway Park Topaz Rhyolite: Insights into Metal Source and Evolution of Magma Parental to the Henderson Porphyry Molybdenum Deposit, Colorado. Journal of Petrology, 56(4), 645-679.

Morgan, L. A., & McIntosh, W. C. (2005). Timing and development of the Heise volcanic field, Snake River Plain, Idaho, western USA. Geological Society of America Bulletin, 117(3-4), 288-306.

Nash, W.P. (1992). Analysis of oxygen with the electron microprobe: Applications to hydrated glass and minerals. American Mineralogist, 77, 453-457

Nash, B. P., Perkins, M. E., Christensen, J. N., Lee, D. C., & Halliday, A. N. (2006). The Yellowstone hotspot in space and time: Nd and Hf isotopes in silicic magmas. Earth and Planetary Science Letters, 247(1), 143-156.

Newhall, C. G., & Self, S. (1982). The volcanic explosivity index/VEI/- An estimate of explosive magnitude for historical volcanism. Journal of Geophysical Research, 87(C2), 1231-1238.

Pamukcu, A. S., Gualda, G. A., Ghiorso, M. S., Miller, C. F., & McCracken, R. G. (2015). Phase-equilibrium geobarometers for silicic rocks based on rhyolite-MELTS—Part 3: Application to the Peach Spring Tuff (Arizona–California–Nevada, USA). Contributions to Mineralogy and Petrology, 169(3), 1-17.

Perkins, M. E., & Nash, B. P. (2002). Explosive silicic volcanism of the Yellowstone hotspot: The ash fall tuff record. Geological Society of America Bulletin, 114(3), 367-381.

Perkins, M. E., Nash, W. P., Brown, F. H., & Fleck, R. J. (1995). Fallout tuffs of Trapper Creek, Idaho—a record of Miocene explosive volcanism in the Snake River Plain volcanic province. Geological Society of America Bulletin, 107(12), 1484-1506.

Pichavant, M. (1987). Effects of B and H_2O on liquidus phase relations in the haplogranite system at l kbar. American Mineralogist, 72(11-12), 1056-1070.

Pichavant, M., Holtz, F., & McMillan, P. F. (1992). Phase relations and compositional dependence of H_2O solubility in quartz-feldspar melts. Chemical Geology, 96(3), 303-319.

Pierce, K. L., & Morgan, L. A. (1992). The track of the Yellowstone hot spot: Volcanism, faulting, and uplift. Geological Society of America Memoirs, 179, 1-54.

Pitzer, K. S. and Sterner, S. M. (1994). Equations of state valid continuously from zero to extreme pressures for H2O and CO2. The Journal of chemical physics, 101(4), 3111-3116.

Putirka, K. D. (2008). Thermometers and barometers for volcanic systems. Reviews in Mineralogy and Geochemistry, 69(1), 61-120.

Putirka, K. D., Canchola, J., Rash, J., Smith, O., Torrez, G., Paterson, S. R., & Ducea, M. N. (2014). Pluton assembly and the genesis of granitic magmas: Insights from the GIC pluton in cross section, Sierra Nevada Batholith, California. American Mineralogist, 99(7), 1284-1303.

Ridolfi, F. and Renzulli, A. (2012). Calcic amphiboles in calc-alkaline and alkaline magmas: thermobarometric and chemometric empirical equations valid up to 1,130° C and 2.2 GPa. Contributions to Mineralogy and Petrology, 163(5), 877-895.

Ridolfi, F., Renzulli, A., & Puerini, M. (2010). Stability and chemical equilibrium of amphibole in calc-alkaline magmas: an overview, new thermobarometric formulations and application to subduction-related volcanoes. Contributions to Mineralogy and Petrology, 160(1), 45-66.

Shervais, J. W., Schmitt, D. R., Nielson, D. L., Evans, J. P., Christiansen, E. H., Morgan, L., Shanks, W.C.P., Prokopenko, A.A., Lachmar, T., Liberty, L.M., Blackwell, D.D., Glen, J. M., Champion, D., Potter, K.E. and Kessler, J.A. (2013). First Results from HOTSPOT: The Snake River Plain Scientific Drilling Project, Idaho, USA. Scientific Drilling, 15, 36-45.

Sisson, T. W., & Grove, T. L. (1993). Experimental investigations of the role of H2O in calc-alkaline differentiation and subduction zone magmatism. Contributions to Mineralogy and Petrology, 113(2), 143-166.

Steiner, J. C., Jahns, R. H. and Luth, W. C. (1975). Crystallization of alkali feldspar and quartz in the haplogranite system NaAlSi3O8-KAlSi3O8-SiO2-H2O at 4 kb. Geological Society of America Bulletin, 86(1), 83-98.

Szymanowski, D., Ellis, B. S., Bachmann, O., Guillong, M., & Phillips, W. M. (2015). Bridging basalts and rhyolites in the Yellowstone–Snake River Plain volcanic province: the elusive intermediate step. Earth and Planetary Science Letters, 415, 80-89.

Thomas, J. B., Watson, E. B., Spear, F. S., Shemella, P. T., Nayak, S. K. and Lanzirotti, A. (2010). TitaniQ under pressure: the effect of pressure and temperature on the solubility of Ti in quartz. Contributions to Mineralogy and Petrology, 160(5), 743-759.

Thomas, J. B., & Watson, E. B. (2012). Application of the Ti-in-quartz thermobarometer to rutile-free systems. Reply to: a comment on:'TitaniQ under pressure: the effect of pressure and temperature on the solubility of Ti in quartz'by Thomas et al. Contributions to Mineralogy and Petrology, 164(2), 369-374.

Thomas, J. B., Watson, E. B., Spear, F. S., & Wark, D. A. (2015). TitaniQ recrystallized: experimental confirmation of the original Ti-in-quartz calibrations. Contributions to Mineralogy and Petrology, 169(3), 1-16.

Tuttle, O. F. and Bowen, N. L. (1958). Origin of granite in the light of experimental studies in the system NaAlSi3O8–KAlSi3O8–SiO2–H2O. Geological Society of America Memoirs, 74, 1-146.

Vazquez, J. A., Kyriazis, S. F., Reid, M. R., Sehler, R. C., & Ramos, F. C. (2009). Thermochemical evolution of young rhyolites at Yellowstone: Evidence for a cooling but periodically replenished postcaldera magma reservoir. Journal of Volcanology and Geothermal Research, 188(1), 186-196.

Whitaker, M. L., Nekvasil, H., Lindsley, D. H., & McCurry, M. (2008). Can crystallization of olivine tholeiite give rise to potassic rhyolites?—an experimental investigation. Bulletin of Volcanology, 70(3), 417-434.

Wilke, S., Klahn, C., Bolte, T., Almeev, R., & Holtz, F. (2015). Experimental investigation of the effect of Ca, Fe and Ti on cotectic compositions of the rhyolitic system. European Journal of Mineralogy, 27(2), 147-159.

Wilson, C. J. N., Seward, T. M., Allan, A. S. R., Charlier, B. L. A., Bello, L. (2012). A comment on: 'TitaniQ under pressure: the effect of pressure and temperature on the solubility of Ti in quartz', by Jay B. Thomas, E. Bruce Watson, Frank S. Spear, Philip T. Shemella, Saroj K. Nayak and Antonio Lanzirotti. Contributions to Mineralogy and Petrology, 164, 359-368

Wilson, C. J. N., & Walker, G. P. L. (1985). The Taupo eruption, New Zealand I. General aspects. Philosophical Transactions of the Royal Society of London A: Mathematical, Physical and Engineering Sciences, 314(1529), 199-228.

Withers, A. C., & Behrens, H. (1999). Temperature-induced changes in the NIR spectra of hydrous albitic and rhyolitic glasses between 300 and 100 K. Physics and Chemistry of Minerals, 27(2), 119-132.

Wright, K. E., McCurry, M., & Hughes, S. S. (2002). Petrology and geochemistry of the Miocene Tuff of McMullen Creek, central Snake River Plain, Idaho. Tectonic and magmatic evolution of the Snake River Plain volcanic province. Idaho Geol Surv Bull, 30, 177-194.

Zhang, C., Holtz, F., Koepke, J., Berndt, J., & Ma, C. (2014). Decompressional anatexis in the migmatite core complex of northern Dabie orogen, eastern China: Petrological evidence and Ti-in-quartz thermobarometry. Lithos, 202, 227-236.

APPENDIX

Appendix Table 1: Glasscomposition of samples for system A

Name	YX90		YX91		YX92		YX93		YX94		YX95		YX96		YX97		YX98		YX99	
SM	HYW1		HYW2		HYW3		HYW4		HYW5		HYW6		HYW7		HYW8		HYW1		HYW2	
	[wt.%]	1σ	[wt.%]	1σ	[wt.%]	1σ	[wt.%]	1σ	[wt.%]	1σ	[wt.%]	1σ	[wt.%]	1σ	[wt.%]	1σ	[wt.%]	1σ	[wt.%]	1σ
SiO_2	77.84	0.17	77.48	0.28	74.26	0.57	76.03	0.14	76.49	0.19	76.21	0.18	77.30	0.32	75.39	0.33	78.06	0.43	77.81	0.51
TiO_2	0.24	0.01	0.23	0.01	0.23	0.02	0.21	0.01	0.22	0.01	0.23	0.02	0.22	0.01	0.25	0.01	0.23	0.01	0.23	0.02
Al_2O_3	11.82	0.12	11.27	0.13	13.44	0.12	11.58	0.08	12.21	0.13	11.99	0.08	11.20	0.09	13.09	0.12	11.45	0.10	10.81	0.19
FeO	1.08	0.12	1.01	0.08	1.02	0.07	0.96	0.05	0.92	0.08	0.78	0.06	0.93	0.07	0.96	0.07	0.89	0.13	0.97	0.08
CaO	0.70	0.03	0.77	0.04	0.72	0.02	0.70	0.02	0.72	0.02	0.73	0.02	0.72	0.03	0.39	0.02	0.78	0.02	0.77	0.05
Na_2O	3.71	0.20	1.27	0.11	2.34	0.11	0.00	0.00	2.82	0.15	1.75	0.07	0.67	0.04	4.42	0.13	3.50	0.13	1.20	0.06
K_2O	4.23	0.07	7.04	0.06	7.45	0.10	8.61	0.05	5.82	0.09	7.27	0.07	7.76	0.09	4.76	0.05	3.90	0.06	6.75	0.09
Total	99.60	0.73	99.08	0.72	99.46	1.01	98.16	0.39	99.19	0.67	98.97	0.49	98.80	0.65	99.26	0.73	98.81	0.89	98.54	1.00
n	19		20		20		5		20		5		20		20		20		20	
Qz	37.97		40.81		29.94		40.94		35.70		36.22		41.56		30.05		40.55		42.73	
Ab	31.38		10.77		19.76		0.00		23.86		14.84		5.66		37.43		29.60		10.12	
Or	24.98		41.63		44.04		50.90		34.42		42.95		45.89		28.11		23.06		39.90	
An	3.13		3.82		3.59		3.49		3.46		3.38		3.57		1.82		3.87		3.84	
Cor[a]	-0.12		0.16		0.22		0.98		-0.03		-0.08		0.39		-0.05		0.05		0.13	

n = number of analyses, Qz = normative quartz content calculated by CIPW-norm, Ab = albite , Or = orthoclase , An = anorthite, Cor = corundum

[a] negative corundum values reflect the amount of corundum that is missing to convert all available CaO to anorthite

Appendix Table1: Continued

Name	YX100		YX101		YX102		YX103		YX104		YX105		YX122		YX123		YX124		YX125	
SM	HYW3		HYW4		HYW5		HYW6		HYW7		HYW8		HYW1		HYW2		HYW3		HYW4	
	[wt.%]	1σ	[wt.%]	1σ	[wt.%]	1σ	[wt.%]	1σ	[wt.%]	1σ	[wt.%]	1σ	[wt.%]	1σ	[wt.%]	1σ	[wt.%]	1σ	[wt.%]	1σ
SiO_2	73.66	0.27	76.18	0.25	76.32	0.28	75.96	0.29	77.90	0.31	74.27	0.41	75.95	0.17	76.56	0.41	74.07	0.33	76.15	0.25
TiO_2	0.22	0.01	0.21	0.01	0.23	0.00	0.21	0.01	0.21	0.02	0.23	0.02	0.25	0.02	0.22	0.02	0.24	0.01	0.21	0.02
Al_2O_3	13.98	0.21	11.59	0.03	12.29	0.10	12.07	0.07	10.94	0.10	13.65	0.16	11.71	0.09	11.06	0.30	12.81	0.11	11.56	0.09
FeO	0.75	0.03	0.79	0.08	0.89	0.03	0.76	0.05	0.89	0.03	0.75	0.10	1.20	0.07	0.93	0.07	0.95	0.08	0.74	0.10
CaO	0.72	0.03	0.69	0.02	0.72	0.02	0.69	0.02	0.69	0.03	0.50	0.03	0.59	0.03	0.70	0.06	0.69	0.03	0.69	0.02
Na_2O	2.31	0.13	0.00	0.00	2.84	0.05	1.73	0.11	0.61	0.05	4.77	0.10	3.35	0.14	1.18	0.07	2.13	0.08	0.00	0.00
K_2O	7.93	0.10	8.66	0.03	5.85	0.06	7.17	0.03	7.50	0.06	4.60	0.08	4.49	0.06	6.96	0.09	6.90	0.07	8.50	0.08
Total	99.57	0.77	98.17	0.45	99.13	0.54	98.59	0.58	98.74	0.60	98.76	0.89	97.54	0.58	97.62	1.02	97.78	0.72	97.90	0.58
n	5		4		5		5		5		20		19		19		16		20	
Qz	27.87		41.06		35.33		36.51		43.57		27.47		37.20		40.95		33.19		41.67	
Ab	19.58		0.00		24.02		14.65		5.19		40.32		28.38		9.99		18.07		0.00	
Or	46.85		51.20		34.58		42.39		44.34		27.17		26.55		41.13		40.75		50.26	
An	3.56		3.42		3.50		3.40		3.42		2.29		2.91		3.49		3.41		3.41	
Cor[a]	0.29		0.96		-0.02		0.21		0.56		-0.08		0.26		0.31		0.58		1.10	

n = number of analyses, Qz = normative quartz content calculated by CIPW-norm, Ab = albite , Or = orthoclase , An = anorthite, Cor = corundum

[a] negative corundum values reflect the amount of corundum that is missing to convert all available CaO to anorthite

Appendix Table 1: Continued

Name	YX126		YX127		YX128		YX129		YX130		YX131		YX132		YX133		YX134		YX135	
SM	HYW5		HYW6		HYW7		HYW8		HYW1		HYW2		HYW3		HYW4		HYW5		HYW6	
	[wt.%]	1σ	[wt.%]	1σ	[wt.%]	1σ	[wt.%]	1σ	[wt.%]	1σ	[wt.%]	1σ	[wt.%]	1σ	[wt.%]	1σ	[wt.%]	1σ	[wt.%]	1σ
SiO_2	75.99	0.22	75.72	0.25	76.43	0.34	76.05	0.40	75.82	0.31	76.11	0.34	76.09	0.34	76.06	0.40	75.79	0.39	76.05	0.30
TiO_2	0.22	0.01	0.22	0.02	0.21	0.01	0.25	0.02	0.25	0.02	0.22	0.01	0.25	0.02	0.21	0.02	0.22	0.02	0.21	0.01
Al_2O_3	12.02	0.14	12.05	0.11	11.32	0.16	12.41	0.19	11.74	0.10	11.58	0.21	12.06	0.19	11.85	0.15	11.94	0.14	12.10	0.15
FeO	1.01	0.07	0.78	0.05	0.82	0.16	1.06	0.13	1.25	0.08	1.10	0.09	1.10	0.08	0.98	0.08	1.05	0.06	0.61	0.07
CaO	0.55	0.02	0.69	0.02	0.72	0.03	0.37	0.03	0.49	0.02	0.72	0.04	0.56	0.03	0.73	0.03	0.48	0.02	0.69	0.03
Na_2O	2.55	0.07	1.65	0.10	0.60	0.06	3.70	0.10	3.33	0.11	1.23	0.07	2.04	0.12	0.00	0.00	2.53	0.12	1.62	0.10
K_2O	5.93	0.07	7.09	0.07	7.70	0.09	4.79	0.09	4.86	0.07	7.20	0.11	6.53	0.08	8.59	0.08	6.03	0.08	7.16	0.09
Total	98.26	0.61	98.20	0.63	97.81	0.85	98.63	0.95	97.73	0.71	98.17	0.88	98.63	0.86	98.48	0.79	98.04	0.83	98.44	0.75
n	20		8		20		8		20		20		10		20		20		19	
Qz	36.62		37.03		41.39		34.72		35.99		39.12		37.32		40.98		36.26		37.37	
Ab	21.56		13.99		5.11		31.33		28.15		10.42		17.29		0.00		21.42		13.73	
Or	35.05		41.89		45.52		28.29		28.73		42.55		38.56		50.74		35.64		42.34	
An	2.74		3.42		3.58		1.82		2.42		3.57		2.78		3.64		2.38		3.40	
Cor[a]	0.41		0.40		0.68		0.48		0.12		0.46		0.62		1.23		0.37		0.43	

n = number of analyses, Qz = normative quartz content calculated by CIPW-norm, Ab = albite , Or = orthoclase , An = anorthite, Cor = corundum

[a] negative corundum values reflect the amount of corundum that is missing to convert all available CaO to anorthite

Appendix Table 1: Continued

Name	YX136		YX137	
SM	HYW7		HYW8	
	[wt.%]	1σ	[wt.%]	1σ
SiO_2	76.20	0.34	76.24	0.56
TiO_2	0.21	0.01	0.26	0.01
Al_2O_3	11.63	0.14	12.33	0.50
FeO	0.97	0.08	0.88	0.33
CaO	0.70	0.02	0.36	0.04
Na_2O	0.60	0.05	3.79	0.20
K_2O	7.97	0.08	4.75	0.12
Total	98.29	0.73	98.61	1.76
n	19		4	
Qz	40.03		34.72	
Ab	5.09		32.09	
Or	47.12		28.06	
An	3.49		1.79	
Cor[a]	0.73		0.30	

n = number of analyses, Qz = normative quartz content calculated by CIPW-norm, Ab = albite , Or = orthoclase , An = anorthite, Cor = corundum

[a] negative corundum values reflect the amount of corundum that is missing to convert all available CaO to anorthite

Appendix Table 2: Glasscomposition of samples for system B

Name	YX1		YX2		YX3		YX4		YX5		YX6		YX7		YX8		YX9		YX10	
SM	HYS1		HYS2		HYS3		HYS4		HYS5		HYS6		HYS7		HYS8		HYS1		HYS2	
	[wt.%]	1σ	[wt.%]	1σ	[wt.%]	1σ	[wt.%]	1σ	[wt.%]	1σ	[wt.%]	1σ	[wt.%]	1σ	[wt.%]	1σ	[wt.%]	1σ	[wt.%]	1σ
SiO_2	76.09	0.34	75.45	0.21	72.47	0.26	76.19	0.29	74.08	0.35	71.13	0.38	71.30	0.25	74.38	0.30	76.90	0.23	75.50	0.24
TiO_2	0.42	0.02	0.40	0.02	0.49	0.02	0.42	0.02	0.43	0.02	0.53	0.02	0.46	0.02	0.46	0.02	0.45	0.02	0.40	0.01
Al_2O_3	11.98	0.11	11.90	0.08	13.84	0.13	11.77	0.12	13.19	0.14	14.37	0.09	14.19	0.15	12.94	0.12	11.82	0.11	11.95	0.09
FeO	2.30	0.08	2.13	0.10	1.79	0.10	2.12	0.09	1.52	0.08	1.93	0.27	2.10	0.09	1.87	0.10	1.98	0.15	2.02	0.11
CaO	0.87	0.04	1.39	0.03	0.94	0.05	0.93	0.03	1.17	0.04	0.84	0.06	0.89	0.05	0.89	0.04	1.01	0.04	1.44	0.03
Na_2O	3.53	0.11	1.39	0.09	2.21	0.08	2.43	0.09	1.82	0.10	4.50	0.06	3.45	0.11	4.02	0.09	3.53	0.09	1.39	0.06
K_2O	4.11	0.05	6.67	0.07	7.70	0.08	5.66	0.07	7.23	0.07	5.33	0.04	6.44	0.07	4.36	0.07	3.72	0.07	6.64	0.06
Total	99.29	0.75	99.34	0.61	99.45	0.71	99.51	0.71	99.44	0.81	98.63	0.91	98.83	0.73	98.91	0.74	99.41	0.72	99.34	0.60
n	17		20		15		20		20		14		17		16		18		20	
Qz	36.39		37.50		27.04		37.03		32.43		21.81		23.37		31.26		38.71		37.70	
Ab	29.90		11.78		18.72		20.55		15.38		38.05		29.23		33.99		29.87		11.74	
Or	24.32		39.43		45.49		33.44		42.71		31.48		38.04		25.75		21.97		39.22	
An	4.30		6.53		4.67		4.50		5.81		3.30		4.20		4.40		5.01		6.79	
Cor[a]	0.13		-0.14		0.16		-0.04		0.25		-0.32		-0.07		0.00		0.15		-0.13	

n = number of analyses, Qz = normative quartz content calculated by CIPW-norm, Ab = albite , Or = orthoclase , An = anorthite, Cor = corundum

[a] negative corundum values reflect the amount of corundum that is missing to convert all available CaO to anorthite

Appendix Table 2: Continued

Name	YX11		YX12		YX13		YX14		YX15		YX16		YX17		YX18		YX19		YX20	
SM	HYS3		HYS4		HYS5		HYS6		HYS7		HYS8		HYS1		HYS2		HYS3		HYS4	
	[wt.%]	1σ	[wt.%]	1σ	[wt.%]	1σ	[wt.%]	1σ	[wt.%]	1σ	[wt.%]	1σ	[wt.%]	1σ	[wt.%]	1σ	[wt.%]	1σ	[wt.%]	1σ
SiO_2	71.70	0.32	76.33	0.32	73.37	0.28	71.07	0.35	71.03	0.23	73.79	0.23	76.76	0.64	75.68	0.30	71.05	0.23	76.32	0.23
TiO_2	0.45	0.02	0.42	0.02	0.42	0.02	0.50	0.03	0.46	0.02	0.45	0.02	0.42	0.03	0.44	0.02	0.45	0.02	0.41	0.03
Al_2O_3	14.13	0.08	11.86	0.12	13.27	0.12	15.09	0.17	14.65	0.08	13.46	0.10	12.22	0.19	12.04	0.08	14.72	0.10	12.13	0.09
FeO	1.74	0.08	2.11	0.07	1.62	0.11	1.57	0.19	2.01	0.09	1.73	0.08	1.66	0.33	1.89	0.06	1.66	0.07	1.99	0.08
CaO	1.06	0.03	1.23	0.05	1.38	0.03	0.90	0.05	1.00	0.03	1.03	0.02	1.39	0.15	1.45	0.04	1.37	0.03	1.43	0.03
Na_2O	2.24	0.08	2.51	0.07	1.81	0.12	4.79	0.08	3.59	0.11	4.16	0.09	3.66	0.21	1.46	0.07	2.33	0.10	2.49	0.10
K_2O	7.65	0.07	5.13	0.06	7.05	0.08	5.24	0.07	6.36	0.05	4.22	0.04	3.40	0.10	6.66	0.09	7.42	0.08	4.96	0.07
Total	98.98	0.68	99.58	0.72	98.92	0.77	99.17	0.94	99.10	0.61	98.86	0.58	99.50	1.65	99.61	0.65	99.00	0.64	99.74	0.63
n	20		17		20		16		16		17		31		10		18		20	
Qz	26.03		38.12		31.92		20.36		22.37		30.12		38.47		37.51		25.17		38.48	
Ab	18.97		21.21		15.28		40.57		30.40		35.24		30.94		12.35		19.69		21.11	
Or	45.23		30.34		41.66		30.98		37.57		24.96		20.08		39.36		43.86		29.29	
An	5.26		5.94		6.86		4.17		4.98		5.13		6.89		6.62		6.80		7.09	
Cor[a]	0.23		-0.05		0.15		-0.11		0.03		0.16		-0.01		-0.22		0.37		0.06	

n = number of analyses, Qz = normative quartz content calculated by CIPW-norm, Ab = albite , Or = orthoclase , An = anorthite, Cor = corundum

[a] negative corundum values reflect the amount of corundum that is missing to convert all available CaO to anorthite

Appendix Table 2: Continued

Name	YX21		YX22		YX23		YX24		YX25		YX26		YX27		YX28		YX29		YX30	
SM	HYS5		HYS6		HYS7		HYS8		HYS1		HYS2		HYS3		HYS4		HYS5		HYS6	
	[wt.%]	1σ	[wt.%]	1σ	[wt.%]	1σ	[wt.%]	1σ	[wt.%]	1σ	[wt.%]	1σ	[wt.%]	1σ	[wt.%]	1σ	[wt.%]	1σ	[wt.%]	1σ
SiO_2	73.13	0.17	70.57	0.26	70.92	0.24	74.03	0.25	76.56	0.57	75.99	0.47	71.28	0.50	76.69	0.79	73.15	0.49	70.39	0.68
TiO_2	0.43	0.02	0.46	0.02	0.44	0.01	0.44	0.01	0.40	0.03	0.41	0.05	0.42	0.03	0.40	0.03	0.42	0.03	0.41	0.03
Al_2O_3	13.32	0.10	15.54	0.12	15.10	0.15	14.04	0.09	12.27	0.27	12.15	0.23	14.80	0.28	12.24	0.22	13.42	0.26	16.16	0.27
FeO	1.70	0.11	1.68	0.13	1.70	0.09	1.24	0.07	1.84	0.24	2.19	0.14	1.04	0.52	1.52	0.52	1.26	0.25	1.00	0.39
CaO	1.41	0.03	1.02	0.03	1.13	0.03	1.13	0.04	1.47	0.11	1.39	0.11	1.34	0.12	1.46	0.11	1.39	0.11	1.19	0.12
Na_2O	1.81	0.08	5.04	0.12	3.67	0.11	4.29	0.10	3.78	0.21	1.50	0.10	2.48	0.17	2.58	0.16	1.91	0.14	5.58	0.16
K_2O	7.04	0.09	5.06	0.07	6.24	0.07	4.11	0.06	3.10	0.06	6.78	0.11	7.42	0.13	4.95	0.10	7.04	0.09	4.77	0.08
Total	98.84	0.59	99.37	0.74	99.20	0.70	99.28	0.63	99.42	1.49	#####	1.21	98.79	1.75	99.84	1.94	98.59	1.38	99.50	1.73
n	20		19		19		17		20		20		20		20		20		20	
Qz	31.59		18.74		22.21		30.20		38.36		37.01		25.04		38.71		31.37		16.82	
Ab	15.30		42.62		31.07		36.34		31.99		12.65		20.99		21.80		16.20		47.20	
Or	41.63		29.92		36.90		24.32		18.33		40.07		43.86		29.22		41.60		28.21	
An	6.98		4.84		5.58		5.58		7.30		6.41		6.67		7.23		6.92		4.95	
Cor[a]	0.17		-0.07		0.25		0.47		0.02		-0.18		0.24		-0.01		0.12		-0.35	

n = number of analyses, Qz = normative quartz content calculated by CIPW-norm, Ab = albite , Or = orthoclase , An = anorthite, Cor = corundum

[a] negative corundum values reflect the amount of corundum that is missing to convert all available CaO to anorthite

Appendix Table 2: Continued

Name	YX31		YX32		DYX1		DYX2		DYX3		DYX4		DYX5		DYX6		DYX7		DYX8	
SM	HYS7		HYS8		HYS15		HYS16		HYS17		HYS18		HYS15		HYS16		HYS17		HYS18	
	[wt.%]	1σ	[wt.%]	1σ	[wt.%]	1σ	[wt.%]	1σ	[wt.%]	1σ	[wt.%]	1σ	[wt.%]	1σ	[wt.%]	1σ	[wt.%]	1σ	[wt.%]	1σ
SiO_2	70.83	0.65	73.54	0.47	76.21	0.27	76.08	0.34	76.20	0.30	74.40	0.27	76.96	0.30	77.46	0.66	76.56	0.27	74.48	0.26
TiO_2	0.42	0.04	0.43	0.05	0.45	0.02	0.43	0.02	0.42	0.02	0.41	0.02	0.43	0.02	0.44	0.02	0.42	0.02	0.41	0.02
Al_2O_3	15.56	0.21	14.52	0.24	11.42	0.11	11.00	0.14	11.20	0.10	12.00	0.11	11.37	0.09	10.68	0.10	10.83	0.12	12.07	0.08
FeO	1.00	0.27	0.67	0.14	1.90	0.17	1.98	0.19	1.98	0.14	1.69	0.10	1.60	0.05	1.58	0.48	1.90	0.10	1.57	0.24
CaO	1.29	0.12	1.41	0.11	1.19	0.04	1.41	0.04	1.50	0.03	1.41	0.05	1.51	0.03	1.53	0.09	1.47	0.02	1.45	0.05
Na_2O	4.05	0.19	4.77	0.16	2.19	0.11	0.00	0.00	0.77	0.07	0.00	0.00	2.08	0.07	0.00	0.00	0.73	0.05	0.00	0.00
K_2O	6.06	0.13	3.96	0.10	5.20	0.07	7.67	0.07	6.77	0.06	8.74	0.11	4.62	0.07	7.15	0.13	6.50	0.06	8.66	0.12
Total	99.21	1.61	99.30	1.26	98.55	0.78	98.56	0.80	98.86	0.72	98.64	0.65	98.57	0.62	98.83	1.47	98.42	0.65	98.64	0.77
n	20		20		20		25		20		25		20		20		10		10	
Qz	20.79		27.47		39.82		42.43		41.35		36.87		42.96		45.87		43.09		37.26	
Ab	34.31		40.38		18.56		0.00		6.54		0.00		17.62		0.00		6.19		0.00	
Or	35.82		23.42		30.71		45.33		40.03		51.66		27.31		42.24		38.43		51.18	
An	6.36		6.48		5.90		6.98		7.09		6.92		7.49		7.57		7.07		7.19	
Cor[a]	-0.01		-0.20		0.02		0.14		-0.13		-0.03		0.20		0.17		-0.08		0.06	

n = number of analyses, Qz = normative quartz content calculated by CIPW-norm, Ab = albite , Or = orthoclase , An = anorthite, Cor = corundum

[a] negative corundum values reflect the amount of corundum that is missing to convert all available CaO to anorthite

Appendix Table 2: Continued

Name	DYX9		DYX10		DYX11		DYX12	
SM	HYS15		HYS16		HYS17		HYS18	
	[wt.%]	1σ	[wt.%]	1σ	[wt.%]	1σ	[wt.%]	1σ
SiO_2	77.84	0.27	77.20	0.34	76.89	0.35	74.61	0.31
TiO_2	0.42	0.01	0.42	0.02	0.41	0.01	0.41	0.02
Al_2O_3	11.19	0.08	10.32	0.10	10.94	0.15	12.13	0.07
FeO	1.59	0.10	2.08	0.10	1.85	0.08	1.59	0.06
CaO	1.49	0.05	1.53	0.03	1.43	0.04	1.43	0.03
Na_2O	2.11	0.13	0.00	0.00	0.72	0.07	0.00	0.00
K_2O	4.52	0.06	6.83	0.09	6.56	0.12	8.73	0.09
Total	99.16	0.70	98.39	0.69	98.80	0.81	98.89	0.58
n	21		20		10		10	
Qz	44.11		46.43		43.33		37.16	
Ab	17.82		0.00		6.08		0.00	
Or	26.72		40.37		38.79		51.57	
An	7.41		7.57		7.10		7.10	
Cor[a]	0.12		0.15		0.05		0.08	

n = number of analyses, Qz = normative quartz content calculated by CIPW-norm, Ab = albite , Or = orthoclase , An = anorthite, Cor = corundum

[a] negative corundum values reflect the amount of corundum that is missing to convert all available CaO to anorthite

Appendix Table 3 Glasscomposition of samples for system C

Name	YX57		YX58		YX59		YX60		YX61		YX62		YX63		YX64		YX73		YX74	
SM	AC 7		AC 50		BA 5		BC 5		BC 25		C		DC 5		D		AC7		AC50	
	[wt.%]	1σ	[wt.%]	1σ	[wt.%]	1σ	[wt.%]	1σ	[wt.%]	1σ	[wt.%]	1σ	[wt.%]	1σ	[wt.%]	1σ	[wt.%]	1σ	[wt.%]	1σ
SiO_2	74.68	0.29	74.45	0.25	74.47	0.17	74.57	0.31	73.54	0.23	72.47	0.20	72.95	0.20	74.53	0.41	73.30	0.27	74.27	0.26
TiO_2	0.20	0.01	0.20	0.01	0.22	0.01	0.20	0.02	0.19	0.01	0.20	0.01	0.20	0.01	0.21	0.02	0.23	0.01	0.21	0.02
Al_2O_3	11.72	0.11	11.89	0.12	11.96	0.10	12.25	0.10	12.51	0.10	12.91	0.10	13.26	0.10	12.93	0.11	12.38	0.13	12.17	0.12
FeO	0.70	0.06	0.58	0.11	0.70	0.06	0.58	0.06	0.70	0.06	0.70	0.06	0.69	0.05	0.72	0.06	1.09	0.04	0.69	0.06
CaO	0.69	0.03	0.66	0.02	0.72	0.03	0.68	0.02	0.66	0.03	0.67	0.02	0.68	0.02	0.50	0.02	0.93	0.02	0.69	0.03
Na_2O	1.66	0.10	1.68	0.09	2.95	0.10	2.85	0.13	2.30	0.09	1.81	0.10	3.27	0.09	4.46	0.18	1.88	0.07	1.66	0.08
K_2O	6.89	0.09	7.14	0.11	4.95	0.07	5.45	0.07	6.67	0.07	7.83	0.09	5.56	0.06	3.43	0.06	6.52	0.08	7.39	0.07
Total	96.55	0.69	96.59	0.71	95.96	0.55	96.57	0.70	96.57	0.59	96.60	0.60	96.61	0.54	96.78	0.85	96.33	0.62	97.08	0.64
n	20		20		20		20		20		20		20		20		20		20	
Qz	36.74		35.59		36.40		35.35		32.78		30.09		30.75		33.97		34.68		34.45	
Ab	14.09		14.22		24.96		24.09		19.46		15.31		27.71		37.74		15.89		14.03	
Or	40.69		42.18		29.26		32.24		39.41		46.30		32.84		20.25		38.55		43.66	
An	3.42		3.30		3.59		3.35		3.28		3.35		3.39		2.48		4.63		3.44	
Cor	0.28		0.19		0.43		0.43		0.31		0.22		0.61		0.98		0.53		0.18	

n = number of analyses, Qz = normative quartz content calculated by CIPW-norm, Ab = albite , Or = orthoclase , An = anorthite, Cor = corundum

Appendix Table 3: Continued

Name	YX75		YX76		YX77		YX78		YX79		YX80		YX81		YX83		YX84		YX85	
SM	BA5		BC5		BC25		C		DC5		D		AC7		BA5		BC5		C	
	[wt.%]	1σ	[wt.%]	1σ	[wt.%]	1σ	[wt.%]	1σ	[wt.%]	1σ	[wt.%]	1σ	[wt.%]	1σ	[wt.%]	1σ	[wt.%]	1σ	[wt.%]	1σ
SiO_2	73.99	0.33	74.08	0.27	73.92	0.28	73.18	0.19	72.86	0.21	74.17	0.31	75.71	0.28	76.13	0.33	75.63	0.19	72.58	0.22
TiO_2	0.22	0.02	0.20	0.01	0.19	0.02	0.21	0.02	0.21	0.02	0.23	0.02	0.21	0.02	0.21	0.02	0.20	0.02	0.21	0.02
Al_2O_3	12.39	0.12	12.56	0.14	12.66	0.11	12.51	0.15	13.17	0.13	12.70	0.13	12.11	0.09	11.65	0.12	12.33	0.13	13.15	0.09
FeO	0.78	0.08	0.67	0.07	0.65	0.04	0.69	0.11	0.71	0.12	0.83	0.11	0.74	0.05	0.79	0.07	0.81	0.07	0.79	0.03
CaO	0.77	0.04	0.70	0.03	0.67	0.02	0.72	0.03	0.66	0.02	0.44	0.02	0.69	0.04	0.69	0.04	0.65	0.04	0.67	0.03
Na_2O	2.90	0.12	2.83	0.12	2.32	0.12	1.78	0.09	3.23	0.09	4.29	0.11	1.69	0.08	2.70	0.10	2.76	0.11	1.79	0.05
K_2O	5.24	0.06	5.72	0.06	6.85	0.08	7.46	0.08	5.75	0.07	3.73	0.05	7.17	0.07	4.85	0.07	5.48	0.05	8.08	0.04
Total	96.29	0.77	96.74	0.69	97.27	0.66	96.56	0.67	96.59	0.66	96.40	0.75	98.32	0.62	97.02	0.75	97.86	0.60	97.27	0.48
n	20		20		10		19		20		19		19		20		10		10	
Qz	34.95		33.86		32.36		32.32		30.23		33.48		36.54		39.85		36.71		29.29	
Ab	24.52		23.92		19.64		15.08		27.31		36.34		14.26		22.88		23.32		15.17	
Or	30.97		33.79		40.51		44.06		34.01		22.02		42.37		28.69		32.41		47.77	
An	3.84		3.45		3.32		3.59		3.26		2.18		3.41		3.43		3.23		3.31	
Cor	0.54		0.45		0.21		0.20		0.44		0.80		0.33		0.69		0.68		0.24	

n = number of analyses, Qz = normative quartz content calculated by CIPW-norm, Ab = albite , Or = orthoclase , An = anorthite, Cor = corundum

Table 3: Continued

Name	YX86	
SM	D	
	[wt.%]	1σ
SiO_2	74.48	0.28
TiO_2	0.20	0.01
Al_2O_3	13.59	0.08
FeO	0.73	0.07
CaO	0.63	0.03
Na_2O	4.69	0.12
K_2O	3.27	0.04
Total	97.59	0.63
n	20	
Qz	32.85	
Ab	39.70	
Or	19.35	
An	3.14	
Cor	1.18	

n = number of analyses, Qz = normative quartz content calculated by CIPW-norm, Ab = albite , Or = orthoclase , An = anorthite, Cor = corundum

Appendix Table 4: Glasscomposition of samples for system D

Name	YX106		YX107		YX108		YX109		YX110		YX111		YX112		YX113		YX114		YX115	
SM	HYW 1		HYW 2		HYW 3		HYW 4		HYW 5		HYW 6		HYW 7		HYW 8		HYW 1		HYW 2	
	[wt.%]	1σ	[wt.%]	1σ	[wt.%]	1σ	[wt.%]	1σ	[wt.%]	1σ	[wt.%]	1σ	[wt.%]	1σ	[wt.%]	1σ	[wt.%]	1σ	[wt.%]	1σ
SiO_2	76.74	0.26	76.53	0.21	73.02	0.24	76.44	0.26	76.18	0.29	75.96	0.29	76.57	0.29	74.41	0.23	77.47	0.23	76.80	0.30
TiO_2	0.25	0.01	0.24	0.01	0.22	0.02	0.22	0.02	0.22	0.01	0.22	0.02	0.22	0.02	0.23	0.02	0.23	0.02	0.23	0.02
Al_2O_3	12.29	0.10	11.53	0.11	13.80	0.12	11.53	0.06	12.21	0.09	12.07	0.09	11.19	0.14	13.97	0.14	11.73	0.08	11.06	0.10
FeO	0.69	0.11	0.84	0.08	0.48	0.06	0.45	0.06	0.70	0.08	0.48	0.11	0.63	0.06	0.65	0.07	0.32	0.07	0.73	0.06
CaO	0.81	0.03	0.80	0.03	0.68	0.02	0.67	0.02	0.71	0.03	0.68	0.02	0.69	0.02	0.62	0.02	0.78	0.03	0.77	0.03
Na_2O	3.82	0.08	1.28	0.07	2.28	0.09	0.05	0.03	2.79	0.10	1.76	0.05	0.62	0.07	4.93	0.12	3.44	0.10	1.17	0.06
K_2O	4.16	0.08	7.11	0.07	7.93	0.09	8.66	0.07	5.74	0.06	7.19	0.07	7.71	0.08	4.43	0.05	3.96	0.07	6.76	0.09
Total	98.76	0.65	98.33	0.58	98.41	0.64	98.02	0.51	98.56	0.67	98.37	0.65	97.63	0.67	99.23	0.64	97.93	0.58	97.52	0.66
n	17		20		20		20		20		20		20		17		17		20	
Qz	36.50		39.65		27.74		41.37		36.07		36.51		41.61		27.14		40.53		42.03	
Ab	32.32		10.81		19.26		0.42		23.59		14.88		5.27		41.70		29.09		9.88	
Or	24.57		42.02		46.87		51.16		33.91		42.51		45.56		26.17		23.42		39.98	
An	4.02		3.99		3.37		3.34		3.52		3.38		3.42		2.91		3.88		3.84	
Cor[a]	0.04		0.27		0.24		0.86		0.13		0.15		0.56		-0.06		0.36		0.41	

n = number of analyses, Qz = normative quartz content calculated by CIPW-norm, Ab = albite , Or = orthoclase , An = anorthite, Cor = corundum

[a] negative corundum values reflect the amount of corundum that is missing to convert all available CaO to anorthite

Appendix Table 4: Continued

Name	YX116		YX117		YX118		YX119		YX120		YX121		YX138		YX139		YX140		YX141	
SM	HYW 3		HYW 4		HYW 5		HYW 6		HYW 7		HYW 8		HYW 1		HYW 2		HYW 3		HYW 4	
	[wt.%]	1σ	[wt.%]	1σ	[wt.%]	1σ	[wt.%]	1σ	[wt.%]	1σ	[wt.%]	1σ	[wt.%]	1σ	[wt.%]	1σ	[wt.%]	1σ	[wt.%]	1σ
SiO_2	76.50	0.34	76.81	0.25	76.53	0.24	76.05	0.26	77.71	0.22	74.12	0.32	75.59	0.34	75.66	0.27	73.04	0.23	76.04	0.22
TiO_2	0.21	0.02	0.20	0.01	0.21	0.02	0.20	0.01	0.20	0.01	0.21	0.02	0.23	0.01	0.23	0.02	0.21	0.02	0.21	0.02
Al_2O_3	11.58	0.09	11.57	0.11	12.18	0.12	12.08	0.11	10.90	0.08	14.13	0.12	12.51	0.12	11.88	0.11	13.83	0.13	11.94	0.09
FeO	0.49	0.05	0.40	0.06	0.58	0.07	0.49	0.09	0.54	0.06	0.56	0.06	0.75	0.13	0.69	0.13	0.81	0.06	0.48	0.06
CaO	0.67	0.02	0.67	0.02	0.71	0.03	0.70	0.02	0.69	0.02	0.72	0.03	0.83	0.03	0.79	0.02	0.70	0.02	0.68	0.02
Na_2O	0.06	0.03	0.06	0.03	2.65	0.09	1.67	0.04	0.59	0.05	4.76	0.17	3.68	0.12	1.25	0.06	2.18	0.10	0.05	0.03
K_2O	8.55	0.08	8.64	0.09	5.74	0.07	7.14	0.08	7.49	0.07	4.33	0.06	4.29	0.06	7.37	0.08	7.78	0.09	8.89	0.08
Total	98.06	0.64	98.36	0.57	98.59	0.64	98.33	0.62	98.10	0.51	98.83	0.76	97.88	0.80	97.87	0.69	98.53	0.64	98.30	0.53
n	19		20		20		20		20		20		20		20		20		20	
Qz	41.75		41.73		37.32		37.27		43.85		28.03		35.55		38.07		28.60		39.99	
Ab	0.50		0.55		22.42		14.13		4.98		40.25		31.16		10.57		18.42		0.45	
Or	50.53		51.08		33.90		42.17		44.24		25.58		25.33		43.58		45.95		52.53	
An	3.31		3.33		3.52		3.46		3.43		3.56		4.10		3.94		3.49		3.39	
Cor[a]	1.02		0.89		0.32		0.34		0.57		0.32		0.32		0.40		0.55		0.99	

n = number of analyses, Qz = normative quartz content calculated by CIPW-norm, Ab = albite , Or = orthoclase , An = anorthite, Cor = corundum

[a] negative corundum values reflect the amount of corundum that is missing to convert all available CaO to anorthite

Appendix Table 4: Continued

Name	YX142		YX143		YX144		YX145		YX154		YX155		YX156		YX157		YX158		YX159	
SM	HYW 5		HYW 6		HYW 7		HYW 8		HYW3+5		HYW3+6		HYW3+8		HYW5+8		HYW3		HYW5	
	[wt.%]	1σ	[wt.%]	1σ	[wt.%]	1σ	[wt.%]	1σ	[wt.%]	1σ	[wt.%]	1σ	[wt.%]	1σ	[wt.%]	1σ	[wt.%]	1σ	[wt.%]	1σ
SiO_2	75.68	0.30	76.01	0.30	76.05	0.29	74.70	0.27	75.10	0.18	75.22	0.34	74.98	0.52	75.66	0.24	75.09	0.30	75.57	0.28
TiO_2	0.21	0.01	0.21	0.02	0.21	0.01	0.22	0.02	0.21	0.02	0.22	0.01	0.23	0.03	0.24	0.01	0.24	0.02	0.23	0.01
Al_2O_3	12.58	0.11	12.06	0.10	11.66	0.11	13.34	0.13	13.04	0.13	12.93	0.14	13.34	0.39	12.90	0.21	13.16	0.12	12.87	0.18
FeO	0.55	0.13	0.57	0.21	0.68	0.09	0.89	0.08	0.92	0.07	0.89	0.08	1.01	0.10	0.89	0.09	0.98	0.04	1.02	0.05
CaO	0.71	0.03	0.69	0.04	0.74	0.03	0.50	0.02	0.70	0.03	0.69	0.03	0.55	0.06	0.51	0.06	0.71	0.04	0.67	0.04
Na_2O	2.76	0.11	1.64	0.08	0.61	0.06	4.29	0.10	2.38	0.11	1.88	0.10	3.15	0.18	3.49	0.08	2.21	0.07	2.76	0.08
K_2O	5.92	0.09	7.12	0.10	8.01	0.08	4.57	0.08	6.86	0.07	7.50	0.10	6.11	0.12	5.41	0.08	7.17	0.09	6.24	0.07
Total	98.41	0.78	98.30	0.83	97.96	0.68	98.52	0.69	99.21	0.61	99.34	0.81	99.37	1.40	99.11	0.77	99.56	0.68	99.36	0.72
n	20		20		20		19		15		15		12		10		15		15	
Qz	35.16		37.40		39.85		30.60		32.92		33.54		31.45		33.03		32.66		33.50	
Ab	23.35		13.88		5.19		36.31		20.15		15.92		26.62		29.50		18.70		23.39	
Or	34.98		42.10		47.32		27.03		40.52		44.31		36.11		31.98		42.36		36.89	
An	3.51		3.43		3.65		2.49		3.47		3.43		2.75		2.53		3.53		3.34	
Cor[a]	0.35		0.39		0.65		0.42		0.43		0.46		0.55		0.38		0.48		0.34	

n = number of analyses, Qz = normative quartz content calculated by CIPW-norm, Ab = albite , Or = orthoclase , An = anorthite, Cor = corundum

[a] negative corundum values reflect the amount of corundum that is missing to convert all available CaO to anorthite

Appendix Table 4: Continued

Name	YX160		YX161		YX162		YX163		YX164		YX165		YX166		YX167		YX168		YX169	
SM	HYW6		HYW8		HYW3+5		HYW3+6		HYW3+8		HYW5+8		HYW3		HYW5		HYW6		HYW8	
	[wt.%]	1σ	[wt.%]	1σ	[wt.%]	1σ	[wt.%]	1σ	[wt.%]	1σ	[wt.%]	1σ	[wt.%]	1σ	[wt.%]	1σ	[wt.%]	1σ	[wt.%]	1σ
SiO_2	75.76	0.30	75.36	0.26	75.09	0.30	75.03	0.31	74.97	0.36	75.46	0.21	74.67	0.33	75.42	0.18	75.36	0.18	75.01	0.46
TiO_2	0.23	0.02	0.26	0.01	0.26	0.02	0.26	0.01	0.25	0.02	0.25	0.02	0.27	0.02	0.27	0.01	0.25	0.02	0.26	0.04
Al_2O_3	12.58	0.11	13.14	0.32	12.87	0.09	12.79	0.21	13.23	0.35	12.77	0.08	13.05	0.18	12.76	0.14	12.64	0.13	13.34	0.50
FeO	0.91	0.06	1.08	0.10	1.10	0.06	1.02	0.09	1.03	0.10	1.12	0.10	1.19	0.08	1.23	0.08	0.99	0.08	1.18	0.18
CaO	0.71	0.03	0.46	0.07	0.69	0.04	0.77	0.03	0.52	0.06	0.48	0.03	0.74	0.03	0.63	0.04	0.80	0.04	0.50	0.11
Na_2O	1.68	0.06	4.12	0.21	2.46	0.11	2.00	0.08	3.24	0.16	3.38	0.11	2.22	0.10	2.76	0.13	1.75	0.09	4.24	0.28
K_2O	7.46	0.09	4.75	0.09	6.59	0.06	7.04	0.13	6.07	0.13	5.61	0.10	6.87	0.21	6.31	0.10	7.30	0.07	4.83	0.30
Total	99.31	0.68	99.17	1.07	99.05	0.68	98.93	0.86	99.30	1.17	99.07	0.65	99.01	0.95	99.37	0.70	99.09	0.60	99.36	1.87
n	15		11		8		10		12		10		14		10		15		7	
Qz	35.33		31.53		33.39		34.13		31.16		32.55		33.13		33.10		34.90		30.02	
Ab	14.22		34.90		20.79		16.96		27.37		28.63		18.76		23.32		14.84		35.89	
Or	44.11		28.06		38.94		41.61		35.85		33.16		40.60		37.27		43.13		28.55	
An	3.50		2.27		3.43		3.83		2.59		2.38		3.69		3.12		3.97		2.48	
Cor[a]	0.45		0.39		0.43		0.47		0.39		0.25		0.62		0.26		0.40		0.23	

n = number of analyses, Qz = normative quartz content calculated by CIPW-norm, Ab = albite , Or = orthoclase , An = anorthite, Cor = corundum

[a] negative corundum values reflect the amount of corundum that is missing to convert all available CaO to anorthite

Appendix Table 5 Glasscomposition of samples for system E

Name	YX33		YX34		YX35		YX36		YX37		YX38		YX39		YX40		YX41		YX42	
SM	HYS1		HYS2		HYS3		HYS4		HYS5		HYS6		HYS7		HYS8		HYS1		HYS2	
	[wt.%]	1σ	[wt.%]	1σ	[wt.%]	1σ	[wt.%]	1σ	[wt.%]	1σ	[wt.%]	1σ	[wt.%]	1σ	[wt.%]	1σ	[wt.%]	1σ	[wt.%]	1σ
SiO_2	75.70	0.34	75.16	0.38	71.71	0.48	75.36	0.43	73.35	0.54	70.86	0.32	71.14	0.46	73.87	0.41	74.28	0.26	73.96	0.27
TiO_2	0.44	0.06	0.40	0.04	0.42	0.04	0.42	0.04	0.42	0.04	0.45	0.03	0.45	0.03	0.42	0.03	0.50	0.03	0.42	0.02
Al_2O3	12.84	0.26	12.25	0.29	14.87	0.28	12.68	0.21	13.43	0.32	15.51	0.20	15.06	0.26	13.94	0.31	12.61	0.07	12.44	0.10
FeO	1.69	0.18	1.83	0.18	1.10	0.10	1.63	0.24	1.52	0.19	0.95	0.33	1.18	0.18	1.14	0.12	2.11	0.15	1.66	0.11
CaO	1.18	0.10	1.44	0.12	1.35	0.10	1.35	0.10	1.40	0.10	1.04	0.06	1.12	0.12	1.20	0.08	1.00	0.05	1.50	0.03
Na_2O	3.90	0.14	1.44	0.11	2.45	0.17	2.75	0.13	1.95	0.13	5.31	0.21	3.91	0.18	4.51	0.21	3.80	0.15	1.54	0.06
K_2O	3.84	0.11	6.75	0.11	7.41	0.12	5.36	0.12	6.99	0.11	5.04	0.09	6.29	0.10	4.11	0.06	4.32	0.07	6.89	0.08
Total	99.59	1.19	99.28	1.22	99.31	1.28	99.56	1.27	99.07	1.42	99.16	1.24	99.15	1.34	99.21	1.21	98.61	0.77	98.42	0.67
n	19		19		18		17		17		15		18		18		20		20	
Qz	34.77		36.70		25.63		34.99		31.32		18.33		21.44		28.78		32.26		34.57	
Ab	32.96		12.20		20.72		23.31		16.51		44.96		33.08		38.16		32.14		13.00	
Or	22.70		39.91		43.79		31.67		41.33		29.80		37.18		24.31		25.53		40.72	
An	5.87		7.00		6.71		6.40		6.95		3.57		4.96		5.65		4.59		6.69	
Cor[a]	0.12		-0.05		0.36		-0.11		0.11		-0.58		-0.21		-0.12		-0.14		-0.28	

n = number of analyses, Qz = normative quartz content calculated by CIPW-norm, Ab = albite , Or = orthoclase , An = anorthite, Cor = corundum

[a] negative corundum values reflect the amount of corundum that is missing to convert all available CaO to anorthite

Appendix Table 5: Continued

Name	YX43		YX44		YX45		YX46		YX47		YX48		YX49		YX50		YX51		YX52	
SM	HYS3		HYS4		HYS5		HYS6		HYS7		HYS8		HYS1		HYS2		HYS3		HYS4	
	[wt.%]	1σ	[wt.%]	1σ	[wt.%]	1σ	[wt.%]	1σ	[wt.%]	1σ	[wt.%]	1σ	[wt.%]	1σ	[wt.%]	1σ	[wt.%]	1σ	[wt.%]	1σ
SiO_2	71.20	0.27	73.80	0.23	73.20	0.24	70.08	0.34	71.21	0.38	73.53	0.33	75.67	0.45	75.48	0.17	71.53	0.18	75.59	0.28
TiO_2	0.46	0.02	0.46	0.02	0.43	0.02	0.50	0.03	0.50	0.02	0.46	0.03	0.46	0.03	0.43	0.02	0.45	0.01	0.43	0.02
Al_2O3	14.14	0.12	12.51	0.14	13.31	0.14	14.82	0.27	14.35	0.11	13.19	0.21	12.68	0.11	12.04	0.11	14.77	0.10	12.35	0.10
FeO	1.21	0.16	1.97	0.12	0.86	0.06	1.83	0.34	1.42	0.18	1.43	0.26	1.11	0.25	1.19	0.09	0.89	0.06	1.30	0.07
CaO	1.11	0.04	1.20	0.05	1.31	0.04	1.01	0.08	0.98	0.04	1.06	0.06	1.34	0.05	1.46	0.05	1.40	0.04	1.44	0.04
Na_2O	2.29	0.10	2.65	0.10	1.91	0.07	4.95	0.22	3.67	0.14	4.31	0.12	3.88	0.14	1.45	0.11	2.38	0.07	2.71	0.09
K_2O	7.48	0.06	5.80	0.08	7.07	0.10	5.08	0.14	6.28	0.08	4.23	0.07	3.50	0.09	6.59	0.06	7.26	0.06	5.05	0.05
Total	97.90	0.78	98.40	0.75	98.09	0.66	98.28	1.42	98.41	0.95	98.21	1.08	98.63	1.12	98.64	0.60	98.68	0.52	98.86	0.64
n	20		16		10		13		25		25		20		10		10		20	
Qz	26.20		32.52		31.85		18.93		23.10		29.42		36.27		38.09		26.53		36.79	
Ab	19.40		22.46		16.15		41.92		31.05		36.44		32.84		12.29		20.14		22.96	
Or	44.22		34.30		41.76		30.03		37.12		25.03		20.66		38.98		42.88		29.82	
An	5.51		5.08		6.52		3.19		4.14		4.15		6.66		6.86		6.93		6.61	
Cor[a]	0.25		-0.32		0.14		-0.67		-0.26		-0.41		0.07		-0.14		0.47		-0.20	

n = number of analyses, Qz = normative quartz content calculated by CIPW-norm, Ab = albite , Or = orthoclase , An = anorthite, Cor = corundum

[a] negative corundum values reflect the amount of corundum that is missing to convert all available CaO to anorthite

Appendix Table 5: Continued

Name	YX53		YX54		YX55		YX56		YX65		YX66		YX67		YX68		YX69		YX70	
SM	HYS5		HYS6		HYS7		HYS8		HYS17		HYS18		HYS19		HYS20		HYS21		HYS23	
	[wt.%]	1σ	[wt.%]	1σ	[wt.%]	1σ	[wt.%]	1σ	[wt.%]	1σ	[wt.%]	1σ	[wt.%]	1σ	[wt.%]	1σ	[wt.%]	1σ	[wt.%]	1σ
SiO_2	72.83	0.21	69.83	0.20	70.58	0.30	72.66	0.22	75.01	0.24	74.70	0.39	74.46	0.44	72.16	0.28	73.16	0.23	75.27	0.40
TiO_2	0.40	0.02	0.45	0.02	0.45	0.02	0.42	0.02	0.45	0.02	0.42	0.02	0.42	0.02	0.45	0.02	0.44	0.02	0.48	0.02
Al_2O3	13.23	0.09	15.93	0.16	15.37	0.11	14.33	0.10	11.61	0.13	12.00	0.10	11.86	0.12	13.13	0.18	13.38	0.14	12.32	0.17
FeO	1.31	0.04	1.09	0.07	0.80	0.09	0.99	0.07	1.60	0.09	0.99	0.35	1.44	0.33	1.71	0.10	1.65	0.06	1.49	0.14
CaO	1.43	0.03	1.20	0.04	1.26	0.04	1.40	0.03	1.58	0.03	1.39	0.06	1.39	0.07	1.40	0.03	1.41	0.03	1.61	0.03
Na_2O	1.96	0.10	5.33	0.18	3.99	0.13	4.66	0.12	0.77	0.05	0.05	0.03	0.74	0.05	1.18	0.09	2.95	0.09	3.75	0.14
K_2O	6.94	0.06	4.81	0.07	6.06	0.09	3.90	0.08	7.02	0.07	8.77	0.11	7.60	0.09	7.91	0.10	5.21	0.06	2.70	0.05
Total	98.10	0.56	98.65	0.73	98.52	0.78	98.36	0.64	98.05	0.63	98.32	1.06	97.91	1.13	97.95	0.81	98.21	0.64	97.63	0.95
n	10		20		20		20		20		18		11		10		10		18	
Qz	31.12		17.42		21.19		27.19		39.39		37.44		37.29		30.95		32.05		38.84	
Ab	16.58		45.08		33.75		39.45		6.52		0.39		6.27		10.02		24.94		31.73	
Or	40.99		28.45		35.82		23.03		41.48		51.86		44.92		46.74		30.80		15.96	
An	6.82		5.32		6.13		6.66		7.49		6.63		6.59		6.96		6.99		7.96	
Cor[a]	-0.11		-0.24		-0.05		-0.11		-0.13		-0.09		-0.11		0.07		0.33		0.31	

n = number of analyses, Qz = normative quartz content calculated by CIPW-norm, Ab = albite , Or = orthoclase , An = anorthite, Cor = corundum

[a] negative corundum values reflect the amount of corundum that is missing to convert all available CaO to anorthite

Appendix Table 5: Continued

Name	YX71		YX72		YX87		YX88		YX89	
SM	HYS24		HYS25		HYS5		HYS19		HYS20	
	[wt.%]	1σ	[wt.%]	1σ	[wt.%]	1σ	[wt.%]	1σ	[wt.%]	1σ
SiO_2	75.75	0.31	75.93	0.32	74.02	0.20	73.67	0.23	74.24	0.64
TiO_2	0.51	0.05	0.51	0.05	0.43	0.11	0.34	0.03	0.44	0.16
Al_2O3	12.86	0.10	12.70	0.19	12.54	0.08	12.23	0.11	12.54	0.27
FeO	1.47	0.10	1.49	0.17	1.86	0.15	1.95	0.15	1.63	0.20
CaO	1.14	0.04	1.25	0.04	1.10	0.04	1.42	0.04	1.22	0.18
Na_2O	5.88	0.20	5.74	0.19	1.81	0.09	0.82	0.06	1.23	0.08
K_2O	0.00	0.00	0.00	0.00	7.01	0.08	7.86	0.10	7.63	0.22
Total	97.62	0.79	97.63	0.96	98.76	0.75	98.28	0.73	98.92	1.75
n	18		11		19		14		14	
Qz	38.28		39.02		33.16		34.59		34.31	
Ab	49.78		48.60		15.28		6.94		10.37	
Or	0.00		0.00		41.43		46.43		45.08	
An	5.65		6.20		5.42		6.48		6.06	
Cor[a]	1.11		0.98		-0.01		-0.20		0.04	

n = number of analyses, Qz = normative quartz content calculated by CIPW-norm, Ab = albite , Or = orthoclase , An = anorthite, Cor = corundum

[a] negative corundum values reflect the amount of corundum that is missing to convert all available CaO to anorthite

Appendix Table 6 – Composition of feldspars from this study (Systems A – E)

Name	YX1		YX2		YX3		YX4		YX5		YX6		YX7		YX8		YX9		YX11		YX12	
SM	HYS1		HYS2		HYS3		HYS4		HYS5		HYS6		HYS7		HYS8		HYS1		HYS3		HYS4	
	[wt.%]	1σ	[wt.%]	1σ	[wt.%]	1σ	[wt.%]	1σ	[wt.%]	1σ	[wt.%]	1σ	[wt.%]	1σ	[wt.%]	1σ	[wt.%]	1σ	[wt.%]	1σ	[wt.%]	1σ
SiO_2	70.88	0.90	55.57	1.67	57.66	1.35	70.52	1.49	56.37	1.17	64.95	0.25	62.95	0.11	64.16	0.74	62.38	0.16	57.98	0.40	58.17	0.63
TiO_2	0.27	0.03	0.08	0.05	0.07	0.01	0.19	0.09	0.04	0.02	0.09	0.01	0.08	0.00	0.08	0.04	0.08	0.01	0.06	0.02	0.05	0.00
Al_2O_3	16.75	0.59	27.76	1.40	24.49	0.92	16.75	0.82	27.68	0.83	21.98	0.05	23.12	0.46	22.51	1.07	23.74	0.86	25.88	0.78	26.37	0.18
FeO	1.55	0.11	0.81	0.20	0.47	0.19	1.08	0.31	0.61	0.10	0.36	0.06	0.38	0.02	0.48	0.13	0.47	0.01	0.39	0.04	0.58	0.02
CaO	3.00	0.45	12.28	0.89	7.44	0.90	4.68	0.21	10.98	0.51	3.19	0.18	4.75	0.06	4.73	0.51	6.71	0.18	9.09	0.45	9.80	0.35
Na_2O	4.06	0.66	3.39	0.09	4.86	0.20	3.91	0.43	4.19	0.25	8.42	0.10	6.99	0.15	7.74	0.37	6.96	0.27	4.99	0.08	5.22	0.25
K_2O	2.29	0.42	1.22	0.34	3.22	1.11	2.49	0.85	1.43	0.29	2.41	0.06	3.00	0.07	1.26	0.25	0.82	0.14	2.13	0.26	0.87	0.10
Total	98.81		101.10		98.19		99.62		101.30		101.40		101.28		100.96		101.17		100.53		101.04	
n	4		5		4		3		4		3		3		3		2		3		3	
An	28.4		61.8		37.1		31.8		54.2		15.0		22.6		23.4		33.1		44.0		48.3	
Ab	62.9		30.9		43.8		48.1		37.4		71.6		60.3		69.2		62.1		43.7		46.6	
Or	8.6		7.3		19.1		20.1		8.4		13.5		17.0		7.4		4.8		12.3		5.1	

n = number of analyses

An = anorthite component, Ab = albite component, Or= orthoclase component

Table 6: Continued

Name	YX13		YX14		YX15		YX16		YX17		YX19		YX22		YX23		YX24		YX27		YX30	
SM	HYS5		HYS6		HYS7		HYS8		HYS1		HYS3		HYS6		HYS7		HYS8		HYS3		HYS6	
	[wt.%]	1σ	[wt.%]	1σ	[wt.%]	1σ	[wt.%]	1σ	[wt.%]	1σ	[wt.%]	1σ	[wt.%]	1σ	[wt.%]	1σ	[wt.%]	1σ	[wt.%]	1σ	[wt.%]	1σ
SiO_2	54.13	0.43	64.74	0.48	63.54	0.81	64.18	0.53	59.18	0.71	55.24	0.49	63.30	0.59	61.61	0.53	62.49	0.99	57.67		62.72	0.21
TiO_2	0.04	0.03	0.10	0.01	0.14	0.06	0.12	0.03	0.07	0.02	0.06	0.01	0.08	0.01	0.12	0.02	0.09	0.02	0.09		0.09	0.04
Al_2O_3	28.79	0.45	22.48	0.21	22.38	1.06	22.40	0.60	25.93	0.65	27.97	0.24	23.21	0.24	23.58	0.38	23.63	0.65	27.33		23.36	0.49
FeO	0.54	0.05	0.31	0.09	0.50	0.16	0.45	0.04	0.44	0.04	0.30	0.07	0.27	0.04	0.53	0.01	0.42	0.06	0.08		0.27	0.08
CaO	12.41	0.36	3.66	0.17	4.97	0.52	5.05	0.35	8.75	0.49	11.11	0.25	4.56	0.26	6.24	0.50	6.26	0.44	10.37		5.29	0.34
Na_2O	3.69	0.16	8.10	0.10	6.47	0.63	7.25	0.51	6.32	0.13	4.40	0.27	8.24	0.06	6.32	0.02	7.08	0.13	3.86		7.77	0.23
K_2O	1.06	0.09	2.00	0.11	2.82	0.34	1.28	0.19	0.45	0.09	1.31	0.05	1.53	0.10	2.11	0.23	1.03	0.17	1.98		1.31	0.15
Total	100.66		101.38		100.82		100.73		101.13		100.39		101.21		100.51		100.99		101.37		100.80	
n	3		5		5		3		5		3		4		3		5		1		5	
An	61.0		17.7		24.8		25.7		42.2		53.9		21.4		30.9		30.8		52.6		25.3	
Ab	32.8		70.8		58.4		66.6		55.2		38.6		70.0		56.7		63.2		35.4		67.3	
Or	6.2		11.5		16.8		7.7		2.6		7.6		8.6		12.4		6.0		12.0		7.5	

n = number of analyses

An = anorthite component, Ab = albite component, Or= orthoclase component

Table 6: Continued

Name	YX31		DYX1		DYX2		DYX4		YX33		YX35		YX36		YX38		YX39		YX40		YX41	
SM	HYS7		HYS15		HYS16		HYS18		HYS1		HYS3		HYS4		HYS6		HYS7		HYS8		HYS1	
	[wt.%]	1σ	[wt.%]	1σ	[wt.%]	1σ	[wt.%]	1σ	[wt.%]	1σ	[wt.%]	1σ	[wt.%]	1σ	[wt.%]	1σ	[wt.%]	1σ	[wt.%]	1σ	[wt.%]	1σ
SiO_2	58.54	0.42	67.55		54.79	0.40	52.26	0.35	68.06	0.95	57.17	0.96	63.46	1.27	64.60	0.44	62.09	0.46	63.89	0.46	71.64	1.46
TiO_2	0.05	0.01	0.07		0.06	0.03	0.10	0.02	0.27	0.11	0.07	0.04	0.10	0.06	0.08	0.03	0.08	0.02	0.09	0.02	0.27	0.02
Al_2O_3	26.10	0.28	20.27		28.12	0.25	28.77	0.49	19.44	0.68	26.59	0.97	22.41	1.15	21.94	0.50	23.58	0.49	22.56	0.68	15.97	0.19
FeO	0.24	0.04	0.52		0.95	0.08	0.90	0.17	0.40	0.37	0.12	0.08	0.31	0.04	0.20	0.06	0.26	0.05	0.33	0.06	1.11	0.36
CaO	8.40	0.32	7.90		15.70	0.44	15.15	0.06	4.55	0.89	9.76	0.53	7.51	0.67	3.53	0.28	5.51	0.37	5.01	0.29	2.78	0.15
Na_2O	6.24	0.18	3.54		0.06	0.02	0.07	0.01	5.73	0.74	4.54	0.32	5.16	0.41	8.33	0.27	6.80	0.22	7.63	0.24	5.25	0.29
K_2O	1.11	0.07	0.60		1.17	0.59	2.41	0.06	1.62	0.65	1.91	0.40	1.47	0.57	2.07	0.17	2.28	0.17	1.25	0.12	2.42	0.49
Total	100.68		100.44		100.85		99.65		100.08		100.16		100.42		100.76		100.60		100.75		99.44	
n	5		1		3		3		3		4		5		6		5		5		3	
An	40.0		52.6		91.3		83.5		27.0		48.2		40.4		16.7		26.8		24.7		18.4	
Ab	53.8		42.6		0.7		0.7		61.5		40.6		50.2		71.5		60.0		68.0		62.6	
Or	6.3		4.7		8.1		15.8		11.5		11.2		9.4		11.7		13.2		7.3		19.0	

n = number of analyses

An = anorthite component, Ab = albite component, Or= orthoclase component

Table 6: Continued

Name	YX43		YX44		YX46		YX47		YX48		YX49		YX54		YX55		YX56		YX62		YX64	
SM	HYS3		HYS4		HYS6		HYS7		HYS8		HYS1		HYS6		HYS7		HYS8		C		D	
	[wt.%]	1σ	[wt.%]	1σ	[wt.%]	1σ	[wt.%]	1σ	[wt.%]	1σ	[wt.%]	1σ	[wt.%]	1σ	[wt.%]	1σ	[wt.%]	1σ	[wt.%]	1σ	[wt.%]	1σ
SiO_2	59.40	0.76	73.25	1.53	65.08	0.55	63.94	0.40	65.39	1.23	67.38	0.98	63.92	0.22	60.22	0.77	60.84	0.13	65.31	0.20	67.38	0.34
TiO_2	0.07	0.01	0.30	0.01	0.08	0.02	0.07	0.00	0.10	0.04	0.06	0.01	0.09	0.01	0.05	0.01	0.05	0.01	0.03	0.01	0.05	0.02
Al_2O_3	24.81	0.54	14.55	1.58	21.12	0.51	21.86	0.15	21.15	0.61	20.36	0.96	22.18	0.23	24.78	0.33	24.58	0.23	18.69	0.12	20.98	0.46
FeO	0.32	0.02	1.24	0.02	0.31	0.09	0.25	0.05	0.44	0.15	0.31	0.07	0.19	0.04	0.20	0.02	0.21	0.07	0.12	0.04	0.24	0.02
CaO	7.50	0.36	2.81	0.30	2.83	0.27	3.91	0.34	4.01	0.28	6.31	0.51	4.08	0.17	6.97	0.12	6.92	0.24	0.18	0.02	2.64	0.12
Na_2O	4.97	0.28	3.30	0.33	8.27	0.25	6.80	0.05	7.93	0.46	5.70	0.15	8.25	0.14	6.67	0.11	7.36	0.11	1.23	0.02	8.17	0.25
K_2O	3.31	0.27	3.89	0.11	2.61	0.25	3.85	0.28	1.56	0.21	0.59	0.07	1.78	0.10	1.51	0.13	0.73	0.04	14.38	0.08	1.18	0.09
Total	100.39		99.33		100.31		100.68		100.57		100.71		100.50		100.41		100.68		99.94		100.64	
n	5		2		5		3		3		3		3		4		3		5		4	
An	36.7		20.9		13.5		18.8		19.8		36.4		19.3		33.4		32.8		0.9		14.0	
Ab	44.0		44.5		71.6		59.2		71.0		59.5		70.7		57.9		63.1		11.4		78.5	
Or	19.3		34.6		14.9		22.0		9.2		4.1		10.0		8.6		4.1		87.7		7.4	

n = number of analyses

An = anorthite component, Ab = albite component, Or= orthoclase component

Table 6: Continued

Name	YX71		YX72		YX73		YX74		YX78		YX79		YX80		YX86		YX87		YX88		YX89	
SM	HYS 24		HYS 25		AC7		AC50		C		DC5		D		D		HYS 5		HYS 19		HYS 20	
	[wt.%]	1σ	[wt.%]	1σ	[wt.%]	1σ	[wt.%]	1σ	[wt.%]	1σ	[wt.%]	1σ	[wt.%]	1σ	[wt.%]	1σ	[wt.%]	1σ	[wt.%]	1σ	[wt.%]	1σ
SiO_2	66.79	0.47	70.15	0.51	76.25	0.36	66.21	0.48	66.19	0.55	63.75	0.08	68.24	0.14	63.59	0.23	64.36	0.27	64.66	0.31	65.89	0.58
TiO_2	0.10	0.03	0.16	0.02	0.09	0.01	0.03	0.01	0.05	0.02	0.02	0.01	0.04	0.01	0.03	0.01	0.07	0.02	0.09	0.05	0.16	0.03
Al_2O_3	21.03	0.33	18.90	0.68	13.10	0.24	18.22	0.32	17.84	0.45	22.56	0.37	20.18	0.42	22.82	0.22	19.02	0.10	18.38	0.15	17.12	0.40
FeO	0.43	0.07	0.40	0.04	0.11	0.01	0.12	0.01	0.18	0.04	0.20	0.05	0.26	0.01	0.19	0.03	0.21	0.04	0.48	0.30	0.58	0.17
CaO	3.52	0.09	3.54	0.16	0.12	0.01	0.18	0.06	0.17	0.06	4.13	0.43	2.18	0.03	4.16	0.11	0.83	0.09	0.38	0.05	0.71	0.09
Na_2O	8.26	0.35	7.36	0.39	1.17	0.04	1.20	0.03	1.26	0.03	7.09	0.06	8.51	0.11	8.63	0.10	1.96	0.04	0.68	0.05	1.12	0.05
K_2O	0.03	0.00	0.02	0.00	9.94	0.23	14.09	0.49	13.80	0.65	2.64	0.85	1.33	0.03	0.67	0.01	13.13	0.15	15.05	0.31	12.59	0.65
Total	100.15		100.53		100.76		100.05		99.49		100.40		100.75		100.08		99.59		99.73		98.17	
n	4		4		4		3		12		2		3		5		4		4		4	
An	19.0		21.0		0.8		0.9		0.9		20.6		11.4		20.2		4.2		2.0		4.0	
Ab	80.8		78.9		15.0		11.4		12.1		63.8		80.3		75.9		17.8		6.3		11.4	
Or	0.2		0.2		84.1		87.7		87.0		15.6		8.3		3.9		78.1		91.7		84.6	

n = number of analyses

An = anorthite component, Ab = albite component, Or= orthoclase component

Table 6: Continued

Name	YX90		YX92		YX94		YX97		YX105		YX113		YX122		YX124		YX126		YX129		YX131	
SM	HYW 1		HYW 3		HYW 5		HYW 8		HYW 8		HYW 8		HYW 1		HYW 3		HYW 5		HYW 8		HYW 2	
	[wt.%]	1σ	[wt.%]	1σ	[wt.%]	1σ	[wt.%]	1σ	[wt.%]	1σ	[wt.%]	1σ	[wt.%]	1σ	[wt.%]	1σ	[wt.%]	1σ	[wt.%]	1σ	[wt.%]	1σ
SiO_2	66.40	1.17	65.34	0.77	63.69	0.11	70.85	2.05	66.76	0.98	66.07	0.27	74.62		64.70	0.32	68.18		68.79		65.81	0.39
TiO_2	0.07	0.02	0.05	0.01	0.06	0.00	0.11	0.03	0.06	0.02	0.04	0.01	0.10		0.06	0.01	0.04		0.09		0.05	0.02
Al_2O_3	20.92	1.08	19.25	0.40	21.22	0.21	18.88	1.50	21.98	1.04	22.71	0.03	14.48		18.54	0.38	17.98		18.72		17.55	0.38
FeO	0.49	0.08	0.13	0.06	0.34	0.07	0.48	0.12	0.24	0.05	0.11	0.01	0.55		0.14	0.07	0.27		0.47		0.25	0.06
CaO	5.14	0.49	1.01	0.42	6.42	0.02	1.84	0.29	3.35	0.37	3.58	0.23	2.38		0.69	0.17	4.11		1.65		0.35	0.10
Na_2O	6.31	0.37	2.55	0.25	5.54	0.06	6.91	0.92	8.12	0.57	8.60	0.10	4.64		2.28	0.07	5.15		6.79		1.16	0.04
K_2O	1.45	0.31	11.99	0.76	1.89	0.04	2.85	0.37	1.66	0.32	1.46	0.04	1.88		12.18	0.47	2.19		3.03		13.59	0.51
Total	100.78		100.31		99.17		101.91		102.17		102.56		98.66		98.59		97.92		99.54		98.76	
n	5		6		2		4		4		3		1		6		1		1		3	
An	28.1		5.1		34.3		10.4		16.7		17.1		18.3		3.6		25.6		9.4		1.9	
Ab	62.5		23.2		53.6		70.5		73.4		74.5		64.5		21.4		58.1		70.1		11.3	
Or	9.4		71.7		12.1		19.2		9.9		8.4		17.2		75.1		16.3		20.6		86.8	

n = number of analyses

An = anorthite component, Ab = albite component, Or= orthoclase component

Table 6: Continued

Name	YX132		YX133		YX134		YX135		YX137		YX140		YX145		YX154		YX155		YX156		YX157	
SM	HYW 3		HYW 4		HYW 5		HYW 6		HYW 8		HYW 3		HYW 8		HYW3+5		HYW3+6		HYW3+8		HYW5+8	
	[wt.%]	1σ	[wt.%]	1σ	[wt.%]	1σ	[wt.%]	1σ	[wt.%]	1σ	[wt.%]	1σ	[wt.%]	1σ	[wt.%]	1σ	[wt.%]	1σ	[wt.%]	1σ	[wt.%]	1σ
SiO_2	66.16	0.99	64.40	0.52	63.29		65.05	1.11	69.55		64.09	0.53	65.57		65.04	0.35	64.59	0.11	65.20	0.45	66.24	0.56
TiO_2	0.09	0.02	0.06	0.01	0.06		0.06	0.01	0.11		0.04	0.02	0.02		0.04	0.02	0.05	0.01	0.04	0.01	0.07	0.01
Al_2O_3	17.52	0.49	18.24	0.25	21.67		17.94	0.63	18.25		18.90	0.09	20.74		19.15	0.19	18.92	0.04	20.02	0.26	20.09	0.38
FeO	0.29	0.11	0.12	0.03	0.30		0.19	0.02	0.64		0.07	0.02	0.13		0.10	0.03	0.06	0.03	0.15	0.04	0.27	0.05
CaO	0.52	0.18	0.22	0.06	4.28		0.61	0.06	1.39		0.59	0.14	2.56		0.96	0.16	0.54	0.07	1.88	0.03	2.55	0.14
Na_2O	2.26	0.11	0.00	0.00	6.27		1.68	0.04	5.71		1.95	0.10	8.43		3.09	0.02	1.91	0.03	6.08	0.01	6.93	0.19
K_2O	11.67	0.71	16.00	0.26	3.48		12.73	0.44	3.22		13.15	0.16	2.12		11.43	0.19	13.38	0.06	6.34	0.22	3.49	0.11
Total	98.51		99.03		99.35		98.27		98.87		98.80		99.57		99.83		99.45		99.71		99.63	
n	5		5		1		3		1		5		1		4		4		3		4	
An	2.8		1.1		21.7		3.3		8.9		3.0		12.6		4.8		2.7		9.2		13.2	
Ab	22.1		0.5		57.4		16.2		66.4		17.9		75.0		27.7		17.4		53.9		65.2	
Or	75.1		98.4		21.0		80.6		24.7		79.1		12.4		67.5		79.9		36.9		21.6	

n = number of analyses

An = anorthite component, Ab = albite component, Or= orthoclase component

Table 6: Continued

Name	YX158		YX159		YX161		YX162		YX163		YX164		YX165		YX166		YX167		YX168		YX169	
SM	HYW3		HYW5		HYW8		HYW3+5		HYW3+6		HYW3+8		HYW5+8		HYW3		HYW5		HYW6		HYW8	
	[wt.%]	1σ	[wt.%]	1σ	[wt.%]	1σ	[wt.%]	1σ	[wt.%]	1σ	[wt.%]	1σ	[wt.%]	1σ	[wt.%]	1σ	[wt.%]	1σ	[wt.%]	1σ	[wt.%]	1σ
SiO_2	65.14	0.11	62.49	0.90	67.66	0.21	65.08	0.36	65.57	0.49	66.15	0.46	66.51	0.78	65.30	0.60	66.68	0.10	65.09	0.19	67.74	0.37
TiO_2	0.05	0.01	0.03	0.01	0.06	0.01	0.06	0.01	0.06	0.01	0.06	0.03	0.06	0.02	0.07	0.03	0.08	0.02	0.05	0.01	0.06	0.02
Al_2O_3	18.40	0.12	22.87	0.64	19.88	0.18	18.71	0.41	18.73	0.30	19.08	0.49	19.77	0.60	18.73	0.46	17.96	0.14	18.67	0.20	19.47	0.37
FeO	0.15	0.05	0.19	0.03	0.30	0.04	0.12	0.01	0.16	0.00	0.17	0.04	0.27	0.03	0.17	0.10	0.25	0.01	0.15	0.05	0.34	0.08
CaO	0.43	0.10	5.15	0.75	1.96	0.05	0.71	0.15	0.51	0.19	1.34	0.14	2.11	0.22	0.77	0.20	0.85	0.05	0.41	0.08	1.58	0.04
Na_2O	2.33	0.05	6.41	0.09	7.70	0.14	3.10	0.09	2.07	0.08	5.12	0.25	6.70	0.35	2.58	0.22	3.58	0.13	1.69	0.10	7.62	0.36
K_2O	12.40	0.14	3.01	0.67	2.88	0.06	11.37	0.28	12.99	0.15	7.66	0.28	4.39	0.22	11.85	0.40	9.53	0.13	13.56	0.19	3.50	0.03
Total	98.91		100.15		100.45		99.14		100.09		99.58		99.80		99.46		98.93		99.63		100.32	
n	4		4		3		3		2		5		5		4		2		5		3	
An	2.2		25.3		10.1		3.6		2.6		6.8		10.8		3.9		4.6		2.1		8.1	
Ab	21.7		57.0		72.1		28.2		19.0		47.0		62.3		23.9		34.7		15.6		70.6	
Or	76.0		17.6		17.7		68.2		78.4		46.2		26.9		72.2		60.7		82.3		21.3	

n = number of analyses

An = anorthite component, Ab = albite component, Or= orthoclase component

Appendix Table 7: Composition of feldspars of system F from the Master Thesis of Klahn (2013)

Name	BD58	DA78	DA77	BD57	AC27	C7	BC26	BC56	DA26	DC56	AC55	AC25	D3	B4	C4	D4	DC54
SM	BD5	DA7	DA7	BD5	AC2	C	BC2	BC5	DA2	DC5	AC5	AC2	D	B	C	D	DC5
	[wt.%]	[wt.%]	[wt.%]	[wt.%]	[wt.%]	[wt.%]	[wt.%]	[wt.%]	[wt.%]	[wt.%]	[wt.%]	[wt.%]	[wt.%]	[wt.%]	[wt.%]	[wt.%]	[wt.%]
SiO_2	63.17	61.14	65.33	64.17	65.44	66.00	65.27	61.70	59.95	64.06	64.32	65.87	64.56	64.89	66.33	66.55	62.34
TiO_2	0.02	0.03	0.05	0.02	0.03	0.05	0.02	0.01	0.01	0.03	0.03	0.04	0.03	0.03	0.03	0.03	0.03
Al_2O_3	23.31	24.54	21.21	23.17	18.77	18.61	19.01	23.84	24.86	22.11	19.28	18.65	22.38	22.19	18.36	21.03	23.64
FeO	0.34	0.35	0.43	0.41	0.25	0.20	0.31	0.41	0.42	0.31	0.15	0.16	0.37	0.33	0.24	0.25	0.31
CaO	4.96	6.09	3.83	4.28	0.32	0.22	0.36	5.76	7.32	3.69	0.23	0.14	3.58	4.49	0.22	2.66	4.96
Na_2O	7.64	7.02	7.54	7.38	1.34	1.16	2.17	6.92	6.00	6.93	1.36	1.32	8.30	7.31	1.21	8.40	7.12
K_2O	0.55	0.82	1.62	0.58	13.86	13.75	12.86	1.37	1.44	2.88	14.63	13.83	0.77	0.77	13.61	1.08	1.60
An	25.5	30.8	19.7	23.4	1.7	1.2	1.8	28.9	36.8	18.8	1.1	0.7	18.3	24.1	1.2	13.9	25.1
Ab	71.1	64.2	70.4	72.9	12.6	11.3	20.0	62.9	54.6	63.8	12.2	12.5	77.0	71.0	11.8	79.4	65.2
Or	3.4	5.0	9.9	3.8	85.8	87.5	78.1	8.2	8.6	17.5	86.6	86.7	4.7	4.9	87.0	6.7	9.7

An = anorthite component, Ab = albite component, Or= orthoclase component

Appendix Table 8: Composition of plagioclase from natural samples

Mineral	SRP12-A05A Steer Basin								SRP12-19B Arbon Valley								SRP12-A02a Wooden Shoe Butte					
	Plg1		Plg2		Plg3		Plg4		Plg1		Plg2		Plg3		Plg4		Plg1		Plg2		Plg3	
	wt.%	1σ	wt.%	1σ	wt.%	1σ	wt.%	1σ	wt.%	1σ	wt.%	1σ	wt.%	1σ	wt.%	1σ	wt.%	1σ	wt.%	1σ	wt.%	1σ
SiO_2	59.50	0.36	59.70	0.21	59.53	0.11	60.13	0.28	65.21	0.24	64.96	0.35	65.16	0.27	65.14	0.33	60.48	0.14	59.15	0.09	59.95	0.33
Al_2O_3	24.70	0.32	24.38	0.20	24.32	0.16	24.05	0.13	21.30	0.25	21.08	0.20	20.82	0.13	21.30	0.16	24.61	0.08	25.22	0.12	24.81	0.11
FeO	0.37	0.05	0.37	0.05	0.37	0.05	0.33	0.03	<0.22		<0.22		<0.22		<0.22		0.34	0.05	0.49	0.05	0.35	0.01
CaO	7.00	0.34	6.51	0.25	6.60	0.10	6.25	0.13	2.28	0.04	2.35	0.12	2.11	0.06	2.30	0.12	6.48	0.03	7.40	0.11	6.70	0.17
BaO	0.18	0.03	0.15	0.03	0.21	0.02	0.16	0.02	<0.09		<0.09		<0.09		<0.09		0.17	0.09	0.19	0.05	0.14	0.07
Na_2O	6.49	0.09	6.74	0.09	6.76	0.07	6.90	0.10	9.54	0.04	9.45	0.13	9.44	0.09	9.39	0.10	6.94	0.06	6.59	0.07	6.80	0.04
K_2O	1.16	0.07	1.26	0.06	1.24	0.02	1.37	0.04	1.12	0.04	1.07	0.04	1.26	0.02	1.40	0.05	1.33	0.03	1.09	0.05	1.25	0.06
total	99.41		99.12		99.03		99.19		99.45		98.90		98.79		99.53		100.39		100.16		100.03	
n	5.00		5.00		5		5		5		10		4		5		4		4		5	

Appendix Table 8: Continued

Mineral	SRP12-A02b Wooden S. B.				KRH1-2052					
	Plg1		Plg2		Plg1		Plg2		Plg3	
	wt.%	1σ	wt.%	1σ	wt.%	1σ	wt.%	1σ	wt.%	1σ
SiO_2	60.14	0.16	59.38	0.24	59.70	0.29	59.99	0.29	59.38	0.16
Al_2O_3	24.61	0.09	25.24	0.13	25.23	0.23	24.97	0.15	25.42	0.10
FeO	0.35	0.03	0.32	0.04	0.42	0.06	0.42	0.04	0.44	0.07
CaO	6.70	0.16	7.27	0.13	7.09	0.19	6.82	0.19	7.20	0.07
BaO	<0.09		<0.09		<0.09		<0.09		<0.09	
Na_2O	6.95	0.08	6.73	0.03	6.53	0.12	6.65	0.10	6.48	0.14
K_2O	1.25	0.03	1.02	0.03	1.12	0.05	1.19	0.05	1.08	0.03
total	100.00		99.98		100.08		100.03		100.00	
n	5		5		10		10		5	

Appendix Table 8: Continued

Mineral	SRP09-24c Greys Landing								KRH2-1946						KRH2-1796							
	Plg1		Plg2		Plg3		Plg4		Plg1		Plg2		Plg3		Plg1		Plg2		Plg3		Plg4	
	wt.%	1σ	wt.%	1σ	wt.%	1σ	wt.%	1σ	wt.%	1σ	wt.%	1σ	wt.%	1σ	wt.%	1σ	wt.%	1σ	wt.%	1σ	wt.%	1σ
SiO_2	59.99	0.14	62.22	0.19	62.07	0.06	58.63	0.32	61.49	0.43	64.20	0.53	64.32	0.04	64.48	0.06	61.83	0.28	64.17	0.15	64.83	0.23
Al_2O_3	25.48	0.12	23.89	0.15	23.92	0.09	25.63	0.27	24.23	0.25	21.63	0.22	21.98	0.22	22.25	0.12	23.90	0.10	21.91	0.13	22.30	0.19
FeO	0.27	0.05	0.35	0.04	0.39	0.05	0.31	0.07	0.27	0.05	<0.22		<0.22		0.24	0.01	0.28	0.06	0.28	0.04	0.28	0.02
CaO	6.94	0.08	5.01	0.13	5.25	0.16	7.84	0.18	5.42	0.31	2.63	0.19	2.75	0.10	2.76	0.12	5.09	0.16	2.77	0.09	2.97	0.04
BaO	0.20	0.02	0.31	0.02	0.25	0.02	0.15	0.03	<0.09		<0.09		<0.09		0.49	0.00	0.25	0.02	0.64	0.01	0.41	0.02
Na_2O	6.83	0.17	7.67	0.06	7.88	0.07	6.61	0.08	7.43	0.12	7.13	0.42	7.48	0.17	8.01	0.17	7.76	0.09	7.33	0.07	8.16	0.04
K_2O	1.05	0.03	1.49	0.13	1.01	0.06	0.75	0.12	1.39	0.14	3.88	0.70	3.40	0.16	3.00	0.48	1.53	0.05	3.82	0.10	2.61	0.11
total	100.77		100.94		100.78		99.92		100.22		99.45		99.94		101.22		100.63		100.93		101.57	
n	3		4		3		3		13		5		5		4		4		4		4	

Appendix Table 8: Continued

Mineral	KRH2-1401								KRH3-716									
	Plg1		Plg2		Plg3		Plg4		Plg1		Plg2		Plg3		Plg4		Plg5	
	wt.%	1σ	wt.%	1σ	wt.%	1σ	wt.%	1σ	wt.%	1σ	wt.%	1σ	wt.%	1σ	wt.%	1σ	wt.%	1σ
SiO_2	63.89	0.20	64.01	0.13	62.37	0.16	63.41	0.14	60.93	0.18	60.52	0.19	60.77	0.30	61.44	0.85	61.79	0.46
Al_2O_3	21.66	0.13	21.52	0.16	23.13	0.05	21.75	0.16	24.18	0.28	24.56	0.17	24.39	0.13	23.98	0.56	23.87	0.21
FeO	<0.22		<0.22		0.32	0.04	<0.22		0.39	0.04	0.37	0.02	0.36	0.03	0.38	0.05	0.37	0.03
CaO	2.85	0.22	2.74	0.07	4.47	0.12	3.04	0.05	6.09	0.24	6.65	0.15	6.39	0.10	5.87	0.62	5.82	0.19
BaO	<0.09		<0.09		<0.09		<0.09		<0.09		<0.09		<0.09		<0.09		<0.09	
Na_2O	7.10	0.21	7.06	0.10	7.63	0.17	7.16	0.13	7.49	0.05	6.87	0.09	7.01	0.08	7.26	0.17	7.50	0.11
K_2O	3.94	0.32	4.11	0.10	1.90	0.06	3.61	0.09	0.96	0.03	1.25	0.09	1.20	0.03	1.21	0.25	0.79	0.02
total	99.44		99.45		99.82		98.96		100.03		100.21		100.12		100.14		100.14	
n	5		5		5		5		5		5		5		5		5	

Appendix Table 8: Continued

Mineral	SRP09-13 Wolverine Creek						SRP09-10E Huckleberry R			
	Plg1		Plg2		Plg3		Plg1		Plg2	
	wt.%	1σ	wt.%	1σ	wt.%	1σ	wt.%	1σ	wt.%	1σ
SiO_2	63.03	0.23	64.30	0.31	63.51	0.26	63.39	0.24	63.67	0.09
Al_2O_3	22.55	0.23	21.92	0.20	22.28	0.19	21.59	0.26	22.45	0.13
FeO	0.24	0.03	0.23	0.01	<0.22		0.24	0.03	0.25	0.05
CaO	4.11	0.12	3.27	0.05	3.88	0.08	2.98	0.12	3.88	0.10
BaO	0.13	0.03	<0.09		0.14	0.02	1.09	0.08	<0.09	
Na_2O	8.17	0.13	8.42	0.26	8.16	0.15	7.26	0.10	8.17	0.09
K_2O	1.42	0.07	1.72	0.08	1.55	0.02	3.38	0.13	1.69	0.05
total	99.66		99.86		99.53		99.92		100.10	
n	10		5		8		6		5	

Appendix Table 9: Composition of sanidine from natural samples

Mineral	SRP12-A05A Steer Basin								SRP12-19B Arbon Valley									
	San1		San2		San3		San4		San1		San2		San3		San4		San5	
	wt.%	1σ	wt.%	1σ	wt.%	1σ	wt.%	1σ	wt.%	1σ	wt.%	1σ	wt.%	1σ	wt.%	1σ	wt.%	1σ
SiO_2	63.80	0.26	64.09	0.49	64.18	0.07	63.55	0.21	65.32	0.19	65.60	0.16	65.19	0.05	65.26	0.12	65.29	0.12
Al_2O_3	19.37	0.15	18.96	0.25	18.86	0.14	19.16	0.11	18.52	0.12	18.70	0.14	18.31	0.09	18.43	0.20	18.52	0.09
CaO	0.71	0.03	0.54	0.04	0.46	0.03	0.69	0.02	0.11	0.01	0.11	0.03	0.12	0.01	0.11	0.03	0.15	0.01
BaO	1.98	0.07	1.77	0.06	1.37	0.07	1.89	0.06	n.d.		n.d.		n.d.		n.d.		n.d.	
Na_2O	4.23	0.08	3.98	0.13	3.88	0.13	4.17	0.07	3.87	0.07	3.90	0.07	3.94	0.07	3.87	0.06	3.97	0.04
K_2O	9.09	0.11	9.49	0.04	9.97	0.10	9.13	0.16	11.09	0.10	11.02	0.05	11.01	0.03	11.04	0.10	10.90	0.03
total	99.18		98.82		98.71		98.59		98.91		99.34		98.57		98.71		98.83	
n	5		10		5		5		10		5		4		5		6	

Appendix Table 9: Continued

Mineral	SRP12-A02a Wooden Shoe Butte								SRP12-A02b Wooden Shoe Butte					
	San1		San2		San3		San4		San1		San2		San3	
	wt.%	1σ	wt.%	1σ	wt.%	1σ	wt.%	1σ	wt.%	1σ	wt.%	1σ	wt.%	1σ
SiO_2	64.17	0.18	65.25	0.31	64.07	0.21	65.10	0.09	65.19	0.16	64.37	0.09	64.71	0.06
Al_2O_3	19.74	0.08	19.43	0.19	19.81	0.08	19.30	0.09	19.27	0.10	19.64	0.07	19.69	0.05
CaO	0.71	0.02	0.48	0.02	0.69	0.03	0.42	0.01	0.33	0.02	0.73	0.03	0.69	0.03
BaO	1.79	0.09	1.17	0.09	1.84	0.09	1.34	0.16	1.14	0.08	1.88	0.04	1.52	0.08
Na_2O	4.28	0.02	5.17	0.48	4.61	0.13	4.14	0.05	4.18	0.04	4.61	0.03	5.09	0.09
K_2O	9.03	0.04	8.44	0.60	8.66	0.04	9.75	0.06	9.84	0.09	8.56	0.04	8.09	0.07
total	99.72		99.93		99.67		100.06		99.96		99.80		99.78	
n	5		5		5		5		4		5		3	

Appendix Table 9: Continued

Mineral	SRP09-24c Greys Landing								KRH2-1946					
	San1		San2		San3		San4		San1		San2		San3	
	wt.%	1σ	wt.%	1σ	wt.%	1σ	wt.%	1σ	wt.%	1σ	wt.%	1σ	wt.%	1σ
SiO_2	64.62	0.13	64.58	0.22	64.76	0.20	64.85	0.19	64.61	0.30	64.38	0.24	64.67	0.24
Al_2O_3	19.79	0.28	20.10	0.17	19.87	0.15	19.24	0.14	19.83	0.17	19.77	0.13	19.89	0.13
CaO	0.67	0.07	0.83	0.05	0.69	0.08	0.58	0.05	0.98	0.08	0.96	0.08	0.97	0.02
BaO	1.95	0.06	2.07	0.03	1.89	0.07	1.79	0.04	n.d.		n.d.		n.d.	
Na_2O	4.94	0.13	5.65	0.18	5.03	0.24	4.81	0.18	5.27	0.14	5.11	0.07	5.57	0.09
K_2O	8.19	0.27	7.30	0.25	8.05	0.43	8.25	0.16	7.68	0.28	7.89	0.16	7.25	0.15
total	100.16		100.53		100.29		99.52		98.37		98.11		98.35	
n	4		4		4		4		17		5		4	

Appendix Table 9: Continued

Mineral	KRH2-1796						KRH2-1401									
	San1		San2		San3		San1		San2		San3		San4		San5	
	wt.%	1σ	wt.%	1σ	wt.%	1σ	wt.%	1σ	wt.%	1σ	wt.%	1σ	wt.%	1σ	wt.%	1σ
SiO_2	63.88	0.10	64.73	0.17	65.18	0.32	63.85	0.25	64.09	0.10	63.76	0.31	63.82	0.08	63.95	0.20
Al_2O_3	19.32	0.06	19.64	0.13	20.04	0.13	19.84	0.09	19.54	0.21	19.65	0.18	19.89	0.13	19.84	0.23
CaO	0.91	0.02	0.74	0.03	0.94	0.07	1.20	0.06	0.91	0.16	0.99	0.10	1.15	0.06	1.16	0.05
BaO	1.23	0.04	1.29	0.06	1.14	0.10	n.d.		n.d.		n.d.		n.d.		n.d.	
Na_2O	5.69	0.07	4.55	0.10	5.74	0.28	5.51	0.11	5.06	0.16	5.24	0.05	5.59	0.19	5.45	0.11
K_2O	7.48	0.07	9.13	0.14	7.44	0.60	7.28	0.11	8.03	0.42	7.58	0.12	7.21	0.10	7.29	0.13
total	98.51		100.08		100.48		97.68		97.63		97.22		97.67		97.68	
n	4		4		4		3		3		3		5		5	

Appendix Table 9: Continued

Mineral	KRH3-716										SRP09-10E Huckleberry Ridge											
	San1		San2		San3		San4		San5		San1		San2		San3		San4		San5		San6	
	wt.%	1σ	wt.%	1σ	wt.%	1σ	wt.%	1σ	wt.%	1σ	wt.%	1σ	wt.%	1σ	wt.%	1σ	wt.%	1σ	wt.%	1σ	wt.%	1σ
SiO_2	65.75	0.14	66.00	0.41	64.00	0.20	64.80	0.24	64.06	0.24	65.46	0.26	63.81	0.11	65.29	0.29	66.00	0.33	64.95	0.35	65.88	0.16
Al_2O_3	18.60	0.25	18.89	0.08	19.10	0.20	18.98	0.33	19.61	0.04	19.28	0.11	20.17	0.10	19.21	0.15	19.09	0.11	19.56	0.17	18.88	0.19
CaO	0.48	0.02	0.55	0.05	0.62	0.06	0.65	0.10	0.97	0.08	0.54	0.02	1.11	0.07	0.52	0.01	0.53	0.02	0.78	0.07	0.45	0.04
BaO	n.d.		n.d.		n.d.		n.d.		n.d.		0.91	0.03	2.36	0.09	1.10	0.01	0.42	0.05	1.34	0.06	0.47	0.03
Na_2O	3.42	0.17	4.47	0.01	2.53	0.10	3.39	0.03	4.97	0.16	4.95	0.08	5.46	0.16	4.80	0.07	5.01	0.11	5.24	0.05	4.92	0.09
K_2O	11.03	0.18	9.83	0.08	11.78	0.15	10.52	0.17	7.90	0.19	8.11	0.10	6.67	0.14	8.49	0.06	8.41	0.05	7.70	0.17	8.96	0.05
total	99.28		99.73		98.04		98.34		97.51		99.25		99.57		99.39		99.45		99.57		99.56	
n	3		2		3		2		5		5		6		6		6		6		6	

Appendix Table 10: Composition of augite from natural samples

Mineral	SRP12-A05A Steer Basin				SRP12-A02a Wooden Shoe Butte					
	Agt1		Agt2		Agt1		Agt2		Agt3	
	wt.%	1σ	wt.%	1σ	wt.%	1σ	wt.%	1σ	wt.%	1σ
SiO_2	49.62	0.24	49.31	0.24	49.42	0.18	49.87	0.13	49.54	0.29
TiO_2	0.27	0.02	0.34	0.02	0.31	0.01	0.36	0.01	0.37	0.01
Al_2O_3	0.67	0.07	0.77	0.04	0.70	0.03	0.82	0.03	0.82	0.03
FeO	22.27	0.33	22.96	0.37	22.54	0.30	22.53	0.24	22.22	0.28
MnO	0.62	0.09	0.68	0.08	0.58	0.05	0.64	0.07	0.63	0.07
MgO	8.55	0.12	8.45	0.09	8.22	0.11	8.47	0.10	8.27	0.09
CaO	17.54	0.20	17.21	0.14	17.24	0.13	16.86	0.10	17.41	0.14
Na_2O	0.23	0.03	0.24	0.03	0.20	0.03	0.22	0.05	0.26	0.00
Total	99.79		99.95		99.22		99.77		99.53	
n	10		8		5		5		3	

Appendix Table 10: Continued

Mineral	KRH1-2052								SRP09-24c Greys Landing									
	Agt1		Agt2		Agt3		Agt4		Agt1		Agt2		Agt3		Agt4		Agt5	
	wt.%	1σ	wt.%	1σ	wt.%	1σ	wt.%	1σ	wt.%	1σ	wt.%	1σ	wt.%	1σ	wt.%	1σ	wt.%	1σ
SiO_2	51.16	0.13	51.12	0.25	50.66	0.16	51.13	0.29	49.31	0.16	49.20	0.07	49.18	0.16	49.72	0.22	49.19	0.34
TiO_2	0.34	0.02	0.33	0.02	0.54	0.01	0.38	0.03	0.41	0.02	0.33	0.02	0.37	0.01	0.34	0.01	0.39	0.02
Al_2O_3	0.92	0.04	0.93	0.08	1.41	0.07	1.12	0.17	0.94	0.02	0.73	0.02	0.84	0.02	0.79	0.02	0.91	0.01
FeO	15.84	0.07	15.89	0.15	15.99	0.17	15.55	0.18	23.77	0.34	24.56	0.19	23.51	0.45	24.25	0.51	24.05	0.15
MnO	0.57	0.05	0.55	0.02	0.56	0.05	0.58	0.06	0.72	0.05	0.82	0.10	0.75	0.06	0.76	0.05	0.79	0.11
MgO	11.98	0.15	11.94	0.16	11.81	0.09	11.87	0.17	7.47	0.12	6.86	0.06	7.64	0.02	7.33	0.05	7.43	0.19
CaO	18.36	0.10	18.22	0.17	18.30	0.07	18.37	0.19	16.71	0.14	16.56	0.05	16.80	0.08	16.57	0.12	16.34	0.07
Na_2O	0.32	0.05	0.29	0.02	0.33	0.02	0.31	0.03	0.28	0.06	0.22	0.05	0.21	0.03	0.24	0.05	0.00	0.00
Total	99.48		99.28		99.61		99.31		99.59		99.29		99.31		100.00		99.10	
n	5		5		5		6		4		4		4		5		4	

Appendix Table 10: Continued

Mineral	KRH2-1946						KRH2-1796						KRH2-1401					
	Agt1		Agt2		Agt3		Agt1		Agt2		Agt3		Agt1		Agt2		Agt3	
	wt.%	1σ	wt.%	1σ	wt.%	1σ	wt.%	1σ	wt.%	1σ	wt.%	1σ	wt.%	1σ	wt.%	1σ	wt.%	1σ
SiO_2	49.07	0.15	49.09	0.25	49.23	0.11	48.97	0.06	49.07	0.11	49.23	0.09	48.88	0.11	48.94	0.13	48.78	0.14
TiO_2	0.32	0.02	0.31	0.01	0.29	0.02	0.32	0.01	0.30	0.02	0.30	0.02	0.27	0.02	0.29	0.01	0.29	0.02
Al_2O_3	0.67	0.04	0.64	0.03	0.62	0.04	0.65	0.02	0.58	0.02	0.62	0.02	0.60	0.03	0.62	0.03	0.62	0.05
FeO	25.11	0.38	25.80	0.07	25.31	0.43	25.84	0.29	24.89	0.47	25.05	0.17	26.22	0.42	25.93	0.35	25.87	0.25
MnO	1.00	0.06	1.04	0.10	1.01	0.05	1.07	0.06	0.94	0.18	1.01	0.11	0.98	0.07	0.99	0.05	1.00	0.03
MgO	6.39	0.19	6.14	0.06	6.33	0.11	5.78	0.08	6.22	0.10	6.28	0.13	6.29	0.11	6.20	0.11	6.35	0.12
CaO	16.44	0.15	16.25	0.04	16.48	0.05	16.52	0.12	16.79	0.07	16.72	0.07	16.42	0.16	16.51	0.06	16.58	0.07
Na_2O	0.25	0.03	0.27	0.03	0.24	0.04	0.27	0.03	0.25	0.04	0.23	0.03	0.22	0.06	0.24	0.04	0.22	0.01
Total	99.24		99.54		99.51		99.42		99.03		99.43		99.88		99.74		99.71	
n	14		5		5		4		4		4		5		5		5	

Appendix Table 10: Continued

Mineral	KRH3-716						SRP09-13 Wolverine Creek										SRP09-10E Huckleberry Ridge					
	Agt1		Agt2		Agt3		Agt1		Agt2		Agt3		Agt4		Agt5		Agt1		Agt2		Agt3	
	wt.%	1σ	wt.%	1σ	wt.%	1σ	wt.%	1σ	wt.%	1σ	wt.%	1σ	wt.%	1σ	wt.%	1σ	wt.%	1σ	wt.%	1σ	wt.%	1σ
SiO_2	50.91	0.10	51.13	0.29	52.52	0.36	53.05	0.29	51.13	0.19	50.70	0.16	48.73	0.10	53.31	0.07	47.64	0.17	48.06	0.28	48.33	0.22
TiO_2	0.34	0.02	0.33	0.02	0.37	0.04	0.24	0.04	0.71	0.02	0.68	0.04	1.10	0.03	0.19	0.02	0.35	0.02	0.35	0.02	0.28	0.02
Al_2O_3	0.84	0.05	0.82	0.04	2.15	0.15	1.16	0.19	2.17	0.07	2.68	0.12	5.26	0.11	1.10	0.05	0.67	0.06	0.61	0.07	0.68	0.10
FeO	17.93	0.16	18.46	0.21	15.47	0.36	6.06	0.30	9.69	0.17	8.80	0.17	9.07	0.20	5.13	0.07	29.08	0.32	28.84	0.21	27.30	0.28
MnO	0.66	0.05	0.66	0.09	0.59	0.04	0.16	0.03	0.23	0.01	0.25	0.05	0.18	0.12	0.17	0.03	0.97	0.07	0.93	0.06	0.95	0.07
MgO	10.76	0.22	10.65	0.09	15.22	0.14	17.56	0.35	15.48	0.15	14.91	0.19	13.60	0.17	17.53	0.15	2.31	0.11	2.38	0.06	4.11	0.27
CaO	17.75	0.06	17.71	0.13	9.60	0.19	21.22	0.24	19.91	0.15	21.14	0.14	21.83	0.34	22.20	0.19	17.69	0.12	17.51	0.07	17.16	0.30
Na_2O	0.27	0.04	0.28	0.05	1.58	0.35	0.36	0.06	0.36	0.03	0.33	0.03	0.39	0.03	0.24	0.04	0.29	0.05	0.31	0.04	0.29	0.02
Total	99.46		100.04		97.49		99.81		99.67		99.50		100.16		99.87		99.02		98.99		99.10	
n	5		5		5		9		5		5		4		3		9		8		10	

Appendix Table 11: Composition of pigeonite from natural samples

Mineral	SRP12-A02a Wooden Shoe Butte						SRP12-A02b Wooden Shoe Butte					
	Pig1		Pig2		Pig3		Pig1		Pig2		Pig3	
	wt.%	1σ	wt.%	1σ	wt.%	1σ	wt.%	1σ	wt.%	1σ	wt.%	1σ
SiO_2	48.75	0.15	48.53	0.09	48.92	0.17	48.72	0.11	48.85	0.20	48.76	0.09
TiO_2	0.23	0.01	0.22	0.00	0.22	0.02	0.20	0.02	0.20	0.02	0.16	0.02
Al_2O_3	0.37	0.02	0.35	0.03	0.34	0.03	0.38	0.02	0.34	0.02	0.30	0.03
FeO	36.08	0.26	35.77	0.28	35.36	0.48	36.13	0.17	36.29	0.51	36.34	0.13
MnO	1.04	0.09	1.00	0.08	0.99	0.09	1.03	0.02	1.08	0.01	1.05	0.03
MgO	9.40	0.07	9.38	0.12	9.65	0.10	9.47	0.06	9.28	0.12	9.97	0.10
CaO	4.08	0.08	4.18	0.08	4.07	0.08	4.08	0.04	4.16	0.08	3.58	0.05
Total	99.96		99.44		99.56		100.00		100.20		100.17	
n	5		3		3		3		4		4	

Appendix Table 11: Continued

Mineral	KRH1-2052						SRP09-24c Greys Landing				KRH2-1946						KRH2-1401					
	Pig1		Pig2		Pig3		Pig1		Pig2		Pig1		Pig2		Pig3		Pig1		Pig2		Pig3	
	wt.%	1σ	wt.%	1σ	wt.%	1σ	wt.%	1σ	wt.%	1σ	wt.%	1σ	wt.%	1σ	wt.%	1σ	wt.%	1σ	wt.%	1σ	wt.%	1σ
SiO_2	50.99	0.25	51.00	0.35	50.94	0.18	48.22	0.12	48.48	0.23	48.15	0.25	48.25	0.17	48.22	1.54	47.70	0.23	48.01	0.30	47.68	0.25
TiO_2	0.24	0.02	0.23	0.02	0.18	0.01	0.21	0.01	0.24	0.01	0.20	0.01	0.19	0.01	0.20	0.01	0.18	0.01	0.20	0.02	0.19	0.01
Al_2O_3	0.47	0.02	0.46	0.02	0.35	0.04	0.38	0.06	0.34	0.03	0.28	0.04	0.29	0.02	0.32	0.14	0.28	0.02	0.27	0.02	0.28	0.01
FeO	29.22	0.26	28.55	0.30	28.52	0.13	37.11	0.40	36.95	0.35	38.00	0.45	37.72	0.26	37.57	1.12	38.97	0.22	38.59	0.38	38.52	0.29
MnO	0.94	0.08	0.93	0.05	1.10	0.07	1.21	0.07	1.27	0.14	1.56	0.06	1.57	0.12	1.56	0.09	1.50	0.08	1.56	0.14	1.64	0.03
MgO	16.66	0.11	16.58	0.08	15.43	0.08	7.79	0.16	7.95	0.03	6.80	0.13	7.05	0.05	7.11	0.46	7.14	0.05	6.86	0.12	7.00	0.09
CaO	1.71	0.03	1.84	0.10	3.47	0.02	4.44	0.06	4.57	0.07	4.30	0.05	4.24	0.07	4.29	0.32	4.32	0.07	4.37	0.07	4.37	0.09
Total	100.23		99.59		99.99		99.36		99.79		99.29		99.30		99.28		100.09		99.87		99.67	
n	10		5		5		4		5		5		5		15		5		5		5	

Appendix Table 11: Continued

Mineral	KRH3-716 Pig1		Pig2		Pig3		Pig4		SRP09-10E Pig1	
	wt.%	1σ	wt.%	1σ	wt.%	1σ	wt.%	1σ	wt.%	1σ
SiO_2	50.73	0.08	50.55	0.36	51.02	0.14	51.46	0.23	47.08	0.28
TiO_2	0.19	0.02	0.20	0.00	0.19	0.02	0.22	0.01	0.15	0.02
Al_2O_3	0.33	0.03	0.33	0.02	0.31	0.02	0.45	0.09	0.25	0.04
FeO	30.25	0.18	30.75	0.43	30.58	0.28	30.30	0.32	42.31	0.24
MnO	1.09	0.06	1.11	0.08	1.10	0.11	1.09	0.10	1.64	0.04
MgO	13.33	0.15	13.24	0.19	13.73	0.13	13.38	0.21	4.36	0.06
CaO	3.71	0.07	3.67	0.05	3.75	0.05	3.71	0.02	3.93	0.14
Total	99.64		99.84		100.68		100.61		99.71	
n	5		5		5		3		8	

Appendix Table 12: Composition of magnetite from natural samples

Mineral	SRP12-A05A Steer Basin Mag1		Mag2		Mag3		Mag4		SRP12-19B Arbon Valley Mag1		Mag2		Mag3		Mag4	
	wt.%	1σ	wt.%	1σ	wt.%	1σ	wt.%	1σ	wt.%	1σ	wt.%	1σ	wt.%	1σ	wt.%	1σ
SiO_2	0.12	0.01	0.12	0.02	0.10	0.01	0.12	0.02	0.14	0.01	0.25	0.12	0.17	0.09	0.15	0.04
TiO_2	25.93	0.54	21.04	0.81	7.97	0.35	22.12	0.69	21.33	0.38	5.28	0.05	20.48	0.98	6.55	0.08
Al_2O_3	1.31	0.21	1.26	0.08	2.19	0.13	1.47	0.07	1.91	0.05	2.43	0.03	1.86	0.11	1.00	0.04
V_2O_3	0.54	0.05	0.50	0.02	0.33	0.01	0.51	0.00	0.56	0.01	0.45	0.01	0.53	0.03	0.11	0.01
FeO	69.68	1.00	72.08	1.04	83.39	0.25	71.12	0.58	69.76	0.58	82.30	0.42	69.42	2.13	85.07	0.98
MnO	0.66	0.16	0.61	0.03	0.31	0.01	0.65	0.04	1.30	0.10	0.60	0.05	0.63	0.17	1.43	0.05
MgO	0.67	0.02	0.56	0.03	0.31	0.02	0.54	0.03	0.60	0.05	1.26	0.07	1.02	0.14	<0.06	
Total	98.90		96.16		94.60		96.52		95.59		92.57		94.12		94.32	
n	4		9		3		5		5		5		5		10	

Appendix Table 12: Continued

Mineral	SRP12-A02a Wooden Shoe Butte								SRP12-A02b Wooden Shoe Butte					
	Mag1		Mag2		Mag3		Mag4		Mag1		Mag2		Mag3	
	wt.%	1σ	wt.%	1σ	wt.%	1σ	wt.%	1σ	wt.%	1σ	wt.%	1σ	wt.%	1σ
SiO_2	0.26	0.09	0.22	0.09	0.46	0.11	0.99	0.08	0.07	0.03	<0.05		<0.05	
TiO_2	22.70	0.51	23.75	2.65	20.72	1.90	23.75	0.94	49.40	0.15	50.99	0.19	49.98	0.10
Al_2O_3	1.43	0.03	1.34	0.08	1.54	0.06	1.49	0.08	0.06	0.02	0.06	0.01	0.09	0.00
V_2O_3	n.d.		n.d.		n.d.		n.d.		n.d.		n.d.		n.d.	
FeO	69.03	0.50	67.44	2.38	70.80	1.74	63.63	0.91	47.40	0.30	46.92	0.33	48.20	0.13
MnO	0.66	0.02	0.68	0.01	<0.12		<0.12		0.98	0.06	1.25	0.06	0.97	0.06
MgO	0.44	0.02	0.16	0.02	0.45	0.03	0.27	0.03	0.71	0.04	0.79	0.02	0.77	0.04
Total	94.53		93.58		93.97		90.14		98.63		100.02		100.02	
n	3		3		5		3		4		4		3	

Appendix Table 12: Continued

Mineral	KRH1-2052						SRP09-24c Greys Landing							
	Mag1		Mag2		Mag3		Mag1		Mag2		Mag3		Mag4	
	wt.%	1σ	wt.%	1σ	wt.%	1σ	wt.%	1σ	wt.%	1σ	wt.%	1σ	wt.%	1σ
SiO_2	0.55	0.18	0.15	0.04	0.47	0.28	0.15	0.03	0.08	0.02	0.11	0.01	0.17	0.13
TiO_2	17.76	0.19	17.90	0.04	17.67	0.30	13.74	0.19	16.37	0.41	15.40	0.01	12.63	0.34
Al_2O_3	1.88	0.09	1.84	0.03	1.79	0.03	1.91	0.03	1.58	0.04	1.66	0.05	1.82	0.07
V_2O_3	n.d.		n.d.		n.d.		0.34	0.01	0.37	0.00	0.35	0.01	0.31	0.02
FeO	70.60	0.77	72.94	0.14	69.61	0.28	78.03	0.04	77.55	0.02	78.42	0.58	79.01	1.08
MnO	2.65	1.19	0.90	0.23	4.56	0.16	0.50	0.04	0.54	0.03	0.44	0.02	0.38	0.07
MgO	0.76	0.27	1.14	0.03	0.49	0.15	0.26	0.00	0.27	0.04	0.27	0.01	0.24	0.03
Total	94.19		94.86		94.60		94.93		96.75		96.64		94.56	
n	4		4		4		2		2		3		4	

Appendix Table 12: Continued

Mineral	KRH2-1946								KRH2-1796					
	Mag1		Mag2		Mag3		Mag4		Mag1		Mag2		Mag3	
	wt.%	1σ	wt.%	1σ	wt.%	1σ	wt.%	1σ	wt.%	1σ	wt.%	1σ	wt.%	1σ
SiO_2	0.71	0.59	0.13	0.02	0.40	0.45	0.49	0.36	0.10	0.04	0.13	0.08	0.10	0.01
TiO_2	20.62	0.46	19.31	0.11	19.25	0.93	20.03	0.14	21.60	0.08	19.54	0.15	18.30	0.07
Al_2O_3	1.38	0.03	1.36	0.04	1.51	0.09	1.42	0.04	0.92	0.02	0.90	0.04	0.84	0.05
V_2O_3	n.d.		n.d.		n.d.		n.d.		0.43	0.01	0.41	0.02	0.38	0.01
FeO	71.84	2.01	75.61	0.35	73.32	1.49	73.29	1.09	67.81	0.77	73.04	0.17	74.68	0.39
MnO	1.11	0.35	0.67	0.03	0.87	0.19	0.85	0.15	3.92	0.74	1.00	0.08	0.83	0.02
MgO	0.26	0.10	0.35	0.02	0.32	0.03	0.36	0.04	0.22	0.03	0.22	0.03	0.08	0.01
Total	95.91		97.43		95.67		96.44		95.00		95.24		95.21	
n	5		5		5		8		3		3		2	

Appendix Table 12: Continued

Mineral	KRH2-1401												KRH3-716		SRP09-13		SRP09-10E Huckleberry Ridge					
	Mag1		Mag2		Mag3		Mag4		Mag5		Mag6		Mag1		Mag1		Mag1		Mag2		Mag3	
	wt.%	1σ	wt.%	1σ	wt.%	1σ	wt.%	1σ	wt.%	1σ	wt.%	1σ	wt.%	1σ	wt.%	1σ	wt.%	1σ	wt.%	1σ	wt.%	1σ
SiO_2	0.14	0.07	0.16	0.03	0.12	0.01	0.10	0.00	0.12	0.01	0.11	0.01	0.13	0.01	0.12	0.04	0.10	0.02	0.07	0.04	0.11	0.02
TiO_2	22.60	0.12	22.54	0.14	22.14	0.02	22.57	0.05	22.34	0.05	22.40	0.14	12.76	0.70	13.57	0.20	21.32	0.86	20.87	0.17	23.69	1.98
Al_2O_3	1.23	0.05	1.21	0.03	1.21	0.03	1.22	0.02	1.23	0.01	1.25	0.03	1.24	0.36	1.26	0.03	1.07	0.14	1.15	0.09	1.19	0.13
V_2O_3	n.d.		n.d.		n.d.		n.d.		n.d.		n.d.		n.d.		0.58	0.01	0.52	0.03	0.48	0.01	0.58	0.03
FeO	71.86	1.41	71.54	1.38	73.78	0.55	72.71	0.11	73.14	0.40	72.51	0.40	81.59	1.57	77.32	0.88	71.43	0.89	71.63	0.29	70.01	2.26
MnO	1.59	1.18	2.07	0.92	0.79	0.05	0.80	0.02	0.75	0.03	0.92	0.22	<0.12	0.00	0.58	0.03	0.69	0.07	0.68	0.09	0.68	0.22
MgO	0.36	0.07	0.37	0.02	0.41	0.01	0.41	0.01	0.41	0.03	0.45	0.02	0.37	0.01	0.56	0.01	0.14	0.02	0.15	0.02	0.16	0.03
Total	97.80		97.90		98.45		97.81		97.98		97.64		96.09		93.99		95.27		95.03		96.43	
n	3		3		3		3		3		4		2		4		10		4		9	

Appendix Table 13: Composition of ilmenite from natural samples

Mineral	SRP12-A05A		SRP12-19B		SRP12-A02a Wooden Shoe Butte								SRP12-A02b Wooden Shoe Butte					
	Ilm1		Ilm1		Ilm1		Ilm2		Ilm3		Ilm4		Ilm1		Ilm2		Ilm3	
	wt.%	1σ	wt.%	1σ	wt.%	1σ	wt.%	1σ	wt.%	1σ	wt.%	1σ	wt.%	1σ	wt.%	1σ	wt.%	1σ
SiO_2	<0.05		0.08	0.02	0.07	0.02	<0.05		<0.05		<0.05		0.07	0.03	<0.05		<0.05	
TiO_2	48.23	0.09	48.71	0.22	49.18	0.21	50.41	0.03	49.61	0.19	49.21	0.25	49.40	0.15	50.99	0.19	49.98	0.10
Al_2O_3	<0.05	0.00	0.13	0.01	0.05	0.01	0.09	0.27	0.09	0.03	0.08	0.04	0.06	0.02	0.06	0.01	0.09	0.00
V_2O_3	0.87	0.01	1.00	0.02	n.d.		n.d.		n.d.		n.d.		n.d.		n.d.		n.d.	
FeO	48.58	0.23	45.91	0.21	48.07	0.38	47.92	0.04	48.06	0.26	48.23	0.18	47.40	0.30	46.92	0.33	48.20	0.13
MnO	0.89	0.05	2.66	0.06	0.93	0.05	0.73	0.00	0.72	0.07	0.89	0.07	0.98	0.06	1.25	0.06	0.97	0.06
MgO	1.02	0.03	0.58	0.01	0.32	0.02	0.90	0.00	0.82	0.06	0.68	0.04	0.71	0.04	0.79	0.02	0.77	0.04
Total	99.60		99.07		98.62		100.06		99.30		99.09		98.63		100.02		100.02	
n	10		6		5		5		6		5		4		4		3	

Appendix Table 13: Continued

Mineral	SRP09-24c Greys Landing						KRH2-1946						KRH2-1796				KRH3-716	
	Ilm1		Ilm2		Ilm3		Ilm1		Ilm2		Ilm3		Ilm1		Ilm2		Ilm1	
	wt.%	1σ	wt.%	1σ	wt.%	1σ	wt.%	1σ	wt.%	1σ	wt.%	1σ	wt.%	1σ	wt.%	1σ	wt.%	1σ
SiO_2	<0.05		0.07	0.01	0.10	0.00	0.08	0.05	0.26	0.38	0.11	0.02	<0.05		<0.05		<0.05	
TiO_2	49.06	0.86	49.94	0.39	49.56	0.07	49.53	0.17	49.65	0.22	49.49	0.07	49.71	0.16	52.29	0.25	50.82	0.29
Al_2O_3	0.09	0.05	0.08	0.04	0.05	0.00	0.06	0.01	0.08	0.04	0.08	0.02	<0.05		<0.05		<0.05	
V_2O_3	0.95	0.03	0.95	0.05	1.01	0.01							0.90	0.02	0.93	0.02		
FeO	47.51	0.36	47.21	0.50	47.09	0.12	48.50	0.47	48.56	0.51	49.55	0.29	45.50	0.66	43.68	0.45	48.18	0.30
MnO	0.84	0.03	0.80	0.03	0.82	0.07	0.87	0.04	0.89	0.05	0.85	0.03	3.00	0.08	0.91	0.17	0.22	0.09
MgO	0.64	0.02	0.63	0.03	0.67	0.01	0.72	0.03	0.73	0.03	0.71	0.05	0.21	0.01	<0.06		1.42	0.01
Total	99.09		99.69		99.29		99.75		100.17		100.78		99.31		97.81		100.63	
n	4		4		2		5		5		5		3		4		3	

Appendix Table 13: Continued

Mineral	KRH2-1796 Ilm1		KRH2-1796 Ilm2		KRH3-716 Ilm1	
	wt.%	1σ	wt.%	1σ	wt.%	1σ
SiO_2	<0.05		<0.05		<0.05	
TiO_2	49.71	0.16	52.29	0.25	50.82	0.29
Al_2O_3	<0.05		<0.05		<0.05	
V_2O_3	0.90	0.02	0.93	0.02	n.d.	
FeO	45.50	0.66	43.68	0.45	48.18	0.30
MnO	3.00	0.08	0.91	0.17	0.22	0.09
MgO	0.21	0.01	<0.06		1.42	0.01
Total	99.31		97.81		100.63	
n	3		4		3	

Appendix Table 14: Composition of biotite from natural samples

Mineral	SRP12-19B Arbon Valley Bt1		Bt2		Bt3		Bt4	
	wt.%	1σ	wt.%	1σ	wt.%	1σ	wt.%	1σ
SiO_2	35.54	0.50	37.91	0.77	40.76	1.08	39.41	0.32
TiO_2	3.10	0.11	2.90	0.14	1.83	0.12	2.04	0.08
Al_2O_3	13.83	0.62	14.48	1.45	19.47	1.03	16.05	0.54
FeO	30.76	1.14	24.34	1.63	19.31	0.96	23.08	0.71
MnO	0.83	0.08	0.58	0.03	0.57	0.14	0.62	0.07
MgO	2.65	0.16	2.60	0.11	1.74	0.08	1.45	0.08
Na_2O	0.38	0.05	0.24	0.06	0.23	0.04	0.19	0.03
K_2O	7.82	0.30	6.00	0.19	4.98	0.28	5.89	0.16
Total	94.91		89.05		88.88		88.74	
n	5		5		6		12	

Appendix Table 15: Composition of fayalite from natural samples

Mineral	SRP09-10E Fa1	
	wt.%	1σ
SiO_2	29.77	0.25
FeO	65.33	0.34
MnO	2.05	0.11
MgO	2.19	0.02
CaO	0.25	0.01
Total	99.59	
n	5	

Appendix Table 16: Titanium contentcs in quartz

Qtz	SRP12-A05A Steer			SRP12-19B Arbon			SRP09-24c Greys L.			KRH2-1401			KRH2-1796			SRP09-13 Wolv.			SRP09-10E Huck.		
No.	Ti [ppm]	1σ [ppm]	n	Ti [ppm]	1σ [ppm]	n	Ti [ppm]	1σ [ppm]	n	Ti [ppm]	1σ [ppm]	n	Ti [ppm]	1σ [ppm]	n	Ti [ppm]	1σ [ppm]	n	Ti [ppm]	1σ [ppm]	n
1	247	14	3	<13	-	3	198	20	3	147	8	6	200	6	3	24	11	3	26	9	3
2	244	2	3	<13	-	3	260	11	3	184	13	6	179	5	3	<13	-	3	<13	-	3
3	217	1	3	<13	-	3	222	3	3	178	6	6	191	8	3	<13	-	6	<13	-	3
4	233	4	3	<13	-	3	218	13	3	199	10	6	176	12	3	<13	-	3	<13	-	3
5	234	7	4	<13	-	3	224	6	3	169	13	13	178	8	5	<13	-	3	187	5	3
6	133	59	3	25	1	3	275	6	3	181	12	6	218	3	3	191	145	3	<13	-	3
7	220	14	3	<13	-	3	241	18	3	1213	4	3	-	-	-	<13	-	3	65	5	8
8	216	4	3	<13	-	3	255	26	10	193	11	6	-	-	-	<13	-	3	<13	-	3
9	482	38	3	<13	-	3	225	17	3	179	10	6	-	-	-	<13	-	3	-	-	-
10	216	13	3	<13	-	3	253	8	3	179	9	6	-	-	-	-	-	-	-	-	-
11	53	33	3	<13	-	6	245	9	3	175	10	6	-	-	-	-	-	-	-	-	-
12	238	17	10	<13	-	3	237	14	10	164	9	6	-	-	-	-	-	-	-	-	-
13	248	13	3	<13	-	3	231	16	9	-	-	-	-	-	-	-	-	-	-	-	-
14	223	3	3	<13	-	3	238	1	3	-	-	-	-	-	-	-	-	-	-	-	-
15	249	7	3	29	2	3	227	6	3	-	-	-	-	-	-	-	-	-	-	-	-
16	252	11	3	-	-	-	-	-	-	-	-	-	-	-	-	-	-	-	-	-	-
17	216	6	3	-	-	-	-	-	-	-	-	-	-	-	-	-	-	-	-	-	-

Curriculum Vitae

Personal details

Sören Wilke
Contact: s.wilke@gmx.de

Education

05.2013 – present	**Ph.D. Petrology/Volcanology** Dissertation: "The system quartz-albite-orthoclase-anorthite-H_2O as a geobarometer: experimental calibration and application to rhyolites of the Snake River Plain, Yellowstone, USA." Leibniz Univesität Hannover (Germany)
09.2010 – 04.2013	**M.Sc. Geowissenschaften ("Earth Sciences")** Thesis: "Experimental studies of phase stability and fluid content of nephelinitic melts from Oldoinyo Lengai volcano, Tanzania." Leibniz Univesität Hannover (Germany) *final grade: 1.4 (very good)*
09.2007 – 07.2010	**B.Sc. Geowissenschaften ("Earth Sciences")** Thesis: "Differenzierung von Magmen des Parinacota Vulkans (Zentral Anden): Experimentelle Untersuchung bei 300 MPa" ("Differentiation of melts of the Parinacota volcano (central Andes): experimental investigation at 300 MPa") Leibniz Univesität Hannover (Germany) *final grade: 2.2 (good)*
2000 – 2007	Gymnasium Burgdorf (Germany) *Abitur: 2.0 (good)*
1998 – 2000	Orientierungsstufe OS I Burgdorf (Germany)
1994 – 1998	Gudrun-Pausewang Grundschule Burgdorf (Germany)

Work experience

05.2013 – present

Research Assistant
Leibniz Universität Hannover (Germany)
- Experimental work with and maintenance of high pressure vessels
- Analytics: EPMA, IR, Raman, KFT
- Supervision of Bachelor theses

2010 – 2012

Student Research Assistant (Mineralogy)
Leibniz Universität Hannover (Germany)
- Synthesis of technical glasses
- Maintenance of high pressure vessels

2009 - 2011

Student Assistant Lecturer (Geostatistics)
Leibniz Universität Hannover (Germany)
- Supervision of calculation exercises
- Introduction to statistic softwares R and GS+

02.2010 – 03.2010

Internship
Federal Bureau of Geoscience and Resources (BGR, Germany)
- Synergies for the modern mining industry
- Availability and accessibility of industrial grade and chemical grade Lithium

2008 – 2009

Student Assistant Lecturer (Crystallography)
Leibniz Universität Hannover (Germany
- Teaching basic skills in mineralogy and crystallography

Honorary posts

2012 – present

Friends of the Geosciences in Hannover, registered charitable association
- Secretary

2011 - 2012

University Panels at the Leibniz Universität Hannover
- Senate (Student Member)
- Student Parliament (Member)
- Association of geoscience students in Hannover (Member, 2007 – 2012)